

# **Process Development and Material Characterization for the Injection Molding of Long Glass Fiber- Reinforced Phenol Formaldehyde Resins**

Zur Erlangung des akademischen Grades eines

**DOKTORS DER INGENIEURWISSENSCHAFTEN**  
(Dr.-Ing.)

von der KIT-Fakultät für Maschinenbau des  
Karlsruher Instituts für Technologie (KIT)  
angenommene

**DISSERTATION**

von

**Robert Maertens, M.Sc.**

Tag der mündlichen Prüfung:	11.11.2022
Hauptreferent:	Prof. Dr.-Ing. Kay André Weidenmann
Korreferent:	Prof. Dr.-Ing. Frank Henning



# Kurzfassung

Im Rahmen dieser Arbeit wird die Verarbeitung langglasfaserverstärkter Phenolharze im Spritzgießverfahren untersucht. Es wird die Entwicklung einer neuen Spritzgießprozessvariante beschrieben, welche mithilfe einer direkten Langglasfaserzuführung die Herstellung von Bauteilen aus kurz- und langglasfaserverstärktem Phenol-Formaldehyd-Harz ermöglicht. Dabei sind die Anteile der kurzen und langen Verstärkungsfasern individuell einstellbar. Die Struktur und die Eigenschaften der mit diesem Verfahren hergestellten Bauteile werden charakterisiert und mit denen von Bauteilen aus langglasfaserverstärkten, granulatformigen Formmassen verglichen.

Im Gegensatz zu thermoplastischen Polymeren stellt das duromere Phenolharz aufgrund der irreversiblen chemischen Vernetzung bei der Verarbeitung zusätzliche Herausforderungen an die Prozessführung. Ein zentrales Entwicklungsziel dieser Arbeit ist die Abwägung zwischen der ungewünschten Faserkürzung einerseits und der erforderlichen Homogenisierung von Fasern und Phenolharz andererseits. Die Entwicklung und die Validierung von duromer-spezifischen Mischelementen für das Spritzgießen werden vorangetrieben.

Charakterisierungsmethoden für die Faserlängenmessung und die Bewertung der Materialhomogenität werden entwickelt, validiert und auf Zwischenprodukte sowie auf spritzgegossene Bauteile angewendet. Im Zusammenspiel mit etablierten Charakterisierungstechniken wie der dynamischen Differenzkalorimetrie, der Rheologie, der Rasterelektronenmikroskopie, der mechanischen Charakterisierung und der optischen Bewertung von Schlifffbildern werden somit die Prozess-Struktur-Eigenschafts-Beziehungen in der Spritzgießverarbeitung von lang- und kurzglasfaserverstärkten Formmassen herausgearbeitet.





# Abstract

Within this thesis, the processing of long glass fiber-reinforced, phenolic resins in the injection molding process is investigated. The development of a new injection molding process variant that enables the manufacturing of phenolic resin parts with an adjustable composition of short and long reinforcement glass fibers is described. The structure and the properties of parts manufactured with this process are characterized and compared to parts molded from long glass fiber-reinforced granular molding compounds, which were originally developed for compression molding applications.

In contrast to thermoplastic polymers, the thermosetting phenolic resin poses additional processing challenges due to the irreversible chemical crosslinking which takes place during the processing. A central development objective of this thesis is balancing the undesired fiber shortening with the required homogenization of the material during the processing. The development and the validation of thermoset-specific mixing elements for the injection molding are advanced.

Characterization methods for the fiber length measurement and the evaluation of the material homogeneity are developed, validated, and applied to intermediate products as well as parts manufactured in the thermoset injection molding process. By using these methods in addition to well-established characterization techniques such as differential scanning calorimetry, rheology, scanning electron microscopy, mechanical characterization and cross-sectional optical microscopy, the process-structure-property relations for the processing of long and short glass fiber-reinforced molding compounds are determined.



# Danksagung

Diese Arbeit entstand während meiner Zeit am Institut für Angewandte Materialien – Werkstoffkunde (IAM-WK) des Karlsruher Instituts für Technologie (KIT) und dem Fraunhofer-Institut für Chemische Technologie ICT. Während dieser Zeit durfte ich zahlreiche nette, hilfsbereite und spannende Personen kennenlernen, die mich in unterschiedlichster Hinsicht bei der Erstellung dieser Arbeit unterstützt haben und denen ich meinen Dank aussprechen möchte.

An erster Stelle möchte ich Prof. Dr.-Ing. Kay André Weidenmann für die hervorragende Betreuung danken. Nicht nur während der Arbeit, sondern auch schon in der Projektbeantragungsphase habe ich unsere zahlreichen Diskussionen schätzen gelernt, da aus ihnen immer wieder neue Ansätze und Lösungsideen entstanden. Für die kurzfristige Übernahme des Korreferats danke ich Prof. Dr.-Ing. Frank Henning. Durch die Schaffung der Rahmenbedingungen in der Abteilung „Polymer Engineering“ des Fraunhofer ICT wurde meine Arbeit überhaupt erst möglich.

Die unkomplizierte und offene Umgangsweise in der Abteilung „Hybride Werkstoffe und Leichtbau“ des IAM-WK, in der ich für den Zeitraum dieser Arbeit tätig sein durfte, wusste ich immer zu schätzen. Ich möchte Dr.-Ing. Wilfried Liebig sehr für diese vertrauensvolle Arbeitsweise und die damit einhergehenden Freiräume danken. Die fachlichen Diskussionen innerhalb der Arbeitsgruppe waren stets eine Bereicherung für mich.

Die Durchführung der praktischen Versuche im Technikum und im Labor wäre ohne die Unterstützung durch Kolleginnen und Kollegen am IAM-WK und am Fraunhofer ICT sowie zahlreichen Studierenden nicht denkbar gewesen. Ich möchte an dieser Stelle herzlich allen danken, die mir damit zur Seite standen.

Abschließend gilt mein Dank meiner Familie, insbesondere meinen Eltern Ines und Rainer, die mir von Kind auf Neugier und einen Wissensdurst vermittelt haben. Meiner Frau Nora danke ich für die stets aufmunternde und ermutigende Unterstützung.



# Contents

<b>Kurzfassung</b> .....	<b>i</b>
<b>Abstract</b> .....	<b>iii</b>
<b>Contents</b> .....	<b>vii</b>
<b>List of Figures</b> .....	<b>xi</b>
<b>List of Tables</b> .....	<b>xvii</b>
<b>List of Abbreviations</b> .....	<b>xix</b>
<b>List of Symbols</b> .....	<b>xxi</b>
<b>1 Introduction</b> .....	<b>1</b>
1.1 Motivation .....	1
1.2 Outline of the thesis .....	3
<b>2 Current State of Research</b> .....	<b>5</b>
2.1 Phenol-formaldehyde resins .....	5
2.1.1 Synthesis and curing .....	5
2.1.2 Phenolic molding compounds and their manufacturing.....	9
2.2 Characterization of phenolic molding compounds .....	12
2.2.1 Single metric flow-hardening measurements .....	12
2.2.2 Rheological measurements .....	15
2.2.3 Differential scanning calorimetry .....	20
2.3 Basics of the injection molding process.....	22
2.3.1 Injection molding of thermoset molding compounds .....	22
2.3.2 Long fiber injection molding processes.....	31
2.3.3 Mixing elements for the injection molding process.....	35
2.4 Fiber length measurement and influence of fiber length on mechanical properties .....	41
2.4.1 Fiber length measurement .....	41
2.4.2 Load transfer mechanisms in discontinuous fiber- reinforced polymers.....	43
2.4.3 Fiber shortening and fiber impregnation during polymer processing.....	45

---

2.5	Research questions .....	48
<b>3</b>	<b>Experimental.....</b>	<b>51</b>
3.1	Materials.....	51
3.2	Characterization methods .....	53
3.2.1	Flow-hardening characterization .....	53
3.2.2	Evaluation of material homogeneity by X-ray computed tomography image texture analysis .....	55
3.2.3	Fiber length measurement .....	58
3.2.4	Micrography of the structure .....	60
3.2.5	Mechanical characterization.....	61
3.2.6	Scanning electron microscopy.....	64
<b>4</b>	<b>Process Development.....</b>	<b>65</b>
4.1	Twin-screw extruder compounding of short fiber- reinforced phenolic resins.....	65
4.2	Long fiber direct injection molding process .....	68
4.3	Mixing elements for the injection molding process.....	76
4.3.1	Mixing during the injection phase.....	76
4.3.2	Design of screw mixing elements.....	78
<b>5</b>	<b>Results.....</b>	<b>91</b>
5.1	Compounding of short fiber-reinforced phenolic resins.....	91
5.1.1	Compounding for injection molding trials with standard barrel .....	91
5.1.2	Compounding for injection molding trials with long fiber barrel.....	95
5.2	Preliminary trials with 30 mm injection molding machine.....	99
5.2.1	Melting phenolic molding compounds by geometrical compression on the screw .....	99
5.2.2	Process data analysis for 1 <sup>st</sup> iteration screw mixing element (30 mm) .....	102
5.2.3	Mechanical and structural characterization of parts molded with 30 mm screw mixing element.....	106
5.3	Long fiber direct injection molding process development.....	108
5.3.1	Material feeding limitations in the long fiber direct injection molding process.....	108
5.3.2	Distributive and dispersive mixing during the injection phase.....	109

---

5.3.3	Process data analysis for 2 <sup>nd</sup> iteration screw mixing element (60 mm) .....	111
5.3.4	Evaluation of separate feeding of granulate and fibers.....	123
5.4	Structural analysis of intermediate process step products and molded parts.....	125
5.4.1	Evaluation of material homogeneity by X-ray computed tomography image texture analysis .....	125
5.4.2	Fiber bundle opening when using the conveying screw geometry.....	130
5.4.3	Micrography along the flow path of the material .....	132
5.4.4	Comparison of destructive and non-destructive fiber length measurement methods .....	135
5.4.5	Fiber shortening along the process route .....	137
5.4.6	Fiber shortening using the screw mixing element .....	138
5.5	Mechanical characterization .....	142
5.5.1	Mechanical characterization of SGF compounds .....	142
5.5.2	Quasistatic mechanical properties .....	143
5.5.3	Dynamic mechanical properties .....	153
5.6	Fracture analysis using scanning electron microscopy .....	158
5.6.1	Tensile test specimens .....	158
5.6.2	Charpy test specimens .....	162
<b>6</b>	<b>Discussion .....</b>	<b>167</b>
6.1	Compounding of short fiber-reinforced phenolic resins .....	167
6.2	Long fiber thermoset injection molding process development.....	169
6.3	Fiber shortening during processing of thermoset molding compounds.....	178
6.4	Homogeneity, structure and mechanical properties of the molded parts .....	182
6.5	Answers to the research questions .....	187
<b>7</b>	<b>Summary and Conclusions .....</b>	<b>190</b>
7.1	Summary.....	190
7.2	Conclusions .....	194
	<b>List of Publications.....</b>	<b>197</b>
	<b>Bibliography .....</b>	<b>199</b>





# List of Figures

Figure 2-1: Reaction of phenol with formaldehyde depending on reaction conditions [9].....	5
Figure 2-2: Curing of a phenolic resol resin [9] .....	7
Figure 2-3: Decomposition of hexamethylenetetramine to ammonia and formaldehyde [9].....	7
Figure 2-4: Curing of a phenolic novolac resin [9] .....	8
Figure 2-5: Excitation and response for oscillatory rheology measurements [70] .....	19
Figure 2-6: Standard thermoset injection molding process .....	22
Figure 2-7: Structure of the melting zone of a phenolic molding compound in the screw.....	23
Figure 2-8: Flow front of thermoset molding compounds during mold filling [55,91,93] .....	25
Figure 2-9: Temperature and viscosity curve according to Kaiser [98] and Stitz and Keller [43].....	26
Figure 2-10: Exemplary machine and mold data for thermoset injection molding.....	27
Figure 2-11: Static mixing nozzle [139].....	36
Figure 2-12: Characteristic dimensions of a spiral Maddock mixing element.....	39
Figure 2-13: Comparison of models for load transfer from matrix to fiber [18] .....	44
Figure 2-14: Critical fiber length as a function of applied matrix strain [173] .....	44
Figure 3-1: Visualization of PF-SGF <sub>x</sub> -LGF <sub>y</sub> formulations.....	52
Figure 3-2: Dilution device for representative taking of fiber length measurement samples [15] .....	59
Figure 3-3: Post-cure cycle for molded plates [26] .....	61
Figure 3-4: Cutting pattern for test specimens [26].....	62
Figure 4-1: Twin-screw extruder layout and temperature profile [24] .....	65
Figure 4-2: Manufactured PF-SGF40-LGF0 phenolic molding compound.....	66

---

Figure 4-3: Comparison of the standard thermoset injection molding process (a) with the long fiber process variant “standard plasticizing unit” (b).....	69
Figure 4-4: Signal flow chart for long fiber process peripheral devices control [218–220].....	71
Figure 4-5: Comparison of standard thermoset barrel (a) to long fiber barrel (b).....	72
Figure 4-6: Comparison of mixing element (a) and standard screw tip (b).....	73
Figure 4-7: Long fiber injection molding process variant “LGF plasticizing unit with conveying screw tip and separate granulate feed port”.....	76
Figure 4-8: Dispersive mixing during injection by means of adjustable sprue bushing (a) and small machine nozzle (b).....	77
Figure 4-9: Nozzle including a static mixer designed for the thermoset injection molding process.....	78
Figure 4-10: Calculated pressure drop for the 30 mm thermoset mixing element.....	82
Figure 4-11: 30 mm spiral mixing element for the thermoset injection molding process.....	83
Figure 4-12: Position of mixing and wiping flight for the thermoset mixing element [25,26].....	84
Figure 4-13: Analytical calculations for 60 mm thermoset mixing element.....	88
Figure 4-14: Pressure profile for the long fiber screw using the optimized mixing element geometry.....	89
Figure 5-1: $\Delta H_R$ and SME of SGF molding compounds for standard plasticizing unit trials [24].....	92
Figure 5-2: Apparent density of SGF molding compounds.....	92
Figure 5-3: Fiber length measurement for short fiber molding compounds [24].....	93
Figure 5-4: Absolute value of complex viscosity $\eta^*$ for SGF compounds for standard barrel trials.....	94
Figure 5-5: Injection pressure for short fiber-reinforced molding compounds.....	95
Figure 5-6: $\Delta H_R$ and SME of SGF molding compounds for long fiber barrel trials.....	96
Figure 5-7: Absolute value of complex viscosity $\eta^*$ for SGF compounds for long fiber barrel trials.....	97

---

Figure 5-8: Multiwave rheology measurements for PF-SGF0 neat resin molding compound.....	98
Figure 5-9: Weighted average fiber length fraction for short fiber molding compounds [24].....	99
Figure 5-10: Melting element experimental setup (a), extruded compound (b) and results (c).....	101
Figure 5-11: Screw position and injection pressure SGF compound with 30 mm mixing element.....	103
Figure 5-12: Screw position and injection pressure LGF compound with 30 mm mixing element.....	104
Figure 5-13: Test specimens molded with 30 mm mixing element and conveying screw .....	105
Figure 5-14: Flexural properties of parts molded with 30 mm mixing element.....	106
Figure 5-15: SEM for PF-SGF0-LGF55 flexural test specimens .....	107
Figure 5-16: Influence of machine nozzle type on injection pressure for PF-SGF40-LGF0.....	109
Figure 5-17: Influence of sprue gap height on injection pressure PF-SGF40-LGF0.....	110
Figure 5-18: Injection work for distributive and dispersive mixing during the injection phase.....	111
Figure 5-19: Material and process variation for injection molding trials with 60 mm mixing element [26] .....	112
Figure 5-20: Injection pressure LGF and SGF formulations conveying and mixing screw [26] .....	114
Figure 5-21: Screw position LGF and SGF formulations conveying and mixing screw [26].....	115
Figure 5-22: Plasticizing work and injection work PF-SGF0-LGF30 screw speed study [26].....	116
Figure 5-23: Plasticizing work and injection work PF-SGF0-LGF30 process stability study [26] .....	117
Figure 5-24: Plasticizing work screw layout and material variations [26] .....	118
Figure 5-25: Injection work for screw layout and material variations .....	119
Figure 5-26: Injection pressure for the non-processable PF-SGF36.3-LGF8.2 formulation.....	121
Figure 5-27: Plasticizing work and plasticizing time for PF-SGFx-LGFy formulations with $\phi = 44.5$ wt.-%.....	122

---

Figure 5-28: Plasticizing time for SGF and LGF compounds using different process layouts.....	123
Figure 5-29: Screw position over time for separate and common material feeding locations .....	124
Figure 5-30: Material distribution on 60 mm screw with 1.5 mm gap compression sleeve .....	125
Figure 5-31: Fiber bundles on fracture surface .....	126
Figure 5-32: Specimen location for material homogeneity investigations [25].....	126
Figure 5-33: $\mu$ CT image before and after statistical region merging for specimen group 1 [25] .....	128
Figure 5-34: ASM calculation for PF-SGF0-LGF30 and PF-SGF20-LGF30 formulations [25].....	129
Figure 5-35: ASM values for PF-SGF0-LGF30 formulation process parameter variations [25].....	130
Figure 5-36: $\mu$ CT image slice of PF-SGF24-LGF21 part molded with conveying screw.....	131
Figure 5-37: Fraction of opened fiber bundles for $\phi = 44.5$ wt.-% formulations .....	132
Figure 5-38: Optical micrograph for PF-SGF0-LGF30 and PF-SGF28.5-LGF0 parallel to flow.....	133
Figure 5-39: Skin layer fraction vs. flow path length for selected 30 wt.-% fiber content specimens .....	135
Figure 5-40: $\mu$ CT images for the non-destructive fiber length measurement [15].....	136
Figure 5-41: Comparison of destructive and non-destructive fiber length measurement [15].....	137
Figure 5-42: Fiber shortening along process for PF-SGF55-LGF0 and PF-SGF0-LGF55 [15].....	138
Figure 5-43: Weighted average fiber length for PF-SGF0-LGF30 using mixing element [26].....	139
Figure 5-44: Weighted average fiber length for PF-SGF0-LGF44.5 using mixing element .....	140
Figure 5-45: Weighted average fiber length for PF-SGF16-LGF14 using mixing element .....	141
Figure 5-46: Weighted average fiber length for PF-SGF28.5-LGF0 using mixing element .....	142
Figure 5-47: Tensile and impact properties of SGF compounds with fiber content $\phi = 0 \dots 60$ wt.-%.....	143

---

Figure 5-48: Tensile strength results for “mixing during injection phase” process development .....	144
Figure 5-49: Tensile stress-strain curves for exemplary PF-SGF-LGF formulations.....	145
Figure 5-50: Tensile strength of 30 wt.-% specimens molded with 60 mm mixing element [26] .....	146
Figure 5-51: Young’s modulus of 30 wt.-% specimens molded with 60 mm mixing element.....	147
Figure 5-52: Tensile strain at break of 30 wt.-% specimens molded with 60 mm mixing element.....	148
Figure 5-53: Comparison of tensile strength for PF-SGF0-LGF55 long fiber granulate and PF-SGF0-LGF30 direct process .....	149
Figure 5-54: Pseudo Young's modulus for circular test specimens made from SGF formulations.....	151
Figure 5-55: Pseudo Young's modulus for circular test specimens made from LGF formulations.....	152
Figure 5-56: Ellipse axes ratio for SGF and LGF formulations .....	153
Figure 5-57: Impact strength as a function of fiber content in 0° and 90° orientation .....	154
Figure 5-58: Charpy impact strength of 30 wt.-% specimens molded with 60 mm mixing element.....	155
Figure 5-59: Comparison of typical force-displacement curves for puncture impact test .....	156
Figure 5-60: Puncture impact energy overview for SGF and LGF formulations .....	157
Figure 5-61: Puncture impact energy of 30 wt.-% specimens with 60 mm mixing element [26] .....	158
Figure 5-62: SEM for PF-SGF28.5-LGF0 tensile test specimens with conveying and mixing screw.....	159
Figure 5-63: SEM detail image for PF-SGF28.5-LGF0 tensile test specimen.....	160
Figure 5-64: SEM for PF-SGF0-LGF55 tensile test specimens with conveying and mixing screw .....	161
Figure 5-65: SEM detail image for PF-SGF0-LGF55 granulate tensile test specimen.....	162
Figure 5-66: SEM for SGF granulate and LGF direct process Charpy test specimens [26] .....	163
Figure 5-67: SEM for PF-SGF0-LGF44.5 direct process with conveying and mixing screw .....	165

---

Figure 5-68: SEM for PF-SGF16-LGF14 formulation.....	166
Figure 6-1: Pressure and screw position during plasticization of PF-SGF0-LGF30 material [26] .....	173

# List of Tables

Table 2-1: Formulation of a PF31 wood flour filled phenolic molding compound [44] .....	9
Table 2-2: Formulations for two inorganically filled molding compounds [46,47].....	10
Table 2-3: Common flow-hardening test methods for thermoset molding compounds [54,56–60].....	13
Table 2-4: Long fiber thermoplastic injection molding processes [113,127–133] .....	32
Table 2-5: Distributive mixing elements for extrusion and injection molding processes [109].....	37
Table 2-6: Dispersive mixing elements for extrusion and injection molding processes [109].....	37
Table 3-1: Parameters for oscillatory rheology measurements .....	55
Table 3-2: Image acquisition parameters for X-ray computed tomography homogeneity evaluation [25].....	57
Table 3-3: X-ray computed tomography image acquisition parameters for non-destructive fiber length measurement [15].....	60
Table 4-1: Specifications of the KM 550 / 2000 GX injection molding machine .....	68
Table 4-2: Comparison of standard and long fiber screw geometries .....	72
Table 4-3: Overview of long fiber direct process layout variants .....	75
Table 4-4: Calculation values for designing the 30 mm thermoset mixing element.....	80
Table 4-5: Calculation values for designing the 60 mm thermoset mixing element.....	86
Table 4-6: Parameters for PSI calculation of 60 mm mixing element .....	87
Table 5-1: Experimental parameters for melting element preliminary trials .....	100
Table 5-2: Process parameters for the evaluation of the 30 mm thermoset mixing element .....	102
Table 5-3: Visual evaluation of micrographs of specimens with 30 wt.-% fiber content [226].....	133

---

Table 6-1: Process and material parameters for calculating shear stress in the machine nozzle .....	181
Table 6-2: Process and material parameters for calculating shear stress in the mixing element .....	182



# List of Abbreviations

$\mu$ CT	<i>micro computed tomography</i>
APC plus	<i>Adaptive Process Control plus</i>
ASM	<i>angular second moment</i>
BFC	<i>back flow compensation</i>
BMC	<i>bulk molding compound</i>
CPI	<i>Composite Products, Inc.</i>
CRD	<i>Chris Rauwendaal dispersive</i>
CSD	<i>controlled strain deformation</i>
CSV	<i>comma separated values</i>
CTM	<i>cavity transfer mixer</i>
DCIM	<i>direct compounding injection molding</i>
DEA	<i>dielectric analysis</i>
DIF	<i>direct incorporation of continuous fibers</i>
DSC	<i>differential scanning calorimetry</i>
E-CR	<i>E-glass corrosion resistant</i>
FASEP	<i>fiber length measurement system (no abbreviation)</i>
FDC	<i>fiber direct compounding</i>
FLD	<i>fiber length distribution, fiber length distribution</i>
GLCM	<i>graylevel co-occurrence matrix</i>
HMTA	<i>hexamethylenetetramine</i>
IMC	<i>injection molding compounder</i>
IR	<i>infrared</i>
ISO	<i>International Organization for Standardization</i>
LGF	<i>long glass fibers</i>
NBR	<i>acrylonitrile-butadiene rubber</i>
OFNL	<i>orifice flow test with press force class "L"</i>
OFT	<i>orifice flow test</i>
P/F	<i>phenol-formaldehyde ratio</i>
PA66	<i>polyamide 6.6 with glass fibers</i>
PF-SGF55	<i>phenol-formaldehyde resin reinforced with 55 wt.-% short glass fibers</i>
PLC	<i>programmable logic control</i>
PP	<i>polypropylene</i>
PVA	<i>polyvinyl acetate</i>
RTM	<i>resin transfer molding</i>
SEM	<i>scanning electron microscopy</i>
SGF	<i>short glass fibers</i>
SMC	<i>sheet molding compound</i>

---

SME

*specific mechanical energy input, specific  
mechanical energy input*

TGA

*thermogravimetric analysis*

# List of Symbols

Symbol	Description	Unit
<b>uppercase letters</b>		
$D$	fiber diameter	$\mu\text{m}$
$E_{\parallel}$	longitudinal (in fiber direction) modulus	GPa
$E_{\perp}$	transverse (perpendicular to fiber direction) modulus	GPa
$E$	general term for modulus	GPa
$E_{\text{flex}}$	flexural stiffness	GPa
$E^*$	pseudo Young's modulus	GPa
$E_{\text{puncture}}$	puncture impact energy	J
$F_{\text{d}}$	shape factor drag flow	-
$F_{\text{p}}$	shape factor pressure flow	-
$F$	force	N
$G'$	storage modulus	N/mm <sup>2</sup>
$G''$	loss modulus	N/mm <sup>2</sup>
$G^*$	complex shear modulus	N/mm <sup>2</sup>
$H$	enthalpy	J
$\Delta H_{\text{R}}$	total heat of reaction	J
$H_{\text{ch}}$	flute (channel) height	mm
$H_{\text{gap}}$	shear gap height	mm
$\text{Inj}_{\text{St}}$	start time of injection phase	s
$\text{Inj}_{\text{End}}$	end time of injection phase	s
$L$	fiber length	$\mu\text{m}$
$L_0$	initial fiber length	$\mu\text{m}$
$L_c$	critical fiber length	$\mu\text{m}$
$L_{\infty}$	asymptotic fiber length	$\mu\text{m}$
$L_m$	axial length of mixing element	mm
$L_n$	number average fiber length	$\mu\text{m}$
$L_p$	weighted average fiber length	$\mu\text{m}$
$M$	torque	Nm
$N_g$	number of graylevels in an image	-

<b>Symbol</b>	<b>Description</b>	<b>Unit</b>
$N_x$	number of pixels in x-direction	-
$N_y$	number of pixels in y-direction	-
$P$	power	W
$Pl_{St}$	start time of plasticizing process	s
$Pl_{End}$	end time of plasticizing process	s
$\dot{Q}$	heat flow rate	W
$R$	number of neighboring cell pairs	-
$R_{th}$	thermal resistance	K/W
$T$	temperature	°C
$Tt$	roving linear weight	tex
$\dot{T}$	heating rate	K/min
$T_g$	glass transition temperature	°C
$U$	voltage	V
$V$	volume	m <sup>3</sup>
$\dot{V}$	volumetric flow rate	m <sup>3</sup> /s
$W_{ch}$	flute (channel) width	mm
$W_{gap}$	shear gap width	mm
$W_{Inj}$	injection work	J
$W_{Imp}$	impactor and pendulum work capacity	J
$W_{Plast}$	plasticizing work	J
<b>lower case letters</b>		
$a$	ellipse major axis length	m
$b$	ellipse minor axis length	m
$d$	diameter	m
$h$	height, thickness	m
$m$	mass	kg
$m_{Res}$	residual mass in the OFT test	kg
$\dot{m}$	mass flow	kg/s
$n$	number	-
$n$	screw speed	1/min
$p$	pressure	bar
$p(i, j)$	number of graylevel co-occurrences	-
$r$	radius	m

Symbol	Description	Unit
$r_{\text{Ellipse}}$	ellipse axes ratio	-
$s$	distance	m
$t$	time	s
$v$	(translatory) velocity	m/s
$\Delta v$	relative velocity in rheological measurements	m/s
$z_m$	unrolled length of mixing element	mm
Greek letters		
$\alpha$	angle increment for circular tensile test specimens	°
$\gamma$	angle for rheology measurements	°
$\gamma_0$	excitation amplitude	°
$\dot{\gamma}$	shear rate	1/s
$\delta$	response lag	°
$\varepsilon$	strain	-
$\eta$	dynamic viscosity	Pa s
$\eta_a$	apparent viscosity	Pa s
$\eta^*$	complex viscosity	Pa s
$\eta_{\text{Hydr}}$	hydraulic efficiency	-
$\mu$	debonding factor in Cox model	-
$\rho$	density	kg/m <sup>3</sup>
$\sigma$	stress	MPa
$\sigma_m$	ultimate tensile strength	MPa
$\tau$	shear stress	N/mm <sup>2</sup>
$\tau_{\text{int}}$	interfacial shear strength	MPa
$\tau_0$	shear stress amplitude	MPa
$\varphi$	fiber volume fraction	-
$\varphi_{\text{fl}}$	flute angle	°
$\phi$	fiber weight content	-
$\psi$	fraction of opened fiber bundles	-
$\omega$	angular frequency	rad/s



# 1 Introduction

## 1.1 Motivation

Phenolic resins are among the oldest industrially synthesized and processed polymers. Since their invention by Baekeland in 1909 [1], they have been used in a wide variety of applications and serve as important constituents in wood composite adhesives, foams and insulation material, refractories as well as in fiber-reinforced molding compounds [2]. Composite parts manufactured from such fiber-reinforced phenolic molding compounds have a high maximum operating temperature, excellent chemical resistance, and a good dimensional accuracy. Consequently, they are often used in the direct surrounding of internal combustion engines [3–5]. Recent developments have demonstrated that parts made from phenolic molding compounds can also be used in the future-oriented field of electric motors for vehicle applications [6–8].

One of the key challenges for the wider use of phenolic resin molding compounds is their brittle failure behavior [9–11]. To increase their impact toughness, two general possibilities exist. First, the phenolic resin can be chemically altered by using additives and modifiers [10–12]. Second, reinforcement fibers can be compounded into the resin. The achievable toughening effect of reinforcement fibers in a composite material significantly depends on the fiber content and the fiber length. In general, for achieving good impact properties, high average fiber lengths are important [12–14]. However, in the state-of-the-art injection molding process of phenolic molding compounds, typically only small average weighted fiber length values of  $L_p = 0.3 \text{ mm} \dots 0.35 \text{ mm}$  are achieved [15].

To quantify the required fiber length for a significant improvement of the mechanical properties, the fundamental models for describing the load transfer from the matrix into the fibers are used. Analytical approaches have been proposed by Kelly and Tyson [16], Cox [17] and Piggott [18]. They assume that the external load is transferred into the fibers via shear stress  $\tau_{\text{int}}$  in the fiber-matrix interface. Using the fiber diameter  $D$  and the tensile

strength of the reinforcement fiber  $\sigma_F$ , they calculated a critical fiber length according to Equation (1-1)

$$L_c = \frac{D\sigma_F}{2\tau_{\text{int}}} \quad (1-1)$$

which is considered the shortest fiber length that is required for fully utilizing the fibers' reinforcement potential. A fiber length  $L < L_c$  still leads to improved mechanical properties, but does not fully use their potential. Even though literature values for the critical fiber length  $L_c$  in glass fiber-reinforced phenolic molding compounds vary in a range between  $L_c = 2$  mm [19] and  $L_c = 8$  mm [20], it can be assumed that – despite the numerous factors influencing  $L_c$  – the above mentioned fiber length in typical, commercially available compounds today is significantly below  $L_c$ . Long reinforcement fibers are particularly beneficial for enhancing the impact strength [12–14]. Thus, increasing the fiber length in parts manufactured from glass fiber-reinforced phenolic molding compounds is an attractive development objective [12].

To achieve this aim, manufacturers of fiber-reinforced polymer composite parts typically can choose between using a semi-finished material like a long fiber granulate or a direct process, which promises longer fibers in the molded part. This decision-making process is a trade-off between higher material costs for a semi-finished long fiber material and more complex direct processing equipment, which typically also involves higher capital investment costs [21,22]. Additionally, direct processes offer a higher formulation flexibility for tailoring the material to the specific application [23]. For fiber-reinforced thermoplastic polymers, both process routes are well-established. Materials and machinery equipment are available from several suppliers. However, for thermosets, neither long fiber-reinforced injection molding compounds nor long fiber injection molding processes exist. It is the scope of this thesis to develop such a process and to identify the central processing challenges. By characterizing the mechanical properties of the manufactured parts and comparing them to parts injection molded from granular long fiber-reinforced compression molding compounds, a decision-making basis for the direction of further developments shall be established.



## 1.2 Outline of the thesis

The first central aim of this thesis is the development of a new injection molding process variant that allows the manufacturing of phenolic resin components with an adjustable composition of short and long reinforcement glass fibers. Based on this process, the second central aim is investigated, namely the material characterization of the parts manufactured from the long glass fiber-reinforced phenolic molding compounds.

To embed these aims in the context of the state of research, Chapter 2 starts with an overview of the chemistry of phenol-formaldehyde resins and the composition of typical, commercially available phenolic molding compounds for the injection molding process. The established characterization methods for the flow-hardening behavior as well as rheological and thermal properties are presented. Based on the conventional, established injection molding process for thermoplastics, the injection molding of thermoset molding compounds is explained. Existing process developments for increasing the fiber length and for improving the homogeneity of thermoplastic materials are described. To stress the importance of the fiber length for the mechanical properties of a discontinuously fiber-reinforced composite material, the load transfer mechanisms between matrix and fiber as well as the mechanisms for the fiber shortening during the processing of these materials are explained. The different available measurement processes for the quantification of the fiber length are summed up and based on the description of the state of research, central questions for this thesis are formulated.

The experimental methods and the materials used are listed in Chapter 3. While the parameters and the processes for some characterization methods are based on the state of research, others have been developed and improved. This applies to the method for investigating the homogeneity of the fiber-matrix composite material and to the fiber length measurement process.

Chapter 4 describes the work that was carried out for achieving the first central aim of this thesis. The process development both for the twin-screw extruder compounding and the injection molding of glass fiber-reinforced phenolic resins is presented. The main challenge of the process development was to achieve a good homogenization of the glass fibers in the phenolic resin matrix. For this reason, the conceptualization and the design of novel mixing elements for the thermoset injection molding process is described.

The subsequent Chapter 5 starts with the presentation of the development results for the twin-screw extruder compounding process of short glass fiber-reinforced phenolic molding resins. After this, results of preliminary trials with a smaller, 30 mm injection molding machine are presented. The injection molding process development results are analyzed by means of machine and process data. The results of the structural and mechanical characterization of the molded parts serve as a basis for Chapter 6 in which the central research questions are answered and the characterization results are reflected based on the state of research.

Parts of the methods and the results that are presented in this thesis have been published by the author in previous publications [15,24–26]. Wherever these results are used in this thesis, it is clearly noted.

## 2 Current State of Research

### 2.1 Phenol-formaldehyde resins

#### 2.1.1 Synthesis and curing

Phenolic resins are thermosetting polymers which are obtained by the reaction of phenol with formaldehyde. The most important type of phenol is the unsubstituted phenol, which can react with formaldehyde in its both ortho positions (o in Figure 2-1) as well as in its para position (p) [9]. A reaction with the meta position (m) of the phenol is untypical.

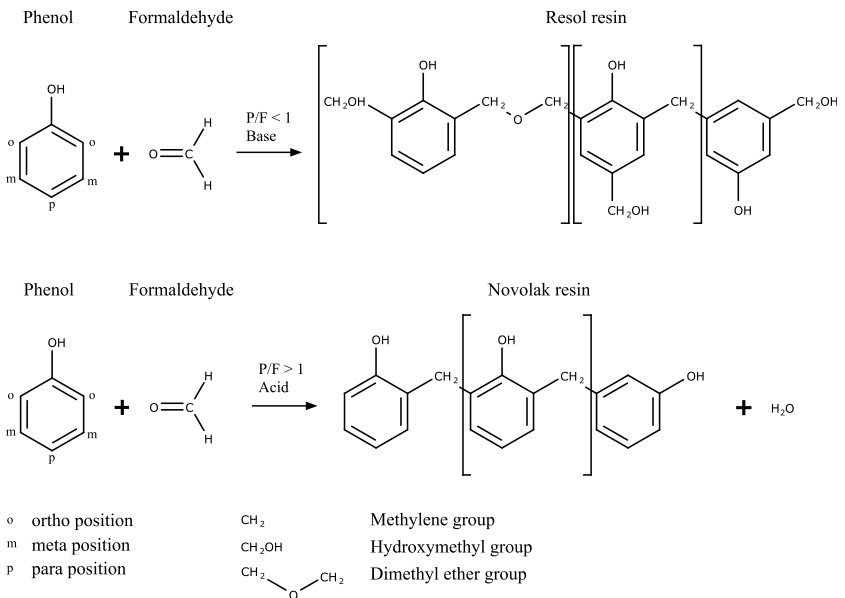


Figure 2-1: Reaction of phenol with formaldehyde depending on reaction conditions [9]

This multi-functionality of the phenol towards the formaldehyde enables the formation of the typical three-dimensional thermoset network. An average functionality of the phenols in the range of 1.49 ... 1.72 has been reported by Shipp and Solomon [27]. The functionality of the phenolic resins depends on

the stoichiometry of the synthesis reaction [9], which is why the reactions are intentionally not balanced. Substituted phenols have a reduced functionality and form linear chains or stop the reaction. The first step in the synthesis of phenol-formaldehyde resins is the addition of formaldehyde to phenol.

The type of reaction depends on the reaction conditions, mainly the phenol-formaldehyde ratio P/F and the pH value of the catalyst as can be seen in Figure 2-1 [28]. An excess of formaldehyde ( $P/F < 1$ ) leads in combination with a base catalyst to the addition of formaldehyde to phenol in the ortho and para positions [29]. The ortho positions are less reactive than the para position, but since two ortho positions are available at the phenol, there is no distinct preferential position for the cross-linking [30,31]. Common catalysts for the synthesis of resol resins are alkali metal hydroxides, alkaline earth hydroxides or ammonia [9,29]. The connection between the phenol cores is established via dimethyl ether and methylene groups. Terminal groups such as hydroxymethyl groups result from the addition of formaldehyde to one of the other functional positions of the phenol. Due to the formaldehyde excess, free formaldehyde remains in the synthesized resin after the reaction is slowed down by cooling the reactants. [32]

A lack of formaldehyde ( $P/F > 1$ ) and an acid catalyst causes a condensation reaction between the phenol and formaldehyde, resulting in a connection of the phenol cores via methylene bridges and the formation of water as a reaction product [29,33]. Common catalysts are oxalic or sulfuric acid [33]. The position of the connection between the phenol cores can be adjusted by choosing the pH value. Lower values  $pH < 3$  favor the condensation in para position, whereas higher pH values between  $3 < pH < 5$  result in connections via the ortho position, as it is depicted in Figure 2-1 [9]. In contrast to the resols with their reactive hydroxymethyl groups, the novolacs do not have any reactive groups after synthesis. They show a reversible melting and solidifying behavior like thermoplastic polymers. Depending on the length of the novolac chain, their softening temperature range varies between  $T = 60\text{ °C} \dots 100\text{ °C}$  [9].

In the case of phenolic molding compounds for the injection molding process, these intermediate phenolic resins are then used in the compounding process, where fillers, fibers and additives can be added according to the requirements. The compounding process is described in Section 2.1.2. The

final curing of the resin takes place after injecting the compound into the mold [10]. For resol resins, the curing process is shown in Figure 2-2.

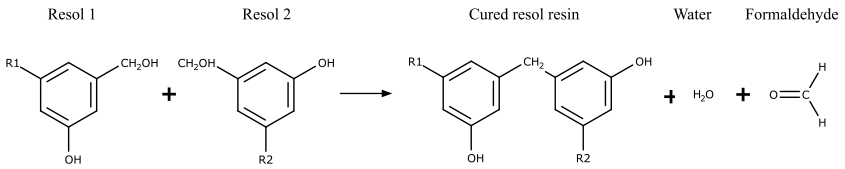


Figure 2-2: Curing of a phenolic resol resin [9]

Resol resins can be cured using heat or acids. Relevant for molding compound applications is the curing by heat, which is described below. At temperatures above  $T = 150\text{ }^\circ\text{C}$ , the free hydroxymethyl groups ( $\text{CH}_2\text{OH}$ ) of the oligomer intermediates form methylene bridges ( $\text{CH}_2$ ) with the release of water and formaldehyde. The formaldehyde accelerates the curing by serving as a crosslinking agent [28,34].

Since a formaldehyde shortage is prevalent in the resin synthesis of novolacs, a formaldehyde releasing hardener is required. Typically, hexamethylenetetramine (HMTA) is used. It is prepared by reacting formaldehyde with ammonia. The reverse reaction shown in Figure 2-3 is then used for donating the formaldehyde required for curing the novolac resin [9].

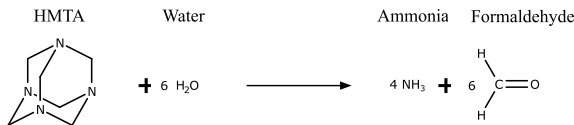


Figure 2-3: Decomposition of hexamethylenetetramine to ammonia and formaldehyde [9]

The hydrolytic decomposition of the HMTA starts at temperatures of  $T = 110\text{ }^\circ\text{C} \dots 120\text{ }^\circ\text{C}$  [35]. Below the HMTA decomposition temperature, a reversible melting and solidifying of the novolac resin is possible. With the free formaldehyde, methylene bridges ( $\text{CH}_2$ ) between the novolac intermediates are formed with the condensation of water. The reaction is shown in Figure 2-4.

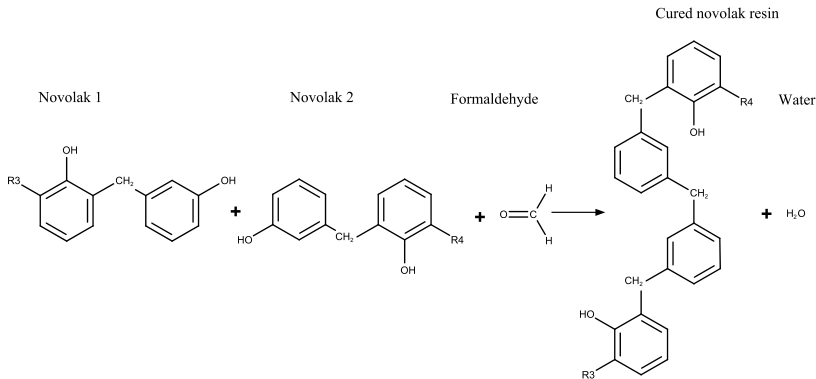


Figure 2-4: Curing of a phenolic novolac resin [9]

Since the released water participates in the further hydrolysis of the remaining HMTA, in total only ammonia is formed as a low-molecular reaction product of the HMTA decomposition. With increasing degree of crosslinking of the thermoset network, the glass transition temperature  $T_g$  increases. Once it surpasses the curing temperature, vitrification occurs and a reduction in molecular mobility is observed [36]. For phenolic resins, a sufficiently long hardening time leads to a  $T_g$  that is  $\Delta T = 20 \text{ K} \dots 30 \text{ K}$  above the curing temperature [37]. Due to the reduced mobility in the vitrified state, increasing the degree of cross-linking by prolonging the curing time is not feasible. If a further increase of  $T_g$  is required by the application, a post-curing oven treatment must be performed. When subjecting the resin to temperatures close to  $T_g$ , the mobility of the molecules increases, making rearrangements and further cross-linking possible [36,38]. However, it is important not to post-cure above the current  $T_g$ , as this can cause thermal degradation of the phenolic resin due to free radicals [38,39]. Furthermore, the formation of cracks due to the pressure generated by escaping gaseous reaction products is possible [40]. Instead, a temperature ramp with an oven temperature remaining below  $T_g$  is recommended for post-curing [38]. As cross-linking progresses during the post-curing process, the mechanical properties of the resin at elevated temperatures can be improved, such as creep resistance under load and dimensional stability. Due to the high oven temperatures during the post-curing process, oxidation of the part surface will occur if the post-curing is done in air atmosphere. This superficial oxidation causes a weakening of the material, which leads to a decrease in strength. When performing the post-

curing under an inert atmosphere, no oxidation and no significant decrease in strength has been observed [41]. At a theoretical 100 % degree of cure, both novolac and resol resins only consist of phenol cores that are connected via a dense network of methylene bridges ( $\text{CH}_2$ ). However, such a perfect network is never achieved due to the reduced mobility with increasing degree of cure.

## 2.1.2 Phenolic molding compounds and their manufacturing

Phenolic resins are used in a large variety of applications, the five largest applications being – in descending order – wood adhesives, molding compounds, insulation, laminates and foundry sand binders [42]. The following paragraph gives a detailed overview of phenolic molding compounds used for injection molding, transfer molding, and compression molding processes. Like most thermoset polymers, cured phenolic resins have an inherently brittle behavior [9], a high curing shrinkage [35,43] and overall unfavorable properties in a neat resin (i.e. unfilled) state. For this reason, phenolic molding resins are compounded with fillers and reinforcements to improve their properties for specific applications. Typical organic fillers for phenolic molding compounds are wood flour, bark flour, shell flour as well as cotton or paper fibers [10]. These organic fillers have a low density and a low price, resulting in a lightweight and price-competitive molding compound. A very common and widely used wood flour filled phenolic molding compound is PF31, for which the formulation according to DIN 7708 [44] is listed in Table 2-1.

Table 2-1: Formulation of a PF31 wood flour filled phenolic molding compound [44]

<b>Component</b>	<b>content in %-wt.</b>
<b>Novolac resin + HMTA</b>	47
<b>Accelerator</b>	2
<b>Release agent</b>	2
<b>Color pigment</b>	2
<b>Wood flour</b>	30
<b>Inorganic filler</b>	17

Typical applications for organically filled phenolic molding compounds are knobs and handles for household appliances, where the material is known for

its high thermal resistance and competitive price. In the past, entire housings for household appliances and electrical devices were made from phenolic molding compounds [45]. Today, electrical devices like switches, power outlets, transformer bobbins and circuit breakers are also made from organically filled molding compounds due to their high inherent flame retardancy [10]. Commonly used inorganic fillers are glass beads, calcium carbonate, clay, mica, silica, talc, wollastonite and metallic hydroxides [10]. Due to their higher modulus compared to the organic fillers, they increase the overall stiffness of the molded parts. Furthermore, heat resistance, dimensional stability and molding shrinkage are reduced. For further improving strength, stiffness and especially impact toughness, glass fibers are added to the molding compound [9]. The compositions of two typical, inorganically filled phenolic molding compounds (Vyncolit® X6952 [46] and Bakelite® PF 1110 [47]) are listed in Table 2-2.

Table 2-2: Formulations for two inorganically filled molding compounds [46,47]

<b>Component</b>	<b>content in %-wt.</b>	
	<b>Vyncolit® X6952</b>	<b>Bakelite® PF 1110</b>
<b>Novolac resin + HMTA</b>	39	14
<b>Accelerator</b>	2	2
<b>Release agent</b>	2	2
<b>Color pigment</b>	2	2
<b>Glass fibers</b>	55	35
<b>Glass beads</b>	0	45

In contrast to the organically filled phenolic molding compounds, these materials have high thermomechanical properties, dimensional stability at elevated temperatures and excellent chemical resistance, enabling their use in automotive applications such as oil and water pumps, intake manifolds, brake pistons and transmission valve blocks [10,48]. Recent developments investigate the use of inorganically filled phenolic molding compounds for structural combustion engine [4] and electric motor applications [6]. The typical competitor material for these high-performance phenolic molding compounds is die-cast aluminum. While aluminum typically has a lower raw material price than the phenolic molding compounds, the total costs of the polymer parts can be lower due to a higher manufacturing accuracy by net-shape molding, which reduces the number of required post-processing machining



steps. For water pump housings, a cost reduction of 10 % in combination with a reduction of the part weight by 30 % is possible [49].

To ease the processing of the molding compounds, release agents with a content of approximately 0.5 wt.-% ... 2 wt.-% are added to the compound, reducing sticking of the material to machine parts such as screw and barrel as well as facilitating the demolding of the cured part. Common release agents are fatty acids and stearates based on calcium, zinc and magnesium [10]. Since the surface of the cured phenolic resin parts oxidizes over time and consequently undergoes discoloration, the molding compounds are typically mixed with colorants at contents of 0.5 wt.-% ... 2 wt.-%. Depending on the application, dyes and / or pigments can be used. Typical colors for commercially available molding compounds are black and dark green. One notable exception is the Vyncolit® X6952 Green [46] molding compound by Sumitomo Bakelite, Co. which is used within this work. It contains copper phthalocyanine as a blue color pigment. Upon heating, it reacts to phthalocyanine green by chlorination [50]. The temperature window of this reaction coincides with the curing temperature of the resin, which means that the color change can be used as an indicator for the material's temperature history. A green color indicates a mostly cured compound, whereas a blue color indicates that the resin is still in its oligomer state. Depending on the specific application, further additives can be compounded into the resin. For example, lubricants such as graphite and molybdenum disulfide improve the tribological properties of the molded part by reducing the friction coefficient [10]. Toughness modifiers like acrylonitrile-butadiene rubber (NBR) and polyvinyl acetate (PVA) or other thermoplastic polymers can increase the elongation at break and impact energy absorption, but they lower the heat resistance and the dimensional stability [10,12]. Reinforcement fibers such as glass or carbon fibers are used for toughening and strengthening the compound [12].

For facilitating the further processing, all components are blended, forming the granular phenolic molding compound. The original compounding process can be described as a liquid resin process. In this process, the phenolic resin is in solution, which means that it can be cold mixed together with the other components of the molding compound. Subsequently, a drying process is required for removing the solvent. In contrast, the melting process starts with the raw materials in a solid, powdery state. They are blended with the other components by melting and mixing, followed by a cooling process [9]. The melting and mixing steps can either be carried discontinuously in masticators

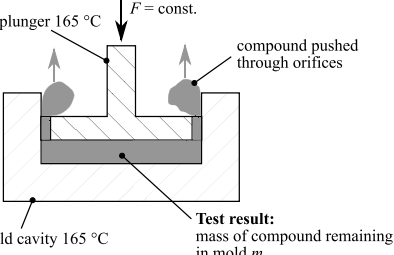
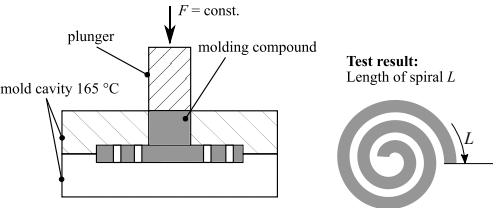
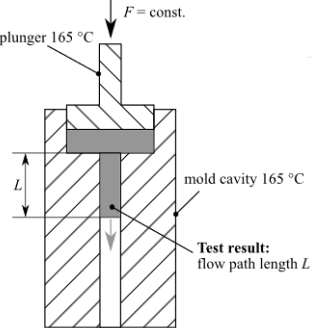
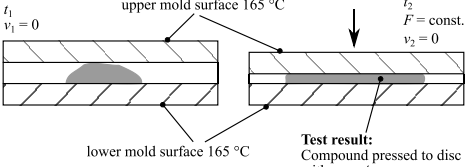
and calendar mills or continuously in extruders [51–53]. Today, most molding compounds are produced using extrusion processes in single- or twin-screw extruders. A continuous monitoring of the manufacturing process by measuring the flow-hardening-behavior of the molding compound is typical for modern production facilities. After the drying (liquid resin process) or the cooling (melting process), the compound is ground to granulate and shipped to the molder. Depending on the type of resin, a shelf life of 3 months for self-hardening resols and up to 24 months for novolac-HMTA mixtures is typical.

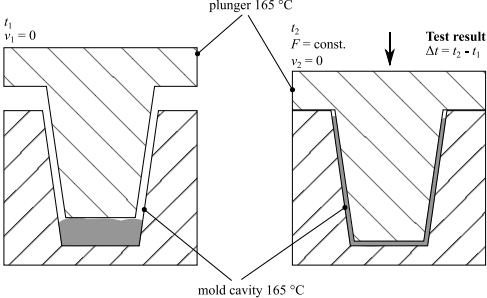
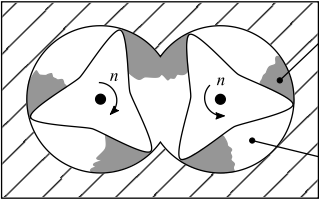
## **2.2 Characterization of phenolic molding compounds**

### **2.2.1 Single metric flow-hardening measurements**

During the processing of thermoset molding compounds, the flowability, curing behavior and mold release behavior of the material are of great importance. These characteristics are typically summarized under the term moldability [54]. Several methods for characterizing the moldability exist and are shown in Table 2-3. They can be divided into three groups according to English [55] and Tonogai et al. [54]. The following overview was given by Maertens et al. in the publication [24].

Table 2-3: Common flow-hardening test methods for thermoset molding compounds [54,56–61]

Test method name	Technical standard	Graphical description
<p><b>Orifice flow test (OFT)</b></p>	<p>ISO 7808:1992 [56]</p>	 <p>plunger 165 °C <math>F = \text{const.}</math> compound pushed through orifices mold cavity 165 °C <b>Test result:</b> mass of compound remaining in mold <math>m</math></p>
<p><b>Spiral flow test</b></p>	<p>ASTM D3123-09(2017) [57]</p>	 <p>plunger <math>F = \text{const.}</math> molding compound mold cavity 165 °C <b>Test result:</b> Length of spiral <math>L</math></p>
<p><b>Stick flow test</b></p>	<p>ASTM D569 (withdrawn) [58]</p>	 <p>plunger 165 °C <math>F = \text{const.}</math> mold cavity 165 °C <b>Test result:</b> flow path length <math>L</math></p>
<p><b>Disc-flow test</b></p>	<p>no technical standard [54]</p>	 <p>upper mold surface 165 °C <math>t_1 = 0</math> <math>v_1 = 0</math> <math>t_2</math> <math>F = \text{const.}</math> <math>v_2 = 0</math> lower mold surface 165 °C <b>Test result:</b> Compound pressed to disc with area <math>A</math></p>

Test method name	Technical standard	Graphical description
<p><b>Cup mold test</b></p>	<p>DIN 53465 (withdrawn) [61]</p> <p>ASTM D731 – 18 [59]</p>	 <p>plunger 165 °C</p> <p><math>t_1</math> <math>v_1 = 0</math></p> <p><math>t_2</math> <math>F = \text{const.}</math> <math>v_2 = 0</math></p> <p>Test result: <math>\Delta t = t_2 - t_1</math></p> <p>mold cavity 165 °C</p>
<p><b>Torque rheometer</b></p>	<p>DIN 53764 (withdrawn) [60]</p>	 <p>molding compound</p> <p>Test result: Torque curve <math>M(t)</math></p> <p>defined cavity temperature</p>

The first group of test methods determines the flow path length covered by the molding compound under defined temperature and pressure conditions. Representatives from this group are the orifice flow test (OFT) [56], spiral flow test [57], stick flow test [58] and disc flow test [54]. The second group of tests is closely related. It measures the time that is required until a defined mold geometry can be closed against the counterpressure of the molding compound. A typical representative is the cup flow test [59]. The third group of moldability tests directly measures the viscosity changes of the molding compound during heating. In the torque rheometer [60], the molding compound is heated to a defined temperature and the required torque for rotating the instrument is measured. The resulting torque vs. time curve gives an indication of the curing time and the minimum viscosity during the processing of the molding compound. Typical single-metric values from this curve are the minimum viscosity and the time until it is reached.

The main advantage of these methods is their simplicity and their ease of use, especially in a production environment. They give a single metric for the material’s moldability, e.g. the flow path length. But this simplicity has some

significant drawbacks, as will be described using the example of the OFT according to ISO 7808 [56]. In this test,  $m = 50$  g of the molding compound is given into a heated mold cavity ( $T = 165$  °C mold temperature). A plunger with two well-defined orifices is pressed down hydraulically to compress and heat the material. Under these conditions, the resin plasticizes and the compound bypasses the plunger through the two orifices. As the curing reaction progresses, the orifices are eventually blocked and the plunger movement is stopped. The value for the test result is determined from the weight  $m_{\text{Res}}$  of the molding compound that remains in the cavity according to Equation (2-1).

$$\text{OFT} = \frac{50 \text{ g} - m_{\text{Res}}}{50 \text{ g}} 100 \quad (2-1)$$

The value range for the OFT is  $0 \leq \text{OFT} \leq 100$ . A higher value is described as a softer flowing material, whereas a lower value describes a hard respectively stiff material. The first limitation of the OFT is the superposition of cure and flow: A low viscous, fast curing molding compound can have the same OFT value as a high viscous, slow curing material. It is obvious that such molding compounds might require different injection molding process parameters. Second, the OFT is used for judging the moldability in the injection process, but it uses a compression molding process at significantly lower pressure levels and shear rates to do so. Lastly, Scheffler [62] showed that additional factors like the molding compound's moisture have a significant influence on the flow characteristics and therefore can strongly influence the resulting OFT value. Similar arguments can be made for the other single metric measurements. To separate the effects of curing and flow, viscosity and calorimetry measurements are carried out as described in Sections 2.2.2 and 2.2.3.

## 2.2.2 Rheological measurements

The typically used viscosity measurements can be separated in inline (during the injection molding process) and offline (laboratory) measurements. Capillary rheometers are commonly used for the characterization of polymer melts as they are able to provide the high shear rates that are typical for manufacturing processes such as injection molding [63]. They work by detecting a pressure drop caused by the viscous friction in the material over a defined flow path length. In the capillary rheometer, this pressure drop  $\Delta p$  is meas-

ured across the distance  $s$  to obtain the pressure gradient  $dp/ds$  at a given volumetric flow rate  $\dot{V}$ . The apparent shear stress  $\tau_a$  and the apparent shear rate  $\dot{\gamma}_a$  for a circular capillary with the radius  $r$  are given by Equations (2-2) and (2-3).

$$\tau_a = \frac{\Delta p r}{2 s} \quad (2-2)$$

$$\dot{\gamma}_a = \frac{4\dot{V}}{\pi r^3} \quad (2-3)$$

This leads to the apparent viscosity  $\eta_a$  for a circular capillary according to Equation (2-4):

$$\eta_a = \frac{\tau_a}{\dot{\gamma}_a} = \frac{\pi \Delta p r^4}{8 s} \quad (2-4)$$

Typical geometries for an offline capillary rheometer are circular dies [64,65], but rectangular channels [63] have been evaluated as well. While capillary rheometers are commonly used for thermoplastic materials, thermosetting resins pose additional challenges. Due to the curing progress, the residence time in the instrument before the start of the measurement must be minimized. For pushing the material through the die, typically higher pressures are required compared to thermoplastic materials. During the measurement, the resin cures, leading to the release of the exothermic heat of reaction. With the typically used electric heaters, a defined temperature control is not possible. Instead, the usage of an oil jacket for improved temperature control has been proposed. Finally, after the end of the measurement the device must be disassembled to remove the cured compound [64,65]. The function principle of a capillary rheometer has been implemented into the injection molding process for thermoplastic polymers by several authors with the aim of creating an inline measurement. For example, Lohr et al. [66] integrated a capillary rheometer into an injection molding tool and used it for investigating the viscosity of gas-laden and long glass fiber-reinforced polypropylene under typical process conditions. Fernandez et al. [67] implemented a similar geometry into the nozzle of the injection molding machine. In contrast to offline rheometers, the inline measurements can be carried out under representative injection molding process conditions such as pressure and shear rate.

For thermoset molding compounds, no application of an inline rheometer integrated into the mold or the injection molding machine was found in literature. It can be assumed that the main challenge to overcome is the removal of cured or solidified molding compound from the capillary of the rheometer setup. Instead, pressure sensors in the mold cavity have been used to calculate the apparent viscosity  $\eta_a$  during the mold filling phase. For example, Hohberg et al. [68] used the pressure drop  $\Delta p$  over multiple sensor locations to characterize the viscosity and the compressibility of sheet molding compound (SMC). Scheffler et al. [62] determined the apparent viscosity  $\eta_a$  as a function of the moisture content and mold temperature of several phenolic molding compounds by measuring the pressure drop  $\Delta p$  in a flow spiral. Wittemann, Maertens et al. [69] used the same approach to validate a novel mold filling simulation model that considers the fiber-induced anisotropic flow behavior of a glass fiber-reinforced phenolic molding compound.

Another measurement setup is a rotational rheometer, in which the material is subjected to a defined excitation (either controlled shear stress or controlled shear rate) and its response is measured. Typical experimental setups for this offline measurement device are concentric inner and outer cylinders with a measurement gap in between them (Couette rheometer) as well as plate-plate or cone-plate arrangements [70–72]. The shear rate is given by Equation (2-5)

$$\dot{\gamma} = \frac{\Delta v}{h} \quad (2-5)$$

with the gap height  $h$  and the relative velocity  $\Delta v$  between the two plates. Using the shear stress  $\tau$  measured by the rheometer, the viscosity  $\eta$  is then defined according to Equation (2-6).

$$\eta = \frac{\tau}{\dot{\gamma}} \quad (2-6)$$

Bakhtiyarov and Overfelt [73] used rotational rheology for determining the viscosity of a liquid phenolic resol resin system as a function of the resin to binder mixture ratio. However, since most rheological studies of thermosetting resins focus on the curing behavior of the resin, rotational measurements are not suitable. Once the gel point of the resin is reached, it loses its ability to flow due to the formation of the three-dimensional crosslinked network [70]. Instead, oscillatory rheology measurements are commonly used. In

contrast to the capillary rheometry or standard rotation rheometers, an oscillatory rheology measurement provides information about the complex viscoelastic deformation behavior of the sample. Typical measurement geometries are plate-plate and cone-plate configurations. The oscillatory measurement method has the advantage that it can be used for a wide viscosity range. In the case of a temperature sweep measurement with phenolic molding compounds, the material is solid at low temperatures, followed by a very low-viscous state at an intermediate temperature and a solidification due to curing at high temperatures again (see Figure 2-9). Because of the small deflection in the oscillatory measurement, it is possible to measure both solid objects and liquids, whereas a rotational viscosity measurement can only be carried out in the liquid state after melting and before the gelation due to curing. [70]

In an oscillatory test setup, the sample is also subjected to a defined shear excitation (either controlled stress or controlled strain), and its response (either strain or stress) is measured. Subsequently, the measurement principle for a controlled strain deformation (CSD) is described briefly based on fundamental literature information [70,71,74]. A sample is excited with a deformation

$$\gamma(t) = \gamma_0 \sin(\omega t) \quad (2-7)$$

with the deformation amplitude  $\gamma_0$  and the angular deformation frequency  $\omega$ . The response of a viscoelastic sample can be described as

$$\tau = \tau_0 \sin(\omega t - \delta) \quad (2-8)$$

with the stress amplitude  $\tau_0$  and the response lag  $\delta$ . Calculating the shear modulus in the same fashion as for the rotational measurement results in a complex expression  $G^*$  with real and imaginary terms, see Equation (2-9) and Figure 2-5.

$$\begin{aligned} G^* &= \frac{\tau(t)}{\gamma(t)} = \frac{\tau_0 \sin(\omega t - \delta)}{\gamma_0 \sin(\omega t)} = \frac{\tau_0}{\gamma_0} e^{i\delta} = \frac{\tau_0}{\gamma_0} (\cos \delta + i \sin \delta) \\ &= G' + i G'' \end{aligned} \quad (2-9)$$



In Equation (2-9)  $G'$  is the storage modulus, which can be considered as a measure of elastic energy storage, and  $G''$  is the loss modulus, which represents the energy dissipated due to viscous friction in the material.

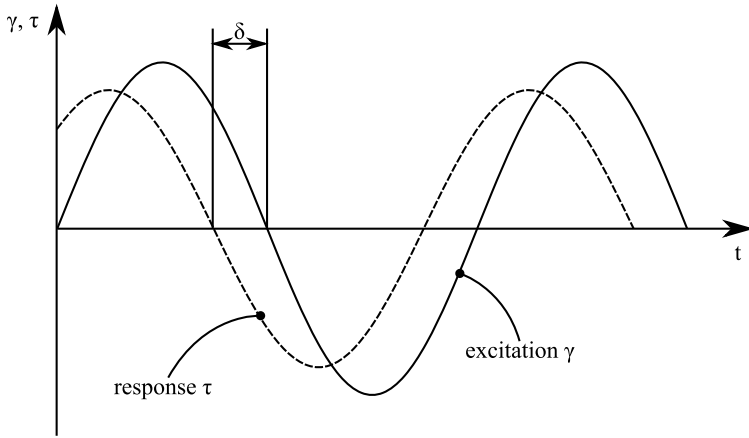


Figure 2-5: Excitation and response for oscillatory rheology measurements [71]

The complex viscosity  $\eta^*$  is calculated accordingly, see Equation (2-10):

$$\eta^* = \frac{\tau(t)}{\dot{\gamma}(t)} = \frac{\tau_0 \sin(\omega t - \delta)}{\gamma_0 \omega \cos(\omega t)} = \frac{G'}{\omega} + i \frac{G''}{\omega} \quad (2-10)$$

Oscillatory rheology measurements for phenolic molding compounds have been carried out by several authors [75–77]. Due to the solid, granular composition of the molding compounds at room temperature, a sample preparation step is required before the actual measurement can be performed. The outcome of the sample preparation is a plane-parallel disk with defined values for thickness and diameter which can subsequently be used for the rheology measurements. Dominguez et al. [75] used a ball mill to grind the compound, followed by a chilled molding process. Höer [76] also ground the molding compound to a powder, but no further information on the sample preparation is given. Scheffler [77] omits grinding the sample and plasticized it at low temperatures of  $T \approx 80^\circ\text{C}$  in a torque rheometer, followed by a molding process at  $T \approx 85^\circ\text{C}$ . During this sample preparation, he does not expect any significant curing progress. After the sample preparation step, the viscosity measurement is carried out in oscillatory measurement mode by all authors. Heating rates between  $\dot{T} = 3\text{ K/min}$  [76,77] and  $\dot{T} = 20\text{ K/min}$

[75,76] are used. All authors used a plate-plate geometry with a plate diameter of  $d = 25$  mm.

Multiwave oscillatory rheology based on the work of Malkin et al. [78,79] replaces the simple sine wave shown in Figure 2-5 with several superimposed harmonics. This makes it possible to cover a wide range of deformation frequencies  $\omega_i$  within a single measurement. During the same measurement time, in which for a conventional measurement only the lowest frequency  $\omega_1$  can be analyzed, multiple frequencies  $\omega_i > \omega_1$  can be measured. In addition to the practical advantage of a shorter total measurement time, the multiwave test is particularly advantageous for fast-curing thermosets, because the different measurement frequencies  $\omega_i$  can all be measured simultaneously and thus in the same material crosslinking state. Consecutive measurements with the same sample would be influenced by the curing progress, and multiple measurements with different samples would include the influence of the sample preparation as well as batch variations [71]. Multiwave oscillatory rheology has been used for curing investigations of several different thermosetting resins such as epoxies [80], thiol-enes [81] and acrylated epoxidized linseed oil [82] as well as for investigating the crosslinking in polyamide 12 [83], but the usage for phenolic molding compounds has not been reported yet.

### 2.2.3 Differential scanning calorimetry

Differential scanning calorimetry (DSC) is a commonly used thermal analysis method. In this technique, the heat flow differences into the measurement object and into a reference object are measured as a function of the temperature. The sample is placed in a small container called crucible. Endothermic (heat flow into the sample) or exothermic (heat flow out of the sample) processes are measured. The heat flow can be of both chemical and physical origin, such as curing of thermosets or crystallization and melting of thermoplastics. A typical analysis objective for thermoset polymers is the total heat of reaction  $\Delta H_R$ , which can be determined by integrating the exothermic cure peak. [36,84]

Two general principles for DSC exist. In the heat-flux calorimetry, both the sample and the reference crucible are heated in the same oven. They are placed on a sample holder that establishes a thermally conductive connection

with the thermal resistance  $R_{\text{th}}$  between them. The temperatures of the sample and the reference are measured by individual sensors. If the sample material undergoes an exothermic or endothermic process, its temperature will differ from the reference crucible by  $\Delta T$ . The heat flow  $\dot{Q}$  can then be calculated according to Ohm's law, see Equation (2-11) [36,84].

$$\dot{Q} = \frac{\Delta T}{R_{\text{th}}} \quad (2-11)$$

In the power compensation calorimetry, the sample and the reference crucibles are completely separated in individual ovens. The heating process is controlled individually with the aim of keeping both temperatures identical. Every exothermic or endothermic process in the sample causes a difference in the heating power which is required to keep the temperatures identical. The heat flow into the sample  $\dot{Q}$  is proportional to the difference in required heating power [36,84,85].

Typical sample sizes for a DSC analysis are a few milligrams. Therefore, the representative sample preparation is crucial for accurate measurement results. For granular molding compounds, the sample must be representative for the entire batch. Domínguez et al. [75] and Stark [86] successfully used a ball mill for the grinding of the sample. In contrast to that, liquid resins are typically much more homogeneous and easier to portion, which is why they can be measured without additional sample preparation steps. The condensation polymerization of the phenolic resin produces reaction byproducts such as water and formaldehyde. In addition, ammonia is produced during the decomposition of HMTA. These substances evaporate endothermically, whereas the curing reaction is an exothermic process. The use of standard crucibles with open or perforated lids would lead to a false determination of the total heat of reaction  $\Delta H_{\text{R}}$ , since the measured heat flow would be a superposition of both effects. Consequently, sealed medium- or high-pressure crucibles that inhibit the evaporation are used by most researchers. The crucible volume is typically either  $V = 120 \mu\text{L}$  or  $V = 270 \mu\text{L}$  [29,34,75,87–89]. In studies where open crucibles were used, inconsistent measurement results for the total heat of reaction have been reported [90].

For determining the total heat of reaction, a ramp from ambient temperature up to  $T = 250 \text{ }^\circ\text{C} \dots 300 \text{ }^\circ\text{C}$  with a heating rate of  $\dot{T} = 10 \text{ K/min}$  is typical. Alonso et al. [87] and Ishida et al. [88] have reported a shift of the exother-

mic peak to higher temperatures with increasing heating rate. However, the total heat of reaction remains independent of the heating rate if the material has enough time for completing the reaction. For molding compounds with fillers and fibers, Scheffler [77] conducted a subsequent thermogravimetric analysis of the exact same sample. The individual determination of the fiber and filler content enables the calculation of the exact heat of reaction for the resin fraction of the sample.

## 2.3 Basics of the injection molding process

### 2.3.1 Injection molding of thermoset molding compounds

#### 2.3.1.1 The injection molding process

The injection molding of the conventional thermoset molding compounds that are described in paragraph 2.1.2 is a well-established, state-of-the-art technology. It is shown in Figure 2-6.

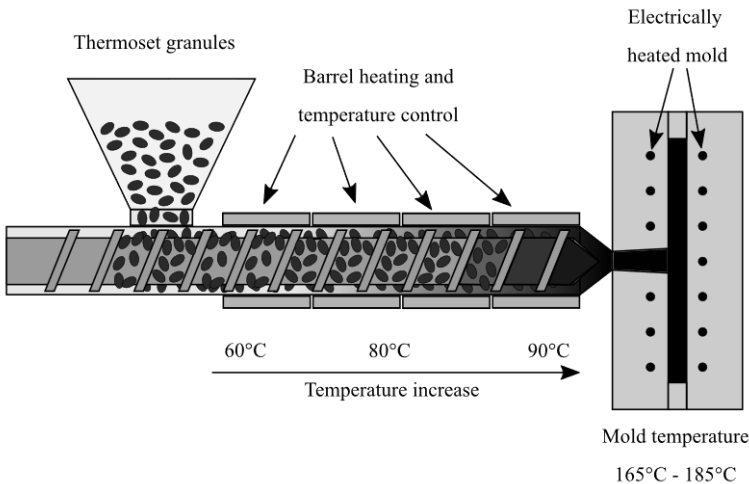


Figure 2-6: Standard thermoset injection molding process

The fundamental principle of the thermoset injection molding process is like the injection molding of thermoplastics. Differences between the processing

of the two polymer families exist regarding the design of the plasticizing screw and the temperature control of the process. The molding compound is fed into the machine via the material hopper. By rotation of the screw, the granulate is conveyed from the hopper into the barrel. In contrast to thermoplastic injection molding, the barrel temperature is controlled by using liquid temperature control devices. Typically, two or three separate control zones can be found on most machines. A gentle temperature increase towards the nozzle supports the heating of the material. The screw for a thermoset plasticizing unit is shorter than for thermoplastics and has a small compression ratio of maximum 1:1.3. The aim of this design is to keep the energy input into the material low to avoid curing in the plasticizing unit. The melting of the thermoset granulate takes place in the front screw flights and generally starts on the pushing screw flank, as Figure 2-7 shows. Due to the continued conveying of the material by the screw, the screw is pushed backwards until the desired amount of material is plasticized. Typical back pressure values for phenolic molding compounds are lower than for thermoplastic, ranging from  $p = 20 \text{ bar} \dots 80 \text{ bar}$ . [91]

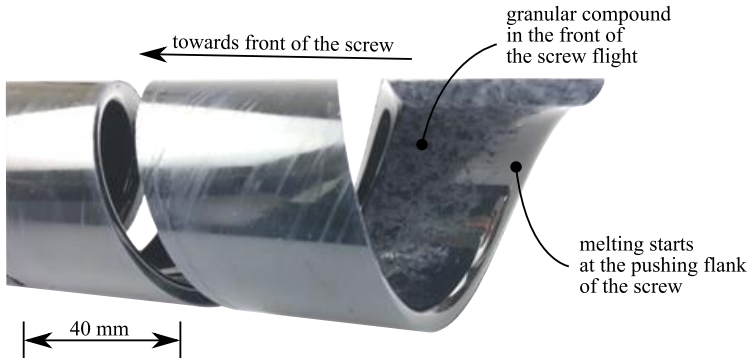


Figure 2-7: Structure of the melting zone of a phenolic molding compound in the screw

Subsequently, the material is injected into the mold by a forward movement of the screw. Screws for granular thermoset molding compounds do not have a non-return valve. At temperatures of  $T = 90 \text{ }^\circ\text{C} \dots 110 \text{ }^\circ\text{C}$  in front of the screw, the molding compound still has a high viscosity, so that a non-return valve is not required. To reduce the backflow, the screw angles of the thermoset screw are steeper than for a thermoplastic screw. Nevertheless, the high injection pressure causes a backflow of material over the screw flights. Depending on the publication, values for backflow in the range of

15 % ... 40 % are reported [77]. The injection pressure is absorbed by the solid bed of granulate in the flights of the screw.

The mold filling behavior of thermoset compounds differs from thermoplastic materials. Several studies have been conducted for analyzing and visualizing the flow. Thienel et al. [92] used a mold with a glass window to observe the compound. The molding compound enters the mold with an unsteady flow front that only has a partial wall contact. With increasing flow path length, they observed a line with full wall contact. It was concluded that the resin with contact to the heated mold surface drops in viscosity and forms a low viscosity layer, which serves as a lubricating film. On this surface layer, the molding compound slides as a plug flow. Tran and English [93] confirmed this mold filling behavior. They visualized the wall slip by means of spot wise painting of the mold cavity wall. For a phenolic molding compound, they observed that the painted lines on the mold surface were smeared by flow of the material, indicating a strong wall slip. In contrast, a thermoplastic polymer did not transport the color pigments due to the fountain-flow mold filling behavior of these materials. Ohta and Yokoi [94] applied a method called the gate-magnetization for a three-dimensional visualization of the mold filling. They compounded magnetic particles into the glass fiber-reinforced phenolic resin with a loading of 2 vol.-%. During the mold filling, the compound was subjected to an on-off magnetization signal in the runner system. The pattern of magnetized particles was later analyzed for several cross-sections of the molded plates. The wall slip on the low viscosity skin layer described above has been confirmed by their investigations. Additionally, they describe that due to the curing of the resin on the hot mold surface, a reacted high viscosity layer forms, narrowing the cavity channel. The thickness of the reacted high viscosity layer decreases with increasing distance from the gate. Figure 2-8 sums up the findings regarding the mold filling behavior.

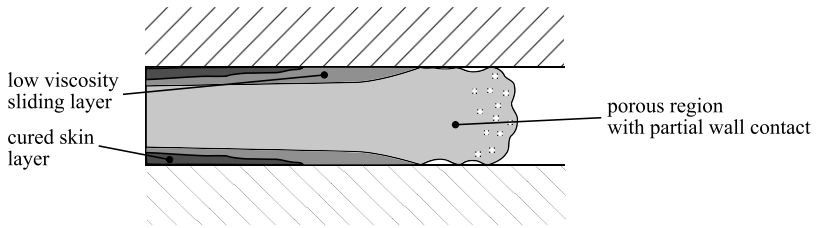


Figure 2-8: Flow front of thermoset molding compounds during mold filling [55,92,94]

In the mold, curing of the thermoset matrix takes place at elevated temperatures. For phenolic molding compounds, temperatures ranging between  $T = 175\text{ °C} \dots 185\text{ °C}$  are typical. Since no cooling of the thermoset part is required, electrically heated molds are commonly used. The general mold design is similar to thermoplastic materials with a few thermoset-specific differences [95,96]. In thermoplastic processing, hot runner systems are commonly used for saving material and for increasing the flexibility regarding the sprue and gate design. For thermoset materials, the curing starts after injection due to the shear energy and thermal energy input, which means that once the material has entered the mold, curing is inevitable. Cold runner concepts exist for polyester bulk molding compounds (BMC) and rubber injection molding and have been investigated for particle and organically filled phenolic molding compounds [97]. The area close to the cold runner was found to be a heat sink in the mold, lowering the mold temperature and negatively influencing the local mechanical properties. For highly filled phenolic molding compounds, no cold runner concepts exist. Consequently, the gate and runner system must be demolded with every single shot, limiting their geometrical complexity. Due to lower minimum viscosity of the thermoset compound compared to a thermoplastic material, tighter tolerances for shear edges are required [98].

During the injection into the mold, the compound is heated up due to friction and the high mold temperature. The increasing temperature causes both an easier relative movement of the molecular chains and an increase in curing rate. These two phenomena have opposite influences on the viscosity, which results from the superposition of the two effects. Only few literature values for the resulting viscosity curve during processing exist. Stitz and Keller [43] describe, in accordance with most other publications, a sharp drop of the viscosity, followed by the increase due to curing. Kaiser [99] describes the

viscosity of the resin upon entering mold as rather constant, as Figure 2-9 illustrates. Both Scheffler [62] and Höer [76] found that an increase in mold temperature reduces the required injection pressure for phenolic molding compounds. This indicates strongly that the influence of the easier relative movement of the molecular chains – and therefore the drop of the viscosity – is dominant during the initial mold filling phase.

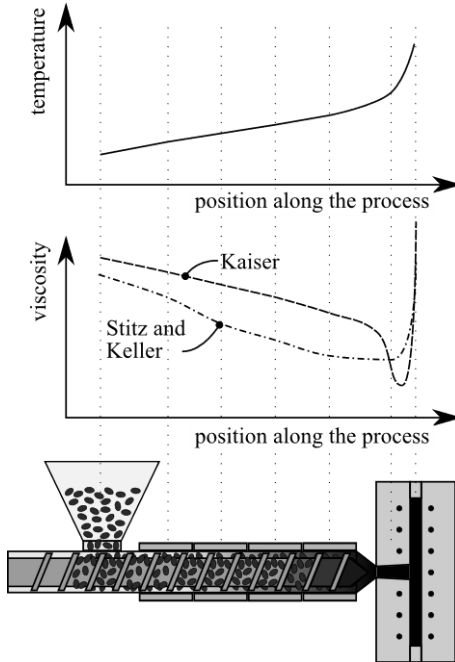


Figure 2-9: Temperature and viscosity curve according to Kaiser [99] and Stitz and Keller [43]

Several methods for the process control are distinguished based on the switchover from the path-controlled injection phase to the pressure-controlled holding phase. In the most basic process, the switchover occurs at a defined screw position [100]. Often, this switchover position is the front end position of the screw [101]. This way of controlling the process has several disadvantages: Most important, since the screw is at its front-end position after the end of the injection phase, it cannot apply a holding pressure to the material. Every change in backflow during the injection phase results in a change in cavity fill level. These problems can partially be mitigated by switching to holding pressure earlier, so that a material cushion remains throughout the



holding phase. The material cushion in front of the screw transmits the pressure from the screw to the part, ensuring a compensation for shrinkage and therefore reducing porosity [100,102]. But even with a process control using the material cushion, changes in plasticizing volume or backflow directly influence the pressure at the switchover point and therefore the fill level of the part. Another possible process control strategy is the determination of the switchover point by measuring the material pressure in the mold. Once a certain pressure threshold is reached, the machine switches from the injection to the holding phase. Changes in backflow and plasticizing volume are compensated by small deviations in the switchover point and the remaining material cushion. Even though this process control strategy had been criticized in earlier publications [100], it is widely used today and considered to be a viable method for reproducibly molding high quality parts [55,69,76,103]. A typical in mold pressure curve for an in-mold pressure-controlled injection cycle is shown in Figure 2-10 (entire cycle in subfigure (a), detail view of the same cycle in (b)).

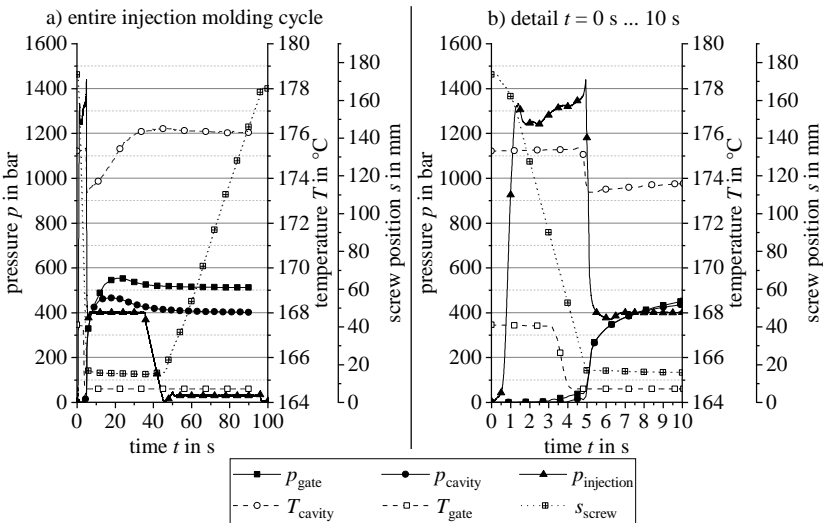


Figure 2-10: Exemplary machine and mold data for thermoset injection molding; a): entire injection molding cycle; b): detail  $t = 0 \text{ s} \dots 10 \text{ s}$

The injection starts with the forward movement of the screw. Initially, the plasticized molding compound in front of the screw is compressed without exiting through the machine nozzle, which leads to a sharp increase in injec-

tion pressure. Once enough injection pressure has been built up, the compound starts to flow and a gradual increase in injection pressure due to the growing flow path length can be observed. The first in-mold sensor that reacts to the flow front is the temperature sensor, whose signal drops immediately upon contact with the relatively cold molding compound. The pressure sensors have a slower response because a full contact of the compound with the sensor surface is required for transmitting the pressure. For the pressure sensor located at the gate, a linear pressure increase can be observed. Once the mold is volumetrically filled, the pressure signal spikes through the defined switchover threshold, triggering the change from the injection to the holding phase. During this phase, a slight forward movement of the screw is visible, indicating the compensation of shrinkage in the mold and a backflow of material in the screw. For a smoother machine operation, a linear decrease in holding pressure can be chosen. No step in the pressure signals is visible at the end of the holding phase, indicating a fully cured and therefore sealed gate. After the release of the holding pressure, the compound for the next step is plasticized. If a constant screw speed during plasticizing is chosen, the existence of an inflection point in the screw position signal indicates a change in apparent density of the material in the screw flights, which is often caused by backflow during the injection and holding phase of the process.

Besides the nowadays commonly used in-mold pressure sensors, several other sensor types for the process monitoring of thermosetting molding compounds have been evaluated. Ageyava et al. [104] give a comprehensive review of commonly used sensors for injection molding. Temperature sensors based on thermocouples are typically mounted in a metal housing that is flush with the cavity wall. Due to their mounting situation in the heated mold, they are thermally coupled to it and mostly only measure the cavity wall temperature. They show a temperature drop when the molding compound flows over them and can mainly be used for detecting the position of the flow front [104,105]. Infrared temperature sensors (IR) measure the radiant energy that is emitted by the melt and are therefore not affected by the temperature of the surrounding steel mold. Since they do not require a direct contact to the molding compound, they can detect the flow front without wall contact, providing a faster response compared to wall mounted thermocouples [104].

Ultrasonic sensors measure the sound velocity and the dampening factor in the molded part, which is directly correlated to the elastic modulus and thereby the state of curing. They are suitable for monitoring the curing once

the mold is filled. During the softening after mold filling, the sound velocity drops and dampening increases. With increasing degree of cure, the sound velocity increases, and the dampening is reduced. Both characteristics reach constant values with increasing degree of cure. The ultrasonic method has proven to be a reliable method which is applicable for a wide range of different molding compounds [86,106,107]. Dielectric analysis (DEA) is based on the principle of a capacitor. Two electrodes are placed in the mold and a sinusoidal excitation voltage  $U$  is applied. By measuring the amplitude and the phase shift of the responding current  $I$ , the relative permittivity, the dielectric loss and the loss factor can be calculated [86]. However, the low molecular reaction byproducts water and ammonia caused by the polycondensation reaction of phenol-formaldehyde resins can interfere with the measurement [86,108].

### 2.3.1.2 Data acquisition and evaluation using the injection molding machine

Recent developments such as the Adaptive Process Control plus (APC plus) by KraussMaffei [109] have the aim to further reduce the variation in the mold filling process despite batch and machine parameter fluctuations. The injection molding machine detects changes in the injection pressure curve, e.g. due to a change in the degree of cure of the molding compound or a change in barrel temperature, and dynamically adjusts the switchover point to holding pressure and the holding pressure level. The aim of this development is to keep the volumetric filling of the mold constant by adapting the process parameters individually for each part. This is a change in paradigm compared to the traditional approach of constant machine parameters described in earlier publications by material suppliers [101,102].

As described in a previous publication by Maertens et al. [26], the quantification of energy input into the polymer during plasticization and injection has become possible with modern data acquisition technologies. This is especially relevant for reactive thermoset polymers like phenolic resins. Several authors monitored and analyzed the screw torque during the plasticizing process  $M_{\text{plast}}$ . According to Rauwendaal [110] it is a good measure to quantify the mechanical power consumed by the melting process. For hydraulic injection molding machines, the plasticizing torque is typically calculated by measuring the pressure drop  $\Delta p_{\text{Hydr}}$  over the hydraulic screw drive according to Equation (2-12)

$$M_{\text{Plast}} = \frac{\Delta p_{\text{Hydr}} \eta_{\text{Hydr}} V_{\text{Drive}}}{20\pi} \quad (2-12)$$

using the hydraulic efficiency  $\eta_{\text{Hydr}}$  and the hydraulic volume of the drive  $V_{\text{Drive}}$ . The pressure drop can be measured by dedicated pressure transducers before and after the motor [111]. If such sensors are not available at the injection molding machine, the total hydraulic pump pressure  $p_{\text{Pump,tot}}$  can be used as well, because during the plasticizing phase the screw drive is the only hydraulic pressure consumer [77,112].

Heinzler et al. used the plasticizing torque for detecting moisture changes in polypropylene (PP) [113]. Since water acts as a plasticizing agent in the polymer, it lowers the viscosity and consequently leads to a lower required plasticizing torque. Similar investigations were carried out by Scheffler et al. for phenolic molding compounds [62]. They identified an initial decrease in plasticizing torque with rising moisture content, followed by an increase towards very high moisture content values. The fundamental softening effect of water in the polymer is the same for thermoplastics and thermosets, which explains the initial decrease in plasticizing torque. However, due to the lack of a non-return valve, further increasing the moisture content leads to a higher backflow during the injection phase for the thermoset molding compounds and consequently a higher number of fully filled screw flights. In those fully filled screw flights, the molding compound is agitated and mixed during the screw rotation, leading to the observed increase in plasticizing torque [62]. In general, Scheffler [77] concludes that the plasticizing torque for thermosetting molding compounds is influenced by multiple factors, but has a strong correlation to the backflow during the injection phase. Several authors [100,112] used the integral of the plasticizing power  $P_{\text{Plast}}$ , which is the plasticizing torque  $M_{\text{Plast}}$  multiplied with the screw speed  $n$ , as a measure for the energy input into the polymer, see Equation (2-13).

$$\begin{aligned} W_{\text{Plast}} &= \int_{\text{PlSt}}^{\text{PlEnd}} P_{\text{Plast}} dt = \int_{\text{PlSt}}^{\text{PlEnd}} (M_{\text{Plast}} \times \omega) dt \\ &= 2\pi \int_{\text{PlSt}}^{\text{PlEnd}} (M_{\text{Plast}} \times n) dt \end{aligned} \quad (2-13)$$

For a standard injection molding process using thermoplastic materials, Kruppa [112] observed an increase of the plasticizing work with increasing screw speed. This increased energy input leads to a stronger shortening of

glass fibers, as described by Truckenmüller [114]: With increasing plasticizing work, fiber length asymptotically approaches a threshold value, which appears to be independent of initial fiber length and glass fiber content. To quantify the energy input into the material during the injection phase of the process, the injection work  $W_{\text{Inj}}$  can be calculated as the integral of the injection force  $F_{\text{Inj}}$  over the injection distance  $s$  according to Equation (2-14).

$$W_{\text{Inj}} = \int_{\text{InjSt}}^{\text{InjEnd}} F_{\text{Inj}} \, ds = A_{\text{Piston}} \int_{\text{InjSt}}^{\text{InjEnd}} p_{\text{Hydr.,Inj}} \, ds \quad (2-14)$$

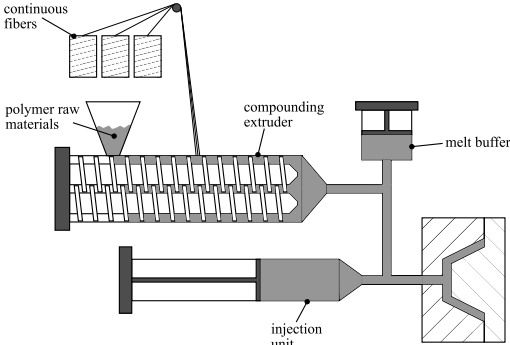
In an analogous manner to the plasticizing work, the hydraulic system pressure during the injection phase  $p_{\text{Hydr.,Inj}}$  can be used for calculating the injection force, because the injection piston is the only hydraulic pressure consumer during that time. Lucyshyn et al. [115] as well as Schiffers [116] use the injection work as a measure for viscosity changes of thermoplastic polymers during the process, e.g. due to a change in moisture content. A higher moisture content leads to a lower viscosity and consequently to a lower injection work. The injection work has also been used as a control parameter for the injection process by several authors. Woebcken [117] describes a method to compensate for changes in the material and / or the machine and mold setup by adjusting the screw movement during injection to reach a specific, previously defined injection work value. Cavic [118] used the injection work for judging the reproducibility of the injection molding process. All cited works deal with thermoplastic materials. The usage of the injection work to evaluate thermoset injection molding processes has not been reported yet. [26]

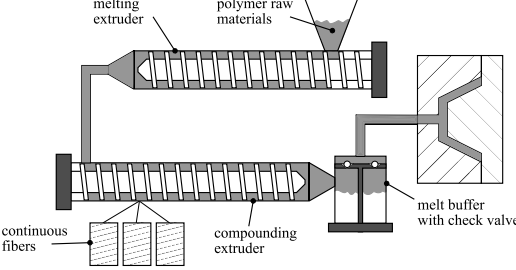
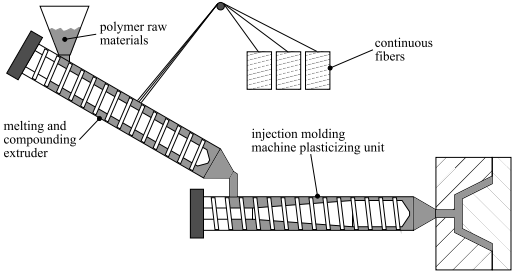
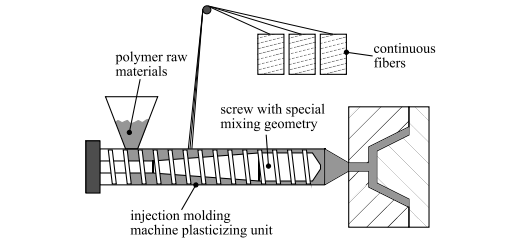
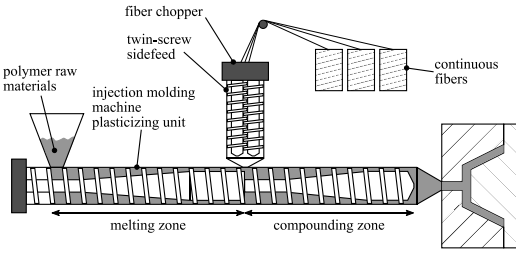
### 2.3.2 Long fiber injection molding processes

As outlined by Maertens et al. in a previous publication [26], the logical first step for increasing the fiber length in the molded product is increasing the fiber length in the raw material. Granulates with longer fibers compared to standard molding compounds exist both for thermoplastic and thermoset matrix systems. The thermoplastic long fiber granulates are available in a variety of different lengths, typically ranging between  $s = 6 \text{ mm} \dots 25 \text{ mm}$  pellet length. Due to the pellet manufacturing process, the maximum initial fiber length, i.e. the fiber length before taking into account any process-induced fiber shortening, is limited to the size of the granulate [21]. The

granulate size in turn is limited by the available dosing and feeding technology. With increasing aspect ratio of the granulate, the tendency to bridging increases, causing problems feeding the material into the injection molding machine. For thermoset matrix systems, no long fiber granulates designed for injection molding is available on the market today. However, there are long fiber phenolic molding compounds for compression molding applications. They have a plate-like shape and are available in length classes of 5 mm, 12 mm and 24 mm [119]. For compression molding applications, impact strength values that are 10 ... 20 times superior to conventional short fiber phenolic molding are claimed [10]. The processing of these long fiber granulates in an injection molding process has been investigated by Saalbach et al. [120] and Raschke [121]. It has been found that the material adheres to the screw and the cylinder wall, causing problems during plasticizing. The addition of zinc stearate as a processing aid reduced the sticking, but also led to a decrease in mechanical properties. Without giving any numerical values, it has been reported that the tensile properties of the injection molded parts were significantly below the compression molded reference parts [120]. To overcome the dosing problems and to reduce costs, several process variants with a direct fiber feeding have been developed for thermoplastic materials [22,122–132]. They will be described in the following paragraphs [26] and are shown in Table 2-4. For thermoset injection molding applications, no process variants with a direct incorporation of long fibers have been reported in literature.

Table 2-4: Long fiber thermoplastic injection molding processes [114,128–134]

Type	Process name	Graphical description
continuous compounding	Injection molding compounder (IMC) [133]	 <p>The diagram illustrates the IMC process. It starts with 'continuous fibers' being fed into a 'compounding extruder' along with 'polymer raw materials'. The extruder is connected to an 'injection unit' which includes a 'melt buffer'. The final output is shown as a fiber-reinforced part in a mold cavity.</p>

Type	Process name	Graphical description
	CPI Advantage [128]	 <p>The diagram shows a process where polymer raw materials are fed into a melting extruder. The output of the melting extruder is fed into a compounding extruder. The compounding extruder also receives continuous fibers. The output of the compounding extruder is fed into an injection molding machine plasticizing unit, which includes a melt buffer with a check valve. The final output is a molded part.</p>
discontinuous compounding	Direct compounding injection molding (DCIM) [129]	 <p>The diagram shows a process where polymer raw materials are fed into a melting and compounding extruder. The output of the melting and compounding extruder is fed into an injection molding machine plasticizing unit. The injection molding machine plasticizing unit also receives continuous fibers. The final output is a molded part.</p>
	Direct incorporation of continuous fibers (DIF) [114,122,134]	 <p>The diagram shows a process where polymer raw materials are fed into an injection molding machine plasticizing unit. The injection molding machine plasticizing unit also receives continuous fibers. The injection molding machine plasticizing unit has a screw with special mixing geometry. The final output is a molded part.</p>
	Fiber direct compounding (FDC) [130–132]	 <p>The diagram shows a process where polymer raw materials are fed into an injection molding machine plasticizing unit. The injection molding machine plasticizing unit also receives continuous fibers. The injection molding machine plasticizing unit has a fiber chopper and a twin-screw sidefeed. The injection molding machine plasticizing unit is divided into a melting zone and a compounding zone. The final output is a molded part.</p>

In the injection molding compounder (IMC), a co-rotating twin-screw extruder is combined with an injection unit. The process was patented by

Putsch [133] and first industrialized by KraussMaffei Technologies GmbH. Continuous roving strands are pulled into the extruder and are wetted by the thermoplastic polymer. The continuous compounding process is coupled to the discontinuous injection process using a melt buffer. Besides the increase in fiber length, the main advantage of the inline compounding process is lowering the material costs. However, due to the high capital investment costs and the responsibility for the material formulation, it is mostly only used for high-volume applications [125]. The IMC process has also been used for the injection molding of long fiber-reinforced thermoplastic foams by adding a gas injection unit to the compounding extruder. Besides a special screw configuration for the compounding extruder, that ensures that the physical blowing agent cannot escape from the system, no further modifications to the equipment are required [126,127].

Another inline compounding process has been developed by Composite Products, Inc. (CPI). Their so called Advantage process combines a continuous compounding process with a discontinuous injection process using a melt buffer [128]. The compounding tasks are divided between two single-screw extruders with the tasks of melting and compounding. In contrast to the process described above, the melt buffer and the injection unit are combined in one component. By using a check valve in the piston head, the compounding extruder can fill the backside of the piston head during the injection and holding phase. After the holding phase, the material can flow through the check valve to the other side of the piston head.

To reduce the capital investment costs and make the direct compounding feasible for lower volume applications, several processes have been proposed. They share the common aspect that the melting and compounding is carried out discontinuously, matching the injection molding cycle. This removes the need for a melt buffer and therefore reduces capital investment costs. The direct compounding injection molding (DCIM) process invented by Exipnos and KraussMaffei Technologies GmbH couples a single screw compounding extruder with a traditional injection molding machine [129]. In the compounding extruder, the molder can tailor the material according to his needs by adding fibers, fillers and other additives to the thermoplastic polymer.

In the DIF process (direct incorporation of continuous fibers) invented by Truckenmüller at the University of Stuttgart, continuous fibers are directly



pulled into the screw of the injection molding machine [122,124]. The aim of the development was to reduce both the costs for the raw materials by replacing long fiber-reinforced granulate as well as the costs for the machine equipment by using a conventional injection molding machine. Mixing elements on the injection molding screw are required for obtaining a good fiber dispersion. The mechanical properties of the produced samples are comparable to conventional long fiber granulate.

Another direct process for the injection molding of long fiber-reinforced thermoplastics was developed by Arburg GmbH + Co KG in cooperation with SKZ Kunststofftechnik GmbH. In this process, called fiber direct compounding (FDC), the unreinforced thermoplastic granulate is passively pulled into the screw and melted like in a conventional injection molding machine [130–132]. In contrast the DIF process, the continuous fibers are cut to a selectable length of  $L = 2 \text{ mm} \dots 100 \text{ mm}$  using a fiber chopper and are fed to the injection molding machine via a twin-screw sidefeed. At the position of the fiber feed, the screw diameter is reduced to facilitate the incorporation of the fibers. Since the injection molding is a discontinuous process, the fiber feed is coordinated with the screw movement via the machine control system.

### **2.3.3 Mixing elements for the injection molding process**

The standard three-zone conveying screw for injection molding and single screw extrusion processes has a low mixing capability and is mainly used for melting and pumping already homogeneous materials. If agglomerations such as colorants [135,136], fiber bundles and fillers [136,137] need to be broken up during plasticization, an increased mixing performance is required. In general, this mixing can either be accomplished during the material plasticization phase (in the barrel of the injection molding machine) or during the injection phase (by influencing the material flow into the mold). The mixing elements can be grouped into distributive mixing and dispersive mixing. Distributive mixing elements work by splitting and reorienting the fluid elements several times so that the randomness of the distribution of the minor constituent is increased without significant change to the particle size [138]. In contrast, a dispersive mixing zone subjects the polymer melt to a high stress, typically shear or elongational stresses. Due to this operation, the

agglomerate size of the constituent is ideally reduced to its ultimate particle size [138].

A typical element for the distributive mixing during the injection phase is a static mixing nozzle which is shown in Figure 2-11. Such elements are generally used for achieving a better colorant distribution in the part. However, due to their rather low dispersive mixing power they are not well-suited for breaking up agglomerates [136,139].

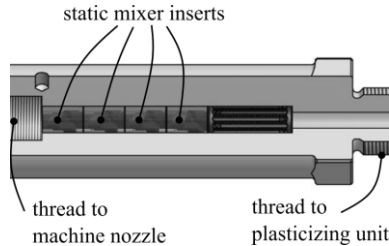


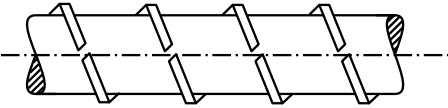
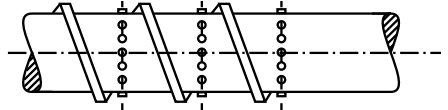
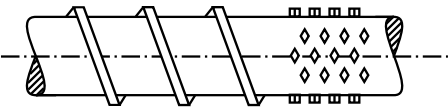


Figure 2-11: Static mixing nozzle [140]

Moritzer et al. [134] investigated the use of a static mixing nozzle in the processing of various short fiber polypropylene compounds with different fiber content and fiber length distributions. Both the fiber shortening and the effect of the mixing nozzle on the mechanical properties were analyzed. Compared to the standard nozzle, a marginal fiber length reduction was found for the mixing nozzle when molding compounds with a high initial fiber length. However, no difference between the two nozzle types was found for compounds with a shorter initial fiber length. Additionally, there was no significant effect of the mixing nozzle on the tensile strength and the tensile stiffness of the molded parts [134]. It can be summarized that static distributive mixing elements are not well suited for increasing the mechanical properties of fiber-reinforced polymers. Dispersive mixing by shear energy input can be achieved by injecting the molten compound through narrow gaps, for example small machine nozzles. However, such cross-section reductions likely have a negative impact on the required injection pressure. For screw mixing elements in the injection molding process, the same functional geometries as in single-screw extruders are used. In the following paragraph, the most important mixing elements are described. This overview was previously published by Maertens et al in [25]. Generally desirable features for screw mixing elements according to Rauwendaal [110] are listed below.

1. Forward pumping capability to minimize the pressure drop over the mixing section
2. Streamlined flow and a complete wiping of the barrel circumference to avoid dead spots and to achieve a narrow residence time distribution
3. Easy cleaning during material changeover and machine downtime

Table 2-5 gives an overview of the most common distributive mixing elements.

Table 2-5: Distributive mixing elements for extrusion and injection molding processes [110]

Mixing element name	Graphical description
<b>slotted extruder screw</b>	
<b>pin mixing section</b>	
<b>pineapple mixing section</b>	
<b>Dulmage mixing section</b>	
<b>Saxton mixing section</b>	

Due to their good compromise between ease of screw element manufacturing and mixing capabilities, the fluted dispersive mixing elements based on the Union Carbide / Maddock mixing sections are commonly used for extrusion and injection molding applications and have been the focus of several investigations [135–138,141–146]. Table 2-6 lists further typical dispersive screw mixing elements [110,147].

Table 2-6: Dispersive mixing elements for extrusion and injection molding processes [110]

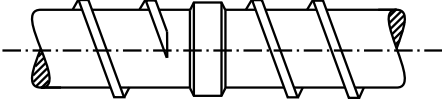




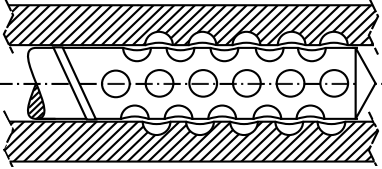
Mixing element name	Graphical description
blister ring	
Union carbide / Maddock mixing Section	
BT mixer	
Egan mixer / spiral Maddock mixing Section	
CRD fluted mixer	
CTM mixing section	

Figure 2-12 shows a spiral Maddock mixing element with its characteristic dimensions:

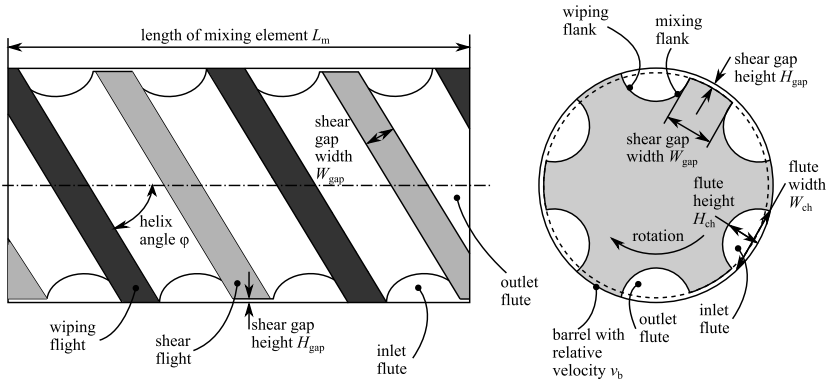


Figure 2-12: Characteristic dimensions of a spiral Maddock mixing element

The main influence factors on the mixing quality of a Maddock element according to Potente and Többen [148] are the length of element, the flute angle and the shear gap geometry. Sun et al. [144,145] conducted numerical and experimental investigations on the influence of the flute channel geometry and the shear gap height for such elements and found that a shallower flute depth results in a narrower residence time distribution, which reduces the potential of dead spots and material degradation. Based on experimental trials with a glass window single screw extruder performed by Kubik et al. [149], the authors concluded that a Maddock mixer design with alternating shear and wiping flights narrows down the residence time distribution compared to an open mixer design which omitted shear wiping flights. This corresponds to the list of desirable characteristics for a mixing element listed in the previous paragraph.

Recent developments for mixing elements include the CRD mixer (Chris Rauwendaal dispersive), which is supposed to achieve a comparable degree of dispersive mixing quality in a single screw extruder as in an intermeshing, co-rotating twin-screw extruder [150]. The mixer design described in US patent 5932159 [151] is based on the spiral Maddock mixing element, but has two distinct differentiating features. First, Rauwendaal implemented more than one mixing flutes between the inlet and outlet flutes of the element. These mixing flutes are closed to both the front and the back of the mixing element, forcing the material through the shear gaps that separate them from the other flutes. Due to the multi-flighted geometry, the material is subjected to the high shear stresses multiple times, improving the mixing behavior.

Kubik et al. confirmed this positive aspect on the mixing power in their own work, describing it as the “key variable for better mixing” [135]. Second, Rauwendaal modified the geometry of the leading flight flank of the mixing section in such a way that they become wedge shaped. This wedge-shaped flank geometry creates additional elongational stress, which is supposedly better suited for breaking up agglomerates. Other authors have drawn conflicting conclusions regarding the mixing effect of elongational stresses. Kubik et al. [135] could not determine any positive influence on the mixing power, whereas Guo et al. [152] found that mixing elements with a high elongational stress preserve the fibers better than dispersive shear-intensive kneading elements. They only compared fiber length distributions and did not investigate the material homogeneity after passing through the mixing element or the mechanical performance of the produced samples. Calculating the ratio of  $FLD = L_p/L_n$  (fiber length distribution, see Section 2.4.1 for details) indicates that the mixing quality of their elongational stress mixing element is worse compared to their shear stress mixing element.

Another recent application of the Maddock mixing element geometry can be found in the back flow compensation (BFC) screw tip design invented by Kruppa et al. [153,154]. It uses the increased flow resistance caused by the narrow shear gaps of the Maddock geometry for reducing the pressure induced backflow during the injection stroke of the screw during the injection molding process cycle. An additional screw rotation during the injection phase causes a forward-oriented drag flow, counteracting the back flow caused by the injection pressure. The geometry was successfully validated using thermoplastic materials and found to be equivalent or superior to conventional multi-part non-return valve assemblies. The geometry has been patented [155], but no industrial application is known to date. None of the described distributive and dispersive mixing elements have been used in the thermoset injection molding process for granular phenolic or epoxy molding compounds. A likely reason is that there was simply no need for additional mixing in the traditional thermoset injection molding process, which is why such developments were not pursued.

## **2.4 Fiber length measurement and influence of fiber length on mechanical properties**

### **2.4.1 Fiber length measurement**

For determining the fiber length distribution in discontinuous fiber-reinforced materials, several measurement methods exist. They can be classified into the categories of destructive and non-destructive methods. The most common measurement route is to first remove the polymer matrix and then to separate the individual fibers. This destructive measurement process can be divided into four steps as described by Goris et al. [156]: In the matrix removal step (1), the polymer material is removed, usually by pyrolysis or solvolysis. In the down-sampling and fiber dispersion step (2), a small sample of fibers is taken from the fiber residue and prepared for the next step, digital imaging (3). Finally, the image is analyzed (4) with image processing software to resolve intersection points and measure the fiber length. The down-sampling and dispersion step is one of the main factors that influence the quality of the measurement results. However, in most cases, the published research does not specify the exact method of homogenization and down-sampling process. Several different approaches to this challenge can be found in literature [156]. The most common approach is to transfer the fibers into an aqueous suspension that is diluted until the desired concentration is obtained. The homogenization of the fibers in the suspension is either done manually by agitating the fluid [157] or by using an ultrasonic bath [14]. Another method is to perform the down-sampling by using a defined amount of low-viscosity resin to bind a small fraction of the dry fiber residue [156,158]. This smaller sample then must undergo pyrolysis or solvolysis again so that the fibers can be dispersed for the subsequent image acquisition. If no aqueous suspension is used for the dispersion step, the dry fibers are often dispersed with brushes, tweezers or wooden sticks [159–161]. Compressed air [156] and – for electrically conductive carbon fibers – a corona field from a high frequency generator [158] have been used for dispersing the fibers as well.

Non-destructive measurement techniques for determining the fiber length distribution by using computed tomography ( $\mu$ CT) have the advantage that the fibers are measured directly in the composite. They do not undergo any additional stress caused by the removal of the polymer matrix and the fiber dilution and dispersion described above. However, due to the small voxel

size required to accurately image single fibers, the total sample size that can be measured is very small. For example, Teßmann et al. [162] analyzed a long fiber-reinforced thermoplastic specimen with a size of 1.2 mm × 3.6 mm × 1.1 mm. Salaberger et al. [163] investigated two cubical specimen sizes with 1 mm and 2 mm edge length. In the work of Pinter et al. [164] a test specimen with a size of 9.2 mm × 7.36 mm × 2.66 mm was used. All cited works state that due to the small sample size, edge effects due to severed fibers occur, especially when considering long fiber-reinforced composite materials. A direct comparison of a  $\mu$ CT analysis by using the method of Pinter et al. and a conventional, optical fiber length measurement method was carried out by Lohr [165]. He used long glass fiber-reinforced polypropylene samples with a size of 3 mm × 4 mm × 5 mm. In general, a good agreement between the two measurement methods was found. Although both measurements were performed on samples produced with identical process parameters, they were not the exact same samples. Due to possible spatial deviations of the fiber length distribution within in the molded part, a direct comparability is therefore not completely given. Salaberger et al. compared the results from their  $\mu$ CT measurements to manual counting of individual fibers and have found a shift to smaller fiber lengths for the  $\mu$ CT data analysis [163]. However, they also did not examine the exact same sample volume with both methods.

From the fiber length distributions obtained by any of the measurement methods, the number average fiber length  $L_n$  and the weighted average fiber length  $L_p$  are calculated according to Equation (2-15) and Equation (2-16).

$$L_n = \frac{\sum_{i=1}^n n_i L_i}{\sum_{i=1}^n n_i} \quad (2-15)$$

$$L_p = \frac{\sum_{i=1}^n n_i L_i^2}{\sum_{i=1}^n n_i} \quad (2-16)$$

In these Equations,  $L_i$  is the individual length of a fiber  $i$ . The weighted average fiber length  $L_p$  is the second moment of the fiber length distribution and is considered more expressive, because it emphasizes long fibers more strongly [156]. The typical method for plotting the fiber length distribution is a histogram that contains the numerical or weighted frequencies of defined fiber length classes.



## 2.4.2 Load transfer mechanisms in discontinuous fiber-reinforced polymers

Fundamental models for describing the load transfer from the matrix into the fibers have been proposed by Kelly and Tyson [16], Cox [17] and Piggott [18]. Kelly and Tyson assume a completely plastic deformation of the matrix material and a load transfer into the fibers via shear stress. The adhesion between fiber and matrix is assumed to be a constant interfacial shear strength  $\tau_{\text{int}}$ . Using the fiber diameter  $D$  and the tensile strength of the fiber  $\sigma_F$ , they calculated the critical fiber length  $L_c$  according to Equation (2-17).

$$L_c = \frac{D\sigma_F}{2\tau_{\text{int}}} \quad (2-17)$$

The stress distribution along a fiber according to the Kelly-Tyson model is shown in Figure 2-13 (a). The constant interfacial shear stress leads to a linear build-up of tensile stress in the fiber until its ultimate strength is reached. The simplicity of this model has led to its widespread use for estimating the required fiber length for short fiber-reinforced polymers [166–173]. However, the Kelly-Tyson model does not take the elastic deformation of fiber and matrix into account [174]. Such a deformation results in a shear lag and consequently a shear stress distribution along the fiber, rather than the constant interfacial shear stress proposed by the model. Cox's shear lag model [17] considers both fiber and matrix to be purely elastic objects and assumes a perfect adhesion between the two components. The interfacial shear stress between fibers and matrix therefore varies along the length of the fiber [175]. Upon deformation of the matrix material, a shear stress is introduced into the fiber-matrix interface due to the deformation difference between the stiff fibers and the more flexible matrix. The resulting stress distribution along the fiber is shown in Figure 2-13 (b). Due to the high interfacial shear stress at the fiber ends, a perfect adhesion along the entire length of the fiber without debonding – as assumed in Cox's model – is unlikely. To consider this debonding at the fiber ends, Piggott [18] introduced the partially elastic model. While debonding takes place at the fiber ends, the middle part of the fiber is coupled elastically to the matrix. The resulting stress distribution is shown in Figure 2-13 (c). Piggott assumes a debonding over a distance  $s = \mu L/2$  from both fiber ends, with  $0 < \mu < 1$  being a factor for defining the extend of the area with debonding. For the case

of total debonding ( $\mu = 1$ ), the Piggott model converges to the Kelly-Tyson model described above.

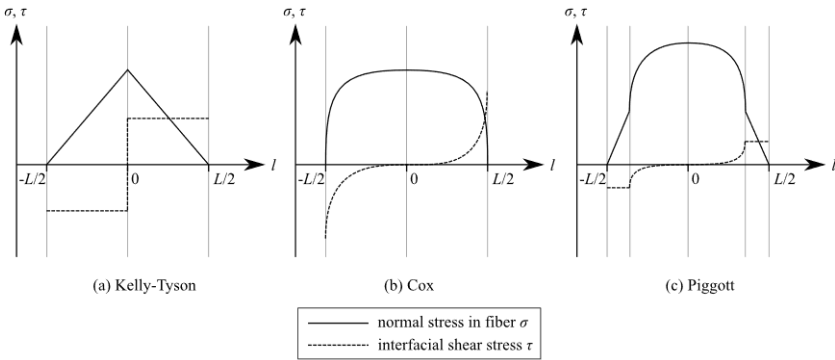


Figure 2-13: Comparison of models for load transfer from matrix to fiber [18]

The Kelly-Tyson approach directly yields an explicit description for the critical fiber length  $L_c$ . In this approach,  $L_c$  is a constant value. Contrarily, the Cox and Piggott models result in expressions that contain the matrix strain  $\epsilon$  as a variable, therefore resulting in changing critical fiber length values depending on the matrix strain, see Figure 2-14.

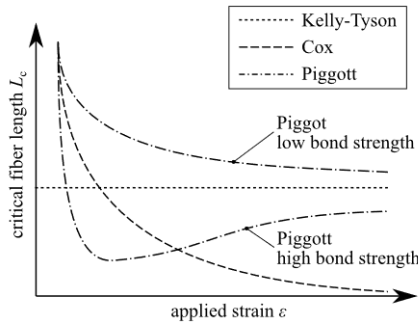


Figure 2-14: Critical fiber length as a function of applied matrix strain [174]

The Kelly-Tyson model often over-estimates the critical fiber length. The fundamental load transfer mechanisms described above are valid for a mechanical load on the composite material that is oriented parallel to the fiber direction. To consider other, non-unidirectional fiber orientations, either simple orientation factors [173,176] or a laminate analogy can be used

[177,178]. Calculations carried out according to the Halpin-Tsai model [178] with using the laminate analogy result in a predicted tensile strength of  $\sigma_{m,SGF} \approx 115$  MPa for a short glass fiber-reinforced phenolic resin ( $L/D = 20$ ) and  $\sigma_{m,LGF} \approx 142$  MPa for a long glass fiber-reinforced material ( $L/D = 50$ ). In both cases, a quasiisotropic fiber orientation with a fiber content of  $\varphi = 40$  %-vol. was assumed and typical mechanical properties for phenolic resin [179] and glass fibers [180,181] were used.

### 2.4.3 Fiber shortening and fiber impregnation during polymer processing

During the injection molding process, the fibers are subjected to high mechanical loads, which cause fiber damage and fiber shortening. Three distinct mechanisms for fiber shortening have been identified [14,182–184] and summarized by Maertens et al. in previous publications [15,26].

- Fluid-fiber interactions
- Fiber-fiber interactions
- Fiber-wall interactions

Fluid-fiber interactions are caused by viscous forces transferred from the polymer matrix into the fibers. For example, Gupta et al. [185] found in their studies on the fiber length reduction of glass fiber-reinforced polypropylene, that a thin polymer film is initially formed on the surface of the screw and barrel wall when the matrix is melted. In this region, fibers that are anchored on one side in solid granulate are exposed to the shear flows of the molten polymer, which can lead to flexural failure of the fibers. The general interaction between fibers and fluid in laminar shear flow has been analyzed by Forgacs and Mason [186]. According to their calculations, forces can occur that lead to fiber damage by buckling. Fiber-fiber interactions can be caused by fiber overlap. The amount of fiber-fiber interactions increases with increasing fiber content and increasing fiber length [187]. At the junction points of two overlapping fibers, the contact forces cause bending deformation of the fibers which might lead to fiber breakage. Even if this bending caused by the fiber overlap does not immediately lead to a fiber break, the already initiated bending of the fibers facilitates the fiber-fluid interaction break due to buckling [184]. Fiber-wall interactions happen at contact locations to machine parts. This is visible by the abrasive wear that can be found

on the screw, the barrel and other machine parts. According to Ren et al. [188], dry (unimpregnated) fibers exist in the early stages of melting. The friction coefficient between these dry fibers and the metal machine surfaces is high compared to the friction coefficient in a lubricated / wetted state. For this reason, fiber breakage due to fiber-wall interaction preferably happens during the very first stage of the plasticizing process. Ren et al. also found that the shear stress near the barrel surface is larger than near the screw, which results in a stronger fiber breakage close to the barrel surface. Additionally, the barrel surface has a higher surface roughness than the screw, further increasing the likeliness of a fiber fracture in this area [188]. According to the simulations carried out by Sasyama et al. [184], fibers close to the wall are deformed when one end is constrained by the wall during the fiber rotation in the viscous polymer melt.

Agglomerations and fiber bundles reduce the overall extend of the fiber shortening, resulting in a higher average fiber length compared to well-homogenized parts. Opening the fiber bundles works in the same way as breaking the fibers. Truckenmüller [114] investigated the opening of fiber bundles in the DIF process (see Section 2.3.2 for process details) and concluded that fiber bundles can be treated as a single fiber with a larger fiber diameter and therefore a smaller  $L/D$  aspect ratio. This underlines the conclusion that fiber bundle opening is not possible without fiber shortening: Once the fiber bundle is opened, the aspect ratio of the individual fiber is significantly larger than the aspect ratio of the bundle from which the fiber originated. If the fluid forces are high enough for opening the fiber bundles, they likely will be high enough for shortening the individual fiber. An indicator for judging the existence of agglomerations and the degree of dispersion quality is the FLD ratio (fiber length distribution) defined by Meyer et al. according to Equation (2-18) [189].

$$\text{FLD} = \frac{L_p}{L_n} \quad (2-18)$$

Meyer et al. calculated a theoretical value of  $\text{FLD} = 1.44$  for a fiber break in the middle due to viscous forces on the fibers. Once this value is reached, no further breakdown of the fibers due to fiber-fluid interactions shall occur. This theoretical conclusion is in accordance with experimental [72,190] and numerical [184] investigations by several other authors, who observed that an asymptotic value  $L_\infty$  for the fiber length during polymer processing exists.

Fibers with a length below  $L_\infty$  are not broken any further by fluid-fiber interactions, because they are too short to introduce sufficiently high loads into them. The initial fiber length does not influence the value of  $L_\infty$ . After a sufficiently long time, all initial fiber length values converge to the same fiber length  $L_\infty$ . The value for  $L_\infty$  only depends on the flow conditions and the shear stresses that the fibers are subjected to during the processing. When  $L_\infty$  is reached, a value of  $FLD \approx 1.44$  is expected. Franzén et al. [191] compared their own experimental investigations with literature values available at the time and confirmed that  $FLD$  is in the expected range of  $FLD = 1.2 \dots 1.5$  for experiments in which a good fiber dispersion and homogenization was achieved. Experiments with a low fiber homogenization quality, e.g. with the presence of fiber bundles and agglomerations, have shown significantly higher values for  $FLD$ , which were in the range of  $FLD = 2 \dots 2.4$ .

Goris et al. [156] give a comprehensive overview of recent research works that investigate the fiber shortening during injection molding. All cited studies examined the fiber shortening in thermoplastic materials. Only very few studies related to thermoset injection molding exist. Singh et al. [192] analyzed the shortening of commercially available short fiber phenolic molding compounds and laboratory synthesized long fiber compounds. For all compounds, the fiber shortening is the strongest in the small transition area in which the plasticizing takes place. The long fiber compounds are shortened significantly stronger than the short fiber molding compounds. Instead of using a granular compound based on solid phenolic resin, the laboratory synthesized long fiber compound used by Singh et al. [192] for the fiber shortening analysis was a dough molding compound, which is also known as bulk molding compound (BMC). No detail information on the rheological behavior of the dough molding compound is given, but it can be assumed that it is different from a solid granular resin. Furthermore, the glass fiber content of the compounds was only  $\phi = 30$  wt.-%, which is significantly lower than in typical state-of-the-art compounds today.

To achieve good mechanical properties, each individual fiber should be in contact with the polymer. This can be achieved either by the impregnation of the fiber bundles themselves, or by disintegrating (opening) and dispersing the bundles [193]. In the first case, the bundles remain intact and a fiber architecture comparable to SMC might exist. In the second case, the fibers are randomly oriented without having a superimposed structure. The impregnation process of fiber bundles has been heavily investigated in the context of

RTM (resin transfer molding) processes. Typically, Darcy's law is used for calculating the impregnation processes of fiber rovings, which are treated as homogenous porous materials. There are few studies regarding the impregnation of dry rovings in the injection molding process. Deringer et al. [194] have investigated the impregnation process of dry carbon fiber rovings in the thermoset injection molding process with an epoxy molding compound. They found that at high mold temperatures, a complete impregnation of the dry fiber rovings could be achieved, whereas low mold temperatures resulted in an incomplete impregnation with air pockets. Niedziela et al. [195] and Müller and Drummer [196] conducted similar investigations for thermoplastics and identified the melt pressure as the main driving force for the quality of the impregnation process. All cited investigations center around the impregnation of the fiber bundles in the mold during the injection process.

## 2.5 Research questions

As outlined in Section 2.1.2, phenolic molding compounds are typically tailored by the material supplier to a specific application by compounding fillers, fibers and functional additives into the resin. It is assumed that these compounds are not suitable for incorporating additional long fibers into them. Within this thesis, the question "Which adjustments to the material formulation and the compounding process are required for the direct processing of long-fiber-reinforced thermosets?" will be addressed.

A central part of the research work within this thesis is the process development for the long fiber direct thermoset injection molding process. As shown in Section 2.3.2, several long fiber injection molding processes exist for thermoplastics, but none are available for thermoset molding compounds. The question "How can a direct fiber feeding process for the manufacturing of long fiber-reinforced thermosets be designed?" will be investigated.

The available thermoset long fiber compression molding compounds (see Section 2.3.2) will be processed in the injection molding process. Challenges regarding the material feeding, the plasticizing and the injection of these compounds are to be expected based on preliminary trials and literature information. This thesis will answer the question "How can a gentle and stable processing of the available long fiber compression molding compounds be realized?".

In Section 2.4.1, the main mechanisms for the fiber shortening during polymer processing are outlined. Many investigations exist for thermoplastics, but only very few for thermosets. Since the understanding of the mechanism for the fiber shortening is essential for the manufacturing of long fiber-reinforced thermoset parts, this thesis will investigate the question “What are the main influencing parameters on the fiber shortening in the injection molding of thermoset compounds?”.

Finally, the two process routes for the injection molding of long fiber-reinforced thermosets – the usage of long fiber granulate and the direct feeding of long fibers into the process – will be compared regarding the resulting mechanical properties and the processing characteristics to answer the questions “Which process route is recommended for the injection molding of long fiber-reinforced thermoset molding compounds?” and “Which fiber length is needed for obtaining a benefit in mechanical properties?”





## 3 Experimental

### 3.1 Materials

The phenolic molding compound used for the experimental work in this thesis is based on Vyncolit® X6952 [46], a short glass fiber-reinforced compound by Sumitomo Bakelite (Gent, Belgium). The commercially available Vyncolit® X6952 is a PF-SGF55 (phenol-formaldehyde resin reinforced with 55 wt.-% short glass fibers) novolac compound. For this work, the short glass fiber content in the molding compound was adjusted from fractions of  $\phi = 0$  wt.-% up to  $\phi = 60$  wt.-% by twin-screw extruder compounding. The compounding was done on lab scale extruders, see Section 4.1. The raw materials for the molding compound were provided by Sumitomo Bakelite as a two-component system consisting of the novolac resin powder with pre-mixed hexamethylenetetramine and a masterbatch, which contains the processing additives. The colorant phthalocyanine in the masterbatch changes its color from blue to green as the phenolic resin cures, thus giving a visual indication during processing [50,197].

Short glass fibers (SGF) for the compounding trials were sourced from 3B fibreglass (Hoeilaart, Belgium) in the form of DS5163-13P [180] chopped strands. These fibers consist of E-CR glass (E-glass corrosion resistant) with a filament diameter of  $D = 13 \mu\text{m}$  and feature sizing designed for compatibility with phenolic and epoxy resin systems. Due to their high bulk density and free-flowing behavior, they are widely used for manufacturing of phenolic molding compounds like Vyncolit® X6952. For the continuous glass fibers roving, the type 111AX11 by 3B fibreglass [181] was used. It is a direct roving with a filament diameter of  $D = 17 \mu\text{m}$  and a roving weight of  $Tt = 2400 \text{ tex}$  and was recommended by the manufacturer for the use with phenolic resins. In preliminary fiber chopping trials, a good cutting behavior with small quantities of fiber fuzz was observed. Due to the lower strand integrity of the direct rovings compared to the chopped strands, they are no longer free flowing once they are chopped. The nomenclature of the material formulations that is used in this thesis follows the scheme PF-SGF $_x$ -LGF $_y$ . The variables  $x$  and  $y$  stand for the fiber weight content  $\phi$  of the short or long

glass fibers. For example, a PF-SGF0-LGF30 formulation contains  $\phi = 0$  wt.-% SGF and  $\phi = 30$  wt.-% LGF. The pure LGF and SGF formulations as well as the mixture formulations with a constant total fiber content, but varying fractions of LGF and SGF are visualized in Figure 3-1.

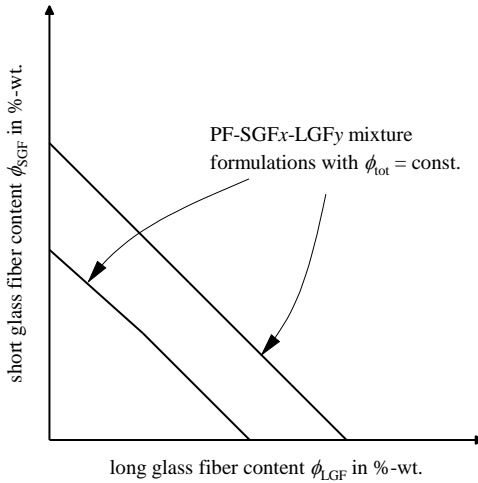


Figure 3-1: Visualization of PF-SGF<sub>x</sub>-LGF<sub>y</sub> formulations

In addition to the self-compounded short fiber-reinforced molding compounds and the X6952, two commercially available long glass fiber (LGF) phenolic molding compounds by Sumitomo Bakelite were used. The long fiber phenolic molding compound Porophen® GF9201 [119] (short name PF-SGF0-LGF55) was supplied in the form of unidirectionally reinforced flakes with a fiber length of  $L = 5$  mm and  $L = 12$  mm and is typically used in compression molding applications.

## 3.2 Characterization methods

### 3.2.1 Flow-hardening characterization

#### 3.2.1.1 Orifice flow test

The orifice flow test was used for obtaining comparison values to commercially available phenolic molding compounds. It was carried out according to ISO 7808 [56]. The mold was mounted to an Arburg 320C 600-250 vertical injection molding machine (Loßburg, Germany). Since the OFT is a compression molding process, only the clamping unit of the injection molding machine was used. The mold temperature was adjusted to  $T = 165\text{ °C}$  and a molding pressure of  $p = 7\text{ MPa}$  was selected, corresponding to the denomination OFNL. The main purpose of the OFT was to determine the correct energy input into the SGF compound for the twin-screw extruder compounding trials. To do so, molding compounds with  $\phi = 60\text{ wt.-%}$  fiber content were manufactured and the extruder process parameters (screw speed and throughput) were manipulated until the desired value of OFNL  $\approx 50$  was achieved. For this extruder parameter setting, the specific mechanical energy input into the resin,  $\text{SME}_R$ , was calculated and subsequently kept constant during the compounding process. Detailed information regarding the calculation and the compounding process can be found in Section 4.1. The OFT was not considered useful for compound formulations with a fiber content of  $\phi \neq 60\text{ wt.-%}$ . Since the fiber content significantly influences the compound's viscosity and therefore the flow-hardening behavior, a comparison between different fiber content values is not possible.

#### 3.2.1.2 Differential scanning calorimetry

Since the OFT is not suitable for comparing compounds with different fiber contents  $\phi$ , differential scanning calorimetry (DSC) was used for determining the heat of reaction of the manufactured short fiber molding compounds. A three-step process was established to obtain valid and repeatable results and has been published by Maertens et al. in a previous publication [24]. In the first step, the granular molding compound was milled and homogenized by using a CryoMill by Retsch (Haan, Germany). In this mill, a compound mass of  $m \approx 5.5\text{ g}$  was ground by impact and friction while being cooled with liquid nitrogen at a temperature of  $T = -196\text{ °C}$ . This process ensured that as little additional energy is put into the resin as possible, so that no further

reaction progress took place. The glass fibers in the molding compound were ground as well, ensuring an even distribution of the inert glass in the reactive resin, which was critical for the following analysis step. The ground compound powder was transferred into the DSC pan for the second step. Due to the condensation reaction of the phenolic resin and the release of ammonia caused by the hexamethylenetetramine, sealed DSC pans were used. Both medium pressure pans with a volume of  $V = 120 \mu\text{l}$  (Mettler Toledo 29990) and high pressure pans with a volume of  $V = 30 \mu\text{l}$  (Mettler Toledo 51140404) were evaluated. Due to the higher pan volume, the medium pressure pans resulted in more repeatable measurement results and were used for all measurements presented in this thesis. Three samples were taken from each ground molding compound sample and analyzed by using a DSC 1 instrument from Mettler Toledo (Columbus, United States). The chosen DSC profile was a temperature ramp of  $\dot{T} = 10 \text{ K/min}$  from  $T = 40 \text{ }^\circ\text{C} \dots 300 \text{ }^\circ\text{C}$  under nitrogen atmosphere. The heat of reaction  $\Delta H_{\text{R}}$  was calculated according to DIN EN ISO 11357-5 [198] by integrating the area between the reaction peak and the interpolated baseline.

To account for the different fiber contents  $\phi$  of the various formulations, every DSC sample was removed from the pan after the measurement and was subjected to a thermogravimetric analysis (TGA). The chosen TGA profile was a temperature ramp of  $\dot{T} = 10 \text{ K/min}$  from  $T = 25 \text{ }^\circ\text{C} \dots 650 \text{ }^\circ\text{C}$  with an additional holding time of  $t = 10 \text{ min}$  under air atmosphere. The TGA serves the purpose of determining the solids content in the sample, so that the heat of reaction  $\Delta H_{\text{R}}$  can be related to the resin content. Additionally, analyzing each of the three samples per specimen allows a judgement of the homogenization quality achieved in the grinding process. Typical deviations between the three specimens were below  $\Delta\phi = 0.5$  percentage points, which indicates a good homogenization.

### 3.2.1.3 Oscillatory rheology

Rheological measurements were carried out by using an Anton Paar Physica MCR 501 rheometer (Graz, Austria) in a plate-plate oscillating configuration. To achieve a good adhesion to the rheometer plates, a sample preparation was required. A small sample mold with a circular cavity of  $d = 25 \text{ mm}$  diameter was mounted on a laboratory press Collin P 200 P/M (Maitenbeth, Germany) for  $t = 90 \text{ s}$  at an in-mold pressure of  $p = 100 \text{ bar}$  and a plate temperature of  $T = 120 \text{ }^\circ\text{C}$ . Since the sample mold itself is not heated, the actual material

temperature in the sample was likely lower than the heating plate temperatures mentioned above. The process parameters were chosen to produce homogeneous specimens with plane-parallel surfaces and a thickness of  $h = 1$  mm, while keeping the thermal energy input into the specimen as low as possible. After pressing, individual granulate pellets were no longer visible. For the oscillatory rheology measurements in controlled strain deformation mode, the parameters listed in Table 3-1 were chosen.

Table 3-1: Parameters for oscillatory rheology measurements

Parameter	Unit	Value
Plate diameter	mm	25
Initial gap size	mm	1
Normal force	N	7
Deformation amplitude	%	0.01
Oscillation frequency	rad/s	10
Start temperature	°C	50
Heating rate	K/min	10
End temperature	°C	200

### 3.2.2 Evaluation of material homogeneity by X-ray computed tomography image texture analysis

The fiber length is only one factor that determines the strength of the composite material. According to Šahinović and Mušič [199], a homogeneous distribution of the fibers in the polymer matrix is equally important. Especially in the case of bundle-shaped material constituents such as long fiber granulate pellets or chopped long fibers, opening the bundles is important for achieving good mechanical properties. To evaluate the homogeneity of intermediate products and molded parts in the long fiber thermoset injection molding process, an image texture analysis method using X-ray computed tomography is presented. The procedure is described in detail in the publication "Study of material homogeneity in the long fiber thermoset injection molding process by image texture analysis" by Maertens et al. [25]. In general, two main elements for the interpretation of graylevel images exist [200]. The tone is defined as the variation of the graylevel values in the image and it can be visualized in a histogram. The spatial distribution of the graylevel values is defined as the texture of the image. No direct visualization of this feature is possible. To overcome this deficit, Haralick et al. [201]

defined a procedure for the extraction of textural features out of 2-dimensional, graylevel images which is described below.

The first step is the calculation of the graylevel co-occurrence matrix (GLCM), which gives the number of occurrences of all graylevel-combinations directly adjacent to each other. An 8-bit image with its  $N_g = 256$  different graylevels consequently results in a  $256 \times 256$  GLCM. The structure of the GLCM describes the texture of the image. In a homogeneous image, there are very few dominant graylevel transitions, because most adjacent pixels have the same or similar graylevels. Consequently, the GLCM has a small number of entries, each of which has a high absolute value. In contrast, in an inhomogeneous image, most adjacent pixels have different graylevels. Therefore the GLCM has a high number of entries with a small absolute value [201]. However, due to the sheer size of the matrices, the direct analysis of the GLCMs themselves is neither descriptive nor comprehensible. For this reason, Haralick et al. defined 14 textural features, which condense the GLCM into a single numerical value each and allow an easy comparison of multiple images. In this work, the textural features angular second moment (ASM) is used. It is calculated according to Equation (3-1).

$$ASM = \sum_i \sum_j \left\{ \frac{p(i,j)}{R} \right\}^2 \quad (3-1)$$

In the Equation above,  $i$  and  $j$  are the index values for the GLCM entries and  $p(i,j)$  is the number of graylevel co-occurrences for the graylevels  $i$  and  $j$ , representing the value of each GLCM entry.  $R$  is the number of neighboring cell pairs in all spatial directions, which is used for normalization purposes. The value for  $R$  is calculated according to Equation (3-2) and Equation (3-3) by using the number of cells  $N_x$  and  $N_y$  in the two orientations of the image:

$$R = R_{\rightarrow} + R_{\uparrow} + R_{\nearrow} + R_{\searrow} \quad (3-2)$$

$$R = 2 \left[ N_y(N_x - 1) + N_x(N_y - 1) + (N_y - 1)(N_x - 1) + (N_x - 1)(N_y - 1) \right] \quad (3-3)$$

For an 8-bit,  $256 \times 256$  GLCM, this results in  $R = 521\,220$  neighboring cell pairs. The possible values for the ASM range from  $1/N_g^2$  to 1 [202]. The lower

limit represents a transition between the extreme values of the graylevels for each pixel in the image, i.e. an image with the lowest possible homogeneity. A value of  $ASM = 1$  results from an entirely homogeneous, constant image where every pixel has the same tone. In short, a homogeneous image results in a high ASM value, whereas an inhomogeneous image results a low ASM value. The ASM textural feature was applied by several authors in the fields of aerial photography [203], chemistry [204,205] and medicine [206] for quantifying the homogeneity of an image. In Haralick's original calculation, only neighboring cell pairs were considered for the calculation of the textural features. However, depending on the image and the aim of the investigation the conclusiveness of the results can be improved using multiple or larger calculation distances [207]. The original 2-dimensional image texture analysis by Haralick et al. has been extended to a 3-dimensional calculation for medical images [208,209], but has not been used for the characterization of composite materials before. Implementations of the calculation procedure exist in the software ImageJ [210]. In this thesis, these existing implementations are used for quantifying the homogeneity of the long glass fiber-reinforced phenolic molding compound at certain stages of the injection molding process (see Section 3.2.2 for the location of the two specimen groups). The 3-dimensional images were acquired by using a XYLON precision  $\mu$ CT with the image acquisition parameters listed in Table 3-2.

Table 3-2: Image acquisition parameters for X-ray computed tomography homogeneity evaluation [25]

Parameter	Unit	Value specimen group 1	Value specimen group 2
<b>Tube head</b>	-	Directional focus tube	
<b>Target</b>	-	Tungsten	
<b>Acceleration voltage</b>	kV	145	120
<b>Tube current</b>	mA	0.15	0.1
<b>Voxel size</b>	$\mu$ m	47	36
<b>Integration time</b>	ms	500	750
<b>Frame binning</b>	-	2	1

Due to the density difference of the glass fibers, the phenolic resin matrix and pores, these three phases were visible in the  $\mu$ CT images. The appropriate choice for the voxel size is a trade-off between the image resolution and the sample volume that can be examined. The LGF that were used in this thesis

have a diameter of  $D = 17 \mu\text{m}$  [181], which means that the chosen voxel sizes does not allow the detection of individual fibers. However, considering that the LGF roving weight of  $Tt = 2400 \text{ tex}$  corresponds to a fiber count of approximately  $n = 4000$  fibers per roving, as calculated using Equation (3-4)

$$n = \frac{m_{\text{Roving}}}{m_{\text{Fiber}}} = 4 \frac{Tt}{\rho \pi D^2} \quad (3-4)$$

the chosen voxel size is deemed adequate for the measurement purpose. In Equation (3-4),  $Tt$  is the roving weight in tex,  $\rho$  is the glass fiber density and  $D$  is the glass fiber diameter. Subsequently, the ImageJ command “smooth” was applied. This filter replaces each voxel with the average graylevel of its  $3 \times 3 \times 3$  neighborhood. Preliminary investigations had shown that the smoothing filter increases the total ASM value difference between homogeneous and inhomogeneous images and thus increases the expressiveness of the results. The 3-dimensional GLCM and the textural feature ASM was calculated for multiple distance values. With a calculation distance that is of the same magnitude as the characteristic pattern, the expressiveness of the results can be improved [211]. To condense the multiple results into a single numerical value again, the average value of the three distances was taken.

### 3.2.3 Fiber length measurement

For the fiber length measurement, both a destructive method based on pyrolytical decomposition of the matrix and a non-destructive method using X-ray computed tomography were used. The exact measurement procedure as well as validation investigations regarding fiber damaging and selectivity towards longer or shorter fibers are described in detail in the publication “Fiber shortening during injection molding of glass fiber-reinforced phenolic molding compounds: Fiber length measurement method development and validation” by Maertens et al. [15]. In the first step of the destructive measurement method, a circular sample with a diameter of  $d = 25 \text{ mm}$  was extracted from the molded plate using waterjet cutting. A typical weight for such a sample is approximately  $m = 3 \text{ g}$ . Subsequently, the phenolic matrix was removed by means of pyrolysis at  $T = 650 \text{ }^\circ\text{C}$  for a duration of  $t = 36 \text{ h}$  under air atmosphere by using a LECO TGA 701 (St. Joseph, USA). The ash residue was transferred into  $V = 1.5 \text{ l}$  distilled water and a small amount of acetic acid was added to support the fiber dispersion. The suspension was the subjected



to  $t = 2$  min in an ultrasonic bath to open the fiber bundles. The fiber concentration in this suspension was too high for obtaining an analyzable image, which is why further dilution was necessary. By transferring the suspension into a newly developed dilution device for further down-sampling, this process can be conducted in a repeatable and controlled manner. Figure 3-2 shows the dilution device, which consists of a beaker glass with a capacity of  $V = 4$  l and an outlet tap with a diameter of  $d = 10$  mm attached to its side. A propeller stirrer keeps the fibers distributed homogeneously within the suspension. [15]

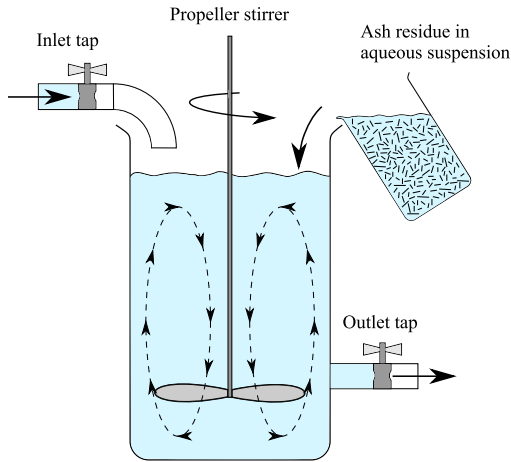


Figure 3-2: Dilution device for representative taking of fiber length measurement samples [15]

The dilution and sample taking process steps are accomplished by opening the outlet tap and re-filling the beaker with distilled water. Once the desired degree of dilution was reached, measurement samples were taken through the outlet tap and transferred to a petri-dish, which was then analyzed using the FASEP system by IDM systems (Darmstadt, Germany). The cropping of the image and thresholding were done manually, but the fiber detection was done automatically using the algorithms provided by the FASEP system. Per petri-dish, approximately  $n = 3000$  (long fiber molding compound) to  $n = 6000$  (short fiber molding compound) fibers were measured. To reduce the influence of the variation of the sampletaking, it was repeated at least four times per specimen. [15]

To verify the optical fiber length measurement process, non-destructive measurements using X-ray computed tomography were carried out. Samples cut from molded parts with a sample size of (5 mm × 5 mm × 4 mm) as well as granulate from the short fiber molding compound were analyzed by using a YXLON CT precision X-ray computed tomography scanner with a flat panel Perkin Elmer Y.XRD1620 detector with a resolution of 2048 px × 2048 px. Table 3-3 shows the image acquisition parameters.

Table 3-3: X-ray computed tomography image acquisition parameters for non-destructive fiber length measurement [15]

Parameter	Unit	Value
Tube head	-	Transmission tube
Target	-	Tungsten
Acceleration voltage	kV	100
Tube current	mA	0.02
Voxel size	μm	3.608
Integration time	ms	1000
Frame binning	-	2

The images generated in this way were evaluated for fiber length distribution with the methods and algorithms described by Pinter et al. [164]. The first analysis step is a so called circular voting filter that thins out the fibers in the direction of thickness to separate adjacent fibers. By applying thresholding and skeletonization operations in the software ImageJ, the image is prepared for the single fiber tracking. In this last step, the algorithm analyses every junction and looks for the best match of adjacent fibers by comparing the alignments [164]. A comma separated values (CSV) file containing every individual fiber and its length is outputted and subsequently used for determining the fiber length distribution and the average fiber length values. The results for the comparison of the μCT method with the optical fiber length measurement are presented in Section 5.4.4.

### 3.2.4 Micrography of the structure

To investigate the filler orientation and the homogeneity of the material, micrographs were made with an M420 macroscope manufactured by the company Wild Heerbrugg. The EcoMet300 Pro and PowerPro4000 grinders from Buehler were used for specimen preparation. Grinding papers with grits

of 120, 320, 600, 1000, 2500, and 4000 were used to start the process, which was finished with a 3  $\mu\text{m}$  polishing disc. Figure 3-4 c) illustrates at which locations of the plates the samples were taken. Only half the plate width was used for the specimens in the 90° orientation to the flow, because a symmetrical filling is assumed across the width of the mold.

### 3.2.5 Mechanical characterization

During all injection molding trials, rectangular plates with a size of 190 mm  $\times$  480 mm and a thickness of  $h = 4$  mm were manufactured. The plates were filled via a central sprue with a  $d = 15$  mm diameter. After molding, all plates were post-cured in a circumventing air oven according to the temperature cycle in Figure 3-3 to make sure that they have the same degree of cure despite the varying fiber and resin contents.

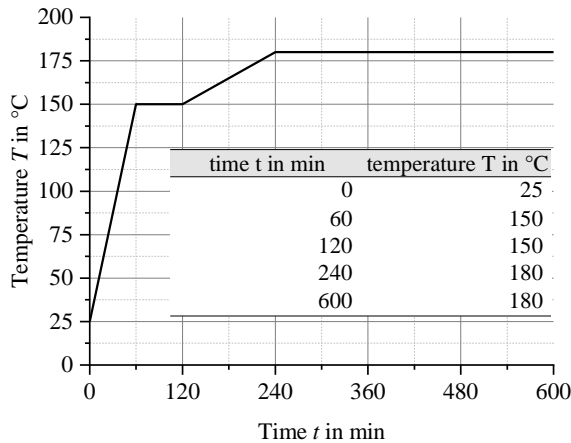
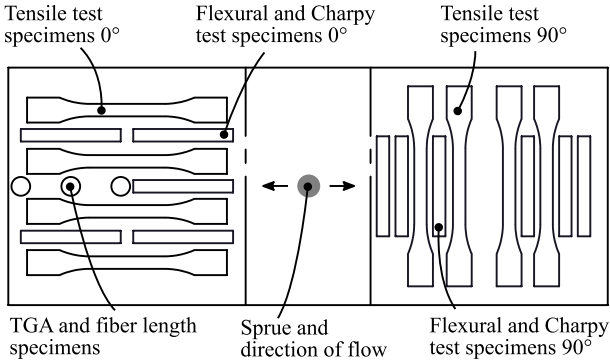


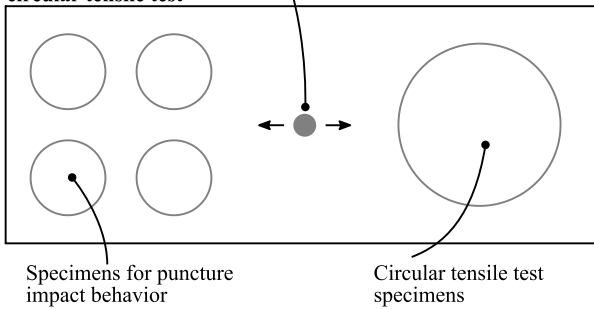
Figure 3-3: Post-cure cycle for molded plates [26]

The test specimens were cut out of the plates by waterjet-cutting according to the cutting patterns shown in Figure 3-4 a) and b).

**a) Tensile, flexural and Charpy test specimens**



**b) Puncture impact and circular tensile test**



**c) Optical micrography of the structure**

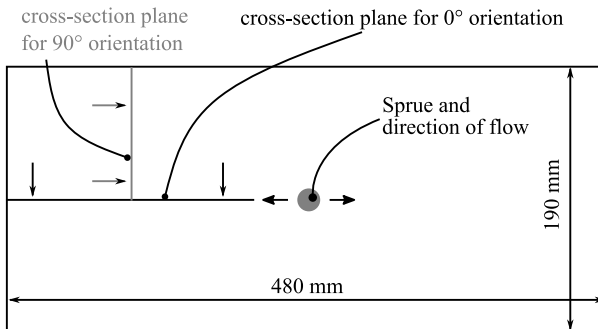


Figure 3-4: Cutting pattern for test specimens [26]

The quasistatic mechanical testing was carried out according to the technical standards DIN EN ISO 527-2 (tensile testing) and DIN EN ISO 14125 (3-point bending testing). To analyze the anisotropy of the stiffness of the

molded parts, a tensile test with circular test specimens was carried out. This is a non-destructive tensile test on circular test specimens with a diameter of  $D = 130$  mm and a thickness of  $h = 4$  mm. The circular test specimens were tested as described by Tröster [212]. They were clamped in a tensile testing machine, subjected to a tensile load, and then rotated by an angular increment of  $\Delta\alpha = 10^\circ$  after each loading. Tröster [212] has shown that multiple loadings do not affect the material properties, because it is only stressed within its linear elastic region. To remove any settling effects in the clamping area, the specimens were preloaded once and then the measurement was performed at a test speed of  $v = 1$  mm/min. From the recorded force-displacement curves, the stiffness of the circular test specimens was determined in the linear elastic range between  $\varepsilon = 0.05\%$  and  $\varepsilon = 0.1\%$  strain [213]. To determine a modulus, an equivalent area had to be calculated from the dimensions of the circular test specimen. Since the calculated modulus does not correspond to the definition of Young's modulus, but is of the same order of magnitude, it is referred to as pseudo Young's modulus ( $E^*$ -modulus). Tröster shows that the force and  $E^*$  modulus curves on the circular tensile test specimen are centrally symmetric and that the values at  $\alpha = 10^\circ$  and  $\alpha = 180^\circ$  are almost identical [212]. For this reason, only tests between  $\alpha = 10^\circ \dots 170^\circ$  were conducted. For each material and process parameter variation, two specimens were examined. To quantify the shape of the ellipses, a mathematical fit according to the method of least squares was performed. From the obtained ellipse function

$$f = \left(\frac{x - x_c}{a}\right)^2 + \left(\frac{y - y_c}{b}\right)^2 - 1 \quad (3-5)$$

the length  $a$  and  $b$  for the major and the minor axis are used for calculating the ellipses' axes ratio  $r_{\text{Ellipse}}$  according to Equation (3-6).

$$r_{\text{Ellipse}} = \frac{b}{a} \quad (3-6)$$

For the characterization of the dynamical mechanical properties, Charpy non-instrumented impact testing according to DIN EN ISO 179-1 was performed. A broad side impact on unnotched specimens with a pendulum work capacity of  $W_{\text{Imp, Charpy}} = 5$  J was chosen. In addition, instrumented puncture impact tests were carried out based on DIN EN ISO 6603-2. At least eight specimens were tested from each material or process parameter variation. The impact velocity of  $v = 4.4$  m/s corresponds to a total impact energy of

$W_{\text{Imp, puncture}} = 24.4 \text{ J}$ . To determine a single numerical value for the impact energy, the resulting force-displacement curves were smoothed with a moving average and subsequently integrated up to the point of complete force drop. For selected specimens, the failure behavior during the puncture impact test was recorded using a high speed camera IDT Os8-S3 (Imaging Solutions, Eningen unter Achalm, Germany) with an image acquisition rate of 8000 frames per second at a video resolution of  $1600 \text{ px} \times 1200 \text{ px}$ .

### 3.2.6 Scanning electron microscopy

The fracture surfaces of selected specimens from the quasistatic and the dynamic mechanical testing were analyzed by using scanning electron microscopy (SEM). The aim was to obtain information about the material structure as well as the fiber-matrix adhesion. For the specimens from the quasistatic testing, a Zeiss EVO50 device was used to generate images with magnification factors of 60, 200 and 500 from the fracture surfaces of tensile test specimens with an acceleration voltage of  $U = 10 \text{ kV}$ . For the dynamic testing, fracture surfaces of specimens from Charpy impact testing were analyzed by using a Zeiss Supra 55VP instrument with magnification factors 19, 50, 200 and 1000 at acceleration voltages of  $U = 3 \text{ kV} \dots 6 \text{ kV}$ .

# 4 Process Development

## 4.1 Twin-screw extruder compounding of short fiber-reinforced phenolic resins

The short glass fiber-reinforced phenolic molding compounds were manufactured using Leistritz 27 co-rotating twin-screw extruders with  $d = 27$  mm screw diameters and processing lengths of 36 D and 52 D, respectively (Leistritz Extrusionstechnik GmbH, Nürnberg, Germany). The main challenge was the process control to adjust the energy input into the resin. The developed method is described in detail in the publication “Compounding of Short Fiber Reinforced Phenolic Resin by Using Specific Mechanical Energy Input as a Process Control Parameter” by Maertens et al. [24]. Figure 4-1 shows the screw layout and the temperature profile.

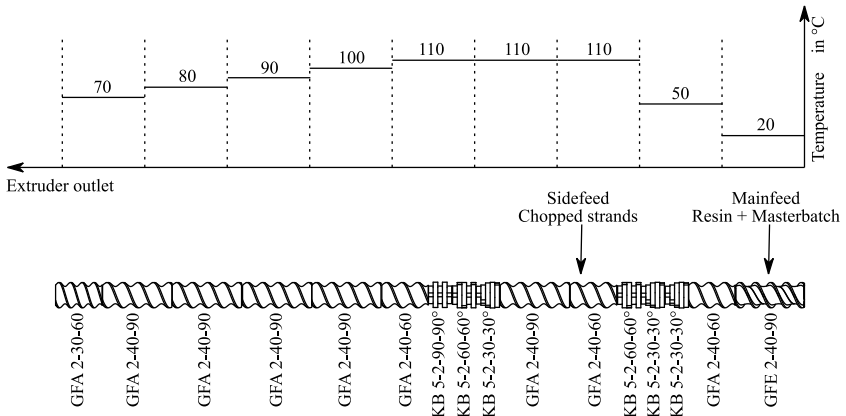


Figure 4-1: Twin-screw extruder layout and temperature profile [24]

Due to the closely intermeshing geometry of the twin-screw extruder, both screws had the identical layout and rotated at the same speed [214]. By shifting the main feed towards the extruder outlet, the processing length of the extruders was reduced to 28 D to shorten the residence time of the molding compound. The three components resin/HMTA, masterbatch and SGF were fed gravimetrically into the extruder by using single screw loss-in-

weight-feeders by Brabender Technologie (Duisburg, Germany). Both resin/HMTA and masterbatch were fed into the main feed and melted up in the first kneading zone, which consisted of kneading elements with  $30^\circ$ ,  $30^\circ$  and  $60^\circ$  angles between the kneading discs. The increase in barrel temperature to  $T = 110^\circ\text{C}$  supported the melting of the resin powder. Downstream of the first kneading zone, the short glass fibers were fed into the melt using a  $d = 26\text{ mm}$  co-rotating twin-screw sidefeed (type Leistritz LSB26). To open the fiber strands, additional kneading elements with  $30^\circ$ ,  $60^\circ$  and  $90^\circ$  angles formed a second kneading zone. In the last three barrel zones, the material was cooled down and conveyed to the open extruder outlet. No die was attached to the outlet to avoid pressure build-up and thus increased energy input into the molding compound. The molding compound exited the extruder in lumps which were subsequently compacted by hand and cooled down by free convection [215]. After cooling, the compound was granulated to using a Hosokawa Alpine (Augsburg, Germany) cutting mill with a  $s = 10\text{ mm}$  rectangular screen. Figure 4-2 shows a sample of the manufactured PF-SGF40-LGF0 molding compound. [24]



Figure 4-2: Manufactured PF-SGF40-LGF0 phenolic molding compound

The granulation process with the cutting mill produces a dust-rich, irregular granulate. After granulation, the mixture was stored in sealed containers at room temperature until molding. During the compounding of reactive materials such as phenolic resins, monitoring and controlling the energy input into the material is crucial. The total power input into the material is the sum of the mechanical power input, the enthalpy change between extruder inlet and



outlet and the power used to increase the material pressure according to Equation (4-1) [216]:

$$\begin{aligned}
 P_{\text{tot}} &= P_{\text{Mech}} + P_{\text{Heat}} + P_{\text{Enthalpy}} + P_{\text{Press}} \\
 &= 2\pi \omega M_{\text{Extr}} + P_{\text{Heat}} + \dot{m} \Delta H + \dot{m} \frac{\Delta p}{\rho}
 \end{aligned}
 \quad (4-1)$$

In Equation (4-1), extruder speed  $\omega$ , extruder torque  $M_{\text{Extr}}$ , mass throughput  $\dot{m}$ , enthalpy difference  $\Delta H$ , pressure difference  $\Delta p$  and material density  $\rho$  are used. The second term in Equation (4-1),  $P_{\text{Heat}}$ , describes the heat transfer between the polymer and the processing chamber walls. No literature that reported a direct measurement of the heat transfer was found. Instead,  $P_{\text{Heat}}$  is typically calculated by estimating the third and fourth term in Equation (4-1) [216]. The enthalpy difference  $\Delta H$  can be calculated with the thermodynamic properties of the compounded material, e.g. heat capacity, heat of fusion and heat of reaction. If a pressure build-up occurs at the end of the extruder, the pressure difference  $\Delta p$  can be used for calculating the power  $P_{\text{Press}}$ . Multiple authors report that the first term, the mechanical power input  $P_{\text{Mech}}$ , is by far dominant for polymer extrusion processes [216–218]. It can be quantified by calculating the specific mechanical energy input (SME) according to Equation (4-2). [24]

$$\text{SME} = \frac{2\pi \omega M_{\text{Extr}}}{\dot{m}} \quad (4-2)$$

For example, Inceoglu et al. [218] identified a good correlation between the SME and the residual fiber length during the compounding of glass fiber-reinforced polyamide. During the compounding of the phenolic molding compounds with varying glass fiber contents, the extruder speed  $\omega$  and the throughput  $\dot{m}$  were adjusted to keep the specific mechanical energy input into the resin ( $\text{SME}_R$ ) as constant as possible. It is calculated using the fiber weight content  $\phi$  according to Equation (4-3). [24]

$$\text{SME}_R = \frac{2\pi \omega M_{\text{Extr}}}{\dot{m} (1 - \phi)} \quad (4-3)$$

## 4.2 Long fiber direct injection molding process

For the long fiber direct thermoset injection molding process development carried out within this thesis, a standard thermoset injection molding machine KM 550 / 2000 GX (KraussMaffei Technologies GmbH, Munich, Germany) was modified. The basic specifications are given in Table 4-1.

Table 4-1: Specifications of the KM 550 / 2000 GX injection molding machine

Specification	Unit	Value
<b>Screw diameter</b>	mm	60
<b>Max. plasticizing volume</b>	cm <sup>3</sup>	792
<b>Number of cylinder heating zones</b>	-	4
<b>Max. injection pressure</b>	bar	2420
<b>Max. injection speed</b>	cm <sup>3</sup> /s	848
<b>clamping force</b>	kN	5500

The long fiber direct thermoset injection molding shares similarities with the Arburg FDC process (Section 2.3.2). Glass fibers are chopped from continuous rovings and are transported into the plasticizing unit with a co-rotating twin-screw sidefeed, which acts as a conveying device. This means that no melting or intentional mixing takes place there. The first process variant “common feeding of granulate and long fibers” can be described as feeding a dry blend of chopped long fibers together with the phenolic molding compound into the barrel of the injection molding machine. Figure 4-3 shows the standard thermoset injection molding process (a) and this process variant (b).

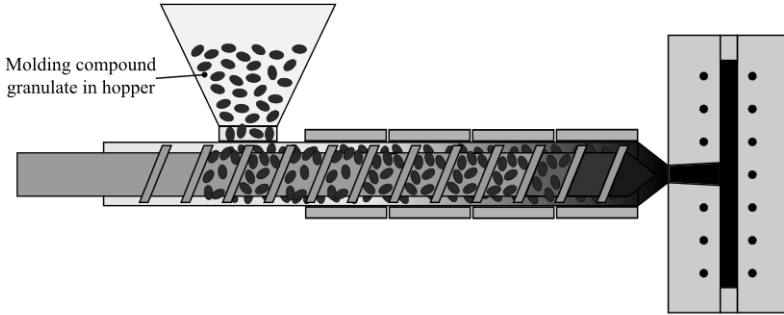
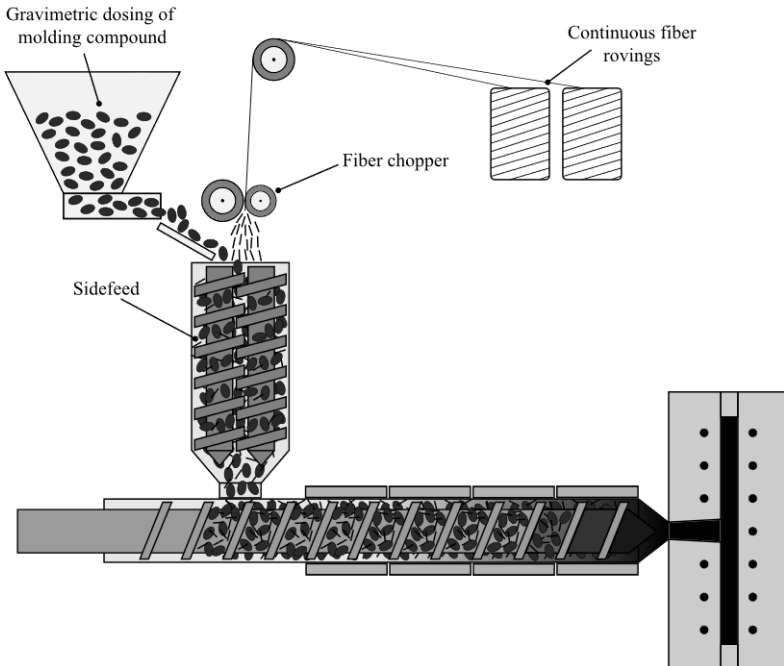
**a) Standard thermoset injection molding process****b) Long fiber thermoset injection molding process "standard plasticizing unit"**

Figure 4-3: Comparison of the standard thermoset injection molding process (a) with the long fiber process variant "standard plasticizing unit" (b)

Basically, only the material hopper of the standard injection molding machine is replaced by the sidefeed and the peripheral devices for dosing the granulate and the long fibers. A co-rotating twin-screw sidefeed ZSA42 with

a screw diameter of  $d = 42$  mm by KraussMaffei Technologies GmbH (Hanover, Germany) is flanged to the plasticizing unit. Due to installation space restrictions at the injection molding machine, an adaption in the  $90^\circ$  angle sketched in Figure 4-3 is not possible. Instead, an angled position of the sidefeed at an angle of  $30^\circ$  above the plasticizing unit is realized. The two material streams, SGF molding compound and LGF, are directly dosed into the sidefeed. To achieve a constant material formulation, the molding compound is fed gravimetrically by using a Brabender DDSR-20 loss-in-weight-feeder. The mass flow of the long glass fibers is adjusted by using a frequency inverter that controls the speed of the fiber chopper Chopcot T5 (Van der Mast Industrial Innovations, Eelde, the Netherlands). Furthermore, the length of the chopped fibers can be set to  $L = 5$  mm,  $L = 10$  mm or  $L = 15$  mm by removing blades from the cutter roll.

Both the roving storage and the fiber chopper are fixed to the moving parts of the plasticizing unit and move back and forth together with it. The loss-in-weight feeder is located on a stationary platform adjacent to the machine to isolate it from vibrations. Due to the discontinuous nature of the injection molding process and the lack of a material buffer, all peripheral devices work in the same stop-and-go manner. The digital trigger signal for the plasticizing process is read from the machine and is used to switch the loss-in-weight-feeder, the fiber chopper and the sidefeed on and off. Figure 4-4 visualizes the signal flow. The set values for the peripheral devices are either defined in the programmable logic control (PLC) software on the control computer (fiber chopper speed, sidefeed speed), directly at the injection molding machine (screw speed, back pressure, plasticizing volume) or at a separate control panel (Brabender OP1 feeder control for gravimetric flow set value).

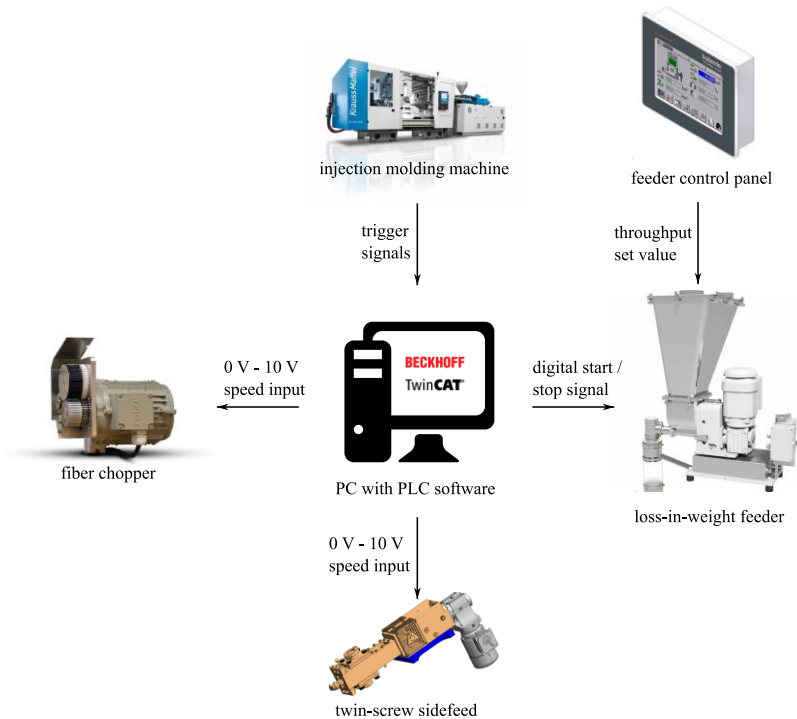


Figure 4-4: Signal flow chart for long fiber process peripheral devices control [219–221]

Two different screw and barrel versions can be used in conjunction with the peripheral long fiber feeding devices. First, the standard thermoset injection molding screw and barrel can be used. Second, a newly designed plasticizing unit with a longer processing length, a modified screw and barrel geometry and interchangeable screw tips can be used. Both screw geometries are compared in Table 4-2 below.

Table 4-2: Comparison of standard and long fiber screw geometries

Screw zone	Standard screw		Long fiber screw	
	Zone pos. in L/D	Core diam. In mm	Zone pos. in L/D	Core diam. In mm
Feed zone for granulate	-	-	0 – 5.5	46
Compression zone	-	-	5.5 – 6	46 – (56,57,58)
Conveying zone after sidefeed	0 – 11.1	46	6 – 16.5	44
Compression zone	11.1 – 12.8	46 – 48	16.5 – 18.2	44 – 46
Metering zone	12.8 – 17.5	48	18.2 – 23	46

Figure 4-5 shows a comparison of the standard thermoset injection molding plasticizing unit (a) with the long fiber barrel (b).

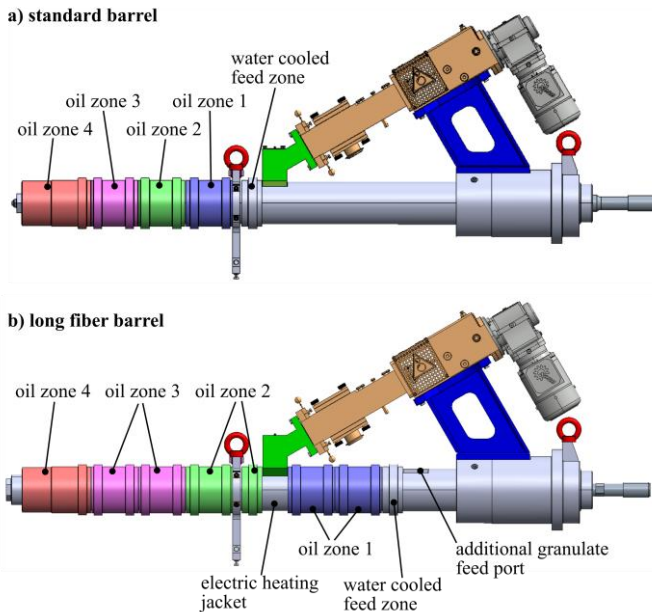


Figure 4-5: Comparison of standard thermoset barrel (a) to long fiber barrel (b)

The 30° angle between the sidefeed and the plasticizing unit barrel is visible. Both plasticizing unit barrels have four separate, oil-tempered temperature

control zones. To account for the greater length of the long fiber barrel, several oil jackets are interconnected. Due to the geometrical complexity of the area around the sidefeed flange position, no oil jacket is used there. Instead, an electric heating band and a thermal insulation are used to avoid a cold spot. Figure 4-6 shows the two interchangeable screw tips in a direct comparison. Three flat areas at each screw tip are visible. Those flat areas serve as an interface for the screw tip disassembly tool, which is required for removing the screw tips from the base body of the screw.

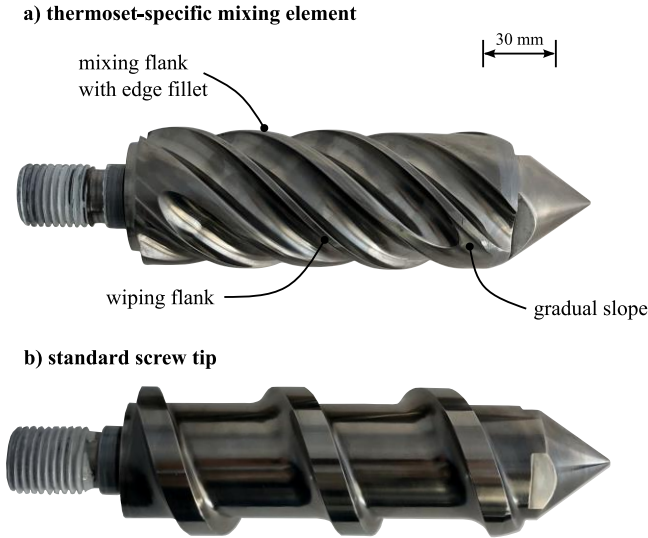


Figure 4-6: Comparison of mixing element (a) and standard screw tip (b)

These screw and barrel geometries allow for various combinations, of which the four combinations listed below were used to perform the experiments within this thesis.

- Standard plasticizing unit: This variant uses the standard screw and barrel with the long fiber feeding periphery. It is shown in Figure 4-3 above and was used for the initial experiments regarding the distributive and dispersive mixing during the injection phase (process results in Section 5.3.2).
- LGF plasticizing unit with conveying screw tip: Due to the different geometry of the long fiber screw compared to the standard screw, this

process variant served as a basis for evaluating the effect of the mixing screw tip (process results in Sections 5.3.3).

- LGF plasticizing unit with mixing screw tip: In comparison to the process variant described above, only the screw tip is changed from the conveying geometry to the mixing geometry (process results in Sections 5.3.3) Reference to Design
- LGF plasticizing unit with conveying screw tip and separate granulate feed port: By using the entire length of the long fiber barrel, a completely different feeding strategy is realized. While the sidefeed remains at the same location, the granulate feed is moved further back. This enables the melting of the phenolic resin before the chopped long fibers are added (preliminary trials regarding the melting in Section 5.2.1, process results in Section 5.3.4). This process layout is shown in Figure 4-7 and explained below.

All process variants are listed in Table 4-3. The theoretically possible combination “LGF plasticizing unit with mixing screw tip and separate granulate feed port” was not used due to the results obtained using the conveying screw geometry.



Table 4-3: Overview of long fiber direct process layout variants

<b>Name of process variant</b>	<b>Standard plast. unit</b>	<b>LGF plast. unit with conv. screw tip</b>	<b>LGF plast. unit with mix. screw tip</b>	<b>LGF plast. unit with conv. screw tip and sep. gran. feed port</b>
<b>Screw</b>	Standard conveying screw	Long fiber screw	Long fiber screw	Long fiber screw
<b>Screw tip</b>	one piece conveying geometry	conveying screw tip	mixing screw tip	conveying screw tip
<b>Barrel</b>	Standard 4-zone barrel	Long fiber barrel using only frontal 3 zones	Long fiber barrel using only frontal 3 zones	Long fiber barrel using all 4 zones
<b>Granulate feeding location</b>	Sidefeed	Sidefeed	Sidefeed	Separate granulate feed port
<b>Fiber feeding location</b>	Sidefeed	Sidefeed	Sidefeed	Sidefeed

Instead of feeding a dry blend consisting of molding compound and long glass fibers, the process variant “LGF plasticizing unit with conveying screw tip and separate granulate feed port” separates the feeding of molding compound from the long fibers, as Figure 4-7 shows. By feeding the granulate at an earlier position, it is possible to melt the compound over the course of the narrow distance between the two feeding locations. The melting is accomplished by shear energy input in a short compression zone on the screw (like a blister ring, see description in Table 2-6 and an external electric heating jacket. Due to a screw core diameter decrease after the melting element’s compression, a partially filled zone is created so that the long fibers can be fed into the plasticized resin. A feed pocket on the barrel’s inner diameter is located at the flange position of the sidefeed to facilitate the fiber integration. Furthermore, the feed pocket prevents molten material from being wiped off and so that there is no material built-up at the leading edge of the fiber feed. From the sidefeed position downstream, the material is compounded and conveyed on the screw towards the machine nozzle. The screw tip is inter-

changeable, so that both the conventional conveying geometry and the mixing element can be evaluated.

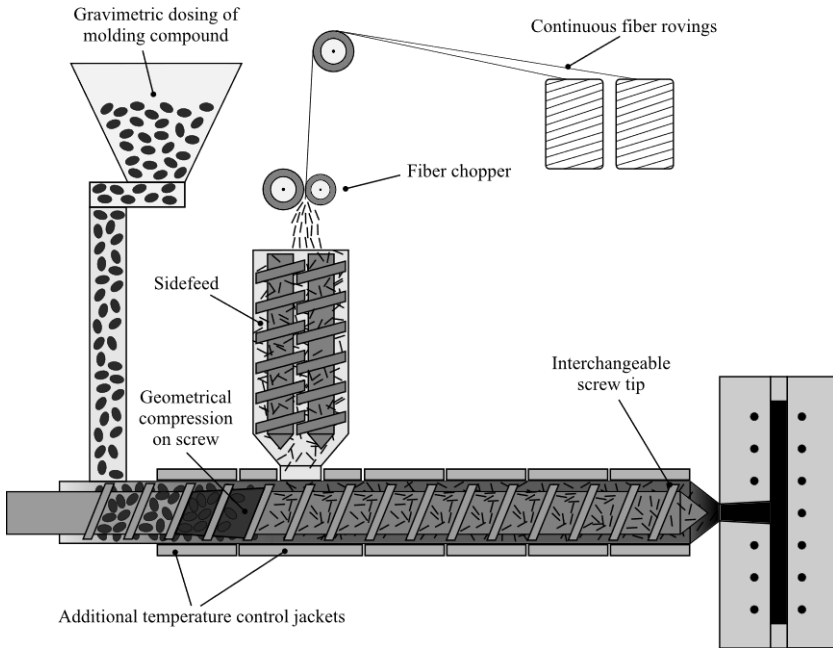


Figure 4-7: Long fiber injection molding process variant “LGF plasticizing unit with conveying screw tip and separate granulate feed port”

## 4.3 Mixing elements for the injection molding process

### 4.3.1 Mixing during the injection phase

As the experimental results for the process variant “standard plasticizing unit” (process description in Section 4.2) will show, the need for a better homogenization in the long fiber direct thermoset injection molding process was identified. In the subsequent sections, the calculations and the design steps for the mixing elements, that were used within this thesis, are described. To evaluate the effect of dispersive and distributive mixing during the injection phase, several actions were implemented. The dispersive mixing was



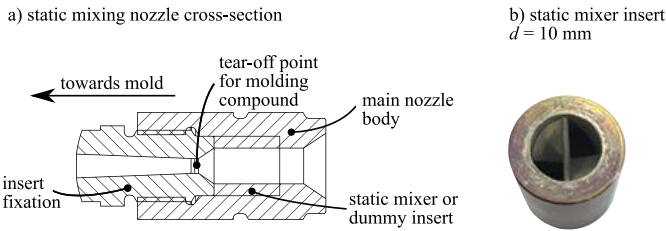


Figure 4-9: Nozzle including a static mixer designed for the thermoset injection molding process

The basic function principle of a mixing nozzle is unchanged, but three main features distinguish the thermoset mixing nozzle from traditional mixing nozzles for thermoplastics (see Figure 2-11 for reference). Both features focus on the nozzle's usability in the thermoset injection molding process. First, it is shorter than typical thermoplastic mixing nozzles to avoid cooling and solidification of the molding compound when the plasticizing unit is retracted from the sprue bushing of the mold. Second, the thermoset mixing nozzle is designed for quick disassembly, which is required during machine down-time and process interruptions. Third, by increasing the nozzle diameter from  $d = 5$  mm immediately after the mixing element to  $d = 8$  mm at the nozzle tip, the tear-off point for the molding compound when retracting the plasticizing unit is located immediately at the outlet of the mixing element. Therefore, the risk of blocking the nozzle with a cold plug is reduced.

### 4.3.2 Design of screw mixing elements

Due to the advantages of the Maddock mixing element described in Section 2.3.3, such as good mixing performance, ease of manufacturing and cleaning, this geometry was chosen for the implementation in the long fiber direct thermoset injection molding process. Within this thesis, two different Maddock mixing elements were designed and evaluated. First, a 30 mm mixing element for a smaller injection molding machine was designed and preliminary trials were conducted using this screw element. Based on the findings and trial results, a 60 mm mixing element was designed for the long fiber screw of the long fiber direct thermoset injection molding process. The calculations were carried out according to analytical equations described by Rauwendaal [110] and with the PSI software [222] developed by Paderborn University. Rauwendaal makes the following assumptions for the calculations:

- The polymer melt is an incompressible Newtonian fluid.
- The process is isothermal and there is no change in polymer viscosity in the shear gap of the mixing element.
- The inlet and outlet flutes of the element have the same geometry.
- There is no material flow over the wiping flanks of the element.

Assumptions (1) and (2) are typical simplifications for the analytical dimensioning of screw elements for extrusion and injection molding processes, which were also made by Tadmor and Klein [141] in their original calculation model published in 1973. The modifications of the Tadmor model implemented by Elbirli et al. [142] and Potente et al. [148] removed this limitation, but made a numerical solution of the equations necessary. For this reason, these modifications to the Tadmor model are not used here. Assumption (3) is not considered a limitation to the calculation described below, because no need for different inlet and outlet geometries was found. Due to the close tolerances between barrel and screw, assumption (4) is also considered valid.

The central dimensioning parameter for the mixing element is the total pressure drop  $\Delta p_{\text{tot}}$  over the element. Rauwendaal separates the total pressure drop  $\Delta p_{\text{tot}}$  into the pressure drop in the inlet and outlet channels  $\Delta p_{\text{ch}}$  and the pressure drop over the shear gap  $\Delta p_{\text{gap}}$  (described as clearance by Rauwendaal), see Equations (4-4) and (4-5).

$$\Delta p_{\text{tot}} = \Delta p_{\text{ch}} + \Delta p_{\text{gap}} \quad (4-4)$$

$$\begin{aligned} \Delta p_{\text{tot}} = 6 \frac{\eta z_m}{F_p W_{\text{ch}} H_{\text{ch}}^3} & \left[ \dot{V}_{\text{ch}} - F_d W_{\text{ch}} (H_{\text{ch}} - H_{\text{gap}}) v_b \cos \varphi \right] \\ & + 12 \frac{\eta W_{\text{gap}}}{z_m H_{\text{gap}}^3} \left[ \dot{V}_{\text{ch}} - \frac{H_{\text{gap}} L_m v_b}{2} \right] \end{aligned} \quad (4-5)$$

#### 4.3.2.1 Analytical calculations and design for a 30 mm mixing screw element

Table 4-4 lists the values that were used for performing the design calculations for the 30 mm thermoset mixing element. For the volume flow rate per flute pair  $\dot{V}_{\text{ch}}$  and the barrel velocity  $v_b$ , assumptions had to be made for the original calculation. During the injection molding experiments, the actual process values were determined and a back-calculation with those values was

performed afterwards. The main difference between the original calculation values and the actual process values are the higher barrel velocity and the significantly lower throughput, which was caused by a much slower feeding rate than anticipated. Increasing the barrel velocity should partially compensate the slow feeding.

Table 4-4: Calculation values for designing the 30 mm thermoset mixing element

Symbol	Parameter	Unit	Value for calculation
$\eta$	material viscosity	Pa s	15 000
$L_m$	length of mixing element	mm	30
$z_m = \frac{L_m}{\sin \varphi_f}$	unrolled length of mixing element	mm	50.2
$F_p$	shape factor pressure flow	-	0.25 [223]
$F_d$	shape factor drag flow	-	0.34 [223]
$W_{ch}$	width of inlet and outlet flute	mm	8
$H_{ch}$	height of inlet and outlet flute	mm	5.2
$\dot{V}_{ch}$	volume flow rate per flute pair	cm <sup>3</sup> /s	assumption for original calculation: 1.5 actual process values for LGF and SGF materials: 0.26 (LGF) ... 1.22 (SGF)
$H_{gap}$	shear gap height	mm	1.5
$W_{gap}$	shear gap width	mm	2.5
$v_b$	barrel velocity	mm/s	assumption for original calculation: 75 actual process values for LGF and SGF materials: 150 (for both materials)
$\varphi_f$	flute angle	°	32.5

As outlined in Section 2.3.3, the main influence factors on the mixing performance and the pressure drop over a Maddock element are the length of element  $L_m$ , the flute angle  $\varphi_f$  and the shear gap geometry. Due to geometrical constraints, the length of the mixing element was fixed at  $L_m = 30$  mm.

Furthermore, the shear gap width for the 30 mm element was set to  $W_{\text{gap}} = 2.5$  mm due its mutual interaction with the inlet and outlet flute width  $W_{\text{ch}}$ . Consequently, the flute angle  $\varphi_{\text{fl}}$  and the shear gap height  $H_{\text{gap}}$  were the geometry parameters that were varied to find the design optimum. A flute angle of  $\varphi_{\text{fl}} = 90^\circ$  corresponds to the conventional, non-spiral Maddock element. The influence of the throughput  $\dot{V}_{\text{ch}}$  on the pressure drop was investigated as well, because unlike a standard injection molding process, the long fiber direct thermoset injection molding process is starve-fed, which makes the throughput an adjustable process variable. Figure 4-10 shows the total pressure drop  $\Delta p_{\text{tot}}$  for the variation of the flute angle (top), the throughput (center) and the shear gap height (bottom) for the 30 mm mixing element. It shows the results for the original calculation (og. calc.) and for the actual process parameters that were determined during the injection molding trials (LGF and SGF).

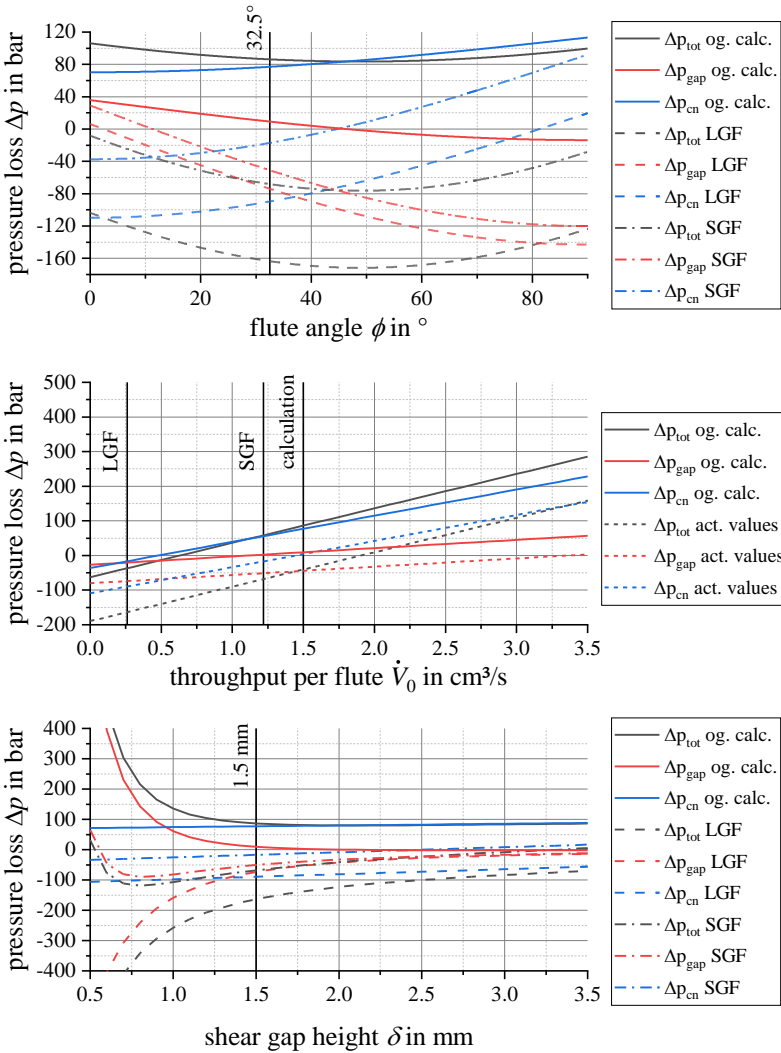


Figure 4-10: Calculated pressure drop for the 30 mm thermoset mixing element

The chosen flute angle of  $\phi_{\text{fl}} = 32.5^\circ$  for the 30 mm mixing element is marked. The total pressure drop  $\Delta p_{\text{tot}}$  is dominated by the channel pressure drop  $\Delta p_{\text{ch}}$ , which increases with increasing flute angle. At the same time, the pressure drop in the shear gap,  $\Delta p_{\text{gap}}$ , decreases, resulting in a minimum for the total pressure drop for flute angles of  $\phi_{\text{fl}} = 45^\circ \dots 50^\circ$ . The overall curve



shape is similar for the original calculation as well as for the calculation using the actual process values. However, these two calculation results show a significantly lower pressure drop compared to the original calculation. The negative pressure drop must be interpreted as a pressure generation over the mixing element. As it can be seen from Figure 4-10 (center), the pressure drop has a linear correlation to the throughput over the mixing element. Additionally, the faster screw speed in the actual molding trials caused the vertical shift of the pressure drop curves. The results for the correlation between the pressure drop and the shear gap height  $H_{\text{gap}}$  are depicted in Figure 4-10 (bottom). Choosing the shear gap height is a tradeoff between pressure drop and mixing power. Based on the original calculations, a shear gap height of  $H_{\text{gap}} = 1.5 \text{ mm}$  was chosen. Values  $H_{\text{gap}} > 1.5 \text{ mm}$  only have a slight influence on the pressure drop, however it can be expected that they reduce the mixing power of the element. Due to the cubical proportionality of the pressure drop to the shear gap high, the strong increase towards small shear gaps can be explained. It is noteworthy that according to the calculation results for the long glass fiber (LGF) compound, the pressure generation increases with decreasing shear gap height. This appears to be counterintuitive, but can be explained using Equation (4-5). For low flute throughput values  $\dot{V}_{\text{ch}}$ , the second terms in the equations for the channel pressure drop  $\Delta p_{\text{ch}}$  and the shear gap pressure drop  $\Delta p_{\text{gap}}$  have higher absolute values than the first ones, resulting in negative values for both sums. The original calculations described above led to a design for the 30 mm mixing element which is shown Figure 4-11.

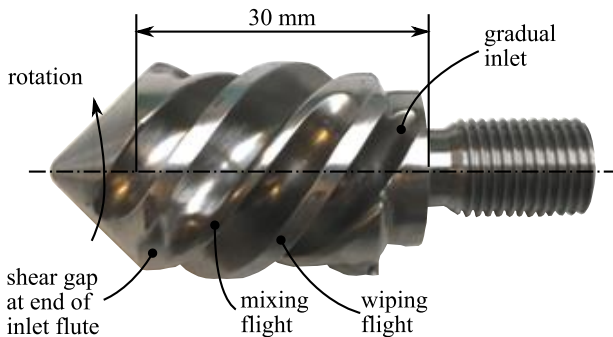


Figure 4-11: 30 mm spiral mixing element for the thermoset injection molding process

In contrast to a traditional Maddock mixing element for thermoplastic materials, the thermoset-specific element has three new and distinct differences, which set it apart from the state-of-the-art. They are described in the publications [25] and [26] by Maertens et al. First, the inlet and outlet channels feature a gradual slope at their ends to facilitate the flow of material and to avoid material accumulations. The front slope of inlet flute ends with a shear gap that has the same height as the shear gap on the mixing flight. This feature is also designed for narrowing the residence time distribution by reducing the danger of material accumulations. By allowing the material to leave the inlet channel in channel direction (without the perpendicular redirection into the outlet flute), it is less likely that a material accumulation occur at the front end of the inlet flute. The second feature difference to the traditional Maddock mixing element is the edge fillet on the mixing flight. Due to the radius on this edge, the material must undergo additional elongational stresses when it enters the shear gap. This principle for incorporating elongational stresses is inspired by the design of the CRD mixer described in Section 2.3.3. For the 30 mm mixing element, an edge fillet radius of  $r = 2.5$  mm was chosen. The third main distinguishing feature when comparing the thermoset mixing element with the traditional geometry for thermoplastics is that the positions of the mixing flight and wiping flight are reversed. Figure 4-12 explains the difference by comparing a conventional Maddock element (a) with the new thermoset-specific design (b). The direction of the flow of material through the shear gap is marked. [25,26]

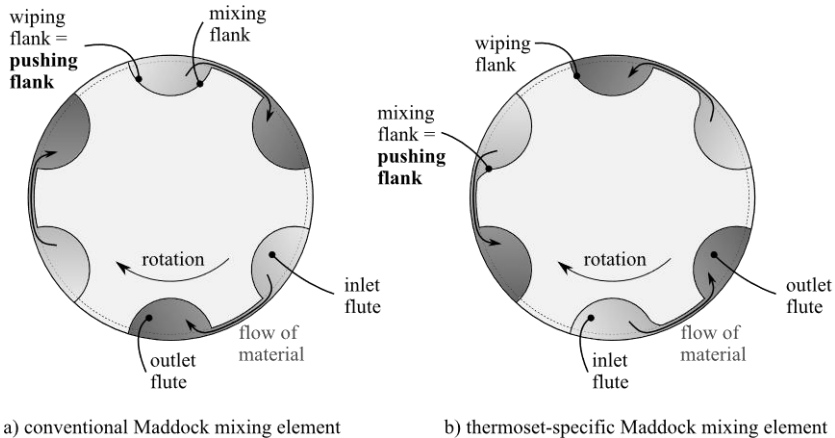


Figure 4-12: Position of mixing and wiping flight for the thermoset mixing element [25,26]

Traditionally, the pushing flank is simultaneously also the wiping flank of the mixing element. This makes sense for thermoplastic materials that enter the mixing element in a completely molten state. However, this condition does not necessarily apply to thermoset molding compounds. They start to melt under the influence of pressure in the foremost screw flights. This pressure is transferred into the molding compound by the screw flanks of the conveying screw, which means that the material close to the pushing screw flanks is molten, whereas the material distant from the pushing screw flanks might still be granular. For reference, this melting behavior can be seen in Figure 2-7. If the molding compound entered a traditional mixing element in such a partially molten state, the granular fraction would be pushed through the shear gap, likely blocking it. In the new thermoset-specific design, the pushing screw flank is simultaneously also the mixing flank. This design ensures that only molten compound is pushed through the shear gap, thus avoiding a blockage. Before the material can enter the shear gap, it melts under the conveying pressure that the screw flanks transfer into it. These design differences could not be considered in the analytical and simplified calculations described above, but have proven to be useful in the preliminary trials that were conducted with the mixing element, see Section 5.2.

#### **4.3.2.2 Transfer and upscaling to a 60 mm mixing screw element**

Based on the design of the 30 mm mixing element, an upscaling process to the  $d = 60$  mm screw diameter of the KraussMaffei 550 / 2000 GX injection molding machine was conducted. The three thermoset-specific features were kept, while the general design was rethought and recalculated using both the analytical approach as well as the design software PSI [222] by Padernborn University. Some changes were applied to the mixing element design based on the trial results described in Section 5.2. The calculation values for the 60 mm element are listed together with the values for the 30 mm element in Table 4-5 below. Some changes to the geometry besides the obvious upscaling requirements (overall dimensions, volume flow rate, barrel velocity) were implemented. These changes were possible due to the elimination of some restrictions that still had to be met when designing the small mixing element.

Table 4-5: Calculation values for designing the 60 mm thermoset mixing element

Symbol	Parameter	Unit	Value for calc. 30 mm	Value for calc. 60 mm
$\eta$	Material viscosity	Pa s	15 000	15 000
$L_m$	Length of mixing element	mm	30	120
$\frac{z_m = L_m}{\sin \varphi}$	Unrolled length of mixing element	mm	50.2	173.7
$F_p$	shape factor pressure flow	-	0.25 [223]	0.75 [223]
$F_d$	shape factor drag flow	-	0.34 [223]	0.79 [223]
$W_{ch}$	width of inlet and outlet flute	mm	8	14.7
$H_{ch}$	height of inlet and outlet flute	mm	5.2	5.8
$\dot{V}_{ch}$	volume flow rate per flute pair	cm <sup>3</sup> /s	og. calc.: 1.5 act. process values for LGF and SGF 0.26 (LGF) ... 1.22 (SGF)	11.5
$H_{gap}$	shear gap height	mm	1.5	1
$W_{gap}$	shear gap width	mm	2.5	5
$v_b$	barrel velocity	mm/s	og. calc.: 75 act. process value for LGF and SGF: 150	125
$\varphi$	flute angle	°	32.5	43.7

The general inlet and outlet flute shape was made shallower by converting the rather rectangular cross-section to a rounded, semi-circle shape. This change was implemented in order to narrow the residence time distribution according to the findings of Sun et al. [144,145]. Consequently, the shape factors  $F_p$  for pressure and  $F_d$  for drag flow were adapted to the new geome-

try. The length of the mixing element was increased from  $L = 1D$  for the small mixing element to a more typical  $L = 2D$  for the 60 mm element. Based on the calculations described above and the observations during the trials, the shear gap height was reduced from  $H_{\text{gap}} = 1.5$  mm to  $H_{\text{gap}} = 1$  mm and the flute angle was increased from  $\varphi_{\text{n}} = 32.5^\circ$  to  $\varphi_{\text{n}} = 43.7^\circ$ . Table 4-6 lists the input values for the PSI calculation.

Table 4-6: Parameters for PSI calculation of 60 mm mixing element

Symbol	Parameter	Unit	Value
<b>a</b>	Carreau viscosity at zero shear rate	Pa s	4 729 180.7
<b>b</b>	reciprocal transition velocity	S	63.8
<b>c</b>	slope		0.513
<b>T<sub>B</sub></b>	reference temperature	°C	50
<b>T<sub>A</sub></b>	standard temperature	°C	26.4
<b>ρ</b>	material density	g/cm <sup>3</sup>	1.7
	bulk density	g/cm <sup>3</sup>	
<b>T<sub>m</sub></b>	melting temperature	°C	65
<b>c<sub>p0</sub></b>	heat capacity	kJ/(kg K)	1.259
<b>λ<sub>0</sub></b>	heat conductivity	W/(m K)	0.306

With these new values, both the analytical calculation according to Rauwendaal, see Equation (4-5) and the calculations using the PSI software were carried out. Figure 4-13 shows the results for the analytical calculation. The new geometry has a negative pressure drop of  $\Delta p_{\text{tot}} \approx -85$  bar in its operating point, which means that it is generating pressure. This is an improvement compared to the original 30 mm mixing element geometry, which had a pressure loss of  $\Delta p_{\text{tot}} \approx 50$  bar in its operating point for the SGF molding compound. The PSI calculation using the same geometry and process values is in accordance with the analytical approach for the 60 mm element, as can be seen from the calculated pressure profile for the long fiber screw in Figure 4-14.

The simplified approach according to Rauwendaal treats the mixing element as an isolated unit, without any external influences. In contrast, PSI considers the entire screw of the injection molding machine as well as injection molding-specific process parameters such as back pressure and dosage volume. Due to these additional constraints, the pressure at the screw tip can never

exceed the entered process parameter for the back pressure, which was  $p = 30$  bar for all calculations.

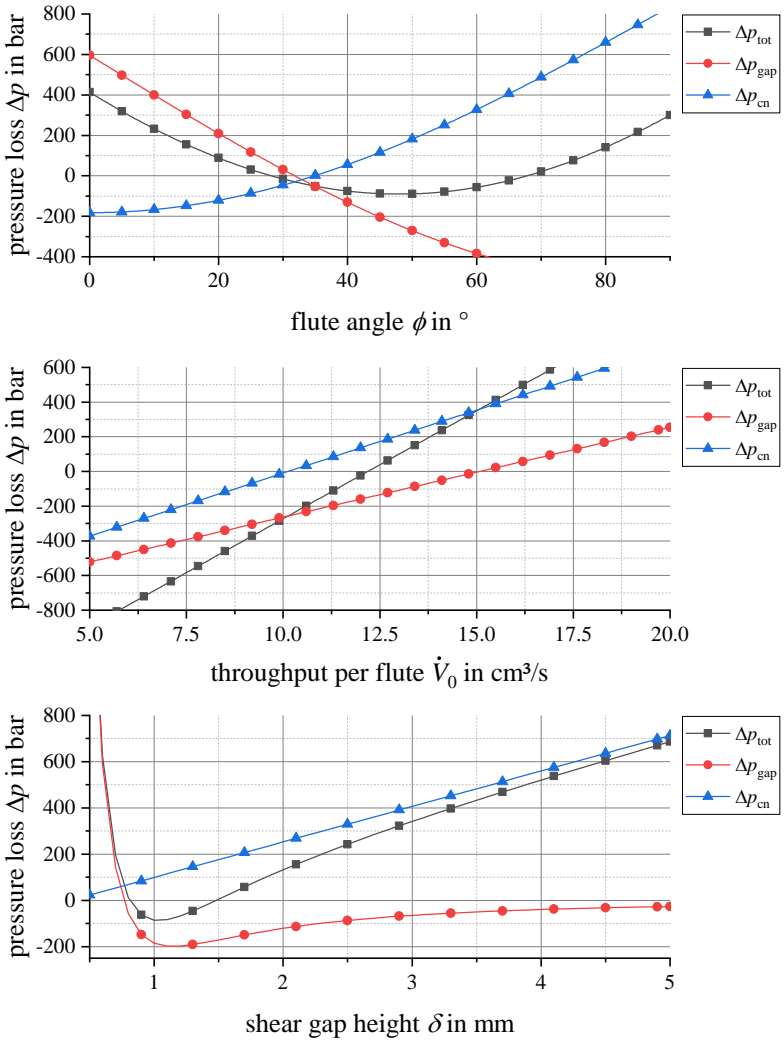


Figure 4-13: Analytical calculations for 60 mm thermoset mixing element

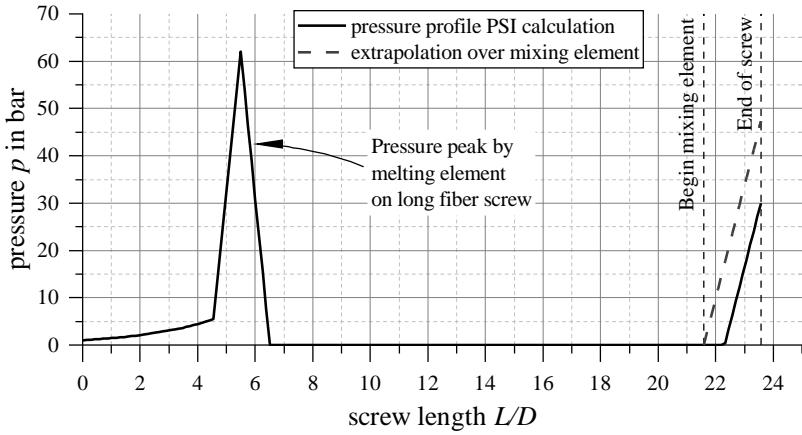


Figure 4-14: Pressure profile for the long fiber screw using the optimized mixing element geometry

The pressure generation of  $\Delta p_{\text{tot}} \approx 85$  bar calculated analytically can therefore never be an output value of the PSI calculation. However, by calculating and extrapolating the pressure gradient over the mixing element to the element's entire length, the theoretical total pressure generation value can be estimated. This approach is illustrated in Figure 4-14 and results in a pressure generation of  $\Delta p_{\text{tot}} \approx 47$  bar. Given the extensive assumptions and simplifications made for the calculations, this agreement is considered sufficiently good.





# 5 Results

## 5.1 Compounding of short fiber-reinforced phenolic resins

### 5.1.1 Compounding for injection molding trials with standard barrel

The short glass fiber-reinforced molding compounds PF-SGF $x$  with different fiber weight content levels  $\phi$  produced by twin-screw extrusion were characterized by calculating the SME during production, by measuring their remaining heat of reaction  $\Delta H_R$  as well as by evaluating their apparent density and their fiber length distribution. The results are described in detail in the publication [24] by Maertens et al. Once a stable compounding process for the PF-SGF60 molding compound was established and an OFT value of OFNL  $\approx 50$  was adjusted, the reference value for the specific mechanical energy input into the resin was set to  $SME_R = 0.28$  kWh/kg. Using the extruder speed  $\omega$  and the throughput  $\dot{m}$ , the energy input was adjusted to achieve this value of  $SME_R$  for all formulations. Figure 5-1 shows the actual values for  $SME_R$  and the corresponding results  $\Delta H_R$  that were determined using DSC. Low fiber weight contents  $\phi$  generally require a higher extruder speed and a lower throughput to maintain the targeted  $SME_R$ . Nevertheless, it decreased from  $SME_R = 0.28$  kWh/kg for the PF-SGF60 formulation to  $SME_R = 0.24$  kWh/kg for PF-SGF0. For the calculation of the  $SME_R$  both the energy input into the material and the energy lost due to the extruder friction is relevant. For this reason, a second data line for the  $SME_R$  including the extruder friction is shown in Figure 5-1. It was calculated by measuring the required extruder power  $P$  while running empty at the different extruder speeds  $n$  and then subtracting this value from the  $SME_R$ . Due to the increasing extruder speed at lower fiber contents, the friction energy in the barrel and in the gearbox of the extruder increases, which leads to a larger difference between  $SME_R$  and  $SME_{R, \text{incl. friction}}$ .  $\Delta H_R$  is highest for the formulations with a low fiber content, indicating that they have undergone less curing

progress during the compounding than the formulations with a high fiber content.

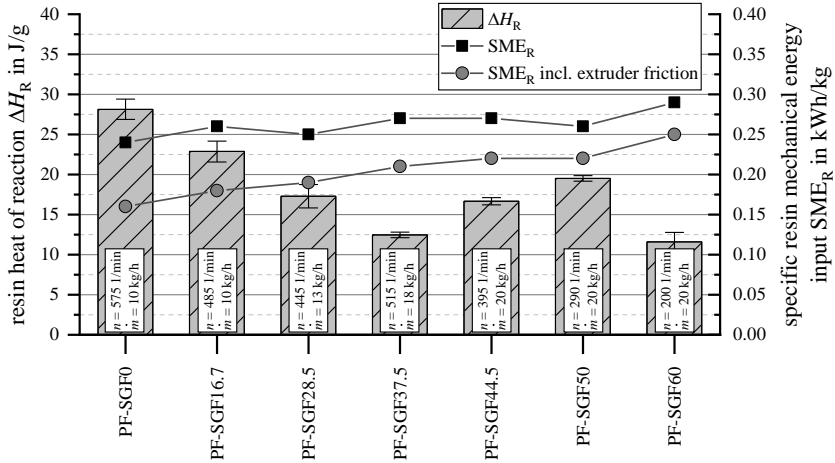


Figure 5-1:  $\Delta H_R$  and SME of SGF molding compounds for standard plasticizing unit trials [24]

After grinding the material in the cutting mill, the apparent density  $\rho_{app}$  of the compounds was determined, see Figure 5-2.

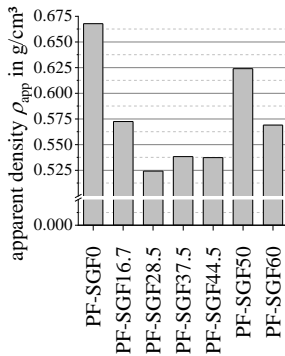


Figure 5-2: Apparent density of SGF molding compounds

The (neat resin) PF-SGF0 formulation has the highest apparent density, despite having the lowest material density due to the absence of any glass fibers. The lack of fibrous filler material creates a dense structure and a brittle material behavior during grinding. Both aspects result in a low-dust and low-

porosity granulate. In contrast, a higher fiber content typically leads to a higher porosity in the lumps that exit the twin-screw extruder outlet. During grinding in the cutting mill, the fibers cause a less brittle material behavior and therefore a higher dust fraction. The porosity leads to a lower apparent density despite the higher material density of the compound.

The fiber length measurements in Figure 5-3 show a decrease in weighted average fiber length  $L_p$  with increasing fiber content. In the first two fiber length classes, the weighted fiber length fraction increases with the fiber content, whereas this correlation is reversed from the 3<sup>rd</sup> fiber length class upwards.

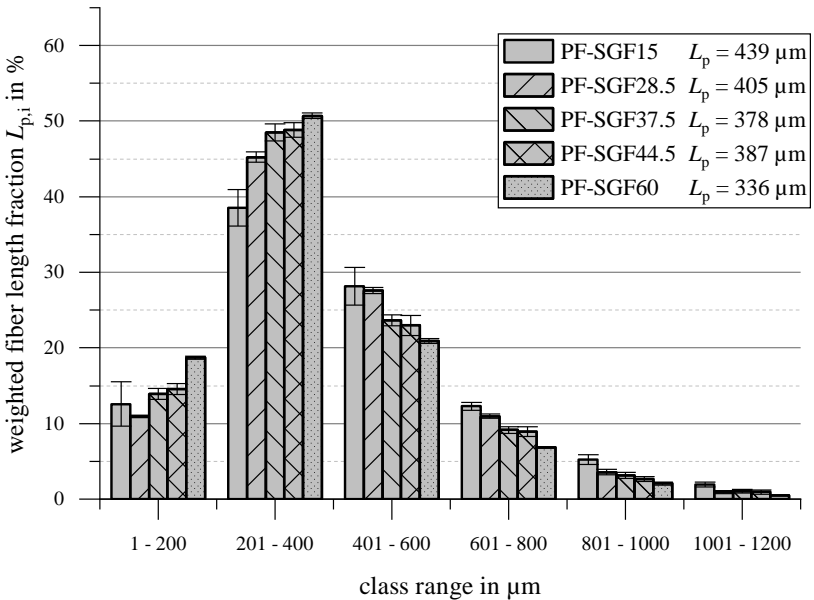


Figure 5-3: Fiber length measurement for short fiber molding compounds [24]

Figure 5-4 shows the absolute value of the complex viscosity  $\eta^*$  for the manufactured short fiber molding compounds. A temperature sweep was performed for two samples of each formulation.

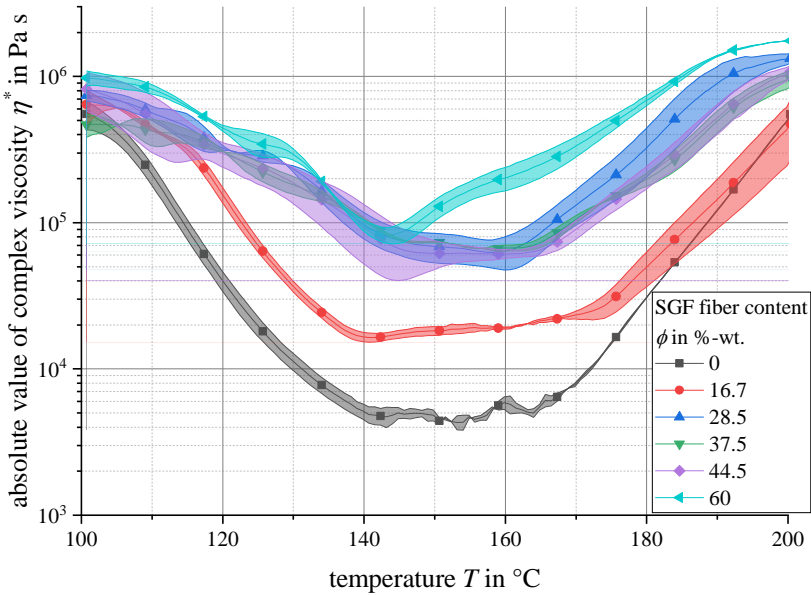


Figure 5-4: Absolute value of complex viscosity  $\eta^*$  for SGF compounds for standard barrel trials

Two measurements were averaged for each fiber content. The fill area represents the area between the two measurements. Due to the logarithmic scale of the plot, the fill area is larger for formulations with a low viscosity than with a high viscosity. As expected, the viscosity curve of all compounds shows a drop during heating and reaches a minimum at  $T \approx 140 \text{ }^\circ\text{C} \dots 150 \text{ }^\circ\text{C}$  before increasing due to curing at higher temperatures. The lowest minimum viscosity is reached for the compound with a fiber content of  $\phi = 0 \text{ wt.-%}$  with  $|\eta^*|_{\min} \approx 3 \times 10^3 \text{ Pa s}$  at in a temperature range of  $T \approx 140 \text{ }^\circ\text{C} \dots 160 \text{ }^\circ\text{C}$ . In contrast, the  $\phi = 60 \text{ wt.-%}$  compound has a minimum viscosity of  $|\eta^*|_{\min} \approx 8 \times 10^4 \text{ Pa s}$ . The compounds with the intermediate fiber contents can be found in between those two formulations. It is notable that the compound with  $\phi = 37.5 \text{ wt.-%}$  fibers has a higher minimum viscosity than the  $\phi = 44.5 \text{ wt.-%}$  formulation. A comparison of the injection pressure curves when molding the different short fiber formulations is carried out. The nozzle of the injection molding machine, through which the material must flow, serves as a capillary like a capillary rheometer. Figure 5-5 shows the injection pressure over time. The fill areas represent  $\pm 1$  standard deviation.

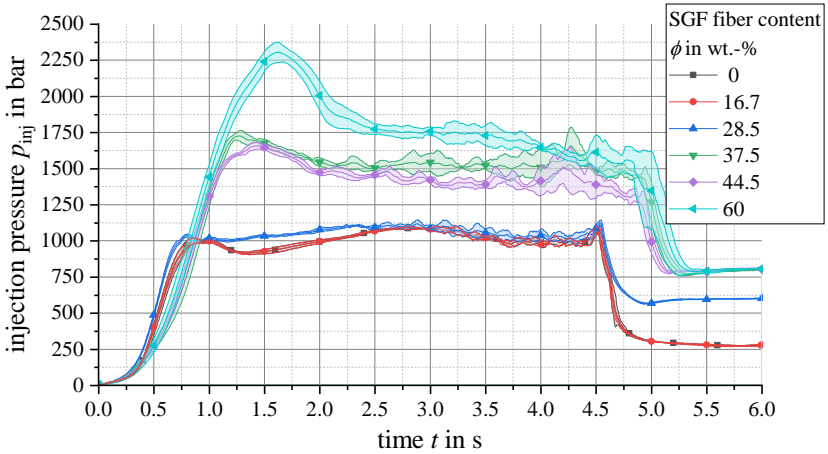


Figure 5-5: Injection pressure for short fiber-reinforced molding compounds

All materials were injected using the same injection speed. The holding pressure was lowered for the compounds with a low fiber content to decrease burr formation. The formulations with a low fiber content require less injection pressure. For  $\phi = 0$  wt.-% to  $\phi = 28.5$  wt.-%, no pressure peak at the beginning of the injection stroke is visible. The curves are very similar, especially for  $\phi = 0$  wt.-% and  $\phi = 16.7$  wt.-%. The required pressure for keeping the material flowing into the mold is approximately  $p = 1000$  bar for the three formulations with the low fiber content. Raising the fiber content increases both the pressure peak at the beginning of the injection stroke and the pressure required for filling the mold, which is approximately  $p = 1500$  bar for the  $\phi = 37.5$  wt.-% ... 44.5 wt.-% formulations and increases to  $p = 1750$  bar for the highest fiber content. The general tendency of increasing required injection pressure with increasing fiber content is in accordance with the observation of the higher viscosity for the higher fiber contents.

### 5.1.2 Compounding for injection molding trials with long fiber barrel

These compounding trials were carried out in the same way as the ones described in Section 5.1.1. Due to machine availability, a different twin-screw extruder with a shorter processing length had to be used. Since the processing length was shortened to  $L = 28 D$  anyway, this did not influence

the compounding trials. However, this extruder has a lower maximum extruder speed of  $n = 405$  1/min, which reduced the available range for adjusting the process parameters to the correct specific mechanical energy input into the resin,  $SME_R$ . In contrast to the previous trials, lower material throughputs were required to come close to the targeted  $SME_R$  values. However, due to gravimetric feeding restrictions, the lowest achievable throughput was  $\dot{m} = 10$  kg/h. The results are shown in Figure 5-6.

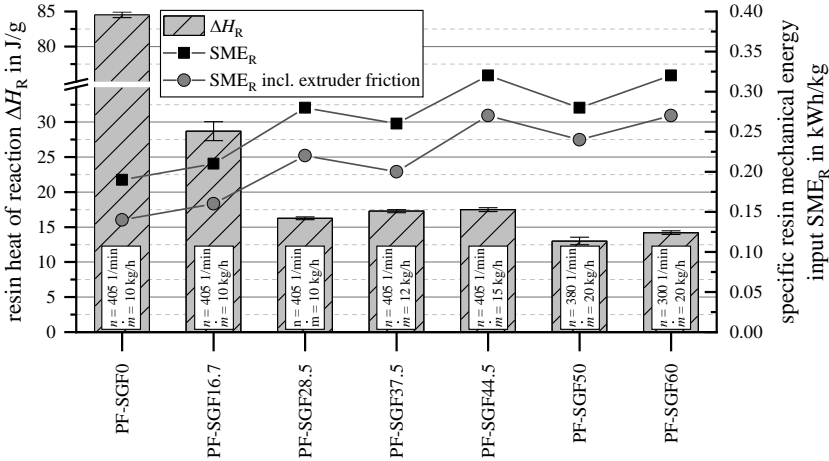


Figure 5-6:  $\Delta H_R$  and  $SME$  of SGF molding compounds for long fiber barrel trials

For the formulations with  $\phi = 28.5$  wt.-% ... 60 wt.-% fiber content, a remaining heat of reaction of  $\Delta H_R \approx 15$  J/g could be adjusted. The deviation between these values is lower than the one that was obtained during the previous compounding trials described above. However, the two formulations with the lowest fiber content, PF-SGF0 and PF-SGF16.7, have a significantly higher heat of reaction of  $\Delta H_R = 28.7$  J/g and  $\Delta H_R = 84.5$  J/g, respectively. The manufactured molding compounds were investigated using oscillatory rheology according to the method described in Section 3.2.1.3. The results for the temperature sweep from  $T = 100$  °C to  $T = 200$  °C are shown in Figure 5-7.

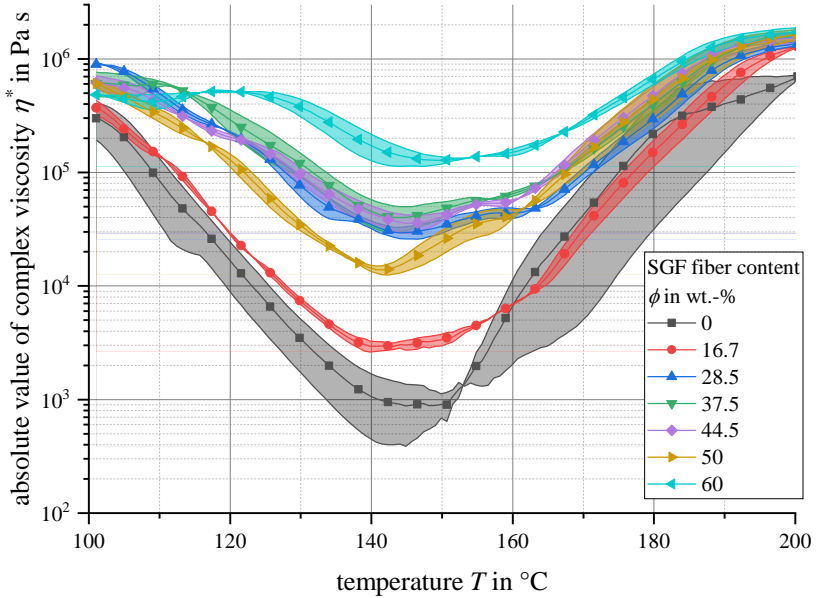


Figure 5-7: Absolute value of complex viscosity  $\eta^*$  for SGF compounds for long fiber barrel trials

As expected, the viscosity curve of the compounds shows a drop during heating and reaches a minimum at  $T \approx 140 \dots 150$  °C before increasing due to curing at higher temperatures. The lowest minimum viscosity is reached for the compound with a fiber content of  $\phi = 0$  wt.-% with  $|\eta^*|_{\min} \approx 10^3$  Pa s. In contrast, the  $\phi = 60$  wt.-% compound has a minimum viscosity of  $|\eta^*|_{\min} \approx 10^5$  Pa s. The compounds with the intermediate fiber contents can be found in between the two extremes, however not necessarily in the expected order of increasing fiber content. Especially, the  $\phi = 50$  wt.-% fiber content formulation has a lower viscosity level than expected. Considering that the DSC measurements for this formulation showed the lowest remaining heat of reaction of all the compounds, which indicates the highest level of crosslinking, a higher viscosity level was expected. To investigate the shear-thinning behavior of the phenolic resin, the PF-SGF0-LGF0 (neat resin) formulation was used for conducting a multiwave measurement at multiple excitation frequencies (see Section 2.2.2 for details). The results for two samples are shown in Figure 5-8.

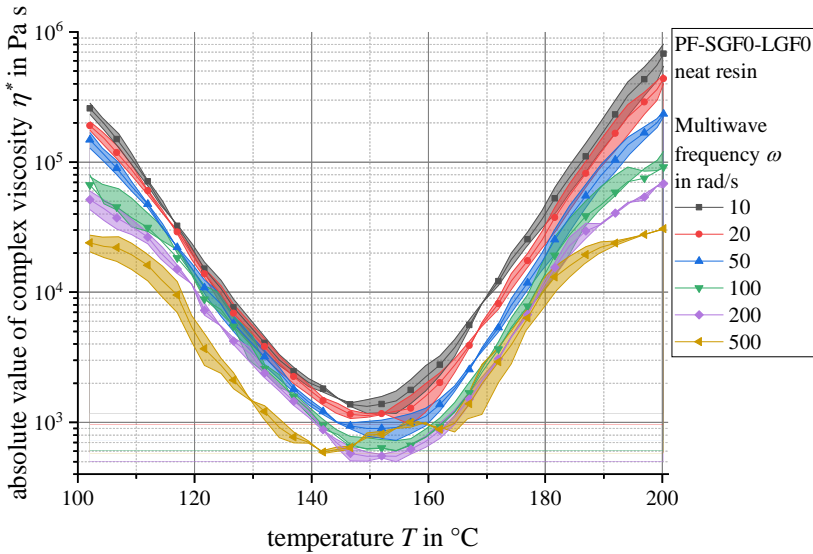


Figure 5-8: Multiwave rheology measurements for PF-SGF0 neat resin molding compound

The results show a drop in decrease in viscosity for increasing excitation frequencies, i.e. increasing shear rates. The results indicate a shear-thinning (pseudoplastic) behavior which is typical for polymers [71]. At a common compounding temperature for phenolic resins of  $T = 120\text{ }^{\circ}\text{C}$ , the drop in viscosity when increasing the measurement frequency from  $\omega = 10\text{ rad/s}$  to  $\omega = 500\text{ rad/s}$  is  $\Delta\eta \approx 16\,600\text{ Pa s}$ .

In addition to the DSC, TGA and rheology measurements, a fiber length analysis was carried out for the short fiber molding compound granulate. The weighted average fiber length distributions  $L_{p,i}$  for the different formulations are shown in Figure 5-9. Four separate samples were analyzed from the diluted ash residue. The respective measurement results were averaged and their standard deviation calculated. For each formulation, between 25 000 and 31 000 fibers were analyzed by using the FASEP method described in Section 3.2.3.



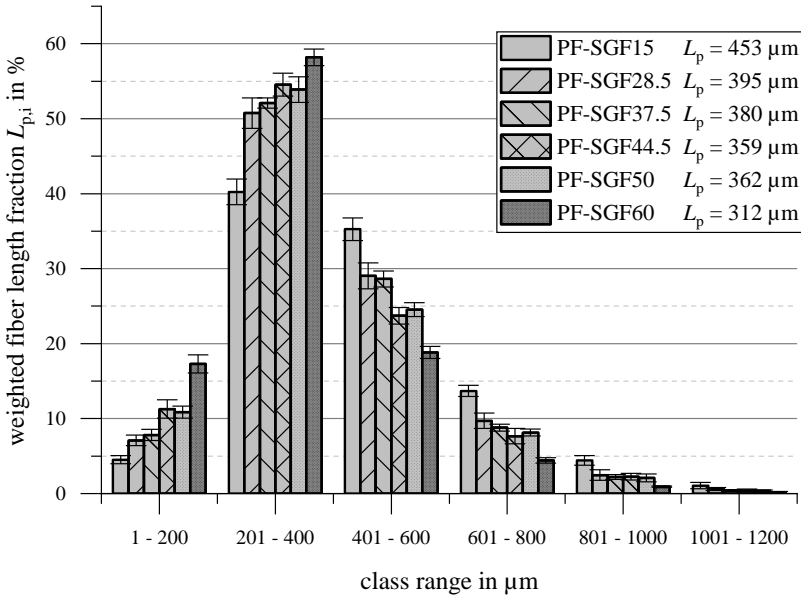


Figure 5-9: Weighted average fiber length fraction for short fiber molding compounds [24]

The weighted average fiber length is the highest for the PF-SGF15 formulation at  $L_p = 453 \mu\text{m}$  and drops down to  $L_p = 312 \mu\text{m}$  for the PF-SGF60 compound. This compound has the highest fraction of fibers in the two shortest fiber length classes. Starting with the length class  $L = 401 \mu\text{m} \dots 600 \mu\text{m}$ , this order is reversed. The criterion  $\text{FLD} = L_p/L_n$  that is in a narrow range of  $\text{FLD} = 1.23 \dots 1.26$  for all compounds, which indicates that a good fiber dispersion without bundles is present. [24]

## 5.2 Preliminary trials with 30 mm injection molding machine

### 5.2.1 Melting phenolic molding compounds by geometrical compression on the screw

A central challenge of the process variant “separate feeding using long fiber barrel, melting element and long fiber screw” is melting the short fiber-reinforced molding compound before the addition of the long fibers. Due to

geometrical constraints, a maximum distance of  $s \approx 485$  mm is available during which the molding compound must be plasticized. A target material temperature of  $T = 110$  °C...  $120$  °C is defined to achieve the lowest possible material viscosity without decomposing the HMTA hardener. As outlined in Section 2.3.1, compressing the phenolic molding compound is a vital part of the melting process. In the process variant “separate feeding using long fiber barrel, melting element and long fiber screw”, the required energy is put into the material by a melting element like a blister ring (see Section 2.3.3) and by additional temperature control jackets on the barrel of the plasticizing unit. To determine the required compression ratio of the melting element, preliminary tests were conducted on a  $d = 30$  mm injection molding machine. The melting element was positioned at the front of the  $d = 30$  mm thermoset screw as a replacement for the screw tip (see Figure 5-10 below for details). With this setup, the injection molding machine was used in an extruder mode without a machine nozzle attached, which means that only the plasticizing step could be investigated. For the trials, three different short fiber phenolic molding compounds were used (PF-SGF0, PF-SGF37.5 and PF-SGF50). As can be seen from Table 5-1, these three material formulations cover the entire range of apparent density values which were produced during the compounding trials. Several different melting elements with varying diameter and therefore varying shear gap heights ( $d = 23$  mm ...  $29$  mm, therefore gap size  $H_{\text{gap}} = 3.5$  mm ...  $0,5$  mm) and shear gap widths ( $W_{\text{gap}} = 5$  mm and  $W_{\text{gap}} = 15$  mm) were tested. The experimental parameters are summarized in Table 5-1.

Table 5-1: Experimental parameters for melting element preliminary trials

Symbol	Parameter	Unit	Value
$\phi$	fiber content	wt.-%	0; 37.5; 5
$H_{\text{gap}}$	melting element shear gap height	mm	3.5 ... 0,5
$W_{\text{gap}}$	melting element shear gap width	mm	5; 15
$T_{\text{barrel}}$	barrel temperature profile	°C	70 – 90 zone 1 – zone 2
$n$	screw speed	min <sup>-1</sup>	95.5

For each combination of shear gap height, shear gap width and compound fiber content, three repeated tests were conducted and the maximum material temperature  $T_{m,max}$  was determined using a penetration thermometer. Figure 5-10 shows the melting element setup (a), a visual impression of the molding compound after cooling it down to room temperature (b) and the measurement results (c). Figure 5-10 (c) shows the results for the shorter shear gap length  $W_{gap} = 5$  mm as solid lines and the values for the longer shear gap length  $W_{gap} = 15$  mm as dashed lines. For the PF-SGF0 compound, no difference between the shorter and the longer shear gap length exists. For this material, a shear gap height of  $H_{gap} = 0.5$  mm results in the desired material temperature of  $T = 105$  °C.

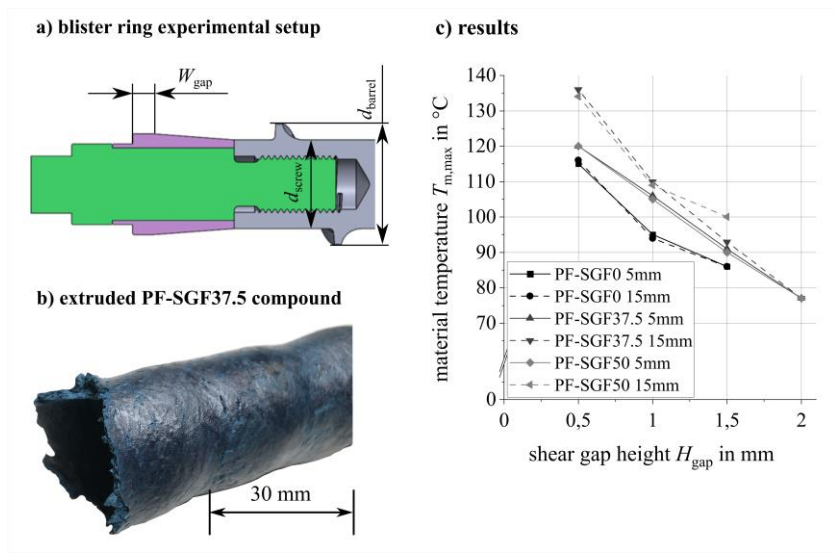


Figure 5-10: Melting element experimental setup (a), extruded compound (b) and results (c)

For the short glass fiber filled compounds PF-SGF37.5 and PF-SGF50, a larger shear gap height of  $H_{gap} = 1$  mm appears to be suitable. For these compounds, an influence of the shear gap width exists. The longer shear gap of  $W_{gap} = 15$  mm resulted in a significantly higher material temperature, most likely due to the prolonged shearing of the material. The results show that melting phenolic molding compounds by using a geometrical compression on the screw is possible. The required compression ratio for a material tempera-

ture of  $T = 110\text{ }^{\circ}\text{C} \dots 120\text{ }^{\circ}\text{C}$  is calculated in according to Equation (5-1) and Equation (5-2). For the PF-SGF0 neat resin, a required compression ratio of

$$\frac{A_{\text{Compression}}}{A_0} = \frac{d_{\text{Barrel}}^2 - d_{\text{Compression}}^2}{d_{\text{Barrel}}^2 - d_{\text{Screw}}^2} = \frac{30^2 - 29^2}{30^2 - 22^2} = 0,14 \quad (5-1)$$

is obtained from the results. For the short glass fiber-reinforced compounds PF-SGF37,5 and PF-SGF50, a different ratio of

$$\frac{A_{\text{Compression}}}{A_0} = \frac{30^2 - 28^2}{30^2 - 22^2} = 0,28 \quad (5-2)$$

is required. The compression ratios are used for upscaling from the  $d = 30\text{ mm}$  preliminary trials to the  $d = 60\text{ mm}$  machine for the design of the long fiber screw.

## 5.2.2 Process data analysis for 1<sup>st</sup> iteration screw mixing element (30 mm)

The developed 30 mm thermoset Maddock mixing element was evaluated in injection molding trials with a SGF (Vyncolit® X655 by Sumitomo Bakelite) and a  $L = 5\text{ mm}$  LGF phenolic molding compound (Porophen® 9201L5 by Sumitomo Bakelite). The process parameters are listed in Table 5-2.

Table 5-2: Process parameters for the evaluation of the 30 mm thermoset mixing element

	Parameter	Unit	trial number value			
			1	2	3	4
setup	material	-	X655 SGF		9201L5 LGF	
	screw	-	standard	mixing	mixing	standard
tempe- ratures	temperature nozzle side	$^{\circ}\text{C}$	170		185	
	temperature ejector side	$^{\circ}\text{C}$	170		185	
	barrel temperature profile	$^{\circ}\text{C}$	70 – 90 zone 1 – zone 2			
plasti- cizing	screw speed	m/min	9			

	Parameter	Unit	trial number value			
			1	2	3	4
	back pressure	bar hydr.	5		2	5
	screw stroke	mm	57		63	57
injection and curing	injection stage 1	mm/s to mm	15 to 15			
	injection stage 2	mm/s to mm	5 to 7			
	switchover to holding pressure	mm	7			
	holding pressure	bar hydr. for s	30 for 14			
	cure time	s	40		80	

The first objective of the molding trials was to determine the process stability when using the mixing element compared to using the standard thermoset conveying screw. To do so, the injection pressure and the screw position over time were investigated for 10 subsequent injection molding cycles, which are shown as a family of curves in the subsequent Figures. Figure 5-11 shows the screw position (left) and the injection pressure (right) for the SGF compound.

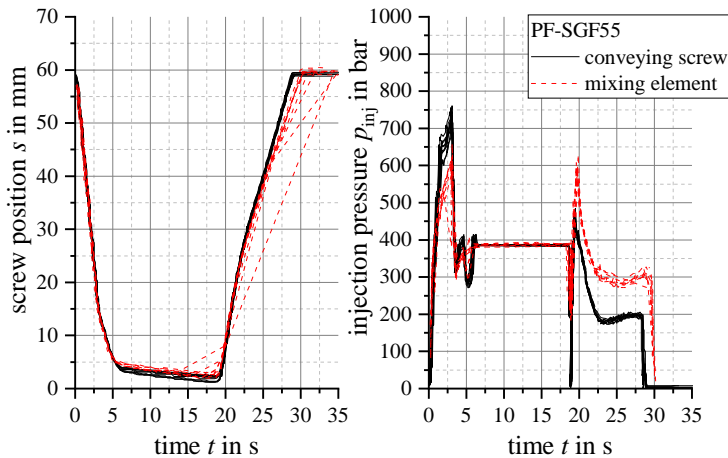


Figure 5-11: Screw position and injection pressure SGF compound with 30 mm mixing element

For both screw configurations a material cushion of  $s = 2 \text{ mm} \dots 3 \text{ mm}$  is left at the end of the holding pressure phase. The slope of the screw position curve during plasticizing is slightly lower for the mixing element, indicating a slightly higher energy input during plasticizing. This is confirmed by the pressure curves on the right side in Figure 5-11. The higher pressure during the plasticizing phase shows that more energy input into the material is taking place during this part of the process. Correspondingly, the measured injection pressure values are lower for the mixing element compared to the standard conveying screw. A lower required injection pressure typically is a sign for a lower material viscosity of the material in front of the screw. This is a plausible conclusion here, because the material encountered a higher energy input during plasticizing, most likely resulting in a higher material temperature in front of the screw when using the mixing element. Figure 5-12 shows the same results for the long fiber material. Again, multiple injection molding cycles are shown for each screw geometry. For the LGF compound, a stronger difference between the standard conveying screw and the mixing element is visible.

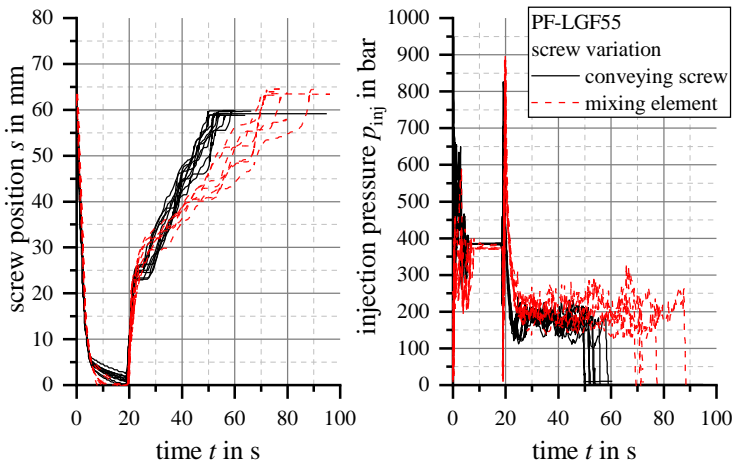


Figure 5-12: Screw position and injection pressure LGF compound with 30 mm mixing element

Compared to the standard conveying screw, an increased backflow can be observed when using the mixing element screw. During the holding pressure phase, the screw is pushing through the material cushion until it rests in the front end position. The increased backflow can also be recognized from the higher position of the inflection point during plasticizing, which means that

more screw flights are filled with densely packed molding compound. To lower the backflow, the back pressure during plasticizing was reduced for the mixing element screw. Still, the material temperature (measured with a penetration thermometer after ejection into the open) was  $\Delta T \approx 10$  K higher when using the mixing element compared to the conveying screw. The dosing of the long fiber material is generally slower compared to the short fiber compound because of the lower apparent density. The more uneven and staggered screw return movement seems to be typical for this material, because it was also observed by Saalbach et al. [120] and Raschke [121]. However, a further slowdown of the plasticizing process can be observed when using the mixing element screw. This is an indication that the mixing element obstructs the material flow and lowers the material intake rate. Furthermore a higher total dosage volume is required for the mixing element screw, which might have been caused by the lower back pressure and the consequently less dense material packaging in front of the screw. Nevertheless, a stable injection molding process was possible using both screw configurations. The parts molded with the mixing element had a smoother, more homogeneous surface with less flow lines, which indicates a positive effect of the mixing element on the material homogenization, see Figure 5-13.

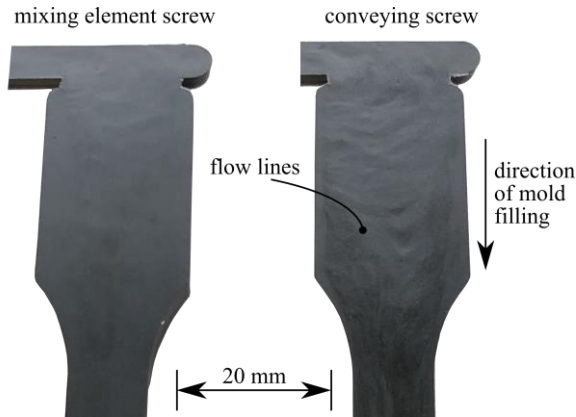


Figure 5-13: Test specimens molded with 30 mm mixing element and conveying screw

### 5.2.3 Mechanical and structural characterization of parts molded with 30 mm screw mixing element

Mechanical characterization of the parts molded using the 30 mm screw mixing element was conducted by 3-point bending tests according to DIN EN ISO 178 [224]. The results are shown in Figure 5-14. With the 30 mm mixing element, a significant improvement by  $\Delta\sigma_{m,flex} = 43$  MPa for the flexural strength of the LGF material Porophen® 9201L5 is observed.

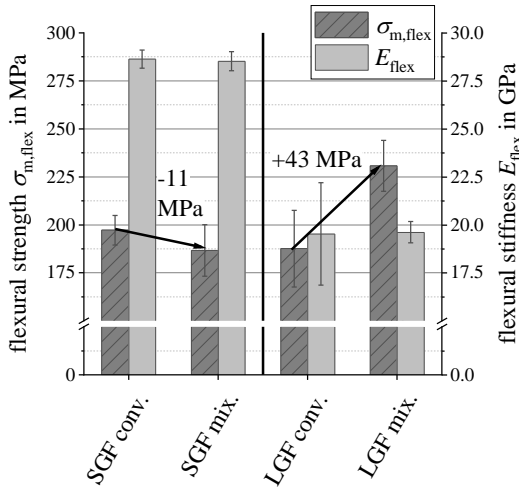


Figure 5-14: Flexural properties of parts molded with 30 mm mixing element

The flexural strength average value is still slightly below the given datasheet value of  $\sigma_{m,flex} = 257$  MPa. The flexural modulus does not change, however the scattering of the test results is reduced. Both observations indicate a better homogenization of the long fiber bundles in the resin due to the mixing element. For the SGF material, the flexural strength decreases insignificantly within the standard deviation of the results. It is still above the datasheet value of  $\sigma_{m,flex} = 185$  MPa given by the material supplier. The flexural modulus of the SGF material is unaffected by the switch from the standard conveying screw to the mixing element. The positive effect of the mixing element on the material homogeneity is also visible from the fracture surfaces which were analyzed using scanning electron microscopy, see Figure 5-15.



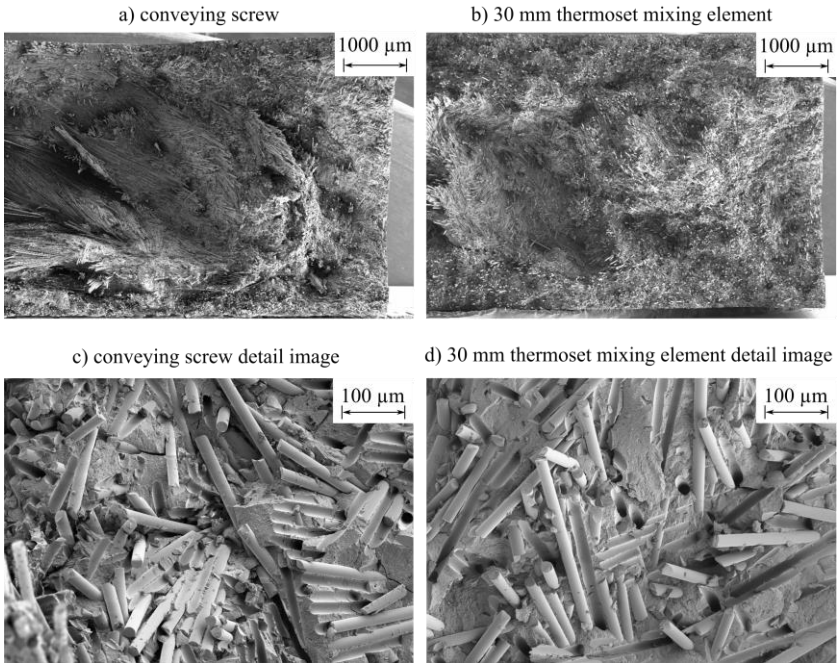


Figure 5-15: SEM for PF-SGF0-LGF55 flexural test specimens

Less fiber bundles and an overall more homogeneous fiber dispersion is visible in Figure 5-15 (b). Although there are still some fiber bundle structures, a skin and core layer structure can be envisaged. The detail images at in Figure 5-15 (c) and (d) show blank and smooth fiber surfaces without any resin adhering to them. This indicates a low fiber-matrix interfacial bonding for the LGF granulate material. No effect of the mixing element on the fiber-matrix adhesion is observed.

## 5.3 Long fiber direct injection molding process development

### 5.3.1 Material feeding limitations in the long fiber direct injection molding process

Multiple trial series were conducted using the process variant “standard plasticizing unit”. The main limitation for the long fiber direct thermoset injection molding process is feeding the dry-blend of the short fiber molding compound and the chopped fibers into the screw of the plasticizing unit. In the engineering implementation of the process scheme (see Figure 4-3), adapting the sidefeed in a 90° angle to the barrel of the injection molding machine was not possible due to design space restrictions. Instead, a 30° angle and a sidefeed position on top of the plasticizing unit are required. For this reason, a dead space between the outlet of the twin-screw sidefeed and the inlet of the single-screw injection molding screw exists. In this dead space, referred to as the downpipe, the fiber-compound mixture must fall into the injection molding screw purely due to gravity. For two reasons, the sidefeed cannot stuff the dry blend into the plasticizing unit: First, the sidefeed is not designed for building up pressure. If a counterpressure is built up, the sidefeed blocks and shuts down. Second, the fiber-compound mixture blocks the downpipe if it is put under axial pressure. Consequently, the feeding rate of the short fiber molding compound and the speed of the fiber chopper must be adjusted so that the fiber-compound mixture can fall unhindered onto the injection molding screw. The potential conveying capacity of the injection molding screw must be greater than the actual fiber-compound feeding rate. The achievable feeding rate largely depends on the apparent density of the fiber-compound mixture and the rotation speed of the injection molding screw. The apparent density mainly increases with a rising long glass fiber content. During the first trial series, plasticizing times in the range of  $t = 30 \text{ s} \dots 120 \text{ s}$  per cycle were required. Due to the long contact time of the nozzle to the hot sprue bushing of the mold, the long plasticizing times caused problems such as curing in the nozzle and an overall too high energy input into the material. The maximum total fiber content that was achievable with the standard thermoset screw was  $\phi = 40 \text{ wt.-%}$ . The long fiber screw which was developed for the process variant with the separate granulate feed port does not only have a larger processing length, but also a smaller core

diameter (see Table 4-2). Additionally, the long fiber barrel has a deeper feed pocket at the sidefeed location. Both measures improved the feeding behavior and increased the processable long fiber content to  $\phi = 60$  wt.-% when using the conveying screw geometry.

However, the range in which process parameters such as the back pressure and the screw speed could be varied, was severely limited at high fiber contents. Since these process parameters are the main influence factors on the material homogenization during plasticizing, the machine operator's possibilities for influencing the process and the component quality are severely restricted. For all combinations of material and process parameters, fiber bundles are visible in the molded plate when a standard conveying geometry is used. For this reason, the focus of the process development work was implementing measures for increasing the distributive and dispersive mixing during the process.

### 5.3.2 Distributive and dispersive mixing during the injection phase

First, the designed mixing elements for the distributive and dispersive mixing during the injection phase are evaluated regarding their impact on the processing characteristics. Figure 5-16 shows the influence of the different nozzle types on the injection pressure and Figure 5-17 shows the injection pressure curve for different shear gap heights using the adjustable sprue bushing. Both experiments were performed using a self-compounded PF-SGF40-LGF0 short fiber molding compound.

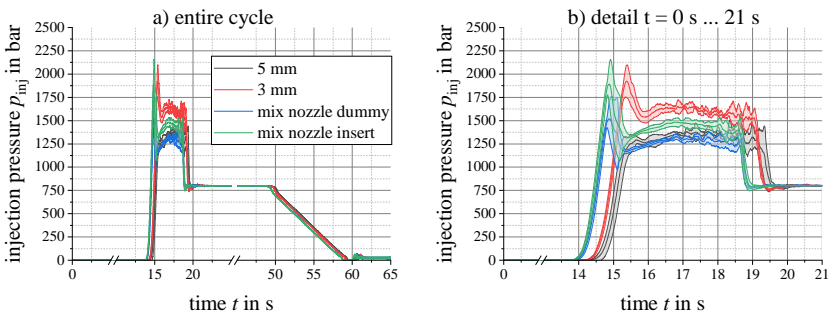


Figure 5-16: Influence of machine nozzle type on injection pressure for PF-SGF40-LGF0

Subfigures (a) show the entire injection and holding pressure phase, whereas subfigures (b) are an enlarged detail of the injection phase. The smaller 3 mm machine nozzle requires a  $\Delta p \approx 250$  bar... 300 bar higher injection pressure compared to the standard 3 mm nozzle due to its smaller cross-sectional area. For the mixing nozzle, a higher initial pressure peak can be observed. Once the compound is flowing through the nozzle, there is no additional injection pressure consumption when using the dummy insert and only a relatively small additional pressure requirement of  $\Delta p \approx 150$  bar for the mixer insert.

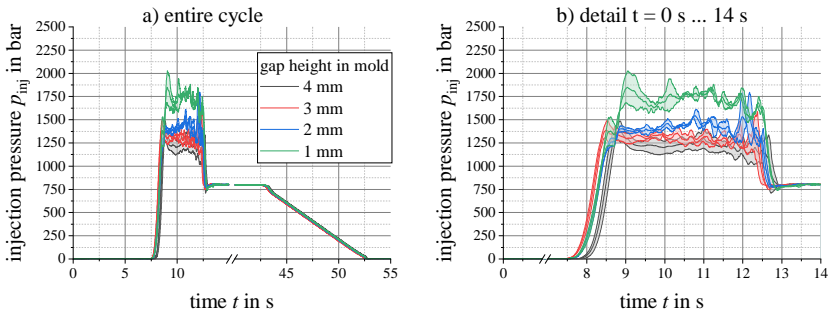


Figure 5-17: Influence of sprue gap height on injection pressure PF-SGF40-LGF0

For the adjustable shear gap using the variable sprue bushing it can be observed that a major increase in required injection pressure only occurs if the smallest gap size of  $H_{gap} = 1$  mm is used. From a process engineering point of view, all measures to increase the mixing during the injection phase are practicable and can be used in the thermoset injection molding process. The slight increase of the injection pressure requirement is also visible from the required injection work, see Figure 5-18.

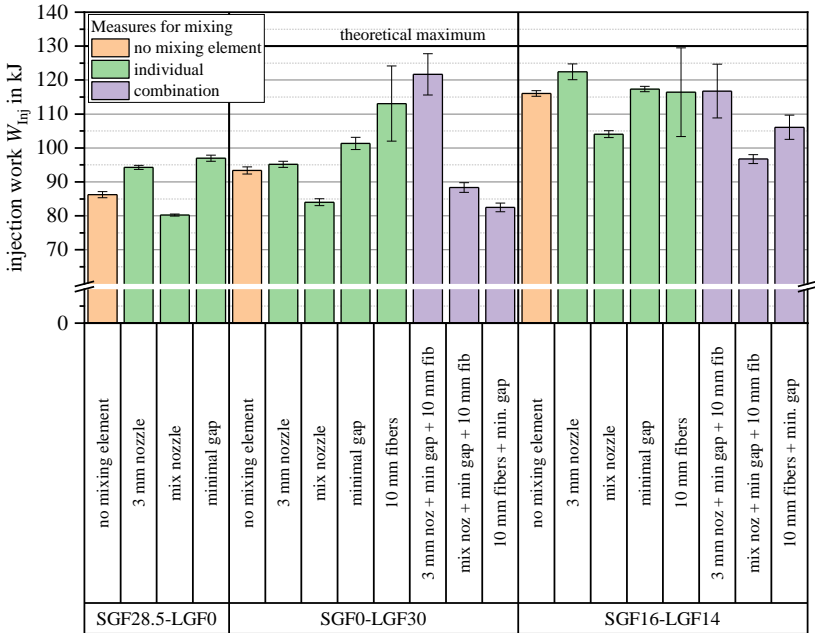


Figure 5-18: Injection work for distributive and dispersive mixing during the injection phase

### 5.3.3 Process data analysis for 2<sup>nd</sup> iteration screw mixing element (60 mm)

With the screw Maddock mixing element for the 60 mm screw size, injection molding trials with extensive material and process variations were performed. Extracts of the results have been published in the publication “Development of an Injection Molding Process for Long Glass Fiber-Reinforced Phenolic Resins” by Maertens et al. [26]. Figure 5-19 gives an overview of the variations that were carried out.

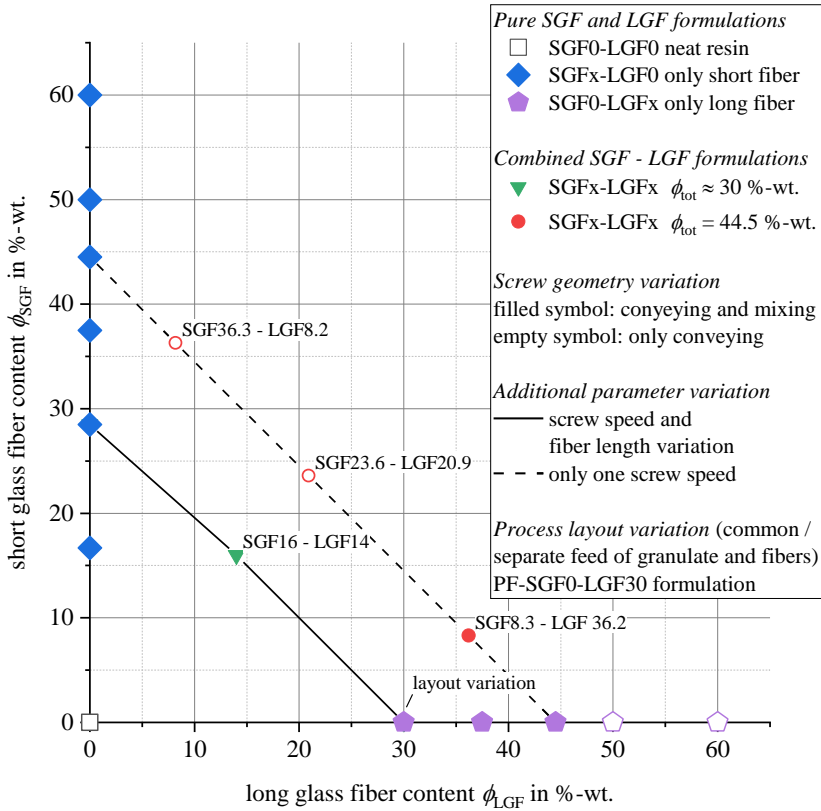


Figure 5-19: Material and process variation for injection molding trials with 60 mm mixing element [26]

Formulations containing either only short glass fibers (SGF), only long glass fibers (LGF) or no fibers at all (neat resin) were molded. These formulations are located on the vertical and horizontal axes of Figure 5-19. For two chosen total fiber contents,  $\phi = 30$  wt.-% and  $\phi = 44.5$  wt.-%, combined SGF-LGF formulations with varying fractions of two fiber types were processed. These formulations are labeled in Figure 5-19. The potential combined SGF-LGF formulations had to be determined before producing the short fiber molding compounds (see Section 5.1 above). At the point of determining the formulations, it was not known which total fiber content values and thus which combined material formulations are processable in the long fiber direct injection molding process. Consequently, the short fiber molding compound

fiber content target values were designed for combined formulations with a total fiber content of  $\phi = 60$  wt.-%. However, these formulations were not moldable due to the feeding limitations mentioned in Section 5.3.1. Instead, the two combined fiber contents  $\phi = 30$  wt.-% and  $\phi = 44.5$  wt.-%, were chosen. This adjustment in the trial plan resulted in uneven combined formulations such as PF-SGF23.6-LGF20.9.

For selected material formulations, additional variations were carried out. They are marked by the symbol and line styles in Figure 5-19. All formulations except those containing a high content of LGF were molded using both the conveying screw geometry and the mixing element. For the three formulations with a total fiber content of  $\phi = 30$  wt.-%, screw speed and LGF fiber length were varied on two levels. The PF-SGF28.5-LGF0 formulation was used to additionally evaluate the separate feeding of granulate and fibers, whereas for all other formulations the common feeding of granulate and long glass fibers was used. Figure 5-20 shows the injection pressure for a PF-SGF0-LGF30 formulation on the left side (a), and for a short fiber formulation with a similar total fiber content (PF-SGF28.5-LGF0) on the right side (b). Both materials were processed with the conveying and the mixing element screw geometries. The injection pressure curve shapes differ between the mixing element and the conveying screw. Using the conveying screw produces a pronounced pressure peak at the beginning of the injection stroke. This can be attributed to the cold plug in the nozzle, which must be put into movement before any material can flow into the mold. The pressure requirement for the remaining injection stroke is constant or slightly decreasing.

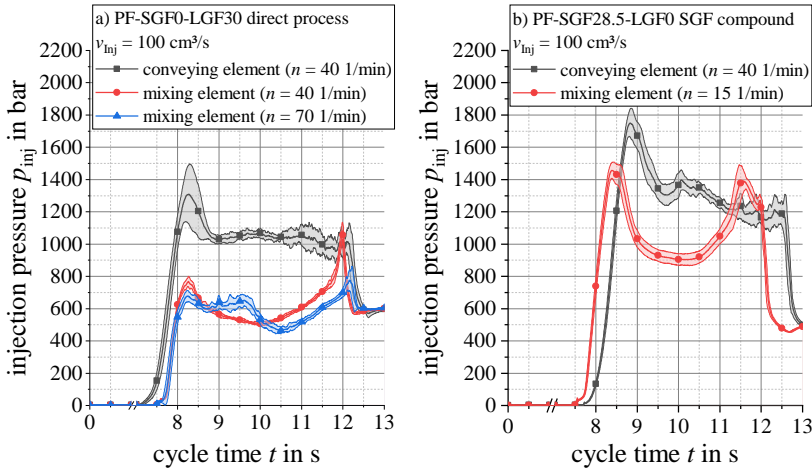


Figure 5-20: Injection pressure LGF and SGF formulations conveying and mixing screw [26]

In contrast, the mixing element has a significantly lower initial pressure peak and a lower pressure requirement during the filling phase. Towards the end of the injection stroke, the pressure rises sharply until the switchover point to the holding pressure is reached. This indicates that the material in front of the screw is hotter and therefore has a lower viscosity and a less pronounced cold plug. The increase in injection pressure requirement towards the end of the stroke can be attributed to the chemical reaction progress, which in turn results in increased viscosity and a higher injection pressure requirement to keep the material flowing at the defined injection speed. [26]

When comparing the two different plasticizing screw speeds  $n = 40$  1/min and  $n = 70$  1/min for the PF-SGF0-LGF30 material formulation on the left side of Figure 5-20, the higher screw speed results in a tendentially lower initial pressure peak. During the remaining injection stroke, no clear distinction between the two screw speeds can be observed. For the same material formulations as above, Figure 5-21 shows the screw position during injection and plasticizing. [26]



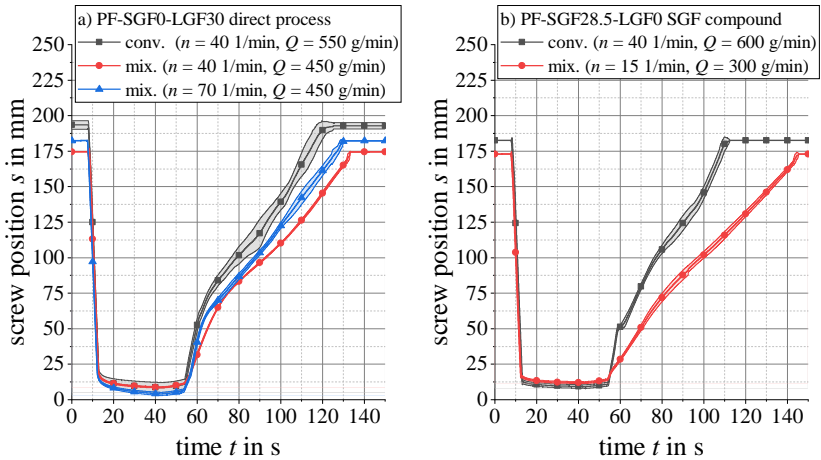


Figure 5-21: Screw position LGF and SGF formulations conveying and mixing screw [26]

The total material throughput  $Q$ , which is dictated by the peripheral devices gravimetric loss-in-weight-feeder and fiber chopper, was adjusted for every trial to get as close to the maximum feeding rate as possible and therefore to minimize the plasticizing time. For the long fiber formulation PF-SGF0-LGF30 on the left side of Figure 5-21 the mixing element leads to a smoother screw movement than the conveying geometry. To a less pronounced extend, this is also valid for the short fiber formulation PF-SGF28.5-LGF0. [26]

The characteristic values plasticizing work and injection work are used for the evaluation of the process stability and the process limits of the long fiber direct injection molding process. In contrast to the conventional injection molding processes, in which the screw is flood-fed by pulling the granulate out of the material hopper, the long fiber direct injection molding process offers the possibility to starve-feed the screw. The material throughput, and therefore the plasticizing time, is defined by the mass flow provided by the gravimetric dosing of the granulate and the cutting speed of the fiber chopper. It is independent of the screw speed, which means that the screw speed can be used as a parameter for influencing the mixing quality and the energy input into the material. Figure 5-22 shows the plasticizing and injection work for a parameter study using a PF-SGF0-LGF30 material formulation and the 60 mm mixing element. [26]

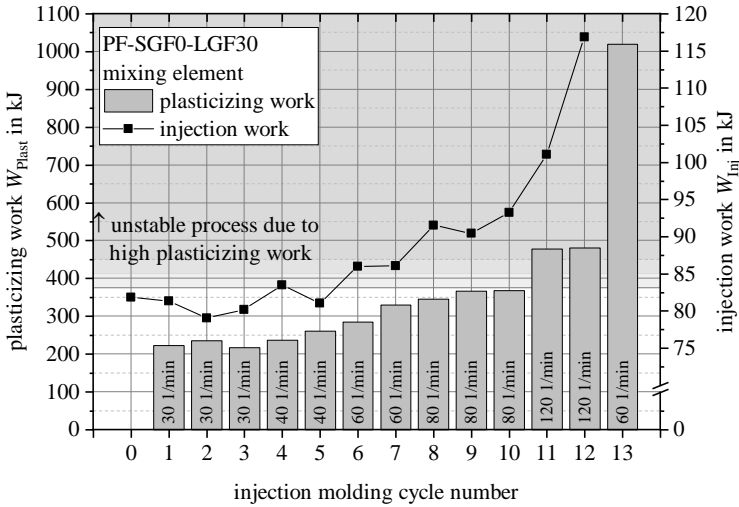


Figure 5-22: Plasticizing work and injection work PF-SGF0-LGF30 screw speed study [26]

Over the course of 13 injection molding cycles, the screw speed was increased from  $n = 30$  1/min up to  $n = 120$  1/min. For each injection molding cycle, Figure 5-22 shows the plasticizing work and the corresponding injection work. For the first cycle 0, the material was plasticized in manual mode, which is why no plasticizing work was recorded. The increase in plasticizing work with increasing screw speed is clearly visible. Up to a screw speed of  $n = 80$  1/min, both work integrals remain stable at the respective screw speed steps. For the highest screw speed value  $n = 120$  1/min, the injection work rises despite a constant plasticizing work. This indicates overheating and an uncontrolled reaction progress of the plasticized material in front of the screw. The cycle 12 was the last moldable part of this parameter study. Despite reducing the screw speed to  $n = 60$  1/min after recognizing the instability of the process, the plasticizing work increased dramatically, and no injection was possible due to a curing of the material on the mixing element. Based on the parameter study findings, an upper limit of  $W_{\text{plast}} \approx 400$  kJ was set. The available data does not allow a sharp distinction between a stable and an unstable process, which is why an approximate range for the plasticizing work is marked in Figure 5-22. This range corresponds to a plasticizing screw speed limit of  $n \approx 80$  1/min ... 90 1/min. For subsequent trials, a limit of  $n = 70$  1/min was defined. Figure 5-23 shows the plasticizing work and the injection work for a process stability study using screw speeds of

$n = 40$  1/min and  $n = 70$  1/min. For both parameter combinations, 10 (trial number 1) respectively 9 (trial number 2) repetitions were performed after a stable process was established. [26]

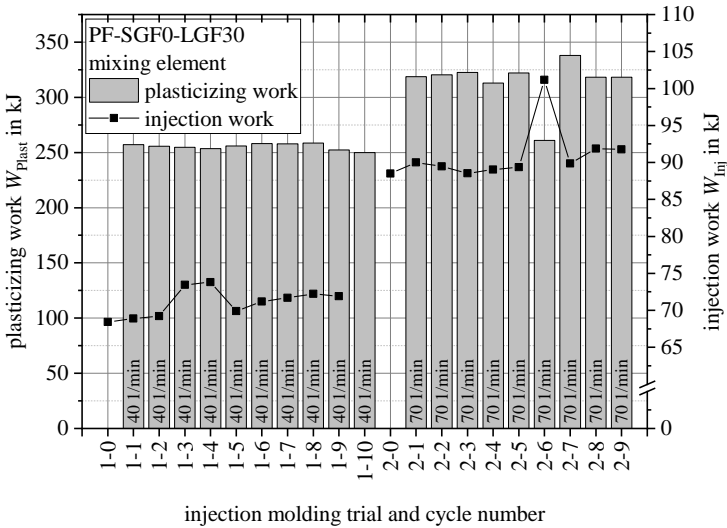


Figure 5-23: Plasticizing work and injection work PF-SGF0-LGF30 process stability study [26]

For both screw speeds, the plasticizing work is stable and remains below the previously defined threshold value of  $W_{\text{plast}} \approx 400$  kJ. The effect of the increased screw speed on the plasticizing work and the injection work is in accordance with the values measured during the parameter study. The slight increase of the injection work over the 10 and 9 repetitions indicates that a complete thermal equilibrium and a fully stable process were not reached during the experimental period. However, the process is considered sufficiently stable so that the results can be used without any restriction. The plasticizing and injection work was analyzed for both the mixing element and the conveying screw for several material formulations, see Figure 5-24 and Figure 5-25. The screw speed for the trials was chosen as a trade-off between the highest possible mixing effect and the quickest possible dosing (screw speed as high as possible) on the one hand and the maximum allowable energy input (screw speed as low as necessary) on the other hand.

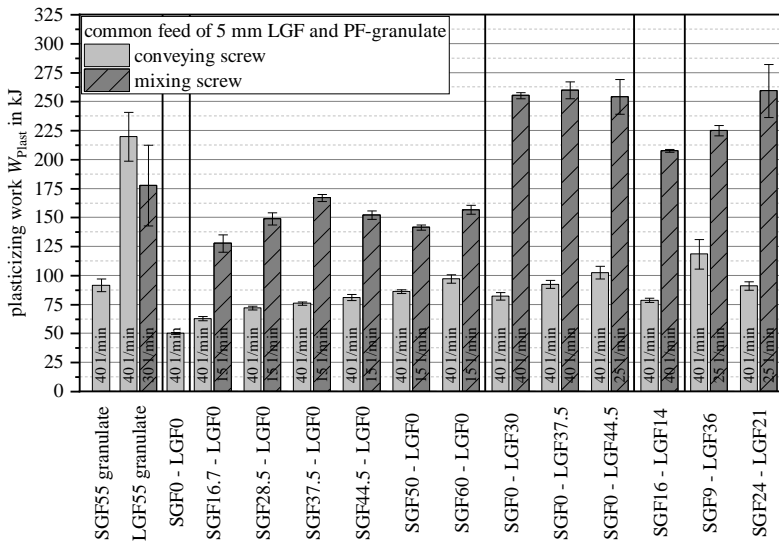


Figure 5-24: Plasticizing work screw layout and material variations [26]

For the conveying screw geometry, a clear increase in plasticizing work with increasing fiber content is visible. This is valid for short glass fiber (SGF), long glass fiber (LGF) and combined (PF-SGF<sub>x</sub>-LGF<sub>y</sub>) material formulations. In contrast to the conveying screw geometry, no clear correlation between the fiber content and the plasticizing work can be drawn for the mixing element. The mixing element causes an overall significantly higher plasticizing work. The only exception from that observation is the granular long fiber molding compound (PF-SGF0-LGF55 granulate), which had a lower plasticizing work for the mixing element compared to the conveying screw geometry. For the long fiber direct thermoset injection molding process, formulations containing long glass fibers require a significantly higher plasticizing work compared to formulations with only short glass fibers. [26]

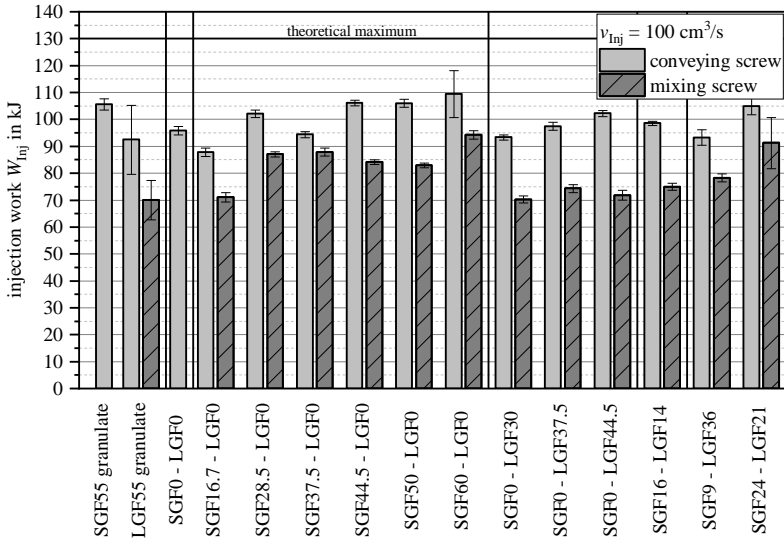


Figure 5-25: Injection work for screw layout and material variations

Comparing the mixing and the conveying screw geometries regarding their influence on the injection work in Figure 5-25 shows that using the mixing element leads to a lower injection work for all material formulations. For both screw geometries, a tendential increase of the injection work with increasing fiber content is visible. Increasing the fiber length from the short fibers to the  $L = 5$  mm chopped long glass fibers leads to a reduction in the required injection work, which can be seen when comparing the formulations PF-SGF28.5-LGF0 with PF-SGF0-LGF30, PF-SGF37.5-LGF0 with PF-SGF0-LGF37.5 and PF-SGF44.5-LGF0 with PF-SGF0-LGF44.5. In all three cases, the injection work is lower for the long fiber formulations, both for the conveying screw and the mixing element. This correlates with the observations regarding the plasticizing work, which increases both with fiber length and with the utilization of the mixing element.

The formulations with a total fiber content of  $\phi = 44.5$  wt.-% were only partially processable with the mixing element. As shown in Figure 5-19, only the combined formulation PF-SGF8.3-LGF36.2 was processable with the mixing element during the trial series on which the presented results are based. The other two combined formulations, PF-SGF23.6-LGF20.9 and PF-SGF36.3-LGF8.2, could only be molded with the conveying screw geometry,

but not with the mixing element. This was caused by a machine damage (broken injection molding screw) that occurred during this specific trial series. To investigate whether the non-processability of the combined formulations with  $\phi = 44.5$  wt.-% and the broken injection molding screw were caused by a process limitation, the molding trials for all formulations with  $\phi = 44.5$  wt.-% were repeated with a newly manufactured, one-piece mixing element screw. The one-piece design of the screw had the purpose of improving the screw's mechanical strength, while no relevant changes were made to the functional geometry of the mixing element.

During this repetition trial series, only the pure SGF and LGF formulations were moldable with the mixing element. All combined formulations with the total fiber content of  $\phi = 44.5$  wt.-% could only be molded with the conveying screw, but not with the mixing element. The non-processability shows as overheating and curing of the molding compound in front of the screw. Over a few injection molding cycles, the injection pressure requirement (and thus the injection work) increases steadily until the nozzle is blocked. This is exemplarily shown in Figure 5-26 for seven injection molding cycles of the PF-SGF36.3-LGF8.2 formulation.

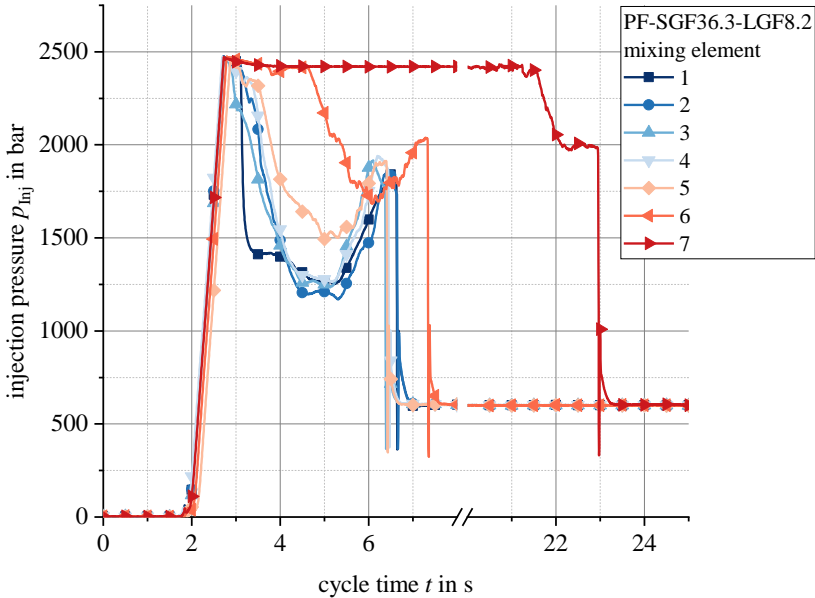


Figure 5-26: Injection pressure for the non-processable PF-SGF36.3-LGF8.2 formulation

While the rise in injection pressure requirement is obvious for this specific formulation, it must be noted that there is often non clear distinction between “processable” and “non-processable”. Instead, there is a highly uncertain transition area. It cannot be ruled out that, with repeated trials, some of the mixing formulations could also have been processed. The process data analysis for these formulations does not give an explanation why some of the formulations were processable while others were not. For example, Figure 5-27 shows the plasticizing work and the plasticizing time. No tendency in plasticizing work can be observed.

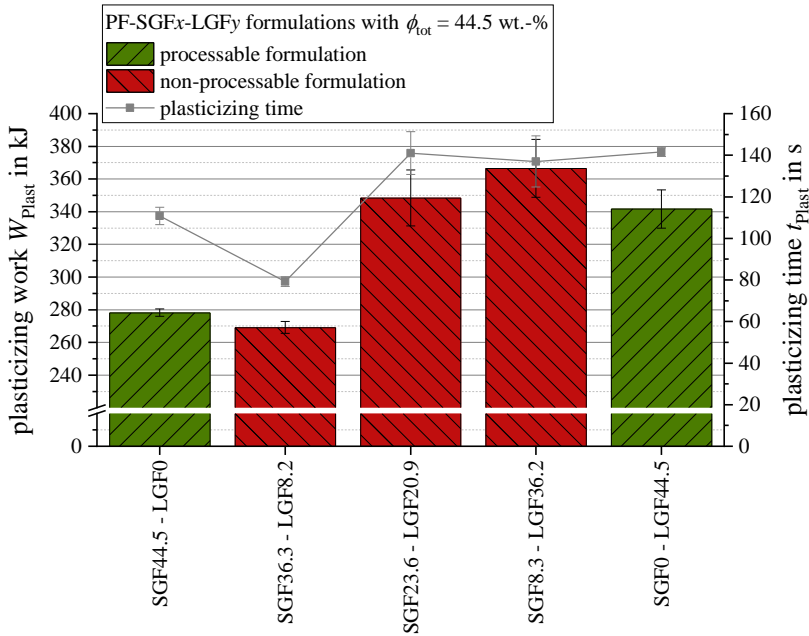


Figure 5-27: Plasticizing work and plasticizing time for PF-SGF<sub>x</sub>-LGF<sub>y</sub> formulations with  $\phi = 44.5 \text{ wt.-%}$

Additionally, back pressure variations, screw position during plasticizing and screw position during injection were analyzed, but no relevant differences between the processable and the non-processable formulations were found.

As noted above, the allowable material throughput had to be adjusted based on the material formulation. Lowering the throughput was required for higher fiber contents and longer fiber lengths. With both factors, the apparent density of the granulate-fiber dry blend decreases and the shear energy input during plasticizing increases. This means that less material is pulled into the screw per screw rotation (apparent density) and at the same time, the screw rotational speed must be decreased (to keep the shear energy input of the mixing element in a controllable range and to avoid overheating). Both aspects result in an increase in plasticizing time, which is depicted in Figure 5-28. [26]



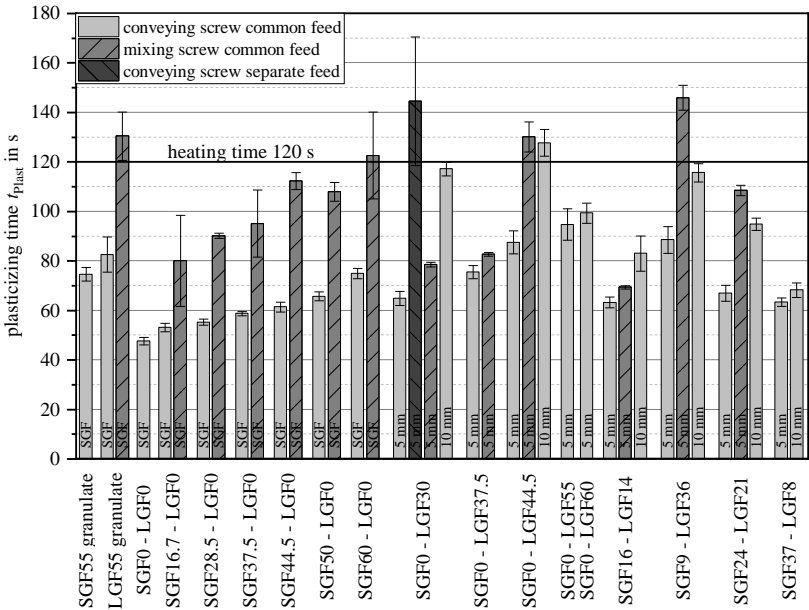


Figure 5-28: Plasticizing time for SGF and LGF compounds using different process layouts

Figure 5-28 also shows the plasticizing time for the process variant “separate granulate feed port”, which was only evaluated for the PF-SGF0-LGF30 formulation with a fiber length of  $L = 5$  mm. As a horizontal line, the chosen heating time of  $t = 120$  s is marked. Plasticizing times that exceed the heating time are undesirable because of the long contact time of the machine nozzle to the hot mold.

### 5.3.4 Evaluation of separate feeding of granulate and fibers

As shown in Section 5.2.1, it is possible to melt the phenolic molding compounds over a short distance by using a compression sleeve on the screw. The geometry was upscaled to the 60 mm screw diameter. With interchangeable melting elements, shear gaps of  $H_{gap} = 1$  mm, 1.5 mm and 2 mm can be realized. The temperature in the fiber feeding zone can be adjusted using an electric heating band in a range of up to  $T = 130$  °C. For a PF-SGF0-LGF0 neat resin molding compound, the shear gap of  $H_{gap} = 1.5$  mm is suited best.

However, as shown in Figure 5-28, the plasticizing time for this process variant is not satisfactory. This is also visible from Figure 5-29.

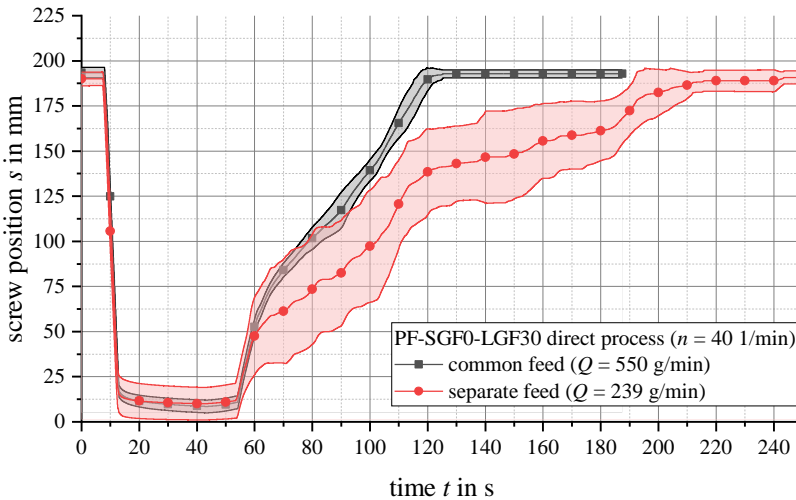


Figure 5-29: Screw position over time for separate and common material feeding locations

The screw positions over time for the common material feed (black) and the separate material feed (red) are shown. Both trials runs used the conveying screw geometry. The red family of curves for the separate feeding of granulate and fibers shows a much more uneven and jumping screw movement. For some injection molding cycles, the screw is stationary for up to  $t = 40$  s before it moves back again. In contrast, the screw movement is much more even for the trial run using the common feed. The maximum achievable material throughput  $Q$  for the separate feed is less than half of that for the common feed, because otherwise a blockage of the downpipe would occur. Figure 5-30 shows the screw with the molding compound on it after it was pulled out of the plasticizing unit.

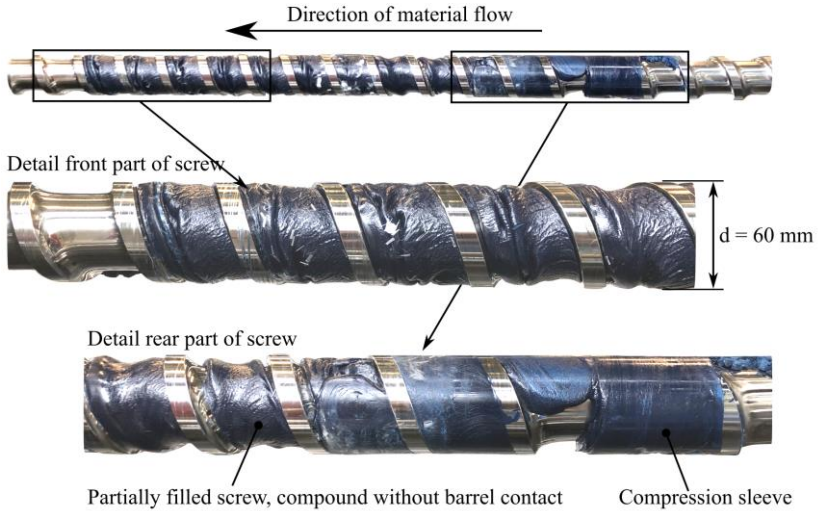


Figure 5-30: Material distribution on 60 mm screw with 1.5 mm gap compression sleeve

The area around the compression sleeve is the only fully filled zone on the screw. All sections further downstream, i.e. towards the screw tip, are only partially filled. Since the chopped fibers are fed directly after the compression sleeve, the partially filled area there was created intentionally by the choice of the screw diameter. Over the process running time of several minutes, no compound was scraped off at the edge of the downpipe of the fiber feed.

## 5.4 Structural analysis of intermediate process step products and molded parts

### 5.4.1 Evaluation of material homogeneity by X-ray computed tomography image texture analysis

In the parts containing long fibers, glass fiber bundles were visible when no mixing element was used, see Figure 5-31 which shows the fracture surface of a Charpy test specimen. It is assumed that these bundles act as defects and lead to stress concentrations.

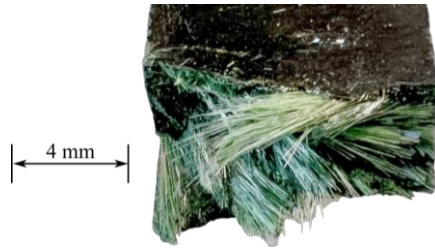


Figure 5-31: Fiber bundles on fracture surface

The fiber bundles were not only visible in the molded parts, but also in the plasticized material in front of the screw. To quantify the inhomogeneity, X-ray computed tomography measurements were carried out as described in Section 3.2.2. and the publication [25] by Maertens et al. The specimen location of the plasticized material is visualized in Figure 5-32.

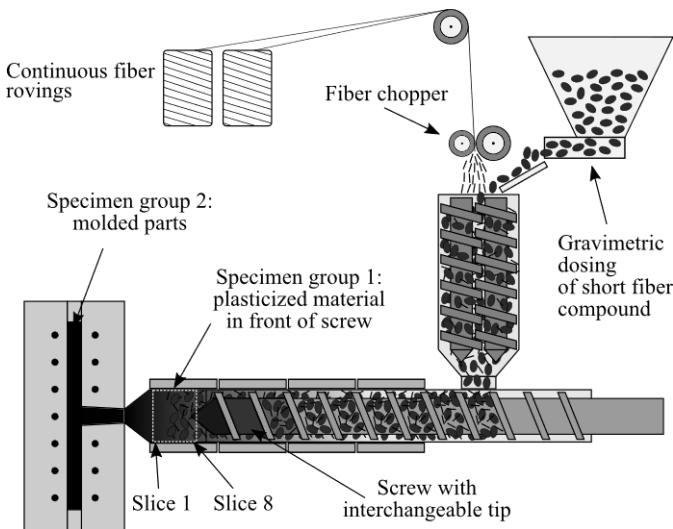


Figure 5-32: Specimen location for material homogeneity investigations [25]

Two different kinds of specimens were obtained: The plasticized compound in front of the screw and the molded parts. For judging the influence of the base material formulation on the fiber dispersion quality, the plasticized compound in front of the screw was analyzed. These specimens are called group 1. To obtain them, a stable injection molding process was stopped after the plasticizing step. The compound in front of the screw, which would have

been injected into the mold in the next process step, was cooled down and removed from the barrel once it was solidified. The conveying screw geometry was used. A PF-SGF0-LGF30 and a PF-SGF20-LGF30 formulation, both containing long glass fibers chopped to a length of  $L = 5$  mm, were investigated. One specimen per formulation was analyzed, which results in a total number of two specimens for this group. The second group of specimens were cut from molded plates. Here, the focus was not on the material formulation, but instead on the influence of the screw geometry and the process parameters on the material homogeneity. Consequently, the same PF-SGF0-LGF30 formulation was used for all specimens within this group, but the screw geometry and the screw speed were varied. The PF-SGF20-LGF30 formulation was not used for the investigations with specimen group 2. Due to the high shear energy input by the mixing element and the overall higher fiber content of the PF-SGF20-LGF30 formulation, an overheating and consequently a premature curing of the phenolic resin occurred, which made it impossible to reliably mold parts. To be able to identify spatial differences in the homogeneity within one specimen, the cuboid images of specimen group 1 were sliced into subsets with a height of  $h = 250 \text{ vx} = 11.75$  mm each. This results in eight slices per specimen. Slice 1 is positioned towards the machine nozzle and slice 8 is located towards the screw of the injection molding machine. The slice position is marked in Figure 5-32. Due to their overall smaller size, no slicing was conducted for the specimens of group 2. [25]

To select suitable calculation distances for generating the GLCMs, the characteristic regions of the images were examined. Figure 5-33 (a) shows a representative cross-section view of a  $\mu$ CT image of a specimen from group 1. By using a statistical region merging algorithm [225] available for the software ImageJ [226], those distinct phases were merged to homogeneous regions as shown in Figure 5-33 (b). [25]

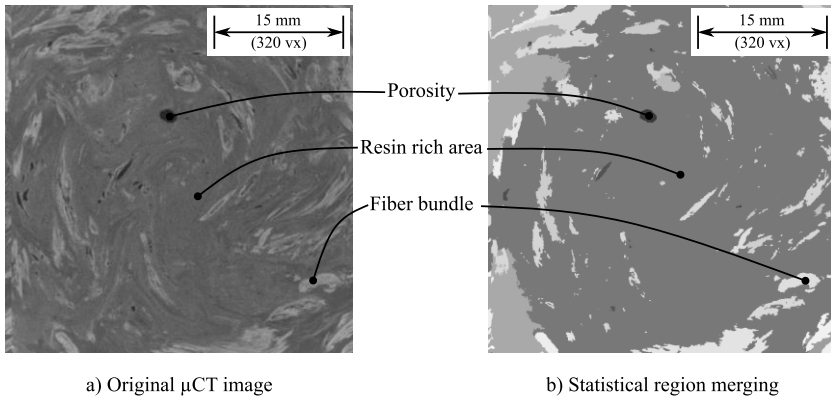


Figure 5-33:  $\mu$ CT image before and after statistical region merging for specimen group 1 [25]

The calculation distances for the GLCMs were defined by manually measuring typical sizes for regions of inhomogeneities. The measurements were carried out in multiple images in the software ImageJ. Based on these sample measurements, size ranges from  $s = 20 \text{ vx}$  to  $s = 60 \text{ vx}$  were determined. For this reason, the calculation distances for determining the GLCMs in specimen group 1 were set to values of  $d = 20 \text{ vx} = 940 \mu\text{m}$ ,  $d = 40 \text{ vx} = 1880 \mu\text{m}$  and  $d = 60 \text{ vx} = 2820 \mu\text{m}$ . This corresponds to bundle sizes of several hundreds of fibers. Some fiber bundles still had the initial fiber length of  $L = 5 \text{ mm}$ . The fiber content has been verified using thermogravimetric analysis at  $T = 650 \text{ }^\circ\text{C}$  for  $t = 36 \text{ h}$ . For all specimens, no relevant deviations of the actual fiber content from the set fiber content were found. Figure 5-34 shows the ASM calculation results for the first group of specimens. [25]

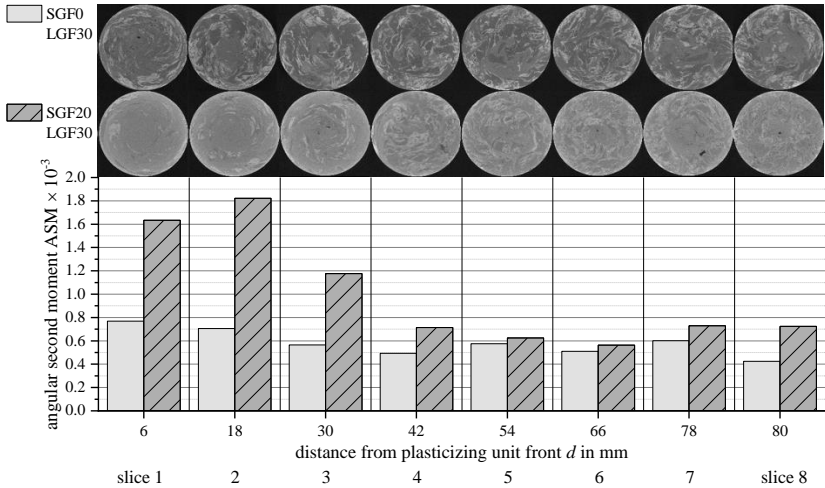


Figure 5-34: ASM calculation for PF-SGF0-LGF30 and PF-SGF20-LGF30 formulations [25]

The PF-SGF0-LGF30 formulation has a low homogeneity, as can be seen by the white fiber bundles in the images shown in Figure 5-34 and the low ASM value. In contrast, the PF-SGF20-LGF30 formulation is more homogeneous, especially in the slices towards the machine nozzle. Both the differences within the individual specimen and the differences between the two specimens are represented by the calculated image textural feature ASM. [25]

The identical statistical region merging and manual measurement procedure led to calculation distances of  $d = 50$  vx,  $d = 100$  vx and  $d = 150$  vx for specimen group 2. However, a direct comparison of the calculated ASM values for specimen group 1 and group 2 is not possible. The group 1 specimens consist of the three phases resin rich areas, fiber bundles and voids. In contrast, the specimens from group 2 were molded under the influence of the high in-mold pressure. Consequently, they do not show any voids and consist only of two phases (resin rich areas and fiber bundles). Furthermore, the image acquisition parameters (Table 3-2) had to be adapted to achieve high-quality images. The ASM results for the specimen group 2 are shown in Figure 5-35. Additionally, representative cross-sectional images are depicted.

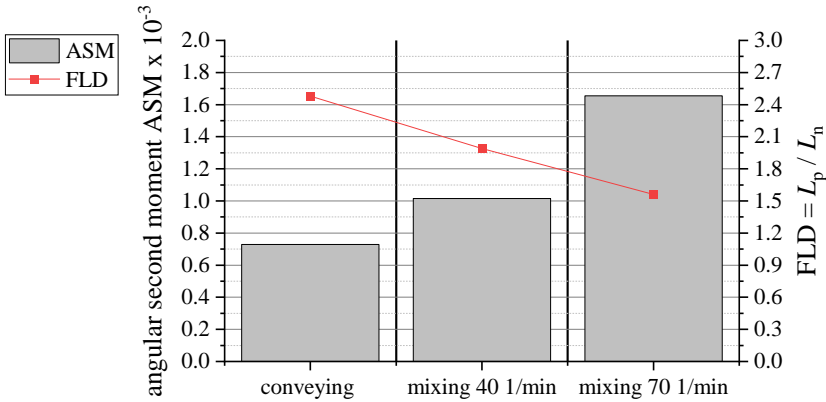


Figure 5-35: ASM values for PF-SGF0-LGF30 formulation process parameter variations [25]

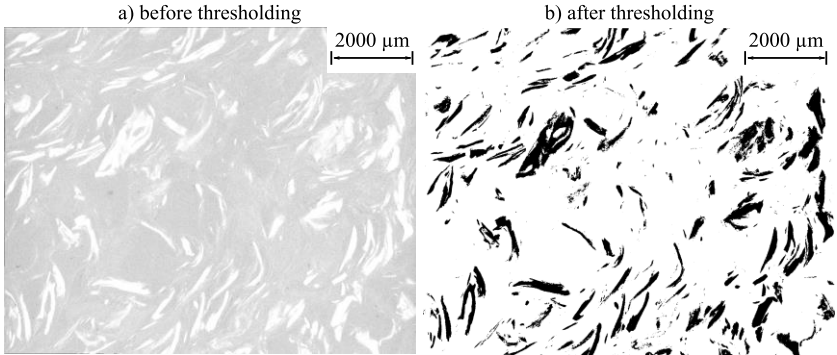
The visual impression of the images clearly indicates a higher homogeneity for the parts molded with the mixing element. The corresponding ASM values are higher for the parts molded with the mixing element and for the higher screw speed. [25]

## 5.4.2 Fiber bundle opening when using the conveying screw geometry

As mentioned several times above, fiber bundles were visible in the parts molded with the conveying screw geometry. To investigate if there is a difference in fiber bundle opening between the different combined PF-SGF<sub>x</sub>-LGF<sub>y</sub> formulations,  $\mu$ CT images of parts molded with the conveying screw for all  $\phi = 44.5$  wt.-% formulations were analyzed. Due to the size ratio of fiber diameter ( $D_{SGF} = 13 \mu\text{m}$ ,  $D_{LGF} = 17 \mu\text{m}$ ) and scan resolution of  $24 \mu\text{m}/\text{vx}$ , well-dispersed individual fibers cannot be detected. However, fiber bundles can be easily recognized by the white color in the  $\mu$ CT image. With the help of a manual thresholding operation, the volumetric images are binarized into the two groups "resin and well dispersed individual fibers" and "fiber bundles". A representative  $\mu$ CT image slice before and after thresholding is shown in Figure 5-36.



## PF-SGF24-LGF21 conveying screw

Figure 5-36:  $\mu$ CT image slice of PF-SGF24-LGF21 part molded with conveying screw

By counting the respective voxels, the volume fraction of the bundles is  $\phi_{\text{Bundles}}$  determined and the fraction  $\psi$

$$\psi = 1 - \frac{\phi_{\text{Bundles}}}{\phi_{\text{LGF}}} \quad (5-3)$$

of the opened fiber bundles is calculated. Equation (5-2) assumes that all LGF are in bundle form at the beginning of the process. Figure 5-37 shows the results.

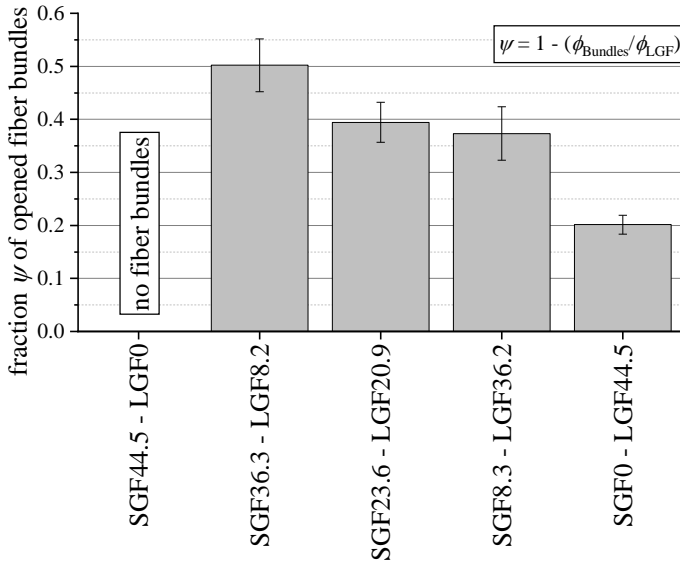


Figure 5-37: Fraction of opened fiber bundles for  $\phi = 44.5$  wt.-% formulations

The fraction  $\psi$  of opened fiber bundles decreases with increasing long fiber content. Put differently, this means that in the pure LGF formulation a lower proportion of fiber bundles is opened than in the combined formulations. A higher SGF content in the combined formulations leads to an increased opening of the fiber bundles.

### 5.4.3 Micrography along the flow path of the material

The optical micrography along the flow path of the material serves two purposes. First, a general visual impression of the structure and the material homogeneity within the specimens is obtained. Second, for selected specimens the skin and score structure of the material is quantified. Figure 5-38 shows two examples for well-dispersed specimens in which a skin and core layer structure is clearly visible.

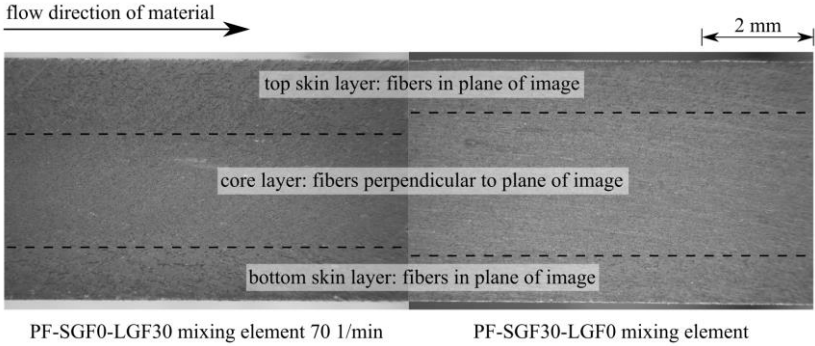


Figure 5-38: Optical micrograph for PF-SGF0-LGF30 and PF-SGF28.5-LGF0 parallel to flow

In the top and the bottom skin layer, fibers are oriented in the direction of material flow, i.e. in the plane of the image. The core layer is oriented perpendicular to the skin layer, therefore perpendicular to the plane of the image. Similar images were taken for several specimens. They were judged visually by the criteria homogeneity and distinctiveness of skin and core structure on a five-step scale ranging from ++ to --, see Table 5-3. For the criterium of homogeneity, ++ stands for a homogeneous image without fiber bundles. ++ for the distinctiveness of the skin and core layers indicates a clearly recognizable layer structure.

Table 5-3: Visual evaluation of micrographs of specimens with 30 wt.-% fiber content [227]

material form.	screw	LGF fiber length	0° orientation		90° orientation	
			hom.	skin / core	hom.	skin / core
SGF28.5-LGF0	conv.	-	+	-	++	-
SGF28.5-LGF0	mixing	-	++	o	++	o
SGF0-LGF30	conv.	5 mm	--	-	--	-
SGF0-LGF30	conv.	10 mm	-	--	--	-
SGF0-LGF30	mixing	5 mm	o	o	+	-
SGF0-LGF30	mixing	5 mm	+	+	+	o

material form.	screw	LGF fiber length	0° orientation		90° orientation	
			hom.	skin / core	hom.	skin / core
<b>SGF16-LGF14</b>	conv.	5 mm	o	o	-	-
<b>SGF16-LGF14</b>	mixing	5 mm	+	++	++	-

In 0° orientation, the highest homogeneity is observed for the short fiber formulation SGF28.5-LGF0 manufactured with the mixing element. Most fiber bundles are found in the long fiber formulations with 5 mm and 10 mm fiber length, which were produced with the conveying tip. A good fiber distribution is also present in PF-SGF16-LGF14 and PF-SGF0-LGF30 molded with the mixing element screw. The highest distinctiveness of the skin and core structure is visible for the same formulations (PF-SGF16-LGF14 and PF-SGF0-LGF30) produced with the mixing element. When produced with the conveying screw, the layered structure is less pronounced. In 90° orientation, a high homogeneity is observed for the short fiber formulations, as well as in the long fiber formulations produced with the mixing element. Again, the long fiber formulations produced with the conveying screw geometry have an inhomogeneous, bundle-rich structure. The skin and core structure is visible but less distinctive for the samples with the image plane in 90° orientation to the flow of material. For the specimens which have a clearly visible skin and core structure, detail images at a higher magnification were taken and the layer thickness was measured manually. The thickness of the individual layers is different from specimen to specimen and is a function of the flow path length, i.e. the distance from the gate of the mold. Figure 5-39 shows the cumulative fraction of the two skin layers.

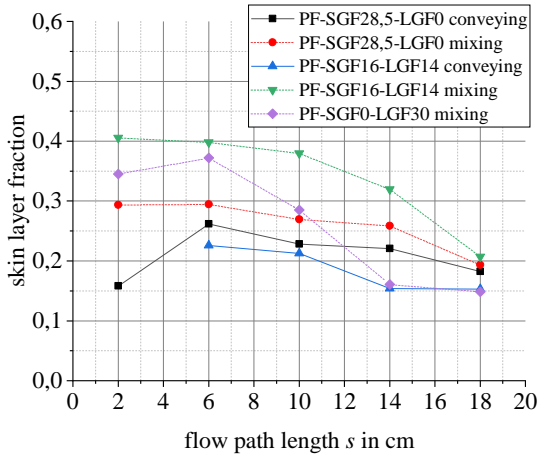


Figure 5-39: Skin layer fraction vs. flow path length for selected 30 wt.-% fiber content specimens

The fraction of the skin layer decreases with increasing flow path length. At the beginning of the flow path, the fraction of the skin layer in the specimens manufactured with the mixing element is higher than in those manufactured with the conveying screw. Towards the end of the flow path, all curves approach a value between 15 % and 20 % skin layer fraction.

#### 5.4.4 Comparison of destructive and non-destructive fiber length measurement methods

The images acquired by using X-ray computed tomography are shown in Figure 5-40 for the short fiber granulate (a) and the long fiber molded part (b). The high packaging density of the glass fibers due to the  $\phi = 55$  wt.-% fiber content in both specimens is visible. The results have been published by Maertens et al. previously in the publication [15].

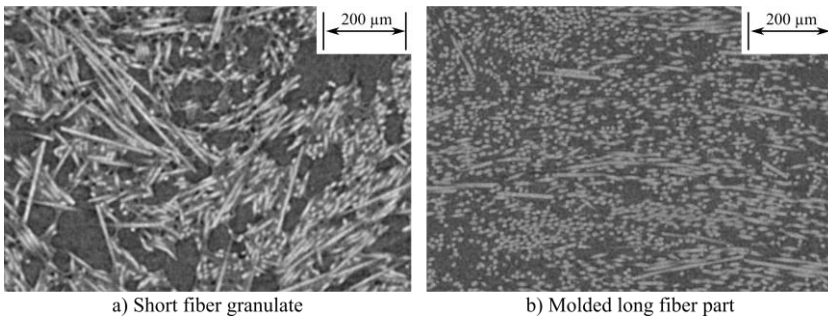


Figure 5-40:  $\mu$ CT images for the non-destructive fiber length measurement [15]

In the image of the granulate, porosities due to entrapped air and reaction gasses during the compounding process can be seen as black spots. The fibers have a bright tone and the phenolic resin has an intermediate gray value. After the  $\mu$ CT image acquisition, the same specimens underwent pyrolysis to remove the matrix material. The entire sample was diluted to an aqueous suspension with a suitable fiber concentration and analyzed by using the FASEP system. For the short fiber granulate sample, the FASEP system counted  $n_{\text{FASEP}} = 121\,839$  fibers, whereas the CT analysis resulted in  $n_{\text{CT}} = 391\,390$  fibers. A similar ratio was obtained for the molded long fiber specimen.

Figure 5-41 shows the fiber length distribution for both the granulate and the long fiber specimen for  $\mu$ CT and FASEP measurement methods. To account for different lower detection limits of the two methods, all fibers with a length below  $L_i = 50\ \mu\text{m}$  were discarded.

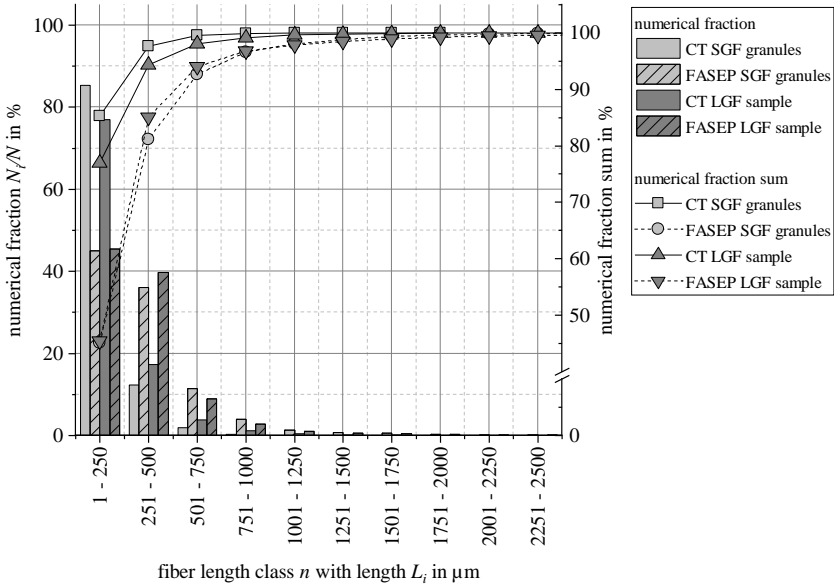


Figure 5-41: Comparison of destructive and non-destructive fiber length measurement [15]

The  $\mu$ CT analysis yields a significantly higher fraction of fibers in the shortest length class. In contrast, the optical fiber length measurement results in an even distribution between the two smallest fiber length classes for the SGF granulate. In the case of the SGF granulate this difference in the fiber length distribution results in a shorter average fiber length for the  $\mu$ CT measurement of  $L_{n,\mu\text{CT}} = 150 \mu\text{m}$  compared to  $L_{n,\text{FASEP}} = 351 \mu\text{m}$  for the optical fiber length measurement for the exact same specimen.

### 5.4.5 Fiber shortening along the process route

Figure 5-42 shows the weighted average fiber length  $L_p$  for the sample positions along the injection molding process route for a commercially available short fiber compound Vyncolit® X6952 (PF-SGF55-LGF0) and for the long fiber molding compound, Porophen® L9201L12 (PF-SGF0-LGF55).

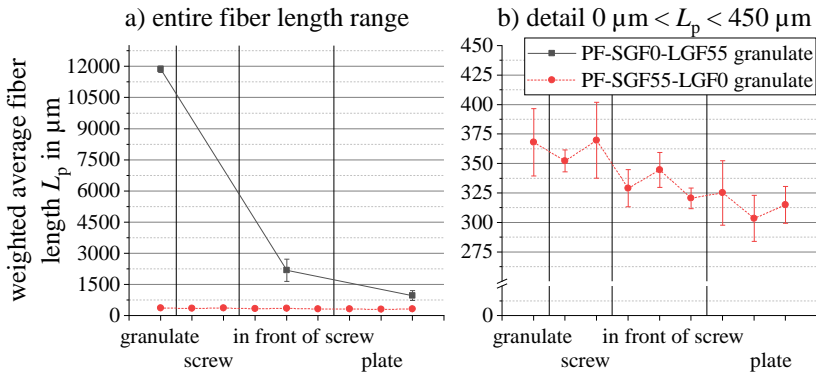


Figure 5-42: Fiber shortening along process for PF-SGF55-LGF0 and PF-SGF0-LGF55 [15]

The results were obtained by using the optical fiber length measurement method based on the FASEP system with the down-sampling and fiber dispersion process described in Section 2.4.1 [228]. For the PF-SGF0-LGF55 long fiber compound, a strong reduction in weighted average fiber length from  $L_p = 11800 \mu\text{m}$  in the granulate to  $L_p = 970 \mu\text{m}$  in the molded part is observed. Most of the length degradation already takes place during the plasticizing process, which results in a weighted average fiber length of  $L_p = 2200 \mu\text{m}$  in front of the screw. The PF-SGF55-LGF0 short fiber material has an initial weighted average fiber length of approximately  $L_p = 370 \mu\text{m}$ . The fiber length reduction throughout the entire injection molding process is less than  $\Delta L_p = 70 \mu\text{m}$ . Since the measurement uncertainty is in the same range as the effect to be measured, it is not possible to identify a specific point at which the fibers are shortened the most.

## 5.4.6 Fiber shortening using the screw mixing element

As described in Section 5.4.1, the homogeneity of the molded parts is improved when using the thermoset Maddock mixing element. The homogeneity can be improved further with an increase in screw speed. Section 2.4.1 outlined that for opening fiber bundles, and consequently for achieving a better homogenization of the fibers in the matrix, the same mechanisms as for shortening the fibers are at work. This is underlined by the fiber length measurement results for PF-SGF0-LGF30 shown in Figure 5-43, which were previously published by Maertens et al. in [26].



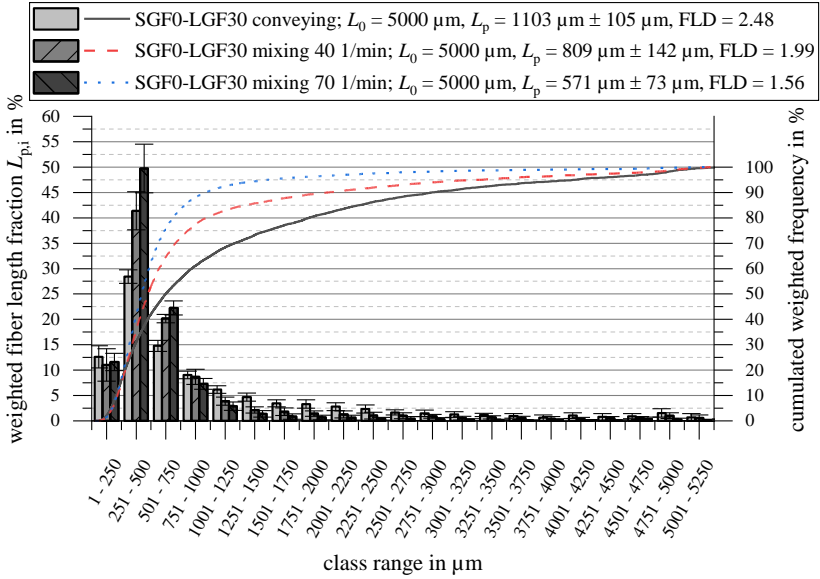


Figure 5-43: Weighted average fiber length for PF-SGF0-LGF30 using mixing element [26]

For all measurements, the initial fiber length  $L_0$  is given in the Figures. For PF-SGF0-LGF30, the weighted average fiber length in the molded part is reduced from  $L_p = 1103 \mu\text{m}$  for the conveying screw tip to  $L_{p, 40 \text{ 1/min}} = 809 \mu\text{m}$  and to  $L_{p, 70 \text{ 1/min}} = 571 \mu\text{m}$  for the Maddock mixing element at  $n = 40 \text{ 1/min}$  and  $n = 70 \text{ 1/min}$ , respectively. The fiber length measurement results show that the frequency of fibers in the length classes from  $L = 251 \mu\text{m}$  to  $L = 750 \mu\text{m}$  is the highest for the mixing element with the high plasticizing screw speed. For all classes  $L > 751 \mu\text{m}$ , the conveying screw tip results in the highest fraction. The cumulative frequency curves in Figure 5-43 confirm these results. For the conveying element, 80 % of all fibers have a weighted length below  $L_{p,80} = 1853 \mu\text{m}$ . For the mixing element, this threshold is reduced to  $L_{p,80} = 962 \mu\text{m}$  and  $L_{p,80} = 680 \mu\text{m}$  for the two chosen screw speeds. The ratio  $\text{FLD} = L_p/L_n$ , which is an indirect measure for the fiber dispersion quality, is also reduced when using the mixing element. At the highest screw speed setting that was investigated,  $\text{FLD}_{\text{mix},70 \text{ 1/min}} = 1.56$  indicates a good fiber dispersion and bundle opening. [26]

Analogous measurements were carried out for the PF-SGF0-LGF44.5 and PF-SGF16-LGF14 formulations, see Figure 5-44 and Figure 5-45. For both formulations, a decrease in weighted average fiber length and a decrease in FLD is measured when using the mixing element and when increasing the plasticizing screw speed. The difference is less pronounced for the PF-SGF16-LGF14 mixture formulation compared to the pure long fiber formulations. When comparing the two pure long fiber formulations PF-SGF0-LGF44.5 and PF-SGF0-LGF30, it is notable that the weighted average fiber length tends to be higher for the higher fiber content formulation.

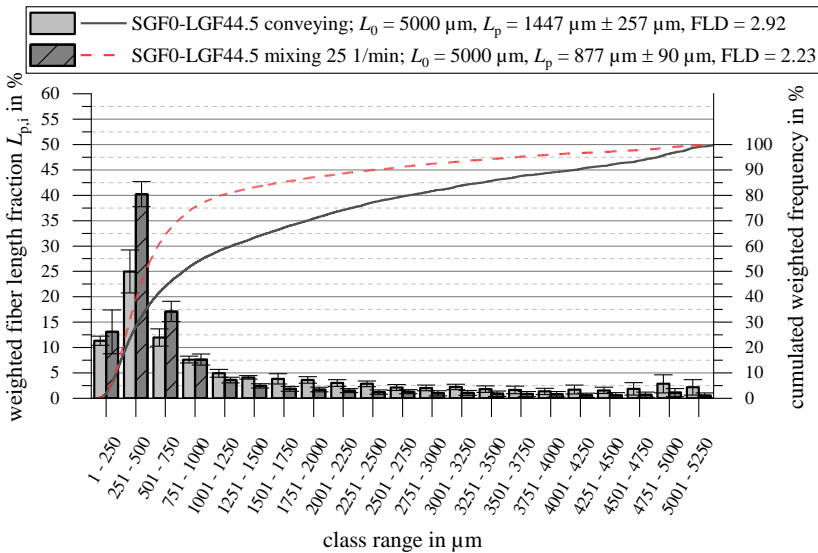


Figure 5-44: Weighted average fiber length for PF-SGF0-LGF44.5 using mixing element

For all formulation and parameter settings, the FLD decreases with decreasing long glass fiber content. For the PF-SGF16-LGF14 mixture formulation,  $\text{FLD}_{\text{mix},70 \text{ 1/min}} = 1.40$  is in the same range as for pure short fiber formulations, which indicates a good fiber dispersion.

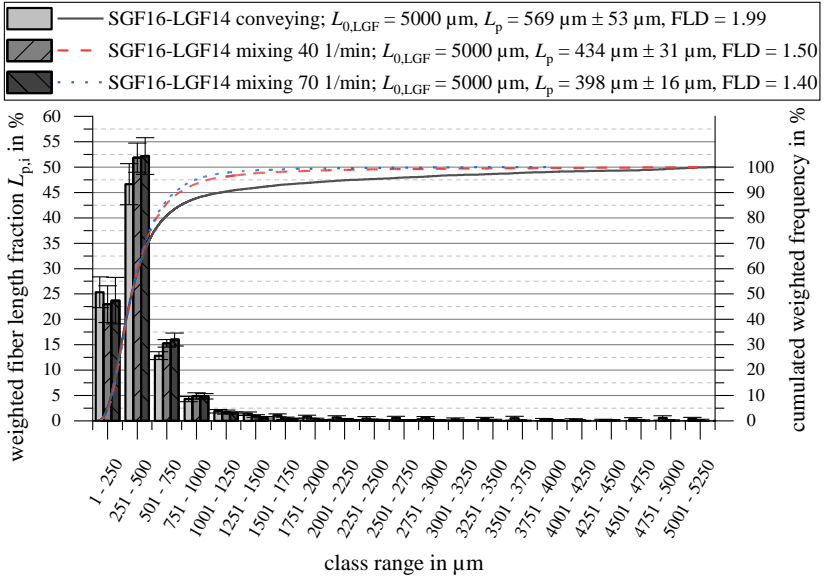


Figure 5-45: Weighted average fiber length for PF-SGF16-LGF14 using mixing element

When using a pure short fiber compound, the fiber shortening is even less. Figure 5-46 shows the fiber length distribution for parts molded from a PF-SGF28.5-LGF0 material and compares it to the fiber length distribution of the granulate.

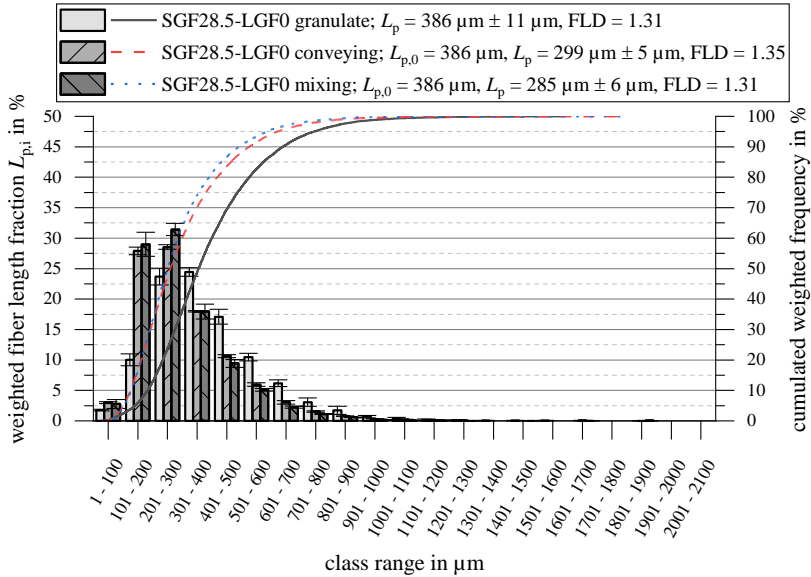


Figure 5-46: Weighted average fiber length for PF-SGF28.5-LGF0 using mixing element

For both screw geometries, a fiber shortening by  $\Delta L_p \approx 80 \mu\text{m} \dots 100 \mu\text{m}$  compared to the granulate takes place. No significant change in the ratio  $\text{FLD} = L_p/L_n$  occurs during the injection molding process.

## 5.5 Mechanical characterization

### 5.5.1 Mechanical characterization of SGF compounds

The mechanical properties of parts molded with the manufactured SGF molding compounds were determined regarding their tensile and Charpy impact characteristics, see Figure 5-47. Since they serve as the baseline for assessing the LGF samples, the conventional thermoset injection molding process with the conveying screw geometry was chosen. In subfigure (a) of Figure 5-47, the  $0^\circ$  orientation relative to the material flow direction is shown, in subfigure (b) the  $90^\circ$  orientation. The cutting pattern with the specimen location is shown in Figure 3-4.

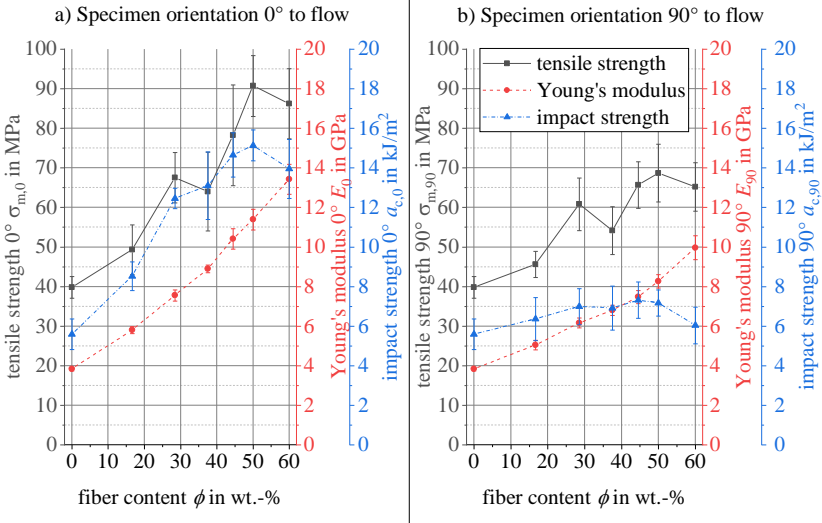


Figure 5-47: Tensile and impact properties of SGF compounds with fiber content  $\phi = 0 \dots 60$  wt.-%

For both specimen orientations, an approximately linear increase in tensile modulus with increasing fiber content can be observed. The modulus for the  $0^\circ$  orientation is approximately 25 % higher than in the  $90^\circ$  orientation. The curve shape for the tensile strength is similar for both orientations as well. It reaches a plateau at fiber contents of around  $\phi > 45$  wt.-%. Again, the  $0^\circ$  specimens are stronger than their  $90^\circ$  equivalents, reaching tensile strength values of  $\sigma_m \approx 90$  MPa. The Charpy unnotched impact strength also plateaus at higher fiber contents above  $\phi = 45$  wt.-% in  $0^\circ$  orientation. For the impact strength perpendicular to the flow, no significant difference for the varying fiber content values is found. Instead, the impact strength stays between  $a_c = 6$  kJ/m<sup>2</sup> and  $a_c = 7$  kJ/m<sup>2</sup> for all fiber contents.

## 5.5.2 Quasistatic mechanical properties

### 5.5.2.1 Mixing during the injection phase

The implemented measures for improving the dispersive and distributive mixing during the injection phase were evaluated by molding plates with a total fiber content of  $\phi = 30$  wt.-% at three different combinations of AGF and LGF (PF-SGF28.5-LGF0, PF-SGF0-LGF30 and PF-SGF16-LGF14).

The results for the tensile strength are shown in Figure 5-48. First, every dispersive and distributive mixing element was evaluated individually. Subsequently, combinations of the mixing elements were tested to further increase the mixing power. Every combination was tested for each of the three material formulations. The error bars represent  $\pm 1$  standard deviation.

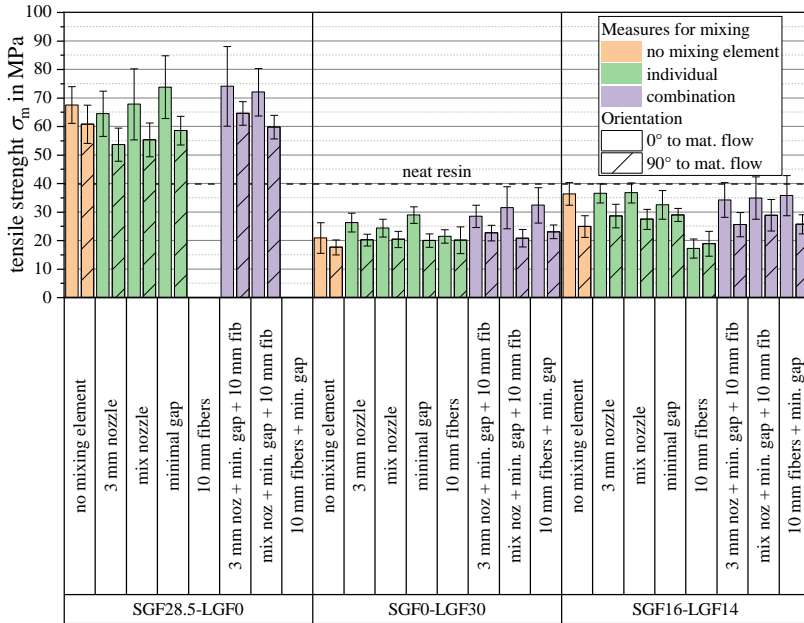


Figure 5-48: Tensile strength results for “mixing during injection phase” process development

Since the formulation PF-SGF28.5-LGF0 does not contain any long fibers, the corresponding columns in Figure 5-48 are left empty. All formulations with LGF have a lower tensile strength than the SGF. Additionally, the tensile strength of the plates molded with a PF-SGF0-LGF0 neat resin formulation is marked by the dashed horizontal line in Figure 5-48. Independent of the process parameter combination, all formulations containing long fibers have an average tensile strength that is below the neat resin value. The PF-SGF16-LGF14 formulation is on average on a slightly higher level than the PF-SGF0-LGF30 formulation, but still below the neat resin and significantly below the SGF compound. In general, the specimens in 0° orientation to the material flow have a higher tensile strength than those in 90° orientation. Analyzing the Young’s modulus of the test specimens shows that on

average, the formulations with LGF are slightly less stiff than the SGF formulations, but still within the standard deviation of the measurement. No significant difference in the Young's modulus is found for the parameter variations and the different dispersive and distributive mixing elements. Exemplary tensile stress-strain curves for the three formulations are compared in Figure 5-49. Both the neat resin and the PF-SGF28.5-LGF0 short fiber compound fail at a tensile strain  $\varepsilon > 1\%$ , whereas the formulations containing LGF fail at  $\varepsilon \approx 0.5\%$ .

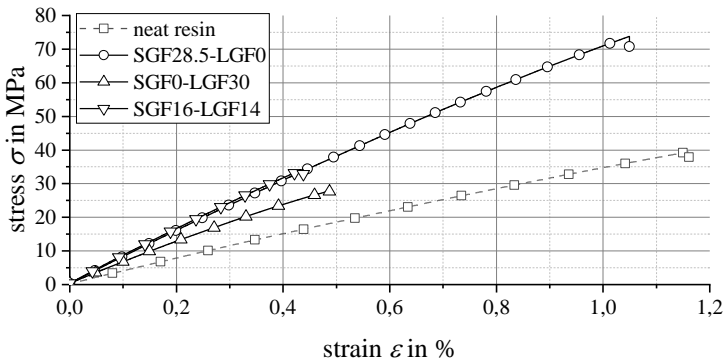


Figure 5-49: Tensile stress-strain curves for exemplary PF-SGF-LGF formulations

### 5.5.2.2 60 mm screw mixing element

For evaluating the effect of the  $d = 60$  mm screw mixing element, the focus is again set on the formulations with a fiber content of  $\phi = 30$  wt.-% and an initial long glass fiber length of  $L = 5$  mm. As described in Section 5.3.1, feeding and processing limitations of the long fiber direct injection molding process made it difficult to carry out all the desired process parameter variations at higher fiber content and fiber length values. Figure 5-50 shows the tensile strength parallel ( $0^\circ$ ) and perpendicular ( $90^\circ$ ) to the flow of material. Parts of these results have been published by Maertens et al. in [26].

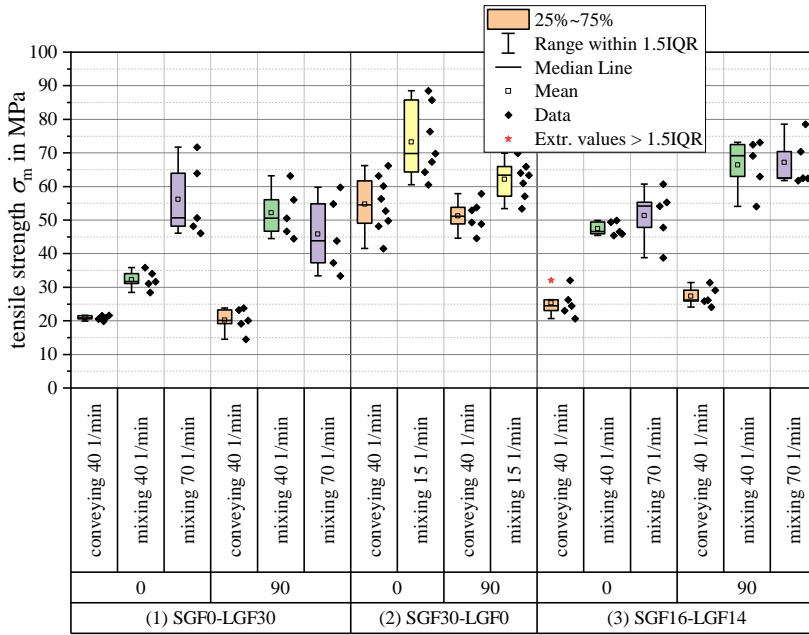


Figure 5-50: Tensile strength of 30 wt.-% specimens molded with 60 mm mixing element [26]

Switching from the conveying screw geometry to the Maddock mixing screw element significantly increases the tensile strength for all formulations and for both specimen orientations. Increasing the plasticizing screw speed when using the mixing element leads to a further increase in tensile strength for the PF-SGF0-LGF30 formulation in 0° orientation. For the other formulations and orientations, the change in tensile strength with increasing screw speed is within the standard deviation of the measurement. For most material formulation and process parameter combinations, the scattering of the measurement results also increases when using the mixing element. While the positive effect of the mixing element on the tensile strength is clearly visible from the measurement results, it must be noted that the overall highest absolute strength value for the formulations with a fiber content of  $\phi = 30$  wt.-% is still reached by the short fiber material PF-SGF28.5-LGF0. Analyzing the Young's modulus of the test specimens shows that a slight increase in stiffness can be observed when using the mixing element and when increasing the plasticizing screw speed, see Figure 5-51 below.



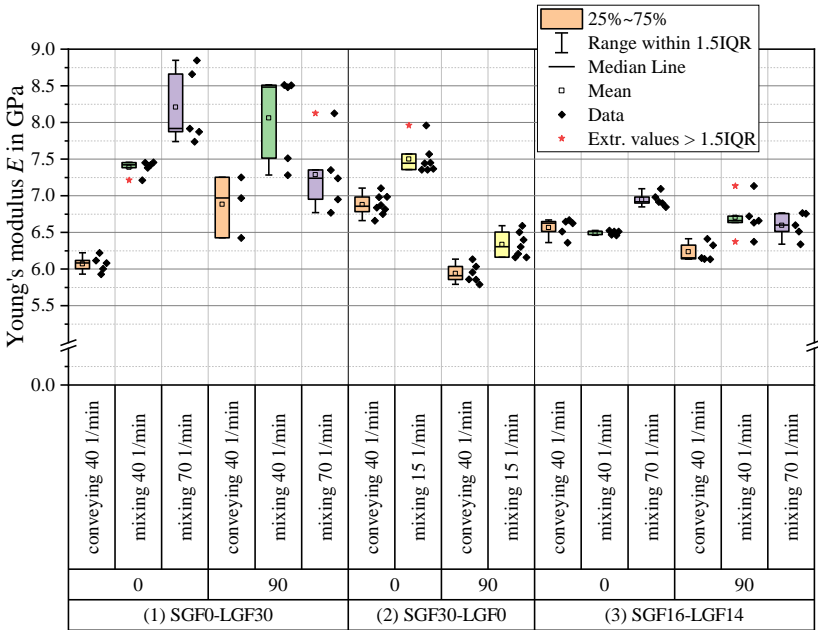


Figure 5-51: Young's modulus of 30 wt.-% specimens molded with 60 mm mixing element

The largest improvement in Young's modulus is detected for the pure long fiber formulation PF-SGF0-LGF30 with an increase by  $\Delta E = 2.5$  GPa in  $0^\circ$  orientation to the flow. All other formulations show less changes in modulus which are mostly within the uncertainty of the measurement. This means that the strong improvement in strength described above does not stem from an increase in modulus, but from an increase in tensile strain at break  $\varepsilon$  as shown in Figure 5-52.

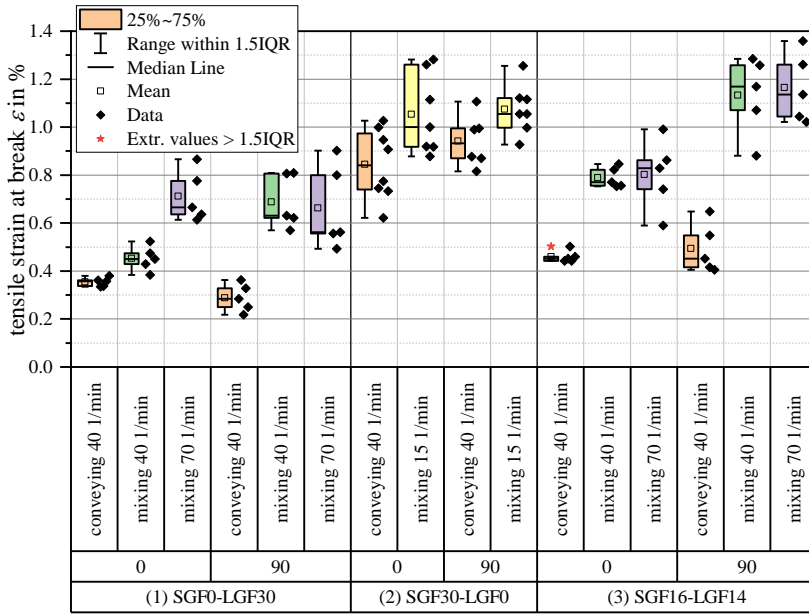


Figure 5-52: Tensile strain at break of 30 wt.-% specimens molded with 60 mm mixing element

For both formulations containing long glass fibers, PF-SGF0-LGF30 and PF-SGF16-LGF14, the tensile strain at break is significantly increased by using the mixing element. The pure short fiber formulation also benefits from the mixing element, but to a lesser extent which is still within the standard deviation of the measurement. Again, the highest absolute values for  $\epsilon$  are obtained when processing a pure short fiber molding compound.

The commercially available long fiber granulate Porophen® 9201L12a [119] was processed in the long fiber injection molding process using both the 60 mm mixing element and the conveying screw geometry. The granulate was fed into the long fiber barrel using the sidefeed. Figure 5-53 shows the tensile testing results in comparison to the long fiber direct thermoset injection molding process with a fiber content of  $\phi = 30$  wt.-%.

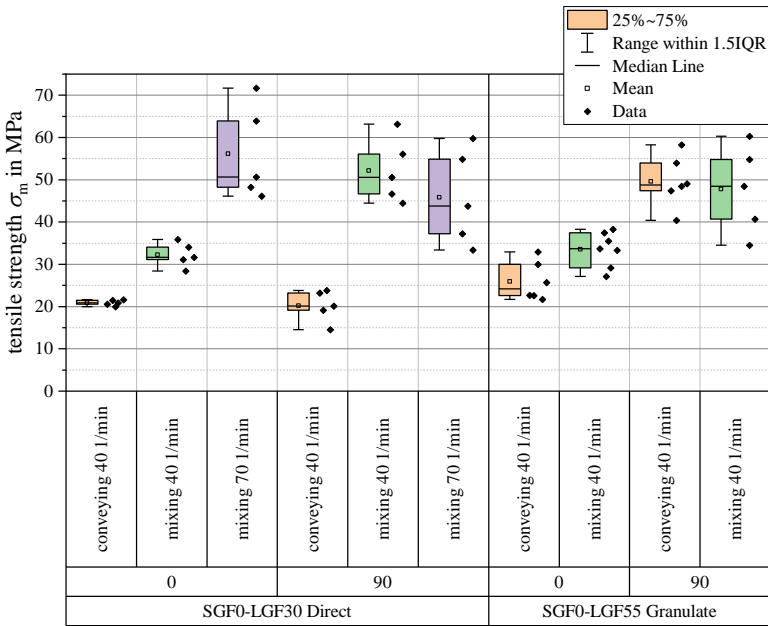


Figure 5-53: Comparison of tensile strength for PF-SGF0-LGF55 long fiber granulate and PF-SGF0-LGF30 direct process

For the long fiber granulate, no clear tendency is visible from the results, neither for the specimen orientation nor for the screw geometry. The tensile strength is higher in 90° orientation compared to 0° for both screw geometries. The tensile strength values are significantly below the datasheet value of  $\sigma_m = 160$  MPa. They are in the same range as the tensile strength of the PF-SGF0-LGF30 direct process, despite the higher fiber content.

### 5.5.2.3 Circular tensile test specimen

Figure 5-54 shows the pseudo Young's modulus  $E^*$  for the circular test specimens cut from plates molded from the pure SGF formulations. In the top half of the diagram, the results for the conveying screw are shown. Since the modulus values are centrally symmetric, only the values for 0° to 180° are shown. The bottom half of the diagram depicts the same formulations, but which were molded using the mixing element. Additionally, the ratio  $b/a$  of the ellipses' major and minor axes for each material and process parameter combination is given. The pseudo Young's modulus  $E^*$  increases with the

fiber content and has an elliptical shape. In  $0^\circ$  orientation to the material flow, it is higher than in  $90^\circ$  orientation. This effect is more pronounced for the formulations with a higher total fiber content. With the screw mixing element, the anisotropy increases for the highest fiber content values of  $\phi = 50$  wt.-% and  $\phi = 60$  wt.-%. Apart from those two formulations, there is no significant influence of the mixing element on the anisotropy of the SGF specimens.

The same analysis is carried out for the pure long fiber formulations, see Figure 5-55. Due to the processing constraints, the maximum achievable LGF content for the mixing element was  $\phi = 44.5$  wt.-%. For the formulations PF-SGF0-LGF30 and PF-SGF0-LGF37.5, the screw speed variation  $n$  is depicted as well. When using the conveying screw geometry, the ellipses of the pseudo Young's modulus are rather circular with a slightly higher stiffness in  $90^\circ$  orientation (perpendicular to the flow of material). Switching to the mixing element increases the absolute value of the pseudo Young's modulus for all formulations. The higher screw speeds during plasticization lead to a further increase of the pseudo Young's modulus.

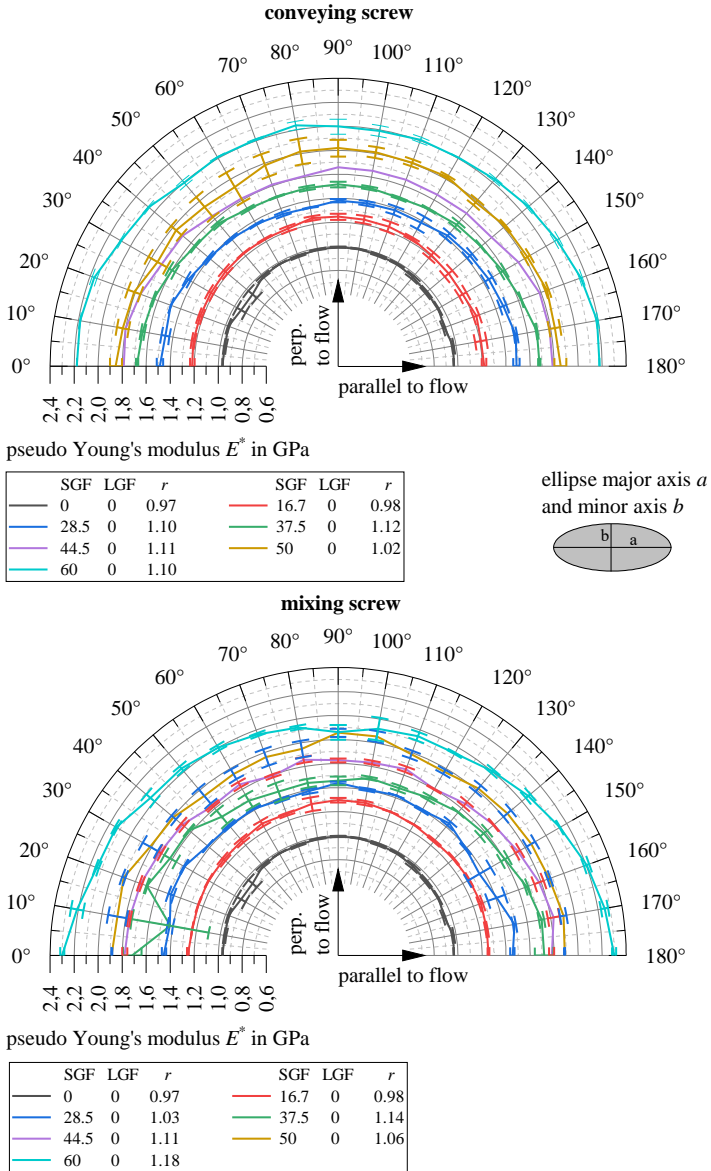


Figure 5-54: Pseudo Young's modulus for circular test specimens made from SGF formulations

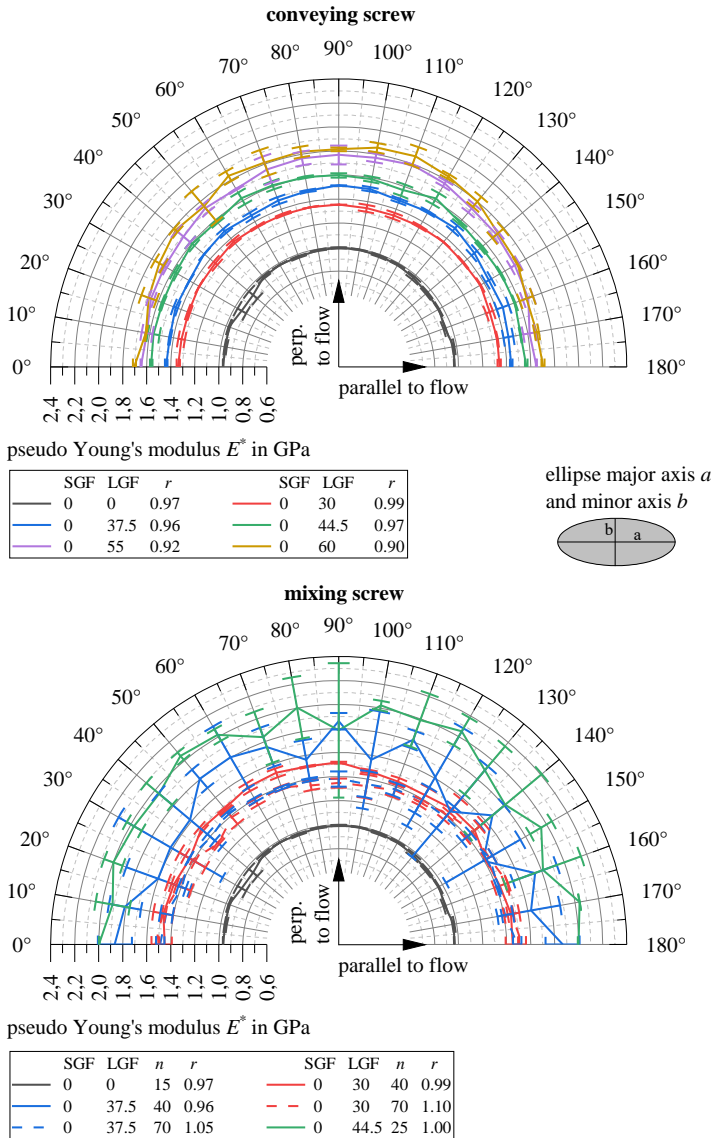


Figure 5-55: Pseudo Young's modulus for circular test specimens made from LGF formulations

The axes ratio  $r = b/a$  of the ellipses is plotted in Figure 5-56. A value of  $r = 1$  describes a circular shape, whereas  $r \neq 1$  stands for anisotropic proper-

ties. Only pure LGF or pure SGF formulations are shown, no SGF-LGF mixture formulations.

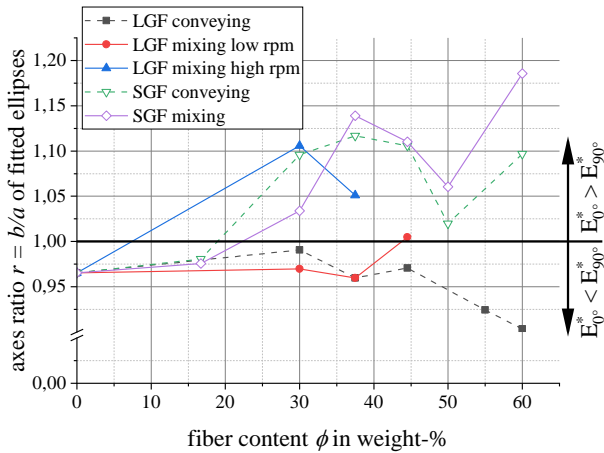


Figure 5-56: Ellipse axes ratio for SGF and LGF formulations

The LGF formulations have an axes ratio close to  $r = 1$  when they are processed with the conveying element or with the mixing element at low plasticizing screw speeds. For the mechanical behavior of the specimens this means an almost isotropic behavior. The SGF formulations (both conveying and mixing) as well as the LGF formulations processed with a high screw speed and the mixing element have an axes ratio of  $r > 1$ , which means that their pseudo Young's modulus  $E^*$  in  $0^\circ$  orientation is higher than in  $90^\circ$  orientation to the material flow.

## 5.5.3 Dynamic mechanical properties

### 5.5.3.1 Charpy unnotched impact

As an overview, Figure 5-57 shows the Charpy unnotched impact strength  $a_c$  of SGF and LGF material formulations as a function of the fiber content for both specimen orientations. Only pure SGF and pure LGF formulations are considered, no mixture formulations.

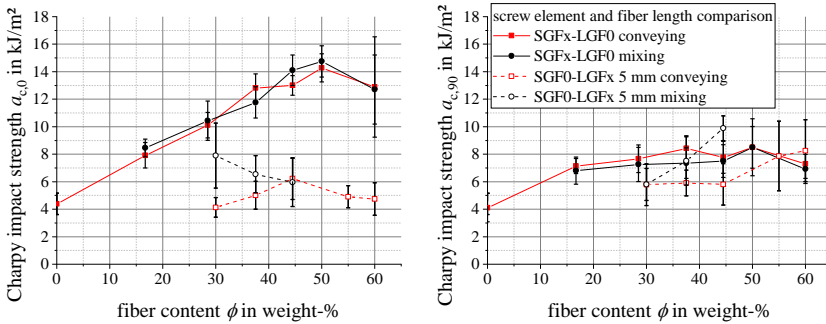


Figure 5-57: Impact strength as a function of fiber content in 0° and 90° orientation

In 0° orientation to the flow direction, the impact strength of the SGF formulations increases approximately linearly up to a fiber content of  $\phi = 50$  wt.-% after which it plateaus or decreases slightly. In 90° orientation, the influence of the fiber content on the impact strength is lower than in 0° orientation. Except for the neat resin, almost all average values are in a range of about  $a_{c,0} = 6$  kJ/m<sup>2</sup> to  $a_{c,90} = 8.5$  kJ/m<sup>2</sup>, and thus below the values in 0° orientation. For the short fiber formulations, no significant difference between the conveying screw tip and the mixing element is found. The LGF formulations have a generally lower impact strength in 0° orientation than the SGF materials. If they are molded with the conveying screw geometry, their impact strength does not exceed that of the neat resin sample. When molding the LGF formulations with the mixing element, the impact strength slightly increases in 0° orientation, however it is still lower than for the SGF materials. In 90° orientation, the usage of the mixing element leads to an increase of the average impact strength of the LGF material up to the level of the SGF formulations. However, all values are subject to a wide measurement variation. Figure 5-58 gives a more detailed comparison for the specimens with total fiber content of  $\phi = 30$  wt.-%.



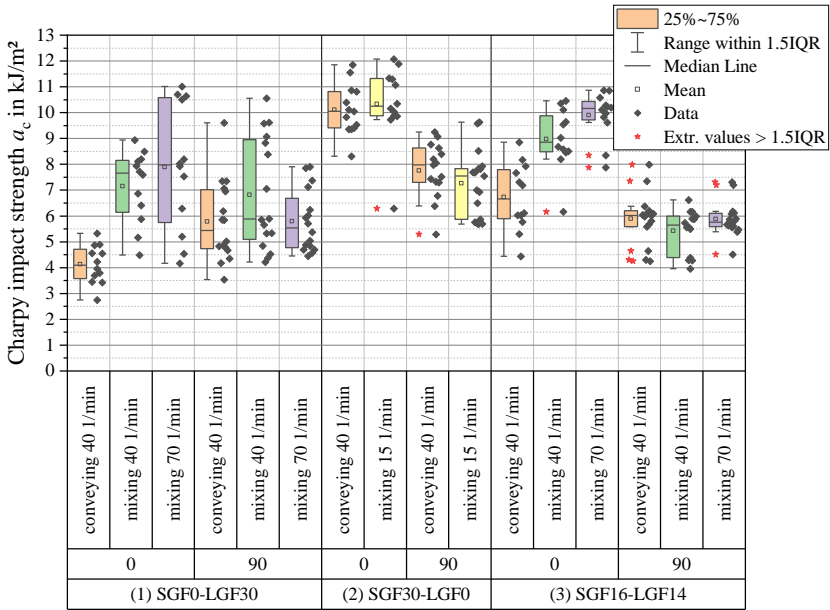


Figure 5-58: Charpy impact strength of 30 wt.-% specimens molded with 60 mm mixing element

The influence of the thermoset Maddock screw mixing element on the impact strength of the two formulations containing LGF is visible. In both cases, the impact strength in 0° orientation increases when switching from the conveying to the mixing element and – to a smaller extend – with a higher screw speed when using the mixing element. In 90° orientation and for the SGF materials, no effect is observed. The overall scattering of the measurement results is large and tendentially increases even further when using the mixing element, especially for the pure LGF formulation PF-SGF0-LGF30.

### 5.5.3.2 Puncture impact

During the puncture impact testing, two different shapes of the force-displacement curves were observed. Figure 5-59 shows representative curves for the two shapes in direct comparison. Both curves are shown in their raw shape and after the smoothing signal processing step that is described in Section 3.2.5.

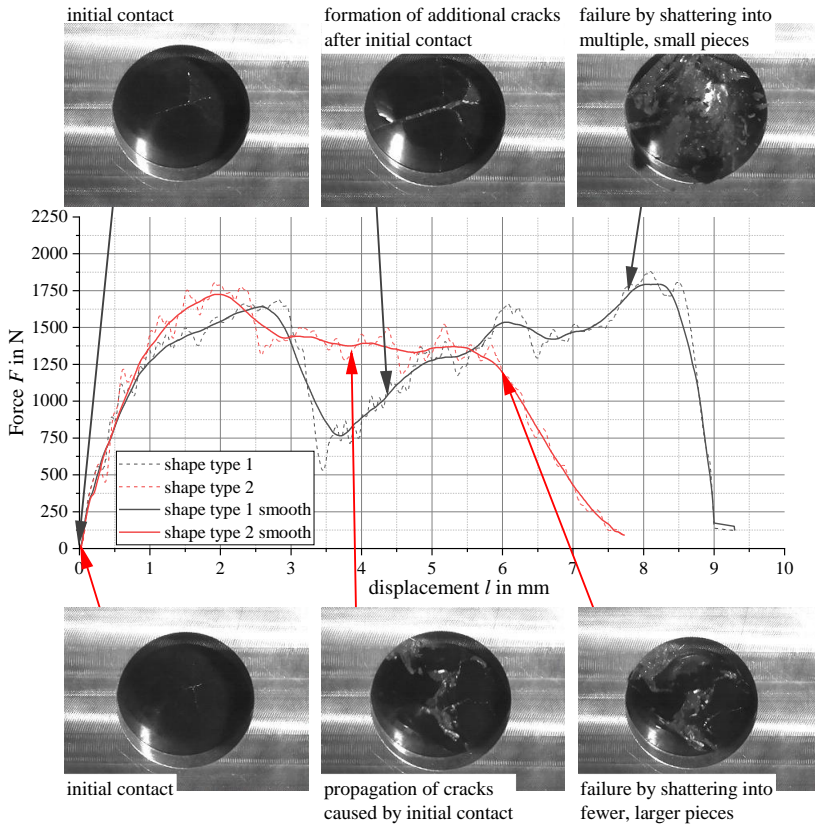


Figure 5-59: Comparison of typical force-displacement curves for puncture impact test

The failure behavior is illustrated with images from the high speed camera. The images were taken from below and show the crack development when the impactor hits the specimen. A PF-SGF0-LGF30 formulation using the conveying screw geometry was used. The first curve shape is characterized by an initial rise in force, followed by a decrease and a second rise (shown in black in Figure 5-59). In contrast to that, curve shape 2 (red) does not show the second rise of the impact force. Due to the lack of the second rise in force, the curve shape 2 drops at a smaller total displacement value, which results in a lower total failure energy value after the integration of the curve. In both cases, initial cracks develop after the first contact of the impactor with the specimen surface. For force curve shape type 1, additional cracks are formed after a few millimeters of impactor displacement. The final failure of

the part is by shattering into many small pieces, both caused by the initial and the secondary cracks. In the case of curve shape 2, the initial cracks grow and lead to the final failure of the part. Secondary cracks do not play a role in the failure. Consequently, the part shatters into fewer, larger pieces. No significant correlation between the type of the force displacement curve shape and the specimen location, the material formulation or the process parameter settings was found. Since both curve shape types represent the actual failure behavior of the individual specimen, it was decided not to exclude any of them from the further analysis.

Figure 5-60 shows the puncture impact energy for SGF and LGF formulations with both screw geometries. For the SGF materials molded with the conveying screw geometry, no significant influence of the fiber content on the puncture impact energy is found. With the mixing element, there is an increase in puncture impact energy with increasing fiber content up to  $\phi = 44.5$  wt.-%, after which the puncture energy drops slightly. A larger scattering of the samples is observed when using the mixing element. For the LGF formulations, the puncture impact energy increases slightly with increasing fiber content up to  $\phi = 50$  wt.-% for the conveying screw geometry. When using the mixing element the average value of the puncture impact energy increases. As with the SGF materials, the scattering range of the results increases when using the mixing element.

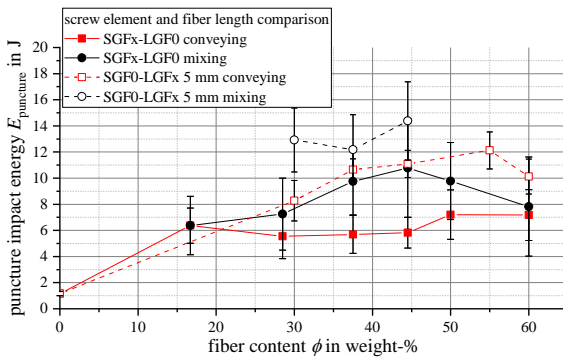


Figure 5-60: Puncture impact energy overview for SGF and LGF formulations

The direct comparison of samples with a total fiber content of  $\phi = 30$  wt.-% shows that the formulations containing LGF profit the most from using the mixing element, see Figure 5-61.

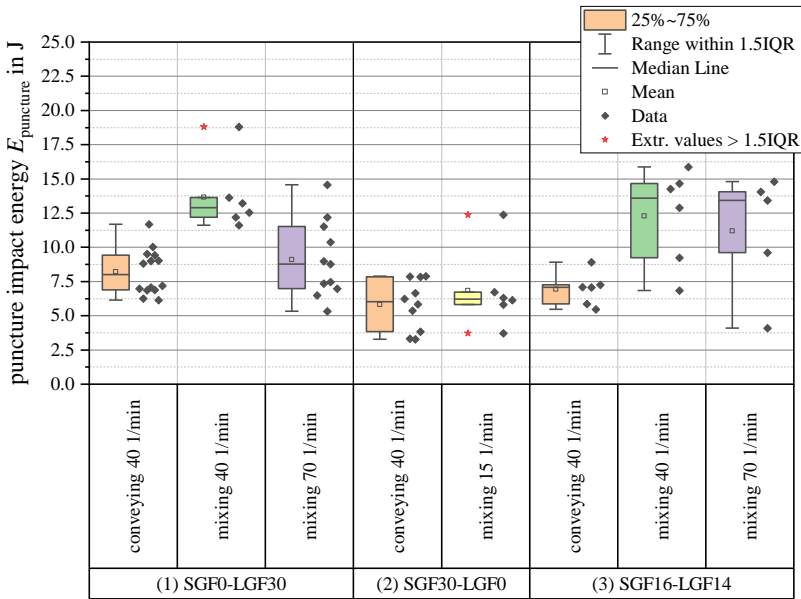


Figure 5-61: Puncture impact energy of 30 wt.-% specimens with 60 mm mixing element [26]

Both for the PF-SGF0-LGF30 and the PF-SGF16-LGF14 material, the puncture impact energy increases significantly when using the mixing element. An increase in screw speed with the mixing element has no significant effect: The average value of puncture impact energy decreases, but within the scattering of the measurement. Compared to the SGF material, both formulations that contain LGF have a significantly higher puncture impact energy when using the mixing element. This conclusion contrasts with the values of the Charpy impact strength, which was highest for the PF-SGF28.5-LGF0 formulation. [26]

## 5.6 Fracture analysis using scanning electron microscopy

### 5.6.1 Tensile test specimens

The subsequent Figure 5-62 and Figure 5-64 show SEM images of the fracture surfaces of tensile test specimens made from PF-SGF28.5-LGF0 and

PF-SGF0-LGF55 (granulate). The parts molded with the conveying screw are shown in the upper half, the ones with the mixing element in the bottom. The left image is taken from the core layer, whereas the right images show one of the skin layers. In the core, the fibers are oriented perpendicular to the flow, which corresponds to an orientation in the plane of the image. Consequently, the fibers in the skin layers are oriented in the direction of the material flow, which corresponds to an orientation perpendicular to the plane of the image. As Figure 5-62 shows, the short glass fibers in the PF-SGF28.5-LGF0 formulation are well dispersed and impregnated by the resin. No significant difference regarding the fiber dispersion can be found when comparing the images for the conveying screw to those for the mixing element. The different fiber orientation in the skin and core layers is clearly visible for both screw layouts.

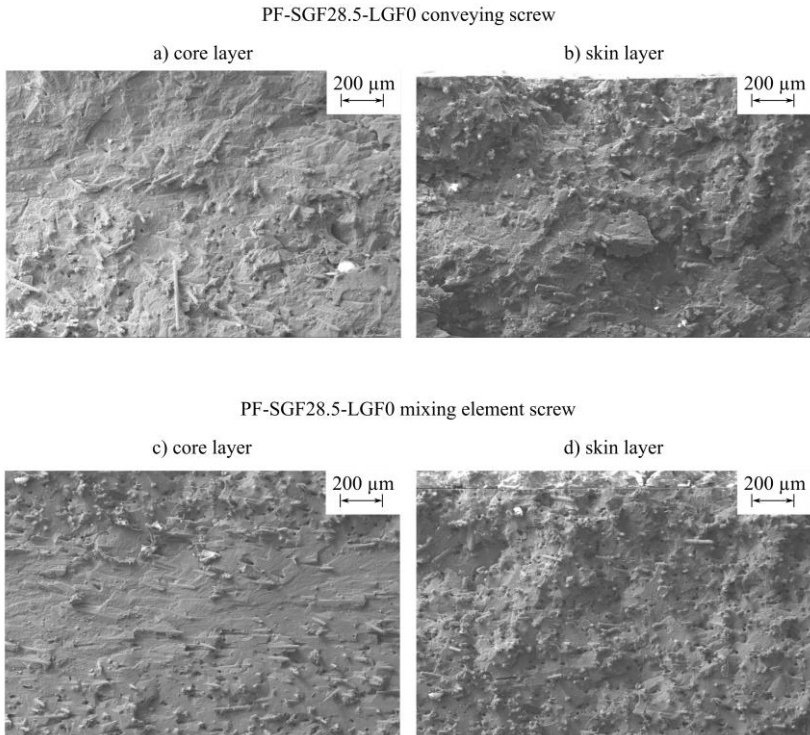


Figure 5-62: SEM for PF-SGF28.5-LGF0 tensile test specimens with conveying and mixing screw

Images taken at higher resolutions (such as Figure 5-63) show a good adhesion of the phenolic resin to the fibers, which is visible by resin residue on the fiber surfaces. Despite the presumably good adhesion, the fibers were pulled out of the matrix during failure. This can be seen by the holes that are left in the matrix and by the resin residue on the face side of the fibers. If the face surfaces were fiber fracture surfaces, they would not have any resin residue on them.

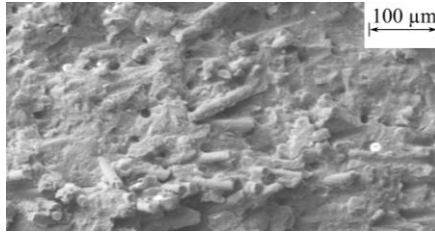


Figure 5-63: SEM detail image for PF-SGF28.5-LGF0 tensile test specimen

The fracture surface PF-SGF0-LGF55 granulate tensile test specimens is depicted in Figure 5-64. Again, the parts molded with the conveying screw are shown in the upper half, the parts molded with the mixing element are shown in the bottom.

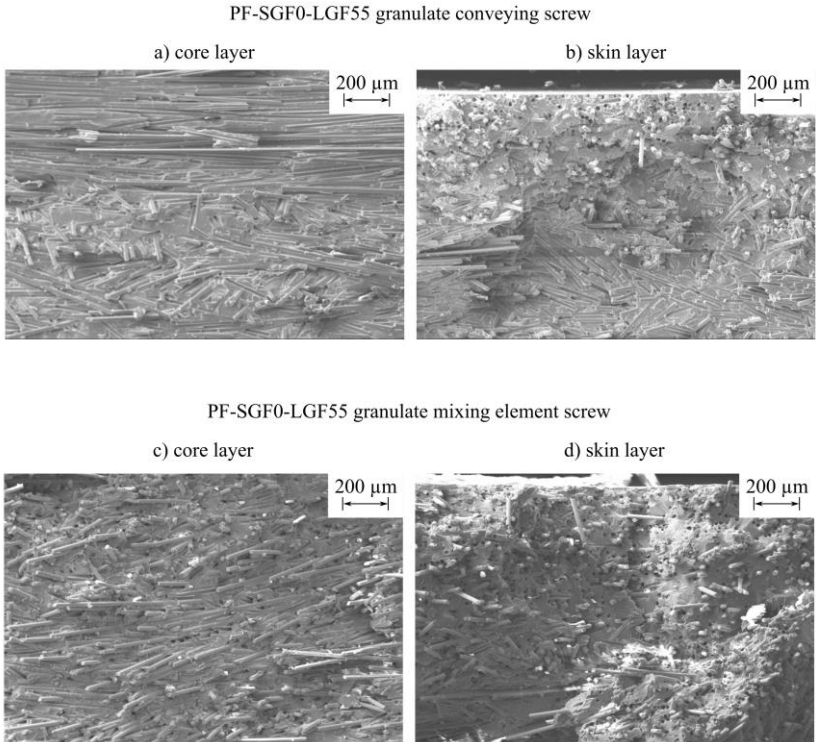


Figure 5-64: SEM for PF-SGF0-LGF55 tensile test specimens with conveying and mixing screw

The overall higher average fiber length compared to the SGF samples in the Figures above is visible. Comparing the mixing element screw with the conveying screw shows that the number of fiber bundles is reduced by using the mixing element. A skin and core layer structure is visible for both screw configurations. Comparing the detail image of the fracture surface for the long fiber granulate test specimen in Figure 5-65 to the one for the short fiber sample (see Figure 5-63 above) shows smooth, blank fiber surfaces.

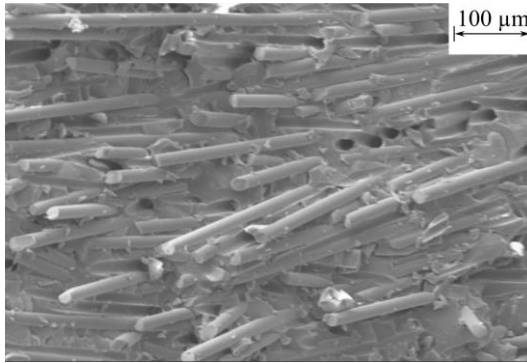


Figure 5-65: SEM detail image for PF-SGF0-LGF55 granulate tensile test specimen

The fibers were pulled out of the fracture surface, which is visible by the holes and the imprints. In contrast to the SGF, the face surfaces of the LGF are mostly smooth without any resin adhering to them. To sum up the SEM fracture surface analysis for the SGF and LGF granulate samples, it is concluded that the LGF granulate samples have a worse fiber-matrix adhesion than the SGF materials. This is especially remarkable, since the granulate material is a commercially available molding compound that is advertised by the material supplier with its “high mechanical strength” of  $\sigma_m = 160$  MPa [119], which is more than three times as high than the measured values.

## 5.6.2 Charpy test specimens

Analyzing the fracture surface of the PF-SGF0-LGF55 long fiber granulate test specimens from the Charpy impact testing does not reveal any additional information compared to the tensile test specimens shown above. For this reason, the focus of this section is on comparing the SGF specimens to the LGF specimens manufactured in the long fiber direct thermoset injection molding process, see Figure 5-66. These SEM images have been published by Maertens et al. in [26] previously.



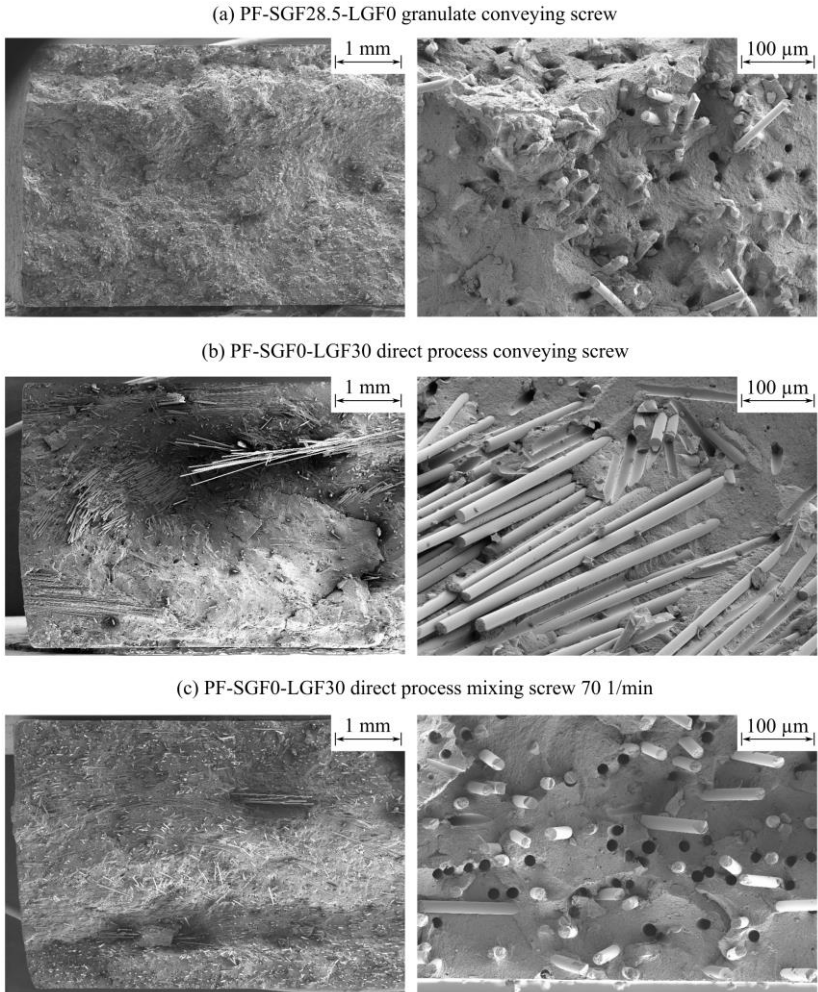


Figure 5-66: SEM for SGF granulate and LGF direct process Charpy test specimens [26]

Figure 5-66 shows a comparison between the PF-SGF28.5-LGF0 sample (conventional conveying screw) and the PF-SGF0-LGF30 sample (with conveying screw and mixing element). The SGF material shows the known skin and core layer structure as well as the good fiber-matrix adhesion, which is again visible by the resin residues on the fiber surface. Fibers are pulled out of the fracture surface with resin residues on the face sides of the fibers. The holes in the matrix created by pulling out the fibers are frayed and

irregular. Comparing the LGF specimens with conveying screw and mixing element shows a strong reduction in the number of fiber bundles. The specimen manufactured with the conveying screw has a very inhomogeneous fracture surface with fiber-rich bundle regions and resin-rich regions where almost no fibers are present. By using the mixing element, the number of bundles is reduced significantly and a more homogeneous distribution of the fibers across the sample is achieved. Additionally, a skin and core layer structure becomes visible, which was not detectable with the conveying screw setup. The overall visual impression indicates that the fibers have been shortened by using the mixing element, which is in accordance with the fiber length measurement results shown in Section 5.4.6. [26]

Analyzing the detail SEM images on the right side of Figure 5-66 reveals a weak adhesion of the resin to the LGF that were used in the long fiber direct thermoset injection molding process. The fiber surfaces are blank and smooth, and fibers are pulled out of the fracture surface leaving sharp and well-defined holes in the matrix. The mixing element improved the dispersion of the fibers and reduced the number of bundles, but no differences are observed regarding the fiber-matrix adhesion. The overall visual impression of the fiber-matrix adhesion is comparable to the PF-SGF0-LGF55 granulate. It is remarkable that a high number of fibers has resin residues on their face sides, which indicates that the resin adhesion there is significantly stronger than at the fiber circumference. Looking at the detail images of the fiber bundles in the PF-SGF0-LGF30 specimen (Figure 5-66 middle, right) it seems that despite the presence of bundles, each individual fiber is wetted with the resin. This indicates that the resin can impregnate the fiber bundles at some stage of the molding process. Figure 5-67 shows a comparison of the conveying screw (a) and the mixing element (b) for the highest fiber content that was processable with the mixing element, which was  $\phi = 44.5$  wt.-%. The image of the fracture surface for the conveying screw part shows a high number of fiber bundles. The number of fiber bundles is reduced when using the mixing element, but there are still bundles remaining. Comparing the PF-SGF0-LGF44.5 formulation to the PF-SGF0-LGF30 formulation shows that the fiber bundles are reduced in both instances, but to a lesser extend for the higher fiber content value.

## PF-SGF0-LGF44.5 direct process

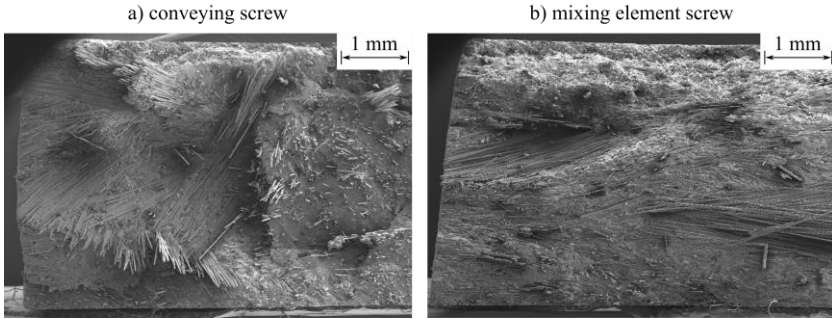
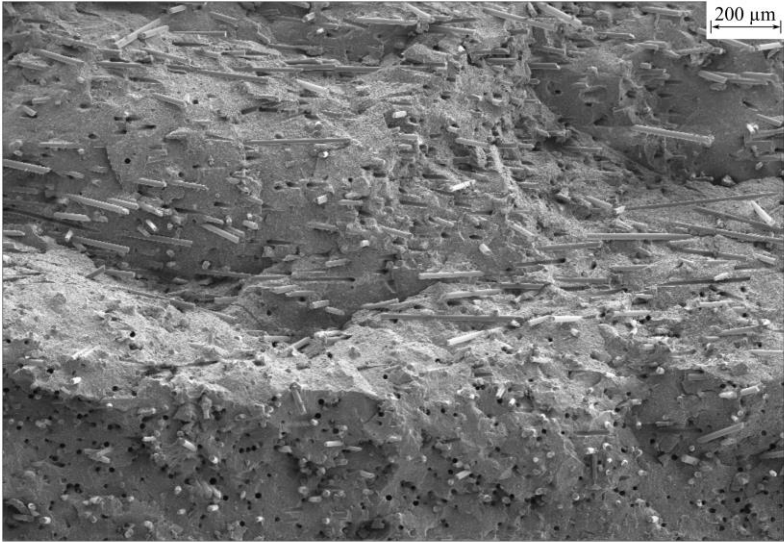


Figure 5-67: SEM for PF-SGF0-LGF44.5 direct process with conveying and mixing screw

The difference in fiber-matrix adhesion between the SGF and the LGF in the direct injection molding process is especially visible when investigating the mixture formulation PF-SGF16-LGF14, see Figure 5-68. These samples contain both types of fibers, but it is possible to distinguish between them using fiber diameter difference of  $D_{\text{SGF}} = 13 \mu\text{m}$  compared to  $D_{\text{LGF}} = 17 \mu\text{m}$ . The images in the bottom row of Figure 5-68 show that if the SGF and the LGF are molded simultaneously in the exact same part, the adhesion of the resin to the SGF is stronger. The overall visual impression of the panoramic image in Figure 5-68 top is that the LGF fiber bundles are opened and that a homogeneous distribution of SGF and LGF is present. The skin and core layer structure is visible as well.

PF-SGF16-LGF14 mixing screw



PF-SGF16-LGF14 mixing screw detail images

- ①  $D = 13 \mu\text{m}$  SGF
- ②  $D = 17 \mu\text{m}$  LGF

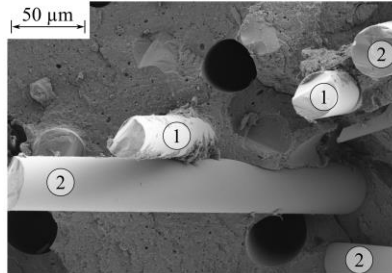
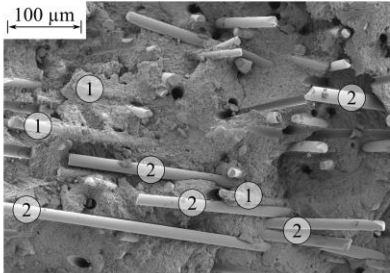


Figure 5-68: SEM for PF-SGF16-LGF14 formulation

## 6 Discussion

### 6.1 Compounding of short fiber-reinforced phenolic resins

Compared to commercially available phenolic molding compounds, adjustments were made to the material formulation (fiber content) and the manufacturing process (lab scale granulation with a cutting mill). However, it should be noted that these adjustments were made based on experience and intuition, and that the compounding process has proven to work well with them. During the compounding of the base material for the long fiber direct thermoset injection molding process, a lower SGF content was required so that the later addition of LGF was facilitated. Adjusting the extruder parameters in a suitable way to lower the degree of cure after the compounding allows for a softer flow, a lower melt viscosity and possibly enables a longer residence time at higher temperatures while still being moldable.

Since the conventional methods for determining the flow-hardening behavior (Section 2.2.1) are not established for low-filled and unfilled thermoset molding compounds, another method for steering the energy input into the resin was required. This was established using the specific mechanical energy input SME. The developed method works sufficiently well, but has its limits towards lower fiber contents below  $\phi = 20$  wt.-%. In this fiber content range, it was not possible to introduce as much energy into the resin as it was desired by adjusting the screw speed and the material throughput. To overcome this limitation, changes to the extruder screw layout would have been necessary. However, as Methe and Gehde have shown, extruder screw layout changes between trial runs [229] make it impossible to compare them using the SME. For this reason, the same screw layout was maintained for all SGF formulations within this thesis and the limitations were accepted. Using only one screw layout for the wide range of different fiber contents means that only throughput and screw speed could be used as parameters for adjusting the SME to the required value. Especially for the formulations with a low fiber content or no fibers at all, the required energy input could not be achieved, because either the maximum extruder speed or the lowest feasible

throughput was reached. However, the large deviation of the total heat of reaction  $\Delta H_R$  for these formulations (see Section 5.1.2) cannot be explained by the difference in SME alone. Other factors, such as a higher heat conductivity due to the higher apparent density and the consequently better cooling might play a role. In general it can be concluded that the basic trend for  $\Delta H_R$  is in accordance with the calculated values for the specific mechanical energy input during compounding, with individual deviations which cannot be explained by the extruder settings alone. However, the injection molding trials were not negatively affected by them.

The fiber length measurement results have shown that with increasing fiber content, the average fiber length in the compound decreases in the twin-screw extrusion process (Sections 5.1.1 and 5.1.2). Most literature results either describe a slight decrease of the residual fiber length with increasing fiber content [230,231] or observe only an minor influence [232]. However, the range in which the fiber content was varied in the cited studies was smaller than  $\Delta\phi = 20$  wt.-% compared to  $\Delta\phi = 60$  wt.-% here. It is assumed that an increase in fiber-fiber and fiber-wall interactions due to the higher number of fibers in the polymer leads to the stronger fiber shortening during the compounding. The tendentially lower remaining heat of reaction  $\Delta H_R$  for the formulations with a higher fiber content also indicates an increased resin viscosity, which causes increased fluid-fiber interactions and a stronger fiber shortening.

The results of the mechanical characterization of the SGF molding compound are in accordance with literature findings by Thomason et al. [13,172,233]. At a comparable fiber content, the tensile strength is approximately 25 % lower than the datasheet values provided by the manufacturer for the compound Vyncolit® X6952 [46], on which the chosen formulation is based. This deviation is most likely caused by two effects. First, waterjet-cut specimens were used for the mechanical characterization within this thesis, in contrast to net-shaped injection molding specimens that were used by the material supplier for the datasheet generation. The waterjet-cut specimens have a lower surface quality compared to the net-shaped injection molded specimens. As Teller and Bergstrom [234] found out, the mechanical properties of water-jet cut tensile test specimens often have a higher scattering than net-shape injection molded specimens. According to them, sanding the cutting surfaces increased the strain at break  $\varepsilon$ , but the scattering remained high. A second aspect is the most likely lower degree of fiber orientation in

specimen direction for the specimens that were cut from plates compared to net-shape molded specimens. The micrography results have shown that close to a mold cavity wall, the fibers are oriented in the direction of the material flow. This observations has been confirmed by English as well [55]. In a net-shape, directly molded specimen, all four sides of the part are outer surfaces with wall contact, whereas in the case of plates, only the top and the bottom sides have wall contact during molding.

The most important adjustment of the material formulation compared to a conventional phenolic molding compound is that the parts produced in the long fiber thermoset injection molding process now contain two kinds of fibers, namely the short glass fibers in the granulate and the long glass fibers that are fed directly into the injection molding machine plasticizing unit. Both fiber types need to be compatible with the resin, which would ideally be achieved by using fibers with the exact same sizing. However, the sizing does not only serve the purpose of creating an adhesion between fibers and resin, but also facilitates handling and processing [235]. Since the chopped fibers for the compounding have entirely different processing requirements (free-flowing, high strand integrity, easy gravimetric dosing) than the continuous long fiber rovings (easy spreading of the roving and opening of bundles, low fuzz while guiding the roving to the chopper), it was not possible to obtain them with the same sizing. Even though the same compatibility was promised by the fiber manufacturer, the SEM images in Section 5.6 clearly show that the adhesion to the long fibers is worse than to the short fibers.

## **6.2 Long fiber thermoset injection molding process development**

As described in Section 4.2, the main limitation of the long fiber direct thermoset injection molding process is the feeding limitation of the dry-blend consisting of the SGF molding compound and the chopped long glass fibers. This limitation is caused by the 30° angle in which the sidefeed is positioned above the plasticizing unit and the dead space between the outlet of the sidefeed screws and the inlet of the injection molding screw that is created by this mounting position. There are two other direct compounding injection molding processes on the market which must overcome similar challenges.

The DCIM process by Exipnos and KraussMaffei Technologies ([129], see Section 2.3.2 for details) uses a similar angled position above the plasticizing unit of the injection molding machine for the first extruder. However, in the DCIM process, the first extruder is a single screw compounding extruder in which the polymer is mixed with additives, fillers and fibers. In contrast to the twin-screw sidefeed used in the long fiber direct thermoset injection molding process here, the polymer is melted in the compounding extruder. Consequently, the single screw extruder can build up pressure and force the molten compound through the dead space and into the injection molding screw. This pressure built-up is not possible with the type of twin-screw sidefeed and the resin-fiber dry blend that is used in the long fiber direct thermoset injection molding process. The FDC process by Arburg and SKZ ([130–132], see Section 2.3.2 for details) uses a twin-screw sidefeed, but manages to position it in a  $90^\circ$  angle to the plasticizing unit. This is made possible by the longer processing length of the FDC process compared to the long fiber direct thermoset injection molding process. For this reason, the sidefeed is positioned further away from the clamping unit of the injection molding machine and the  $90^\circ$  angle becomes possible. Positioning the sidefeed in the  $90^\circ$  angle minimizes the dead space between it and the injection molding screw and likely enables a better fiber feeding into it. With this machine layout, Arburg and SKZ manage to feed dry fibers with a length of  $L = 11.2$  mm at a fiber content of  $\phi = 30$  wt.-% into molten polypropylene [132]. Even without the challenge of the different sidefeed mounting position, feeding dry fibers into the plasticized phenolic resin has proven to be no viable alternative to feeding of the fibers together with the resin granulate, here.

As described in Section 5.3.4, the process variant using the separate granulate feed port is negatively affected by the poor fiber intake behavior. The reason for this is the adhesion of the molten molding compound to the screw. Due to the screw adhesion, the compound is not conveyed by the typical single screw melt conveying mechanism of wiping the polymer from the barrel [110,236]. Instead, the molten compound remains at its location on the screw until enough material is accumulated further upstream to push it forward. An intermittent, surge-like conveying of the material is observed. During the phases without axial molding compound material transport, the chopped fibers agglomerate in the downpipe and block it if the fiber chopper feeding rate is too high. Due to the lack of material contact with the tempered barrel,



the surface of the molten molding compound cools and becomes hard and non-sticky, further impeding the transportation and dispersion of the chopped fiber bundles. Throughout the partially filled screw flights between the fiber feeding location and the screw tip, the two mass streams molding compound and chopped long fibers remain separate instead of being mixed. In Figure 5-30, some fiber bundle residues are visible on the molding compound surface. Increasing the electric heating band set temperature at the location of the fiber feed from  $T = 80\text{ }^{\circ}\text{C}$  up to  $T = 130\text{ }^{\circ}\text{C}$  improves the fiber feeding behavior. It is suspected that the increased temperature leads to a lower viscosity and a stickier surface of the compound. The neat resin viscosity in this temperature range is approximately  $\eta = 10^3\text{ Pa s} \dots 10^5\text{ Pa s}$  (based on measurements presented in Sections 5.1.1 and 5.1.2), which is still significantly higher than the typical processing viscosity  $\eta = 200\text{ Pa s} \dots 800\text{ Pa s}$  for thermoplastic polymers [237]. Achieving an even higher processing temperature and therefore a lower viscosity of the novolac phenolic resin is not feasible, because it would lead to early curing. Consequently, fiber bundles are still visible and the overall achievable material throughput, which in turn defines the plasticizing time, remains significantly higher compared to all other process variants. A more extensive adjustment of the resin formulation would be required to achieve a lower processing viscosity while maintaining a high residence time. Using slow curing, directly hardening resol resins might be an option, because unlike the novolacs, they do not have the rapid increase in chemical reaction at the hexamethylenetetramine decomposition temperature.

A completely alternative process layout that omits the requirement for feeding chopped fibers is pulling in continuous fibers and breaking them in the injection molding screw. This process layout was investigated by Truckenmüller for thermoplastics [122] and has other challenges as well, but might be a viable alternative option to overcome the described feeding limitations.

The original intention behind the chosen long fiber direct thermoset injection molding process variants was to find an as gentle as possible process for molding parts with the highest possible fiber length. However, the results along the development route have led to an entirely opposite aim, namely the incorporation of as much shear energy input as possible without curing the thermoset resin too early in the process. The main reason for this is the high strand integrity of the chosen long glass fiber roving. The advantage of the

high strand integrity is the ease of chopping it in the fiber chopper, but this results in hard-to-open fiber bundles later in the process. The first step towards more shear energy input was the usage of mixing elements during the injection phase. These findings are plausible and within the expectations. The higher required injection pressure for the smaller 3 mm machine nozzle can be explained with its smaller cross-sectional area. Since the mixing nozzle with the dummy insert has the same diameter as the standard nozzle, no additional injection pressure consumption when using the dummy insert is observed. The injection pressure peaks visible in Figure 5-16 is likely caused by a cold plug in the long, unheated and exposed part of the nozzle. The low additional pressure requirement of  $\Delta p \approx 150$  bar when using the static mixer insert is in accordance with typical pressure drop values of  $\Delta p \approx 50$  bar ... 150 bar for thermoplastic polymers given by the mixing nozzle manufacturers [238,239]. The conclusion from these investigations is that from a processing standpoint, the dispersive and distributive mixing machine nozzles can be used in the thermoset injection molding process. However, the mechanical properties of the molded parts clearly show that the minor improvement in mechanical performance does not justify the additional processing hurdles.

Therefore, it is concluded that the fiber-matrix compound cannot be homogenized during the injection phase. Instead, a homogeneous material must be provided by the screw before the injection step. The two developed thermoset-specific mixing screw elements based on the established Maddock mixing geometry worked and fulfilled their purpose of homogenizing the fiber-matrix compound. Compared to the conventional conveying screw geometry without non-return valve and with only a very slight geometrical compression, the thermoset-specific 60 mm screw mixing element reduces the process value scatter both during the injection and the plasticizing phase of the process, especially for material formulations containing long fibers. It is assumed that the shear gaps of the mixing element reduce the backflow during the injection phase due to the higher flow resistance. This assumption is in agreement with the findings of Kruppa et al. [153,154], who found that the small gaps of their mixing element act equal or better than a standard non-return valve. Despite the higher energy input during plasticization and the consequently lower viscosity of the material in front of the screw, the backflow during injection does not increase. It is deduced that the effect of backflow reduction outweighs the effect of the lower material viscosity. To

investigate the lower process scattering with the mixing element during the plasticizing phase of the injection molding process, the back pressure and the screw position during plasticizing is analyzed, see Figure 6-1. This analysis was previously published by Maertens et al. in [26].

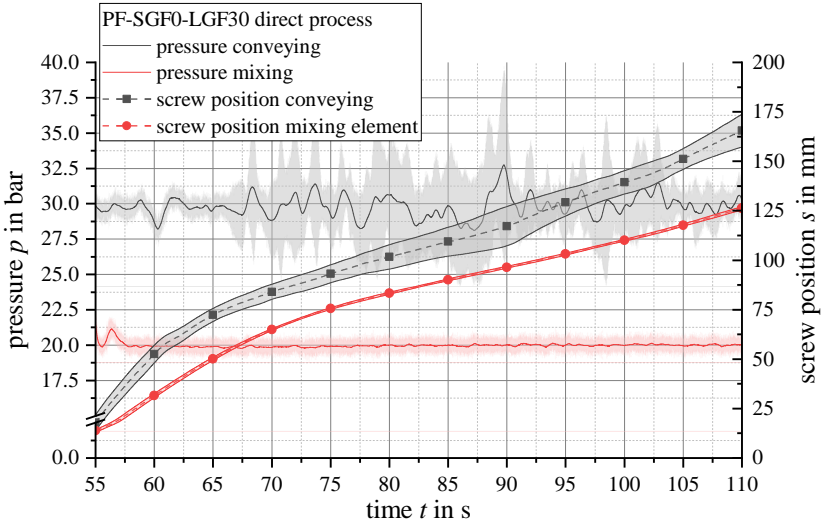


Figure 6-1: Pressure and screw position during plasticization of PF-SGF0-LGF30 material [26]

When using the conveying screw geometry, the pressure that is required for melting and homogenizing the compound is applied by the injection molding machine's hydraulic system. Especially for long fiber materials with a low apparent density, the injection molding machine's hydraulic system had difficulties to maintain a constant back pressure. It is assumed that this variation in back pressure resulted in the unsteady backward screw movement. When using the mixing element, this pressure for melting is applied geometrically by the reduction of the flow channel cross-section in the shear gap of the element [148]. The back pressure of the injection molding machine is only applied to compact the already molten material in front of the screw. Consequently, the machine was able to maintain a much more stable back pressure level and a steady backward screw movement. [26]

From the plasticizing times that were recorded with the mixing element and the conveying screw, it is concluded that the short glass fiber formulations PF-SGF<sub>x</sub>-LGF0 can be molded up to a fiber content of  $\phi = 60$  wt.-% with the

mixing element. The underlying assumption for this conclusion is that a plasticizing time that exceeds the heating time is not acceptable. For long glass fiber materials with  $L = 5$  mm fiber length, up to  $\phi = 60$  wt.-% are possible with the conveying element, whereas only  $\phi = 44.5$  wt.-% can be molded with the mixing element. When increasing the fiber length to  $L = 10$  mm, the upper limits for the conveying geometry and the mixing element are reduced to  $\phi = 44.5$  wt.-% and  $\phi = 30$  wt.-%, respectively. [26]

With the process data that can be obtained from the injection molding machine, it is not possible to verify the analytical calculations that were carried out for designing and upscaling the mixing element. The main decision factor for determining the geometrical features (mixing element length, flute angle and shear gap height) was the pressure drop over the mixing element. However, due to the lack of pressure sensors in the plasticizing unit, a direct verification of the design calculations was not possible. The assessment of the material homogeneity using X-ray computed tomography (Section 5.4.1) shows an improved homogeneity, which is represented by a reduced number of fiber bundles and which is quantified by calculating the textural feature angular second moment (ASM). Micrographs of the molded plates (Section 5.4.3) and microscopy images of the fracture surfaces (Section 5.6) confirm the improvement in homogeneity when using the mixing element and when increasing the screw plasticization speed. The increased shear energy input, which leads to the better homogeneity, also shorted the fibers (Section 5.4.6). This tradeoff between homogeneity and residual fiber length is in accordance with the observations by several other authors, as summed up by Franzén et al. [191].

Of the four different process variants of the long fiber direct thermoset injection molding process, the layout “LGF plasticizing unit with mixing screw tip” is the most reliable, stable and flexible option. All microstructural and mechanical characterization results prove the beneficial effect of the screw mixing element. The analysis of the material homogeneity using the texture analysis method proves that the mixing element fulfills its purpose of opening the fiber bundles. Feeding fibers and granulate as a dry-blend at the same location resulted in the highest achievable throughput and the largest formulation flexibility. The separate feed of fibers and granulate was not successful and is not recommended.

Within this thesis, two different granular long fiber compression molding compounds were used. For the preliminary trials with the 30 mm screw mixing element, the compound Porophen® 9201L5 with a fiber length of  $L = 5$  mm was used, whereas for the trials with the 60 mm screw, Porophen® 9201L12 with a fiber length of  $L = 12$  mm was chosen. While the 5 mm granulate is still free-flowing and can easily be fed via a standard injection molding machine hopper, the 12 mm granulate causes bridging in the hopper. To solve this problem during the trials, the screw was either starve-fed, the granulate was pushed into the screw using a stick, or a cylindrical hopper was used. Similar optimization were carried out by Saalbach et al. [120]. Once the granulate was in the screw, a sticking to the metal surfaces of the screw and the barrel was observed. According to the material supplier, this is caused by the lack of optimization of the material for the injection molding process. To a certain extent, these challenges can be overcome using optimized processing parameters, but an optimization of lubricants and other additives would certainly ease the injection molding process.

The homogeneity of the parts molded from the long fiber granulate improves by using the screw mixing elements. This is visible by the surfaces of the parts and the fracture surfaces. Both the structural investigations and the mechanical characterization results indicate that the benefit of using the mixing elements for the long fiber granulate is not as strong as for the long fiber direct process. It is assumed that this is caused by the overall lower platelet integrity of the long fiber granulate compared to the dry fiber bundles. Because of the lower strand integrity, it is possible to open and disperse the long fiber granulate with less shear energy input compared to the dry long fiber bundles. For this reason, the positive effect of the mixing element is lower. While a stable processing of the long fiber compression molding compounds can be realized by implementing the measures described here, the mechanical properties of the molded parts are significantly below the datasheet values given by the manufacturer, despite the good homogenization with the mixing elements. Especially in the case of the 12 mm granulate, the tensile and flexural strength is only approximately 1/3 of the datasheet value. In contrast, the flexural strength of the parts molded from the 5 mm granulate is only  $\approx 12\%$  lower than the manufacturer value. The low fiber-matrix adhesion in the parts molded from the 12 mm granulate is the likely cause for the large discrepancy. The fiber-matrix adhesion must be optimized by the material supplier to achieve higher mechanical properties.

The material comparison between the long fiber direct thermoset injection molding process to the process route of using the semi-finished granular long fiber compound Porophen® is impeded by the weak fiber-matrix adhesion that was observed in both process routes. Both routes profit from the mixing element and should be processed in the process layout “LGF plasticizing unit with mixing screw tip”. To draw definite conclusions regarding the mechanical properties, an optimization of the fiber sizing chemistry is required.

As shown in Section 5.3.3, only the pure LGF and SGF formulations with  $\phi = 44.5$  wt.-% fiber content are processable with the mixing element, but not the combined SGF-LGF formulations. To develop a hypothesis for this observation, the formulations are considered as bimodal suspensions consisting of large (LGF) and small particles (SGF). Since both the fiber diameter and the fiber length differ for LGF and SGF, this assumption is considered valid. According to Farris [240], blends of different particle sizes reduce the overall suspension viscosity. For a constant volume fraction of particles, the viscosity of a bimodal suspension is lower than the viscosity of a suspension with a monomodal particle size distribution. A monomodal suspension with the same volume fraction always has the highest viscosity [241]. Fidleris and Whitmore concluded that if the particle size ratio small/large is less than 1/10, then the larger particles behaves as if they were moving through a pure fluid with the viscosity and density of the small-particle suspension [242]. The cited studies [240–242] consider particle fractions of  $\phi > 50$  vol.-%. Additionally, the authors investigated spherical particles, not fibrous ones. For the following hypothesis, it is assumed that the basic effect of a bimodal particle size distribution on the viscosity of a suspension remains unchanged, although the magnitude of the effect may be different if fibers are considered instead of particles.

The influence of a bimodal suspension known from literature and described above has the exact opposite effect than what was observed during the experiments: In a bimodal suspension, the viscosity is lower for the same volume fraction, which would lead to a lower – and not a higher – shear energy input for the combined formulations compared to the pure SGF and LGF formulations. For this reason, a hypothesis that focuses on the effect of opening the fiber bundles is proposed.

In the pure LGF and SGF formulations, fiber bundles (LGF) or well-dispersed single fibers (SGF) are present in the phenolic resin. The aspect

ratio of the LGF bundle is approximately 5 L/D, and that of a single SGF is approximately 15 L/D. It was shown in Section 5.4.5 that the SGF single fibers do not undergo a significant fiber shortening during processing. This means that the fibers exist as single, separate objects that do not interact with each other. Since the aspect ratio of the LGF bundles is even lower, the assumption is made that these are also not opened until they pass through the shear gap of the mixing element. According to Truckenmüller [114], the mechanisms for opening a fiber bundle are similar to those that cause fiber breakage. Since the SGF with 15 L/D are not broken, it is assumed that the LGF bundles with 5 L/D are also not opened. The LGF bundles behave like the SGF single fibers as individual, non-interacting objects, only on a different size scale. Both the SGF single fibers and the LGF bundles are surrounded by the pure resin, i.e. a fluid with relatively low viscosity. In the case of combined formulations, LGF bundles are present in a homogeneous SGF single fiber-resin suspension. This can be thought of as a bimodal suspension consisting of large (the LGF bundles) and small particles (the SGF single fibers). Following [240,242], it is assumed that the LGF bundles in the combined formulations move in a much higher viscosity fluid than in the pure LGF formulation. The higher viscosity results in an increased opening of the fiber bundles, releasing individual LGFs. Since the aspect ratio of a single LGF is much larger than that of the LGF bundle at about 300 L/D, numerous fiber-fiber interactions and fiber breakage occur. The fiber-fiber interactions can, for example, cause mutual blockages and obstructions, which in turn then leads to the increased energy input and the overheating and curing of the phenolic resin. In the combined formulations, this behavior occurs as soon as the resin is melted, i.e. already in the conveying zone upstream of the mixing element and in the inlet channels of the mixing element. In the pure LGF formulations, the bundles are present until they pass through the shear gap of the mixing element, which means that this behavior, which leads to increased energy input, can only occur in a much smaller part of the screw. The micro-structural investigations described in Section 5.4.2 show that the fraction  $\psi$  of opened fiber bundles in parts molded with the conveying screw geometry decreases with increasing LGF content. It is assumed that the samples investigated in Section 5.4.2 are representative for the material behavior in the mixing element screw until the material enters the mixing element itself. Up to this point of material flow, the screw channels have the exact same conveying screw geometry. It is

deducted that the results for the opened fiber bundle fraction  $\psi$  are indicators that support the above hypothesis.

As a limitation to this hypothesis, however, it must be noted that the presumed additional energy input due to the earlier opening of the fiber bundles is not reflected by the measured plasticizing work. As Figure 5-27 shows, no correlation between processability and plasticizing work can be derived.

### **6.3 Fiber shortening during processing of thermoset molding compounds**

The main influence parameter on the fiber shortening is the shear stress input during compounding and plasticization. The shear stress is a function of the process and material parameters, e.g. the screw geometry and the screw speed. Both for the twin-screw extruder compounding and the injection molding trials, the energy input can be quantified. During the twin-screw extruder compounding of the short glass fiber-reinforced molding compounds, the energy input was quantified with the specific mechanical energy input (SME). In the long fiber direct thermoset injection molding process, the energy input during plasticization was correlated to the plasticizing work.

In the compounding activities for this thesis, the SME was intentionally kept constant to achieve a comparable degree of reaction into the resin, which means that no conclusions regarding the correlation between the fiber shortening and the energy input can be drawn. Inceoglu et al. [218] found out that an increase in SME leads to shorter fibers, which is a plausible conclusion and which is most likely applicable to the phenolic molding compounds as well.

A higher plasticizing work for the same material formulation in the long fiber direct thermoset injection molding process leads to stronger shortening of the fibers. This is visible for the long fiber formulations PF-SGF0-LGF30 and PF-SGF0-LGF44.5. In both cases, switching from the conveying screw to the mixing element increases the plasticizing work, which leads to a stronger shortening of the fibers. In this regard no difference to thermoplastics was found. Most studies for thermoplastics state that the fiber length in the molded part decreases with increasing screw speed, which is represented by the increased plasticizing work. Moritzer and Bürenhaus [243] confirmed this



for PP-GF, Lafranche et al. have drawn the same conclusions for PA66-GF [244,245]. As an exception to the general consensus, Rohde et al. [14] only found a slight, but not statistically significant shortening effect of the screw speed for PP-GF. While a stronger fiber shortening for higher plasticizing work values is observed for the long fiber formulations, this is not the case for a pure short fiber formulation such as PF-SGF28.5-LGF0 (Figure 5-46 in Section 5.4.6). No additional shortening of the fibers compared to the conventional conveying screw is observed. Since the ratio  $FLD=L_p/L_n$  is also unaffected, it is concluded that the slight fiber shortening is caused by abrasive wear on the machine surfaces and not by breakage due to fluid forces. [26]

Looking at the influence of the injection parameters on the fiber length, the experiments with different mixing elements (Section 5.3.2) indicate that the injection parameters do not have any significant influence on the fiber shortening in the thermoset injection molding process. Due to the strong bundle structure in these parts, no fiber length measurements were carried out. However, the underlying mechanisms for bundle opening and fiber shortening are identical according to Truckenmüller [114]. Since the bundle structure is not changed by using the mixing elements, the conclusion is drawn that no significant fiber shortening occurs with changing injection parameters or changing nozzle and gate geometries. For thermoplastics, most studies come to the conclusion that higher injection speeds lead to a strong [246] or at least slight [14] shortening of the fibers. Narrower gate and nozzle geometries [247] also have a strong shortening effect. A possible explanation for this discrepancy between thermosets and thermoplastics is the different mold filling behavior. Thermoplastics fill the mold in a fountain flow [193], which leads to a more thorough mixing of the polymer, whereas thermosets tend to have a plug flow with a strong slip on the hot mold surface [92,93]. The plug flow causes a low shear rate in most of the material, which is unaffected by parameter and geometry changes. Increasing the injection speed leads to a higher shear rate gradient in the small slip layer at the mold wall, but does not affect the plug in between the two wall layers. It is concluded that in the thermoset injection molding process, the bundle opening and fiber shortening occurs in the plasticizing unit during the material plasticization. During the injection phase, no significant shortening takes place. Once the compound is injected into the mold, fiber bundle impregnation due to the viscosity drop of the resin and the high in-mold pressure during the holding phase might occur.

In the following paragraphs, an estimation for the critical fiber length  $L_c$  is carried out based on literature data. For the material system of phenolic resin and glass fibers which is used within this work, Gore and Cuff [20] estimated the critical fiber length in the range of  $L_c = 5 \text{ mm} \dots 8 \text{ mm}$ . Calculating  $L_c$  according to the Kelly-Tyson model on the basis of literature data for the interfacial shear strength of phenolic resin and glass fibers [19] results in a value of  $L_c = 2 \text{ mm}$ . Even assuming a perfect interfacial adhesion with a shear strength between resin and fibers that equals the neat resin shear strength results in  $L_c = 630 \text{ }\mu\text{m}$ . This means that even under the most optimistic assumptions, the critical fiber length is still longer than typical weighted average fiber length values that are present in commercially available phenolic molding compounds for injection molding. The SEM images of the fracture surfaces of the SGF molding compounds strengthen this conclusion. Despite the good adhesion between resin and fibers, the dominant failure mode is fiber pull out. If the fiber length in the SGF parts was in the range of  $L_c$ , a fiber fracture should have occurred. For the long glass fiber-reinforced parts, no conclusions regarding the critical fiber length are possible due to the obviously weak interfacial bonding.

An estimation for the asymptotic fiber length value  $L_\infty$ , below which fibers are not broken any further by the fluid-fiber interactions is presented in the following paragraph. The calculations are outlined in [15] and will be summarized here. Forgacs and Mason [186] introduced a theory on the buckling of rod-like particles in sheared suspensions, which has later been corrected by DeTeresa [248]. Equation (6-1) given by DeTeresa enables the calculation of a fluid shear stress  $\tau_{\text{req}}$

$$\tau_{\text{req}} = \frac{5.12 E_b \ln\left(2 \left(\frac{L}{D}\right) - 1.75\right)}{\left(\frac{L}{D}\right)^4} \quad (6-1)$$

that is required for buckling a fiber with the aspect ratio  $L/D$  and the bending modulus  $E_b$ . The required fluid shear stress  $\tau_{\text{req}}$  is now equated to two actual fluid shear stress values  $\tau_{\text{act}}$ . First, the actual fluid shear stress value  $\tau_{\text{act, nozzle}}$  in the nozzle during the injection is considered, and second the actual fluid shear stress value  $\tau_{\text{act, mix element}}$  is calculated.

$$\tau_{\text{act, nozzle}} = \dot{\gamma}\eta = \frac{4\dot{V}}{\pi r_{\text{nozzle}}}\eta \quad (6-2)$$

where  $\dot{V}$  is the volume flow rate during injection,  $\eta$  is the resin viscosity and  $r_{\text{nozzle}}$  is the radius of the injection molding machine nozzle. Applying the values provided in Table 6-1 and equating  $\tau_{\text{req}} = \tau_{\text{act}}$  leads to an estimation for the fiber aspect ratio that is not reduced further by fluid-fiber interactions.

Table 6-1: Process and material parameters for calculating shear stress in the machine nozzle

Symbol	Parameter	Unit	Value
$E_b$	Bending modulus of fiber	GPa	68.9 [249]
$Q$	Injection volume flow	cm <sup>3</sup> /s	100
$r_{\text{nozzle}}$	radius of machine nozzle	mm	4
$\eta$	resin viscosity at 140 °C (obtained from oscillation rheology measurements)	Pa s	300

For the given fiber diameters  $D = 13 \mu\text{m}$  (SGF) and  $D = 17 \mu\text{m}$  (LGF), the results are  $L_{\infty, \text{nozzle}}(13 \mu\text{m}) = 455 \mu\text{m}$  and  $L_{\infty, \text{nozzle}}(17 \mu\text{m}) = 595 \mu\text{m}$ , respectively. For the shear gap of the mixing element,  $\tau_{\text{act, mix element}}$  is calculated according to the simple plate-plate rheometer Equation (6-3)

$$\tau_{\text{act, mix element}} = \eta\dot{\gamma} = \eta \frac{\Delta v}{h} \quad (6-3)$$

Applying the values provided in Table 6-1 and equating  $\tau_{\text{req}} = \tau_{\text{act}}$  once more leads to an estimation for the fiber aspect ratio that is not shorted further by fluid-fiber interactions in the mixing element.

Table 6-2: Process and material parameters for calculating shear stress in the mixing element

Symbol	Parameter	Unit	Value
$\Delta v_{40 \text{ 1/min}}$	relative velocity at $n = 40 \text{ 1/min}$ screw speed	m/s	0.121
$\Delta v_{70 \text{ 1/min}}$	relative velocity at $n = 70 \text{ 1/min}$ screw speed	m/s	0.213
$H_{\text{gap}}$	shear gap height	mm	1
$\eta$	resin viscosity at the 130 °C (obtained from oscillation rheology measurements)	Pa s	2000

For the mixing element, the results are  $L_{\infty, \text{mix}}(13 \mu\text{m}) = 78 \mu\text{m}$  and  $L_{\infty, \text{mix}}(17 \mu\text{m}) = 102 \mu\text{m}$ , respectively, which is significantly shorter than the values for  $L_{\infty, \text{nozzle}}$  calculated above. These values represent the lower limit down to which the fibers are shortened due to fluid-fiber interactions. Comparing the results for  $L_{\infty}$  with the results for  $L_c$  presented above indicates that a fiber shortening to fiber length values below the critical fiber length will take place in the thermoset injection molding process, especially if the mixing element is used. However, it has to be kept in mind that in the rheometer measurements performed by Goris et al. [72], the required residence time until  $L_{\infty}$  was reached, was longer than  $t = 60 \text{ s}$  even for the highest shear rates. In contrast to that, typical mold filling times in the thermoset injection molding process are approximately  $t = 5 \text{ s}$  and the residence time in the shear gap of the mixing element is most likely significantly shorter. All fiber length measurements indicate that no shortening down to  $L_{\infty}$  occurs in the thermoset injection molding process.

## 6.4 Homogeneity, structure and mechanical properties of the molded parts

As concluded in the publication [25], the results for specimen group 1, the plasticized material in front of the screw, show that a higher total fiber content leads to a higher material homogeneity. In general, the viscosity of a fiber-reinforced polymer material increases with increasing fiber and filler content [70]. Therefore, it can be assumed that the PF-SGF20-LGF30 material has a higher viscosity than the PF-SGF0-LGF30 formulation. The increased viscosity has two effects on the thermoset injection molding process.

First, it leads to a higher shear energy input while plasticizing action in the injection molding screw. Second, it results in a higher required injection pressure for pushing the compound through the machine nozzle and into the mold. The first aspect serves as an explanation for the overall higher level of inhomogeneity in the PF-SGF0-LGF30 specimen. Since the shear energy input for this formulation is lower, less fiber bundles are opened. The second aspect, the higher required injection pressure, creates a larger amount of backflow during the injection phase, which contributes to the better mixing and consequently the higher homogeneity in the front parts (slices 1-3) of the PF-SGF20-LGF30 specimen compared to its rear section (slices 5-8). Both aspects are visible in the illustrative images in Figure 5-34 and are represented by the calculated ASM values. [25]

The results for the molded parts (specimen group 2) show that the thermoset-specific Maddock mixing element has a positive influence on the material homogeneity. By using the mixing element, both the number and the size of the fiber bundles are reduced, resulting in a more even and therefore more homogeneous distribution of the fibers in the polymer matrix. Again, the visual impression of the cross-section view is in accordance with the calculated ASM results. The screw speed has a linear correlation to the shear rate in the shear gap between the screw and the barrel [146]. Consequently, the molding compound that was plasticized with the higher screw speed contains less fiber bundles, which in turn results in a higher homogeneity of the molded part. For all investigations, the calculation of the ASM confirms the visual impressions. Using the image texture analysis method to determine the homogeneity has the inherent advantage that the entire image stack in all three dimensions is considered for the calculation. The calculation procedure provides a single numerical value for an image, which enables simple and quick comparisons between multiple images or image slices. However, the reduction of a 3-dimensional image into a single numerical value is always accompanied by a loss of information. For example, the ASM does not contain any information about the shape or type of inhomogeneities. It simply returns a value for the homogeneity of the image. Additional information needs to be obtained by visual inspection of the image or the calculation of other textural features. [25]

The SEM images shown in Section 5.6 indicate that at least a partial impregnation of the fiber bundles occurs. Subsequently, it is investigated whether such an impregnation of the bundles is feasible. Deringer et al. [194] ob-

served an impregnation of dry continuous carbon fiber rovings which were overmolded with a thermosetting epoxy molding compound. To draw a comparison between their results and the results for the long fiber direct thermoset injection molding process described here, the resin viscosity values at the typical processing temperatures are analyzed. Deringer et al. measured a minimum viscosity of  $\eta = 3.3 \times 10^3$  Pa s at a temperature of  $T = 115$  °C when performing oscillatory temperature sweep measurements. Comparable measurement performed with the PF-SGF0-LGF0 phenolic molding compound used for the long fiber direct thermoset injection molding process (see Sections 5.1.1 and 5.1.2) resulted in a minimum viscosity of  $\eta \approx 5 \times 10^3$  Pa s. Since this viscosity value is of a similar magnitude compared to Deringer's results, it is concluded that an impregnation of the fiber bundles with the phenolic resin is possible. No values for the in-mold pressure are given in [194], but based on general processing recommendations for epoxy molding compounds [95] it is safe to assume that the in-mold pressure values in their process are lower than the values in the long fiber direct thermoset injection molding process using phenolic resins.

Both in the micrographs and the SEM fracture surface images, the size and the number of fiber bundles are reduced when using the mixing element. It appears that the reduction of the fiber bundle count is less effective at higher fiber fractions. A possible explanation is the generally higher number of fiber bundles at higher fiber fractions. Additionally, the process limitations of the long fiber direct thermoset injection molding process required a reduction of screw speed when using the mixing element at high fiber contents. This reduction to  $n = 25$  1/min compared to  $n = 40$  1/min ... 70 1/min when increasing the fiber content from  $\phi = 30$  wt.-% to  $\phi = 44.5$  wt.-% was required to maintain a stable process, but it most likely reduced the mixing power of the element. The weak fiber-matrix adhesion that was observed for the PF-SGF0-LGF55 commercially available granulate has also been suspected by Saalbach et al. [120] and Raschke [121] due to the low mechanical performance. For example, both publications measured a tensile strength that was less than half of the value that is given in the technical data sheet [119]. However, no SEM images are provided to back up the conclusion of the low fiber-matrix adhesion. For manufacturing the samples in the long fiber direct injection molding process, continuous fiber rovings of the type 111AX11 [181] with a 2400 tex roving size were used. This fiber type was recommended by the fiber and the resin suppliers, because this exact fiber type 111AX in

a 1200 tex size is used for manufacturing the PF-SGF0-LGF55 granulate [250]. For this reason, the observation of the weak fiber-matrix adhesion for all the long fiber specimens is plausible.

The micrography investigations confirmed that the typical three-layer setup of the plates, consisting of two skin layers with fibers oriented in the direction of flow and a core layer with perpendicular fiber orientation, exists. As described in Section 5.4.3, this structure could be observed and measured for those materials that have a high homogeneity. If there are too many bundles the part, a skin and core layer structure is not visible. The thickness of the core layer decreases along the flow path, which is in accordance with the results of English [55]. The low distinctiveness of the skin and core layer structure for the micrographies perpendicular to the orientation of material flow is attributed to the increasing skin layer fraction towards the sides of the parts [55]. In the micrography images, the skin layer appears to be dominating with little to no core layer existing. For those specimens where a skin and core structure is visible, it is notable that using the screw mixing element leads to a higher fraction of the skin layer. A higher fraction of the skin layer consequently leads to a higher fraction of fiber oriented parallel to the direction of material flow. The SGF formulations investigated here show the same behavior as described by English [55] with the highest skin layer fraction close to the gate of the mold. With increasing distance to the gate, the skin layer fraction decreases. The same correlations are valid for the well-dispersed and bundle-free long fiber formulations manufactured in the long fiber direct thermoset injection molding process. Long fiber formulations with a low homogeneity, i.e. with a high fraction of fiber bundles, do not show the three-layer structure. Instead, fiber bundles with a predominantly perpendicular orientation dominate the structure. If there is a skin layer, it is relatively small compared to the core layer. This conclusion is in accordance with the results of Raschke and Saalbach et al. who either only found a very small surface layer [121] or no three-layer structure at all [120].

The process development results (Section 5.3.3 and publication [26]) have shown that the mixing element and the screw speed both increase the plasticizing work, i.e. the energy input into the resin during plasticization. This likely results in a further advance in the resin's curing process. The formation of the skin layer happens by the incremental curing of the resin on the surface [93]. English [55] found out that higher mold temperatures and longer injection times result in a thicker skin layer, because the incremental curing on the

mold surface is either quicker (higher mold temperature) or has more time (longer injection time). In this thesis, the conclusion that a higher energy input during plasticization also causes a thicker skin layer is drawn, because the resin's curing is progressed further which consequently facilitates the incremental final curing on the hot mold surface. [26]

Analyzing the results of the circular tensile test specimens (Section 5.5.2.3) shows that the usage of the mixing element leads to a more pronounced anisotropy with a higher stiffness in  $0^\circ$  orientation. This is valid both for the SGF and for the LGF formulations. It is concluded that this increase in anisotropy is caused by the fiber orientation due to the more distinct skin and layer structure. The increased anisotropy is also a likely reason why the mechanical properties of the SGF and LGF (Section 5.5.2.2) profit more in  $0^\circ$  orientation than in  $90^\circ$  orientation when using the mixing element and when increasing the screw speed while doing so.

The predominantly perpendicular fiber orientation in the PF-SGF0-LGF55 granulate specimens results in low mechanical properties in  $0^\circ$  orientation to the flow. For example, Saalbach et al. [120] found that the tensile strength of specimens oriented perpendicular to the material flow is more than twice as high as the strength for specimens with a parallel orientation. The mechanical testing carried out with the PF-SGF0-LGF55 granulate material here confirms their findings, with tensile strength values of  $\sigma_{m,0^\circ} \approx 25$  MPa and  $\sigma_{m,90^\circ} \approx 50$  MPa. Even the higher value in  $90^\circ$  orientation is still three times lower than the datasheet value, indicating again this significant discrepancy which was observed by other studies as well and which is most likely caused by the weak adhesion of fiber and matrix.

The mechanical characterization results have shown that the mixing element often leads to a higher scattering of the mechanical properties. That is especially visible for the PF-SGF0-LGF30 long fiber formulation in the tensile and Charpy impact testing. At first, this observation might appear counterintuitive, because the mixing element increases the homogeneity of the material. One might conclude that the increased homogeneity might lead to less scattering instead of more. The analysis of the individual measurement results in the box plots (Figure 5-50 and Figure 5-58) shows that the few extreme values that cause the larger scattering have significantly higher mechanical properties than most of the tested specimens. The failure of the specimens is typically caused by defects, which are in this case unopened



fiber bundles. The existence of several fiber bundles in a specimen likely leads to a failure according to the weakest link theory, in which the largest defect leads to the final failure of the part. The exact number of defects most likely does not play a strong role in this failure behavior, as long as at least a few defects exist in the test specimen. For this reason, a reduction of the number of unopened fiber bundles by using the mixing element does not immediately lead to much better properties, if there are still enough fiber bundles present. It is assumed that in the case of the high extreme values, the defects are eliminated altogether or at least reduced significantly. This leads to the conclusion that those high extreme values show the true potential of the long glass fiber-reinforced phenolic molding compounds.

Another indicator for the potential of the long glass fiber-reinforced compounds are the results of the puncture impact testing. This characterization method clearly shows that the absorbed impact energy increases with increasing LGF content and is further improved by using the mixing element (see Figure 5-61). This positive correlation stands in contrast to the inverse relation that is determined for the same materials in the Charpy unnotched impact testing. In the Charpy test, the short glass-fiber reinforced specimens have the highest impact resistance. A likely explanation for this discrepancy is the test specimen geometry and especially the specimen size. The puncture impact specimens are larger, which means that a bigger area is mechanically stressed during the testing. The LGF are likely better capable of distributing the load into this bigger area than the SGF. It is assumed that this is not possible in the smaller Charpy specimens, which is why the positive potential of the LGF is not reflected in this test.

## 6.5 Answers to the research questions

*Which adjustments to the material formulation and the compounding process are required for the direct processing of long-fiber-reinforced thermosets?*

To facilitate the feeding of additional long glass fibers, the molding compounds that were tailored to the requirements of the long fiber direct thermoset injection molding process needed to have a lower short glass fiber content than commercially available compounds, or even contained no fibers at all. Due to the wide fiber content range, the state-of-the-art method of using the orifice flow test OFT for judging the moldability and for steering the com-

pounding process could not be used. Instead, a new method which uses the specific mechanical energy input into the resin was developed and validated.

*How can a direct fiber feeding process for the manufacturing of long fiber-reinforced thermosets be achieved?*

A direct long fiber feeding into the injection molding machine by chopping direct glass fiber rovings and conveying them into the plasticizing unit with a twin-screw sidefeed is possible. The central processing challenge is to open the fiber bundles at the right step of the process, which is after feeding the fibers into the plasticizing unit, but before injecting the compound into the mold. With a newly developed, thermoset-specific mixing element based on the established Maddock screw element, a good fiber-matrix homogenization was achieved.

*How can a gentle and stable processing of the available long fiber compression molding compounds be realized?*

The lack of optimization long fiber compression molding compounds for the injection molding process led to a strong sticking of the compound to the screw and the barrel. While these challenges could be overcome by optimizing the injection molding processing parameters, the available process parameter range was severely limited. Compared to the long fiber direct thermoset injection molding process, less mixing energy input was required to obtain a good fiber dispersion quality.

*What are the main influencing parameters on the fiber shortening in the injection molding of thermoset compounds?*

The main influence parameter on the fiber shortening is the shear stress input during compounding and plasticization. The experimental results for the incorporation of shear stress during the injection phase indicate that less fiber shortening occurs during this process step.

*Which process route is recommended for the injection molding of long fiber-reinforced thermoset molding compounds? Which fiber length is needed for obtaining a benefit in mechanical properties?*

Considering the shortcomings of the commercially available long fiber granular thermoset molding compounds the process layout “LGF plasticizing unit with mixing screw tip” of the long fiber direct thermoset injection molding process is the most reliable, stable and flexible option. The fiber length measurement and calculation results strongly indicate that a fiber shortening to fiber length values below the critical fiber length will take place in the thermoset injection molding process, especially if the mixing element is used. Nevertheless, by using the long fiber direct injection molding process, the weighted average fiber length was increased by a factor of 2...4 compared to conventional phenolic molding compounds. This was especially beneficial for the impact energy absorption, which could be increased by a factor of 2.

# 7 Summary and Conclusions

# 7 Summary and Conclusions

## 7.1 Summary

This thesis investigated the topic of processing long glass fiber-reinforced phenolic resins in the thermoset injection molding process. The aim of increasing the fiber length in the molded part compared to conventional, state-of-the-art thermoset injection molding was pursued to achieve an improvement in the parts' mechanical properties, especially impact toughness. To increase the fiber length compared to the small average weighted fiber length values of  $L_p = 0.3 \text{ mm} \dots 0.35 \text{ mm}$  that are typical for commercial available phenolic molding compounds [15], two process routes have been investigated. First, a semi-finished granular long fiber phenolic molding compound was processed. This compound was designed for compression molding applications. It is not optimized for injection molding processes and consequently has no industrial injection molding application to date. Second, a new thermoset injection molding process variant that enables the manufacturing of phenolic resin parts with an adjustable composition of short and long reinforcement glass fibers was developed. With both process routes, parts were molded and characterized regarding their quasistatic and dynamic mechanical properties and compared to state-of-the-art conventional short fiber-reinforced molding compounds.

The newly developed long fiber thermoset injection molding process required tailored material formulations with a wide range of fiber contents that are not commercially available. To obtain these phenolic molding compounds, they were compounded from the raw materials with twin-screw extruders. The extruder compounding process was controlled by calculating the specific mechanical energy input SME into the resin [24]. By adjusting the process parameters material throughput and extruder speed, a constant energy input and hence a comparable degree of chemical reaction progress was targeted.

The calorimetric characterization has shown that this was possible for formulations with a fiber content  $\phi > 28.5$  %-wt. At lower fiber content values, the processing and machine constraints limited the necessary adjustment of the extruder parameters.

To enable an adjustable composition of short and long reinforcement glass fibers in the newly development long fiber thermoset injection molding process, the mass streams of the phenolic resin and the long glass fibers were separated. The phenolic resin, all required processing additives and short glass fibers were compounded into the granular molding compound as described above and fed gravimetrically into the process. The long glass fibers were chopped from a direct roving, enabling a formulation control by adjusting the speed of the fiber chopper. They were subsequently fed into the plasticizing unit with a twin-screw sidefeed that was positioned in a  $30^\circ$  angle above the barrel of the injection molding machine. Depending on the process layout variant, the granular molding compound was either fed together with the long fibers or at a separate position further away from the screw tip of the plasticizing unit. The main processing limitation for the long fiber direct thermoset injection molding process was the achievable feeding rate of the long glass fibers. Due to the  $30^\circ$  angle above the barrel of the injection molding machine in which the twin-screw sidefeed is positioned, the long glass fibers must fall into the injection molding screw by gravity. No stuffing or forcing them into the screw was possible. Falling into the plasticizing unit was facilitated by the high strand integrity of the chosen direct roving type and by feeding the phenolic molding compound together with the long fibers at the same location. The spatially separated feeding of the molding compound and the long fibers was not feasible as it significantly reduced the achievable feeding rate and consequently leads to unacceptably long plasticizing times.

The high strand integrity of the chosen direct glass fiber rovings improved fiber chopping and fiber feeding into the injection molding machine, but it also caused problems regarding the opening of the fiber bundles and the dispersion of the long fibers in the phenolic resin matrix. With the conventional thermoset injection molding screw geometry, fiber bundles were visible in the molded parts. These fiber bundles acted as defects and led to tensile strength values below the unreinforced neat resin. To open the bundles, several measures for increasing the mixing power during the injection molding process were evaluated. First, distributive and dispersive mixing

during the injection phase was accomplished by forcing the material through narrow gaps and small machine nozzles and by using a purpose-designed, thermoset-specific static mixing nozzle. However, no significant improvement of the mechanical properties of the long glass fiber-reinforced parts compared to the neat resin was achieved. To ensure that the fiber-matrix-compound is already homogeneous before it is injected into the mold, thermoset-specific screw mixing elements based on the Maddock mixing element geometry were designed, manufactured and evaluated. These mixing elements have three distinct differences to traditional Maddock elements for thermoplastics to achieve a narrow residence time distribution by avoiding material agglomerations, to introduce both shear and elongational stresses into the material and to take into consideration the specific melting behavior of thermoset molding compounds. They were achieved by (1) implementing a gradual slope at the end of the inlet flutes that has the same height as the shear gap on the mixing flight, by (2) adding an edge fillet on the mixing flight and by (3) reversing the positions of the element's mixing and wiping flights. With these mixing elements, parts with an improved fiber-matrix homogeneity were manufactured. The additional energy input into the material during the plasticization was quantified by calculating the plasticizing work. An increase in plasticizing work with increasing fiber content and with increasing screw speed was observed.

To quantify the effect of the mixing elements on the material homogeneity and the fiber length distribution in the molded parts, two characterization techniques were used. First, a method for quantifying the material homogeneity by using image texture analysis was developed. This method is based on the three-dimensional extension of the Haralick texture features which has been used for investigating medical images, but which is new for composite materials [25]. The application of the texture analysis method both for the material in front of the screw and for the molded parts show that the Maddock screw mixing element improves the material homogeneity. Process parameter variations such as changes in the fiber content and the screw speed are reflected by the calculated texture features. For example, increasing the screw speed leads to a higher homogeneity. The second characterization method that was developed refined the fiber length measurement process compared to the state-of-the-art [15]. By using a guided measurement process instead of the typical manual sample taking, the potential operator's influence on the measurement results is reduced. The combination of the guided sample

taking with a semi-automatic image processing enables the measurement of several thousands of fibers per specimen, which is significantly higher than what is found in most other published research works. An existing, non-destructive measurement method using  $\mu$ CT image analysis was evaluated, but it was found that this method does not yield accurate results for the high fiber packaging density that exists in phenolic molding compounds. The usage of the screw mixing element led to a stronger shortening of the long glass fibers compared to the conventional conveying screw geometry. Increasing the screw speed when using the mixing element led to even shorter fibers, but which were still significantly longer than those found in typical short fiber molding compounds. The counteracting effects of fiber bundle opening on the one hand and fiber length conservation on the other hand that are described in literature were clearly visible.

Micrographical investigations showed a skin and core layer structure in the molded parts that had a good fiber dispersion, with fibers oriented parallel the flow in the skin layers and a perpendicular orientation in the core. Parts with a low homogeneity, e.g. with fiber bundles, did not show this structure. In general, the usage of the screw mixing element resulted in a higher homogeneity and consequently a more pronounced formation of the skin and core layer structure and to a higher skin layer fraction compared to the conveying screw geometry. The usage of the screw mixing element also led to a significant improvement of the long fiber materials' mechanical properties compared to the standard conveying screw geometry. The tensile strength in direction parallel to the flow of material was improved by more than 2.5 times for a formulation with  $\phi = 30$  wt.-% glass fibers. Not only the long fiber materials, but also the short fiber compounds profited from using the screw mixing element, albeit to a smaller extend which was still within the margin of measurement uncertainty. Despite the significant relative improvements that were observed for the long fiber materials, the absolute strength values were below or at the same level as for the short fiber compounds. The parts molded from the granular long fiber material did not show an improvement over a conventional short fiber molding compound, either. In the Charpy impact testing, a clear improvement by a factor of 2 was measured for a  $\phi = 30$  wt.-% long fiber material when using the mixing element, but the absolute value remained in the same range as the short fiber compound. Only in the puncture impact testing, the long fiber material had a significantly higher energy absorption than the short fibers compounds. In

this test, the energy absorption of a PF-SGF0-LGF30 material was more than twice as high than the comparable PF-SGF28.5-LGF0 formulation.

The fracture analysis using scanning electron microscopy revealed a weak fiber matrix adhesion of the phenolic resin to the long fibers, both for the commercially available long fiber granular compression molding compound and for the samples produced in the long fiber direct thermoset injection molding process. This weak fiber matrix adhesion is regarded as the central reason why the absolute values of the strength and impact toughness of the long fiber materials are often below those of the short fiber compounds. Consequently, the effect of formulation changes, machine parameter settings and the screw mixing elements must be judged separately for long fiber and short fiber materials.

## 7.2 Conclusions

With the newly developed long fiber direct thermoset injection molding process, a significant increase of the fiber length in the molded parts compared to the state-of-the-art was achieved. Depending on the process and material parameter settings, the average weighted fiber length was up to four times higher, resulting in values in the range of  $L_p = 500 \mu\text{m} \dots 1100 \mu\text{m}$ . Even though this is a significant improvement, the obtained fiber length is still less than half of the fiber length that is achieved in similar long fiber injection molding processes for thermoplastics [114,130]. It is also significantly below the literature and calculation values for the critical fiber length  $L_c$  for the combination of phenolic resin and glass fibers. The strong fiber shortening is likely caused by the viscosity and temperature profile of the thermoset injection molding process: Except for the final curing in the mold, the molding compound is processed at low temperatures and thus high viscosity values, which in turn causes high fluid stresses on the fibers. In contrast, the melt conveying, homogenization and injection of thermoplastics takes place at significantly lower viscosities. Additionally, the possible residence time of thermoplastics at the processing viscosities is longer, which enables more sophisticated screw geometries with a more gradual and possibly more gentle mixing. For the thermoset molding compounds, a much more careful balancing of mixing energy input, residence time and temperature control is required.



Specifically, this means that the plasticizing work input by the screw mixing element must be carefully adjusted to avoid overheating and curing of the resin. Numerous additional factors besides the main parameter screw speed have an influence on the energy input, among others the material parameters fiber content, initial viscosity and initial state of curing of the resin as well as processing parameters like the plasticizing unit barrel temperature profile, the degree of starve feeding and the typical injection molding parameters back pressure, injection speed and holding pressure. A complete and exhaustive investigation of all these influence factors was not possible within the scope of this thesis – but neither was this the aim. Instead, the focus was on the identification and the variation of the main influence factors while keeping everything else as constant as possible. This led to the decision to concentrate on material formulations with a total fiber content of  $\phi = 30$  wt.-%, since for the main influencing factors of screw speed, screw geometry, long fiber content and long fiber feeding point could be varied, while for everything else a constant and thus comparable set of parameters was maintained. Although this chosen fiber content is lower than in typical industrial applications, conclusions regarding the processing and the effect of long fibers on the mechanical properties can be drawn. The analysis of material homogeneity, fiber length and mechanical properties shows that in the trade-off between fiber dispersion and fiber length, the focus must be on good glass fiber dispersion in the phenolic matrix. Every mechanical property characteristic investigated was increased by improved material homogeneity, despite the associated fiber shortening. It is notable that not only the mechanical properties of the long glass fiber-reinforced materials are improved by using the screw mixing element, but also those of the parts molded from the short fiber compounds. The main purpose of the mixing element is to improve the homogeneity, which is why the inherently inhomogeneous long fiber materials profit more than the already homogeneous short fiber compounds.

Besides the glass fiber length, other structural characteristics such as the distinctiveness of the skin and core layer structure are affected by the mixing element. The additional shear energy input leads to a clearer development of this structure and to a tendentially higher skin layer fraction, which in turn leads to a higher fraction of fibers oriented parallel to the direction of flow. This causes an increasingly anisotropic mechanical behavior with higher mechanical strength and stiffness in direction parallel to the material flow. [26]

The processing and characterization results that were obtained for the 12 mm granular long fiber-reinforced compression molding compound show that in its current development state, this material is not a viable alternative to the long fiber direct thermoset injection molding process. It creates several processing challenges due to its low pourability and its adhesion to the screw and the barrel of the injection molding machine, without offering any significant mechanical benefit over either conventional short fiber-reinforced molding compounds or the direct long fiber thermoset injection molding process. Further work by the material supplier on the compound formulation is required to facilitate the processing and to increase the mechanical properties. A shorter initial fiber length in the granulate is recommended. All fiber length measurements within this thesis indicate a strong shortening during the plasticization of the thermoset molding compound. It is assumed that both the current fiber length of  $L = 12$  mm and a shorter length in the range of  $L = 5$  mm are well above the asymptotic fiber length  $L_{\infty}$ . With a shorter initial fiber length, the pourability and the material intake behavior of the injection molding screw will most likely improve. Adjusting the composition of the additives to reduce the sticking to barrel and screw will facilitate the processing and enable a wider range of possible process parameter variations.

With the initial development work and the identification of the main processing challenges, this thesis has laid the groundwork for future research studies. A strong interdependence of several material and processing parameters is observed, which cannot be fully separated from each other. In addition, the poor fiber-matrix adhesion reduces the expressiveness of some results. Despite these restrictions, it is concluded that the key point for good mechanical properties is a homogeneous distribution of the fibers in the phenolic resin matrix. This homogenization is more important than the fiber length. A homogeneous fiber-matrix compound must be achieved during the plasticization phase by the injection molding screw. With the successful process development of the overall long fiber feeding periphery and the novel screw mixing element for thermoset molding compounds as well as the central material characterization methods, future research studies can now focus on detailed investigations of the individual process and material parameter variations.

---

# List of Publications

## Journal articles as first author

R. Maertens, A. Hees, L. Schöttl, W. V. Liebig, P. Elsner, K. A. Weidenmann. Fiber shortening during injection molding of glass fiber-reinforced phenolic molding compounds: Fiber length measurement method development and validation. *Polym.-Plast. Tech. Mat.* **2021**;60. 8:872–85. DOI:10.1080/25740881.2020.1867170.

R. Maertens, W. V. Liebig, P. Elsner, K. A. Weidenmann. Compounding of short fiber reinforced phenolic resin by using specific mechanical energy input as a process control parameter. *J. Compos. Sci.* **2021**;127. 5:1–17. DOI:10.3390/jcs5050127.

R. Maertens, L. Schöttl, W. V. Liebig, P. Elsner, K. A. Weidenmann. Study of material homogeneity in the long fiber thermoset injection molding process by image texture analysis. *Adv. Manuf.: Polym. Compos.* **2022**;8. 1:22–32. DOI:10.1080/20550340.2022.2033905.

R. Maertens, W. V. Liebig, K. A. Weidenmann, P. Elsner. Development of an injection molding process for long glass fiber-reinforced phenolic resins. *Polymers* **2022**;14. 14. DOI:10.3390/polym1414890.

## Journal articles as contributing author

F. Wittemann, R. Maertens, A. Bernath, M. Hohberg, L. Kärger, F. Henning. Simulation of reinforced reactive injection molding with the finite volume method. *J. Compos. Sci.* **2018**;5. 2:1–16. DOI:10.3390/jcs2010005.

A. Langheck, S. Reuter, O. Saburow, R. Maertens, F. Wittemann, L. F. Berg et al. Evaluation of an integral injection molded housing for high power density synchronous machines with concentrated single-tooth winding. In: Institute of Electrical and Electronics Engineers. *2018 8th International Electric Drives Production Conference*; **2018**, p. 187–192. DOI:10.1109/EDPC.2018.8658324.

P. Griesbaum, S. Ilinzeer, M. Laux, R. Maertens. Funktionsintegrierte Duro-mere Faserverbundwerkstoffe für neue Anwendungen. Translated title:

Functionally integrated thermoset fiber composites for new applications. In: Institut für Wissenschaftliche Veröffentlichungen. *Jahresmagazin Kunststofftechnik*. Lampertheim; **2019**, p. 30–34.

F. Wittemann, R. Maertens, L. Kärger, F. Henning. Injection molding simulation of short fiber reinforced thermosets with anisotropic and non-newtonian flow behavior. *Compos. Part A Appl. Sci. Manuf.* **2019**;124. 9:1–9.  
DOI:10.1016/j.compositesa.2019.105476.

T. Beran, J. Hübel, R. Maertens, S. Reuter, J. Gärtner, J. Köhler et al. Study of a polymer ejector design and manufacturing approach for a mobile air conditioning. *Int. J. Refrig.* **2021**;126:35–44.  
DOI:10.1016/j.ijrefrig.2021.01.023.

## Supervised student theses

A. Hees. Characterisation of fibre length and mechanical properties of injection moulded fibre reinforced thermoset composites. Bachelor Thesis. Karlsruhe: Karlsruhe Institute of Technology (KIT); **2019**.

H. Bremer. Compounding and characterization of glass fiber reinforced phenolic molding compounds. Master Thesis. Karlsruhe: Karlsruhe Institute of Technology (KIT); **2020**.

N. Weigel. Influence of fiber length and content on the quasi-static mechanical properties of long glass fiber reinforced phenolic resins. Bachelor Thesis. Karlsruhe: Karlsruhe Institute of Technology (KIT); **2021**.

M. Nägele. Influence of fiber length and content on the dynamic mechanical properties of long glass fiber reinforced phenolic resins. Bachelor Thesis. Karlsruhe: Karlsruhe Institute of Technology (KIT); **2022**.

---

# Bibliography

- [1] L. H. Baekeland. Condensation product of phenol and formaldehyde and method of making the same. US942700A; **1909**.
- [2] L. Pilato. Phenolic resins: 100 Years and still going strong. *React. Funct. Polym.* **2013**;73. 2:270–7. DOI:10.1016/j.reactfunctpolym.2012.07.008.
- [3] T. Beran, J. Hübel, R. Maertens, S. Reuter, J. Gärtner, J. Köhler et al. Study of a polymer ejector design and manufacturing approach for a mobile air conditioning. *Int. J. Refrig.* **2021**;126:35–44. DOI:10.1016/j.ijrefrig.2021.01.023.
- [4] M. Jauernick, D. Pohnert, W. Kujawski, R. Otte. Hybrid lightweight cylinder crankcase: Challenges and feasibility. *MTZ Worldw.* **2019**;80. 12:70–5. DOI:10.1007/s38313-019-0145-6.
- [5] K. Schindele, T. Sorg, T. Hentschel, J. Liebertseder. Lightweight camshaft module made of high-strength fiber-reinforced plastic. *MTZ Worldw.* **2020**;81. 9:26–31. DOI:10.1007/s38313-020-0263-1.
- [6] A. Langheck, S. Reuter, O. Saburow, R. Maertens, F. Wittemann, L. F. Berg et al. Evaluation of an integral injection molded housing for high power density synchronous machines with concentrated single-tooth winding. In: Institute of Electrical and Electronics Engineers. *2018 8th International Electric Drives Production Conference*; **2018**, p. 187–192. DOI:10.1109/EDPC.2018.8658324.
- [7] P. Griesbaum, S. Ilinzeer, M. Laux, R. Maertens. Funktionsintegrierte Duromere Faserverbundwerkstoffe für neue Anwendungen. Translated title: Functionally integrated thermoset fiber composites for new applications. In: Institut für Wissenschaftliche Veröffentlichungen. *Jahresmagazin Kunststofftechnik*. Lampertheim; **2019**, p. 30–34.
- [8] S. Reuter, L. F. Berg, M. Doppelbauer. Performance evaluation of a high-performance motor with thermoset molded internal cooling. In: Institute of Electrical and Electronics Engineers. *2021 11th International Electric Drives Production Conference*. IEEE; **2021**, p. 1–5. DOI:10.1109/EDPC53547.2021.9684222.

- [9] A. Gardziella, L. A. Pilato, A. Knop. Phenolic resins: Chemistry, applications, standardization, safety and ecology. 2nd ed. Berlin, Heidelberg: Springer; **2000**.
- [10] K. Koizumi, T. Charles, H. D. Keyser. Phenolic molding compounds. In: L. A. Pilato. *Phenolic Resins: A Century of Progress*. Berlin, Heidelberg: Springer; **2010**, p. 383–437.
- [11] B.-R. Paulke, F. Börner, M. Hahn, M. Jobmann, S. Englich, M. Gehde et al. Thermosets impact modification by means of phase-compatilizing, amino resin-coated latex particles. *CIT* **2015**;87. 10:1342–7. DOI:10.1002/cite.201400184.
- [12] M. L. Boroson, B. B. Fitts, B. A. Rice. Advances in toughening of phenolic composites. In: Society of Automotive Engineers, Inc. *SAE Technical Paper Series*. Warrendale: SAE International; **1991**, p. 1–10. DOI:10.4271/910044.
- [13] J. L. Thomason, M. A. Vlug. The Influence of fibre length and concentration on the properties of glass fibre-reinforced polypropylene: 4. Impact properties. *Compos. Part A Appl. Sci. Manuf.* **1997**;28. 3:277–88. DOI:10.1016/S1359-835X(96)00127-3.
- [14] M. Rohde, A. Ebel, F. Wolff-Fabris, V. Altstädt. Influence of processing parameters on the fiber length and impact properties of injection molded long glass fiber reinforced polypropylene. *IPP* **2011**;26. 3:292–303. DOI:10.3139/217.2442.
- [15] R. Maertens, A. Hees, L. Schöttl, W. V. Liebig, P. Elsner, K. A. Weidenmann. Fiber shortening during injection molding of glass fiber-reinforced phenolic molding compounds: Fiber length measurement method development and validation. *Polym.-Plast. Tech. Mat.* **2021**;60. 8:872–85. DOI:10.1080/25740881.2020.1867170.
- [16] A. Kelly, W. R. Tyson. Tensile properties of fibre-reinforced metals: Copper/tungsten and copper/molybdenum. *J. Mech. Phys. Solids* **1965**;13. 6:329–50. DOI:10.1016/0022-5096(65)90035-9.
- [17] H. L. Cox. The elasticity and strength of paper and other fibrous materials. *Br. J. Appl. Phys.* **1952**;3. 3:72–9. DOI:10.1088/0508-3443/3/3/302.
- [18] M. R. Piggott. Expressions governing stress-strain curves in short fibre reinforced polymers. *J. Mater. Sci.* **1978**;13. 8:1709–16. DOI:10.1007/BF00548734.
- [19] F. Chen, D. Tripathi, F. R. Jones. Determination of the interfacial shear strength of glass-fibre-reinforced phenolic composites by a bimatrix

- 
- fragmentation technique. *Compos. Sci. Technol.* **1996**;56. 6:609–22. DOI:10.1016/0266-3538(96)00038-3.
- [20] C. R. Gore, G. Cuff. Long-short fiber reinforced thermoplastics. In: Society of Plastics Engineers. *ANTEC 1986*. Boston; **1986**, p. 47–50.
- [21] H. Ning, N. Lu, A. A. Hassen, K. K. Chawla, M. Selim, S. Pillay. A review of Long fibre thermoplastic (LFT) composites. *Int. Mater. Rev.* **2020**;65. 3:164–88. DOI:10.1080/09506608.2019.1585004.
- [22] M. Schemme. LFT – Development status and perspectives. *Reinf. Plast.* **2008**;52. 1:32–9. DOI:10.1016/S0034-3617(08)70036-5.
- [23] X. Yan, S. Cao. Structure and interfacial shear strength of polypropylene-glass fiber/carbon fiber hybrid composites fabricated by direct fiber feeding injection molding. *Compos. Struct.* **2018**;185. 3:362–72. DOI:10.1016/j.compstruct.2017.11.037.
- [24] R. Maertens, W. V. Liebig, P. Elsner, K. A. Weidenmann. Compounding of short fiber reinforced phenolic resin by using specific mechanical energy input as a process control parameter. *J. Compos. Sci.* **2021**;127. 5:1–17. DOI:10.3390/jcs5050127.
- [25] R. Maertens, L. Schöttl, W. V. Liebig, P. Elsner, K. A. Weidenmann. Study of material homogeneity in the long fiber thermoset injection molding process by image texture analysis. *Adv. Manuf.: Polym. Compos.* **2022**;8. 1:22–32. DOI:10.1080/20550340.2022.2033905.
- [26] R. Maertens, W. V. Liebig, K. A. Weidenmann, P. Elsner. Development of an injection molding process for long glass fiber-reinforced phenolic resins. *Polymers* **2022**;14. 14. DOI:10.3390/polym1414890.
- [27] D. A. Shipp, D. H. Solomon. Functionality in phenol-formaldehyde step-growth polymerization. *Polymer* **1997**;38. 16:4229–32. DOI:10.1016/S0032-3861(96)01013-0.
- [28] G. He, B. Riedl, A. Ait-Kadi. Model-free kinetics: Curing behavior of phenol formaldehyde resins by differential scanning calorimetry. *J. Appl. Polym. Sci.* **2003**;87. 3:433–40. DOI:10.1002/app.11378.
- [29] Y.-K. Lee, D.-J. Kim, H.-J. Kim, T.-S. Hwang, M. Rafailovich, J. Sokolov. Activation energy and curing behavior of resol- and novolac-type phenolic resins by differential scanning calorimetry and thermogravimetric analysis. *J. Appl. Polym. Sci.* **2003**;89. 10:2589–96. DOI:10.1002/app.12340.
- [30] M.-F. Grenier-Loustalot, S. Larroque, P. Grenier, D. Bedel. Phenolic resins: 4. Self-condensation of methylolphenols in formaldehyde-free

- media. *Polymer* **1996**;37. 6:955–64. DOI:10.1016/0032-3861(96)87277-6.
- [31] M. Higuchi, S. Nohno, M. Morita, S. Tohmura. Kinetics of the hydroxymethylation of phenol II: Values of rate parameters and results of simulation experiments. *J. Wood Sci.* **1999**;45. 4:306–12. DOI:10.1007/BF00833495.
- [32] J. Lang, M. Cornick. Resole production. In: L. A. Pilato. *Phenolic Resins: A Century of Progress*. Berlin, Heidelberg: Springer; **2010**, p. 139–146.
- [33] H. Aiba. Novolak production. In: L. A. Pilato. *Phenolic Resins: A Century of Progress*. Berlin, Heidelberg: Springer; **2010**, p. 147–151.
- [34] A. W. Christiansen, L. Gollob. Differential scanning calorimetry of phenol–formaldehyde resols. *J. Appl. Polym. Sci.* **1985**;30. 6:2279–89. DOI:10.1002/app.1985.070300601.
- [35] A. Gardziella, H.-G. Haub. Phenolharze. Translated title: Phenolic resins. In: W. Woebcken, W. Adam, G. W. Becker, D. Braun. *Duroplaste*. Munich: Hanser; **1988**, p. 12–40.
- [36] J. D. Menczel, J. Lawrence, R. B. Prime, H. E. Bair, M. Reading, S. Swier. Differential Scanning Calorimetry (DSC). In: J. D. Menczel, R. B. Prime. *Thermal analysis of polymers*. Hoboken: Wiley; **2009**, p. 7–239.
- [37] V. R. Landi, J. M. Mersereau. The glass transition in novolac phenolic molding compounds and the kinetics of its development during cure and postcure. I. *Adv. Polym. Tech.* **1987**;7. 1:49–57. DOI:10.1002/adv.1987.060070106.
- [38] T. N. Morrison. Practical guidelines for the efficient postbaking of molded phenolics. Itasca; **2004**.
- [39] G. S. Learmonth, D. P. Searle. Thermal degradation of phenolic resins. *V. J. Appl. Polym. Sci.* **1969**;13. 3:437–43. DOI:10.1002/app.1969.070130304.
- [40] Vyncolit NV. Knowledge of engineering phenolics; **2013**.
- [41] T. Scheffler, S. Englich, U. Heyne, M. Gehde. Effects of post-curing on the thermo-mechanical behavior and the chemical structure of highly filled phenolic molding compounds. *Mater. Test.* **2016**;58. 1:56–62. DOI:10.3139/120.110810.
- [42] Polaris Market Research. Phenolic resins market share, size, trends: Industry analysis report; **2020**.



- 
- [43] S. Stitz, W. Keller. Spritzgießtechnik: Verarbeitung, Maschine, Peripherie. Translated title: Injection molding technology: processing, machine, periphery. 2nd ed. Munich: Hanser; **2004**.
- [44] DIN. 7708-1 Plastic moulding materials; **1988**.
- [45] D. Crespy, M. Bozonnet, M. Meier. 100 years of bakelite, the material of a 1000 uses. *Angewandte Chemie International Edition* **2008**;47. 18:3322–8. DOI:10.1002/anie.200704281.
- [46] Sumitomo Bakelite Europe n.v. Technical data sheet X6952 green; **2022**.
- [47] Hexion Inc. Technical data sheet Bakelite PF 1110; **2022**.
- [48] K. Hirano, M. Asami. Phenolic resins—100 years of progress and their future. *React. Funct. Polym.* **2013**;73. 2:256–69. DOI:10.1016/j.reactfunctpolym.2012.07.003.
- [49] C. Ball. Phenolic molding compounds in automotive powertrain applications. In: SPE Automotive. *17th Annual Automotive Conference & Exhibition*; **2017**, p. 1–11.
- [50] H. Panda. Modern technology of textile dyes & pigments. 1st ed. Delhi: National Institute of Industrial Research; **2004**.
- [51] D. M. Kalyon, M. Hallouch. Compounding of thermosets in continuous kneaders. *Adv. Polym. Tech.* **1986**;6. 3:237–49. DOI:10.1002/adv.1986.060060301.
- [52] B. Rudin, D. Drummer. Heat conductive thermosets for the injection molding process. In: Institute of Electrical and Electronics Engineers. *2012 2nd International Electric Drives Production Conference*. IEEE; **2012**, p. 1–4. DOI:10.1109/EDPC.2012.6425136.
- [53] NPCS Board of Consultants & Engineers. Phenolic resins technology handbook. Delhi: NIIR Project Consultancy Services; **2007**.
- [54] S. Tonogai, K. Hasegawa, A. Fukuda. The disk cure test - An evaluation method for flow and curing characteristics of thermosetting molding compounds. *Polym. Eng. Sci.* **1980**;20. 15:985–94. DOI:10.1002/pen.760201502.
- [55] S. Englich. Strukturbildung bei der Verarbeitung von glasfasergefüllten Phenolformaldehydharzformmassen. Original language: German. Translated title: Structure formation during injection molding of glass fiber filled phenolic formaldehyde resin molding compounds. Dissertation. Chemnitz: Technische Universität Chemnitz; **2015**.
- [56] ISO. Plastics: Thermosetting moulding materials - Determination of transfer flow. 7808; **1992**.

- [57] ASTM. D3123 – 09 Standard test method for spiral flow of low-pressure thermosetting molding compounds; **2009**.
- [58] ASTM. D569 Method for measuring the flow properties of thermoplastic molding materials; **1990**.
- [59] ASTM. D731 – 18 Standard test method for molding index of thermosetting molding powder; **2020**.
- [60] DIN. 53764 Test method for flow and cure properties of pourable thermosettings using a torque rheometer and a measuring mixer; **1992**.
- [61] DIN. 53465 Testing of Plastics: Determination of the Closing Time of Thermosetting Compression Moulding Materials; **1963**.
- [62] T. Scheffler, M. Gehde, M. Späth, P. Karlinger. Determination of the flow and curing behavior of highly filled phenolic injection molding compounds by means of spiral mold. In: U. Wagenknecht, P. Pötschke, S. Wiessner, M. Gehde. *Proceedings of the Europe/Africa Conference Dresden 2017*: Polymer Processing Society PPS. AIP Publishing; **2019**, p. 1–5. DOI:10.1063/1.5084897.
- [63] Y. Son. Determination of shear viscosity and shear rate from pressure drop and flow rate relationship in a rectangular channel. *Polymer* **2007**;48. 2:632–7. DOI:10.1016/j.polymer.2006.11.048.
- [64] L. L. Blyler, H. E. Bair, P. Hubbauer, S. Matsuoka, D. S. Pearson, G. W. Poelzing et al. A new approach to capillary viscometry of thermoset transfer molding compounds. *Polym. Eng. Sci.* **1986**;26. 20:1399-144. DOI:10.1002/pen.760262008.
- [65] S. C. Malgaurnera, D. R. Carroll, M. A. Colaluca. Design and use of a thermoset capillary rheometer. *Ind. Eng. Chem. Prod. Res. Dev.* **1984**;23. 1:103–6. DOI:10.1021/i300013a022.
- [66] C. Lohr, S. Dieterle, A. Menrath, K. A. Weidenmann, P. Elsner. Rheological studies on gas-laden and long glass fiber reinforced polypropylene through an inline high pressure capillary rheometer in the injection molding process. *Polym. Test.* **2018**;71. 7:27–31. DOI:10.1016/j.polymertesting.2018.08.015.
- [67] A. Fernandez, M. Muniesa, C. Javierre. In-line rheological testing of thermoplastics and a monitored device for an injection moulding machine: Application to raw and recycled polypropylene. *Polym. Test.* **2014**;33. 1:107–15. DOI:10.1016/j.polymertesting.2013.11.008.
- [68] M. Hohberg, L. Kärger, F. Henning, A. Hrymak. Rheological measurements and rheological shell model considering the compressible behavior of long fiber reinforced sheet molding compound (SMC). *Com-*

- 
- pos. Part A Appl. Sci. Manuf.* **2017**;95. 4:110–7.  
DOI:10.1016/j.compositesa.2017.01.006.
- [69] F. Wittemann, R. Maertens, L. Kärger, F. Henning. Injection molding simulation of short fiber reinforced thermosets with anisotropic and non-newtonian flow behavior. *Compos. Part A Appl. Sci. Manuf.* **2019**;124. 9:1–9. DOI:10.1016/j.compositesa.2019.105476.
- [70] T. A. Osswald, N. Rudolph. *Polymer rheology: Fundamentals and applications*. Munich: Hanser; **2014**.
- [71] T. Mezger. *The rheology handbook: For users of rotational and oscillatory rheometers*. 4th ed. Hannover: Vincentz Network; **2014**.
- [72] S. Goris, S. Simon, C. Montoya, A. Bechara, M. V. Candal, D. Brands et al. Experimental study on fiber attrition of long glass fiber-reinforced thermoplastics under controlled conditions in a couette flow. In: Society of Plastics Engineers. *ANTEC 2017*. Anaheim; **2017**, p. 600–606.
- [73] S. I. Bakhtiyarov, R. A. Overfelt. Study of Rheological Properties of ISOCURE® LF-305/904 G Binder System. *J. Elastomers Plast.* **1997**;29. 4:314–25. DOI:10.1177/009524439702900404.
- [74] M. T. Shaw. *Introduction to Polymer Rheology*. Hoboken: Wiley; **2012**.
- [75] J. C. Domínguez, M. V. Alonso, M. Oliet, E. Rojo, F. Rodríguez. Kinetic study of a phenolic-novolac resin curing process by rheological and DSC analysis. *Thermochim. Acta* **2010**;498. 1-2:39–44.  
DOI:10.1016/j.tca.2009.09.010.
- [76] M. Höer. Einfluss der Material- und Verarbeitungseigenschaften von Phenolharzformmassen auf die Qualität spritzgegossener Bauteile. Original language: German. Translated title: Influence of material and processing properties of phenolic resin molding compounds on the quality of injection-molded components. Dissertation. Chemnitz: Technische Universität Chemnitz; **2014**.
- [77] T. Scheffler. Werkstoffeinflüsse auf den Spritzgussprozess von hochgefüllten Phenol-Formaldehydharz-Formmassen. Original language: German. Translated title: Material influences on the injection molding process of highly filled phenol-formaldehyde resin molding compounds. Dissertation. Chemnitz: Technische Universität Chemnitz; **2018**.
- [78] A. Malkin, V. P. Begishev, V. A. Mansurov. Determining dynamic characteristics of polymeric materials by a non-sinusoidal vibration technique. *Polymer Science U.S.S.R.* **1984**;26. 4:971–3.  
DOI:10.1016/0032-3950(84)90271-5.

- [79] A. Y. Malkin. On the optimal form of a signal in fourier transform mechanical spectroscopy. *Rheol. Acta* **2004**;43. 1:1–5. DOI:10.1007/s00397-003-0310-2.
- [80] P. J. Halley, M. E. Mackay, G. A. George. Determining the gel point of an epoxy resin by various rheological methods. *High Perform. Polym.* **1994**;6. 4:405–14. DOI:10.1088/0954-0083/6/4/008.
- [81] B.-S. Chiou, R. J. English, S. A. Khan. Rheology and Photo-Cross-Linking of Thiol–Ene Polymers. *Macromolecules* **1996**;29. 16:5368–74. DOI:10.1021/ma960383e.
- [82] G. Wuzella, A. R. Mahendran, C. Beuc, H. Lammer. Isoconversional cure kinetics of a novel thermosetting resin based on linseed oil. *J. Therm. Anal. Calorim.* **2020**;142. 2:1055–71. DOI:10.1007/s10973-020-09529-7.
- [83] D. Dörr, U. Kuhn, V. Altstädt. Rheological study of gelation and crosslinking in chemical modified polyamide 12 using a multiwave technique. *Polymers* **2020**;12. 4:1–10. DOI:10.3390/polym12040855.
- [84] B. Wunderlich. Thermal analysis of polymeric materials. Berlin, Heidelberg: Springer; **2005**.
- [85] S. Tanaka. Theory of power-compensated DSC. *Thermochim. Acta* **1992**;210. 21:67–76. DOI:10.1016/0040-6031(92)80277-4.
- [86] W. Stark. Investigation of curing behaviour of melamine/phenolic (MP) thermosets. *Polym. Test.* **2010**;29. 6:723–8. DOI:10.1016/j.polymertesting.2010.05.008.
- [87] M. V. Alonso, M. Oliet, J. M. Pérez, F. Rodríguez, J. Echeverría. Determination of curing kinetic parameters of lignin–phenol–formaldehyde resol resins by several dynamic differential scanning calorimetry methods. *Thermochim. Acta* **2004**;419. 1-2:161–7. DOI:10.1016/j.tca.2004.02.004.
- [88] H. Ishida, Y. Rodriguez. Curing kinetics of a new benzoxazine-based phenolic resin by differential scanning calorimetry. *Polymer* **1995**;36. 16:3151–8. DOI:10.1016/0032-3861(95)97878-J.
- [89] B.-D. Park, B. Riedl, E. W. Hsu, J. Shields. Differential scanning calorimetry of phenol–formaldehyde resins cure-accelerated by carbonates. *Polymer* **1999**;40. 7:1689–99. DOI:10.1016/S0032-3861(98)00400-5.
- [90] E. S. de Medeiros, J. A. M. Agnelli, K. Joseph, L. H. de Carvalho, L. H. C. Mattoso. Curing behavior of a novolac-type phenolic resin analyzed

- 
- by differential scanning calorimetry. *J. Appl. Polym. Sci.* **2003**;90. 6:1678–82. DOI:10.1002/app.12838.
- [91] C. Rauwendaal, P. J. Gramann. Plasticating. In: T. A. Osswald, L.-S. Turng, P. J. Gramann, J. Beaumont. *Injection molding handbook*, 2nd ed. Munich: Hanser; **2007**, p. 125–180.
- [92] P. Thienel, B. Hoster, H. Bayerl, U. Braun. A mold with a window allows the development of the filling pattern for thermosetting molding compounds. *Kunststoffe Int.* **1990**;80. 12:11–3.
- [93] N. T. Tran, S. English, M. Gehde. Visualization of Wall Slip During Thermoset Phenolic Resin Injection Molding. *Int. J. Adv. Manuf. Tech.* **2018**;3. 9-12:1–7. DOI:10.1007/s00170-017-1524-2.
- [94] T. Ohta, H. Yokoi. Visual analysis of cavity filling and packing process in injection molding of thermoset phenolic resin by the gate-magnetization method. *Polym. Eng. Sci.* **2001**;41. 5:806–19. DOI:10.1002/pen.10778.
- [95] Raschig GmbH. Processing and mould design recommendations; **n.d.**
- [96] Plastics Engineering Company. Thermoset injection mold design tips; **2017**.
- [97] W. Michaeli, T. Kloubert. Application of the cold-runner-technology for free flowing thermosetting molding compounds. In: Society of Plastics Engineers. *ANTEC 1995*. Boston; **1995**, p. 832–838.
- [98] B. Catoen, H. Rees. Injection mold design handbook. Munich: Hanser; **2021**.
- [99] W. Kaiser. Kunststoffchemie für Ingenieure. Translated title: Polymer chemistry for engineers. Munich: Hanser; **2015**.
- [100] G. B. M. Fischbach. Prozessführung beim Spritzgießen härtpbarer Formmassen. Original language: German. Translated title: Process control in injection molding of thermosetting molding compounds. Dissertation. Aachen: RWTH Aachen; **1988**.
- [101] H.-F. Buchmann. Höhere Prozesssicherheit beim Spritzgießen von Epoxid-Formmassen. Translated title: Higher process reliability in the injection molding of epoxy molding compounds; **n.d.**
- [102] Plastics Engineering Company. Injection molding startup procedure for phenolic and melamine-phenolic molding compounds; **2014**.
- [103] F. Wittemann, R. Maertens, A. Bernath, M. Hohberg, L. Kärger, F. Henning. Simulation of reinforced reactive injection molding with the finite volume method. *J. Compos. Sci.* **2018**;5. 2:1–16. DOI:10.3390/jcs2010005.

- [104] T. Ageyeva, S. Horváth, J. G. Kovács. In-mold sensors for injection molding: On the way to industry 4.0. *Sensors* **2019**;19. 16:2–21. DOI:10.3390/s19163551.
- [105] T. Scheffler, H. Saalbach, S. Englich, M. Gehde. Process monitoring during injection moulding of thermosetting materials. *Int. Polym. Sci. Technol.* **2015**;42. 5:234–40.
- [106] M. Rath, J. Döring, W. Stark, G. Hinrichsen. Process monitoring of moulding compounds by ultrasonic measurements in a compression mould. *NDT & E Int.* **2000**;33. 2:123–30. DOI:10.1016/S0963-8695(99)00029-8.
- [107] H. Saiki, Z. H. Zhan, Y. Marumo, S. Miyhara, T. Morooka. Ultrasonic examination of curing state of thermosets used for plastic encapsulated ICs and contact state in molding processes. *JSMET* **1996**;62. 593:353–8. DOI:10.1299/kikaic.62.353.
- [108] M. Sernek, F. A. Kamke. Application of dielectric analysis for monitoring the cure process of phenol formaldehyde adhesive. *Int. J. Adhes. Adhes.* **2007**;27. 7:562–7. DOI:10.1016/j.ijadhadh.2006.10.004.
- [109] C. Wieland, N. Topic, J. Hirz. More precision for sensitive fast curing compounds: APC plus from KraussMaffei now available for thermosets. *Kunststoffe Int.* **2018**;156. 12:20–3.
- [110] C. Rauwendaal. Polymer extrusion. 5th ed. Munich: Hanser; **2014**.
- [111] T. Löhl, M. Weidlich, S. Wolf. The injection molding machine as measuring instrument: In-process quality assurance procedure for thermosetting plastics. *Kunststoffe Int.* **2016**;124. 4:32–6.
- [112] S. Kruppa. Adaptive Prozessführung und alternative Einspritzkonzepte beim Spritzgießen von Thermoplasten. Original language: German. Translated title: Adaptive process control and alternative injection concepts in the injection molding of thermoplastics. Dissertation. Duisburg: Universität Duisburg-Essen; **2015**.
- [113] F. A. Heinzler, S. Kruppa, R. Schiffers, J. Wortberg. Useful process data from the injection molding machine. *Kunststoffe Int.* **2014**;98. 2:42–6.
- [114] F. Truckenmüller. Direktverarbeitung von Endlosfasern auf Spritzgießmaschinen: Möglichkeiten und Grenzen. Original language: German. Translated title: Direct processing of continuous fibers on injection molding machines: Possibilities and limitations. Dissertation. Stuttgart: Universität Stuttgart; **1996**.

- 
- [115] T. Lucyshyn, M. Kipperer, C. Kukla, G. R. Langecker, C. Holzer. A physical model for a quality control concept in injection molding. *J. Appl. Polym. Sci.* **2012**;124. 6:4927-4394. DOI:10.1002/app.35590.
- [116] R. Schiffers. Verbesserung der Prozessfähigkeit beim Spritzgießen durch Nutzung von Prozessdaten und eine neuartige Schneckenhubführung. Original language: German. Translated title: Improving process capability in injection molding by using process data and a new type of screw stroke guide. Dissertation. Duisburg: Universität Duisburg-Essen; **2009**.
- [117] W. Woebcken. Processes and devices for controlled injection molding on different plastic injection molding machines with the same molded part properties and the same masses. DE3524310C1; **1986**.
- [118] M. Cavic. Kontinuierliche Prozeßüberwachung beim Spritzgießen unter Einbeziehung von Konzepten zur Verbesserung der Schmelzequalität. Original language: German. Translated title: Continuous process monitoring in injection molding, with incorporation of concepts for improving melt quality. Dissertation. Stuttgart: Universität Stuttgart; **2005**.
- [119] Sumitomo Bakelite Europe n.v. Technical data sheet Porophen® GF9201L12a; **2019**.
- [120] H. Saalbach, T. Maenz, S. Englisch, K. Raschke, T. Scheffler, S. Wolf et al. Faserverstärkte Duroplaste für die Großserienfertigung im Spritzgießen: Ergebnisbericht des BMBF-Verbundprojektes FiberSet. Translated title: Fiber-reinforced thermosets for high-volume production in injection molding; **2015**.
- [121] K. Raschke. Grundlagenuntersuchungen zur Prozess- und Struktursimulation von Phenolharzformmassen mit Kurz- und Langglasfaserverstärkung. Original language: German. Translated title: Fundamental investigations on process and structure simulation of phenolic resin molding compounds with short and long glass fiber reinforcement. Dissertation. Chemnitz: Technische Universität Chemnitz; **2017**.
- [122] F. Truckenmüller, H.-G. Fritz. Injection molding of long fiber-reinforced thermoplastics: A comparison of extruded and pultruded materials with direct addition of roving strands. *Polym. Eng. Sci.* **1991**;31. 18:1316–29. DOI:10.1002/pen.760311806.
- [123] M. McLeod, É. Baril, J.-F. Héту, T. Deaville, M. N. Bureau. Morphological and mechanical comparison of injection and compression moulding in-line compounding of direct long fibre thermoplastics. In:

- Society of Plastics Engineers. *ACCE 2010*: Troy, Red Hook, NY: Curran; **2010**, p. 109–118.
- [124] F. Truckenmüller. Direct processing of continuous fibers onto injection molding machines. *J. Reinf. Plast. Comp.* **1993**;12. 6:624–32. DOI:10.1177/073168449301200601.
- [125] J. Markarian. Long fibre reinforced thermoplastics continue growth in automotive. *Plast. Add. Comp.* **2007**;9. 2:20–4. DOI:10.1016/S1464-391X(07)70025-9.
- [126] A. Roch, T. Huber, F. Henning, P. Elsner. LFT foam: Lightweight potential for semi-structural components through the use of long-glass-fiber-reinforced thermoplastic foams. In: V. Altstadt, J.-H. Keller, A. Fathi. *Proceedings of PPS-29: The 29th International Conference of the Polymer Processing Society*. AIP Publishing; **2014**, p. 471–476. DOI:10.1063/1.4873824.
- [127] C. Lohr, B. Beck, F. Henning, K. A. Weidenmann, P. Elsner. Mechanical properties of foamed long glass fiber reinforced polyphenylene sulfide integral sandwich structures manufactured by direct thermoplastic foam injection molding. *Compos. Struct.* **2019**;220. 14:371–85. DOI:10.1016/j.compstruct.2019.03.056.
- [128] C. Weber, S. Ledebuhr, R. Enochs, J. Busch. A novel, new direct injection technology for in-line compounding and molding of LFT automotive structures. In: Society of Automotive Engineers, Inc. *Proceedings of the 2002 SAE International Body Engineering Conference and Automotive & Transportation Technology Conference*; **2002**, p. 1–4. DOI:10.4271/2002-01-2036.
- [129] P. Hirsch, M. Menzel, J. Klehm, P. Putsch. Direct compounding injection molding and resulting properties of ternary blends of polylactide, polybutylene succinate and hydrogenated styrene farnesene block copolymers. *Macromol. Symp.* **2019**;384. 1:1–6. DOI:10.1002/masy.201800167.
- [130] P. Heidenmeyer, C. Deubel, K. Kretschmer, K. Schink. Spritzgießanlage und Spritzgießverfahren zur Herstellung von faserverstärkten Kunststoffteilen. Translated title: Injection molding machine and injection molding method for the production of fiber-reinforced plastic parts. DE102012217586A1; **2014**.
- [131] M. Holmes. Expanding the market for long fiber technology. *Reinf. Plast.* **2018**;62. 3:154–8. DOI:10.1016/j.repl.2017.11.005.



- 
- [132] B. Keck. Economical alternative to high-performance polymer: Ros reduces costs and part weight with fiber direct compounding. *Kunststoffe Int.* **2017**;141. 9:39–41.
- [133] P. Putsch. Compounding-injection moulding process and device. WO92/00838; **1992**.
- [134] E. Moritzer, C. Budde, E. Albring. Fiber length reduction and homogeneity of injection-molded short fiber reinforced thermoplastics with special regard to the influence of a static mixing nozzle. In: Society of Plastics Engineers. *ANTEC 2012*. Orlando; **2012**, p. 1487–1493.
- [135] P. Kubik, J. Vlcek, C. Tzoganakis, L. Miller. Method of analyzing and quantifying the performance of mixing sections. *Polym. Eng. Sci.* **2012**;52. 6:1232–40. DOI:10.1002/pen.22191.
- [136] C. P. J. M. Verbraak, H. E. H. Meijer. Screw design in injection molding. *Polym. Eng. Sci.* **1989**;29. 7:479–87. DOI:10.1002/pen.760290708.
- [137] Y. Wang, J.-S. Huang. Single screw extrusion compounding of particulate filled thermoplastics: State of dispersion and its influence on impact properties. *J. Appl. Polym. Sci.* **1996**;60. 11:1779–91. DOI:10.1002/(SICI)1097-4628(19960613)60:11<1779:AID-APP1>3.0.CO;2-I.
- [138] M. Gale. Compounding with single-screw extruders. *Adv. Polym. Tech.* **1997**;16. 4:251–62. DOI:10.1002/(SICI)1098-2329(199711)16:4<251:AID-ADV1>3.0.CO;2-U.
- [139] B. A. Salamon, M. A. Spalding, J. R. Powers, M. Serrano, W. C. Sumner. Color mixing performance in injection molding. *Plast. Eng.* **2001**. 4:52–8.
- [140] Odenwalder Filtersysteme GmbH. OFS-mixing-nozzle type FMD; Available from: <https://www.ofs-filtersysteme.de/english.html>.
- [141] Z. Tadmor, I. Klein. Design of certain fluted mixing sections of extruder screws. *Polym. Eng. Sci.* **1973**;13. 5:382–9. DOI:10.1002/pen.760130510.
- [142] B. Elbirli, J. T. Lindt, S. R. Gottgetreu. Analysis of the performance of maddock head mixer. In: Society of Plastics Engineers. *ANTEC 1983*. Chicago; **1993**, p. 104–108.
- [143] C. Rauwendaal. Design of fluted mixing sections. In: Society of Plastics Engineers. *ANTEC 1984*. New Orleans; **1984**, p. 59–63.

- [144] X. Sun, Q. Gou, M. A. Spalding, T. W. Womer, N. Uzelac. Optimization of maddock-style mixers for single-screw extrusion. In: Society of Plastics Engineers. *ANTEC 2016*. Indianapolis; **2016**, p. 898–904.
- [145] X. Sun, M. A. Spalding, T. W. Womer, N. Uzelac. Design optimization of maddock mixers for single-screw extrusion using numerical simulation. In: Society of Plastics Engineers. *ANTEC 2017*. Anaheim; **2017**, p. 1017–1023.
- [146] M. Esseghir, C. G. Gogos, D.-W. Yu, D. B. Todd, B. David. A comparative study on the performance of three single-screw elements in melt-melt mixing of immiscible blends. *Adv. Polym. Tech.* **1998**;17. 1:1–17. DOI:10.1002/(SICI)1098-2329(199821)17:1<1:AID-ADV1>3.0.CO;2-Y.
- [147] C. Rauwendaal. The ABC's of extruder screw design. *Adv. Polym. Tech.* **1989**;9. 4:301–8. DOI:10.1002/adv.1989.060090404.
- [148] H. Potente, W. H. Többen. Improved design of shearing sections with new calculation models based on 3D finite-element simulations. *Macromol. Mater. Eng.* **2002**;287. 11:808–14. DOI:10.1002/mame.200290010.
- [149] P. Kubik, M. Zatloukal, Y. Asai, J. Vlcek, I. Paseka, R. Haruna et al. Experimental and numerical analysis of performance of two fluted mixer designs. *Plast. Rubber Compos.* **2014**;43. 10:337–46. DOI:10.1179/1743289814Y.0000000105.
- [150] C. Rauwendaal, P. Gramann, B. A. Davis. New dispersive mixers for single screw extruders. In: Society of Plastics Engineers. *ANTEC 1998*. Atlanta; **1998**, p. 111–116.
- [151] C. Rauwendaal. Screw extruder with improved dispersive mixing. US5932159; **1999**.
- [152] M. Guo, X. Li, J. M. Maia. Fiber length distribution in twin-screw extrusion of fiber-reinforced polymer composites: A comparison between shear and extensional mixing. *IPP* **2021**;36. 4:350–7. DOI:10.1515/ipp-2020-3978.
- [153] S. Kruppa, G. Karrenberg, J. Wortberg, R. Schiffers, G. P. Holzinger. Backflow compensation for thermoplastic injection molding. In: Society of Plastics Engineers. *ANTEC 2016*. Indianapolis; **2016**, p. 1034–1039.
- [154] S. Kruppa, J. Wortberg, R. Schiffers. Injection molding is getting more continuous. *Kunststoffe Int.* **2016**;129. 9:81–4.

- 
- [155] S. Kruppa, S. Moser, M. Busl, J. Wortberg. Method for operating an injection molding machine. EP3294519B1; **2017**.
- [156] S. Goris, T. Back, A. Yanev, D. Brands, D. Drummer, T. A. Osswald. A novel fiber length measurement technique for discontinuous fiber-reinforced composites: A comparative study with existing methods. *Polym. Compos.* **2018**;39. 11:4058–70. DOI:10.1002/pc.24466.
- [157] M. R. Hartwich, N. Höhn, H. Mayr, K. Sandau, R. Stengler. FASEP ultra-automated analysis of fibre length distribution in glass-fibre-reinforced products. In: P. H. Lehmann. *Optical measurement systems for industrial inspection VI*. Munich; **2009**, p. 1–6. DOI:10.1117/12.827503.
- [158] V. Kunc, B. Frame, B. N. Nguyen, C. L. Tucker, G. Velez-Garcia. Fiber length distribution measurement for long glass and carbon fiber reinforced injection molded thermoplastics. In: Society of Plastics Engineers. *ANTEC 2007*. Cincinnati; **2007**, p. 1003–1029.
- [159] S. H. Bumm, J. L. White, A. I. Isayev. Glass fiber breakup in corotating twin screw extruder: Simulation and experiment. *Polym. Compos.* **2012**;33. 12:2147–58. DOI:10.1002/pc.22356.
- [160] R. M. Bajracharya, A. C. Manalo, W. Karunasena, K.-T. Lau. Experimental and theoretical studies on the properties of injection moulded glass fibre reinforced mixed plastics composites. *Compos. Part A Appl. Sci. Manuf.* **2016**;84. 5:393–405. DOI:10.1016/j.compositesa.2016.02.025.
- [161] J. Wang, C. Geng, F. Luo, Y. Liu, K. Wang, Q. Fu et al. Shear induced fiber orientation, fiber breakage and matrix molecular orientation in long glass fiber reinforced polypropylene composites. *Mat. Sci. Eng. A.-Struct.* **2011**;528. 7:3169–76. DOI:10.1016/j.msea.2010.12.081.
- [162] M. Teßmann, S. Mohr, S. Gayetskyy, U. Haßler, R. Hanke, G. Greiner. Automatic determination of fiber-length distribution in composite material using 3D CT data. *EURASIP J. Adv. Signal Process.* **2010**;2010. 1:1–9. DOI:10.1155/2010/545030.
- [163] D. Salaberger, K. A. Kannappan, J. Kastner, J. Reussner, T. Auinger. Evaluation of computed tomography data from fibre reinforced polymers to determine fibre length distribution. *IPP* **2011**;26. 3:283–91. DOI:10.3139/217.2441.
- [164] P. Pinter, B. Bertram, K. A. Weidenmann. A novel method for the determination of fiber length distributions from  $\mu$ CT-data. In: Universi-

- ty of Applied Sciences Upper Austria. *6th Conference on Industrial Computed Tomography*; **2016**, p. 1–8.
- [165] C. Lohr. Prozess-Struktur-Eigenschafts-Beziehung integral im Hochdruckverfahren gefertigter, langglasfaserverstärkter Polymer-schaumsandwichbauteile. Original language: German. Translated title: Process-structure-property relationship of integral high pressure fabricated long glass fiber reinforced polymer foam sandwich components. Dissertation: Karlsruhe Institute of Technology (KIT); **2018**.
- [166] P. Hancock, R. C. Cuthbertson. The effect of fibre length and interfacial bond in glass fibre-epoxy resin composites. *J. Mater. Sci.* **1970**;5. 9:762–8. DOI:10.1007/BF00562162.
- [167] D. McNally, W. T. Freed, J. R. Shaner, W. Sell. A method to evaluate the effect of compounding technology on the stress transfer interface in short fiber reinforced thermoplastics. *Polym. Eng. Sci.* **1978**;18. 5:396–403. DOI:10.1002/pen.760180511.
- [168] T. Ohsawa, A. Nakayama, M. Miwa, A. Hasegawa. Temperature dependence of critical fiber length for glass fiber-reinforced thermosetting resins. *J. Appl. Polym. Sci.* **1978**;22. 11:3203–12. DOI:10.1002/app.1978.070221115.
- [169] J. L. Thomason. The Influence of fibre length and concentration on the properties of glass fibre-reinforced polypropylene: 6. The properties of injection moulded long fibre PP at high fibre content. *Compos. Part A Appl. Sci. Manuf.* **2005**;36. 7:995–1003. DOI:10.1016/j.compositesa.2004.11.004.
- [170] W. Thodsaratpreeyakul, P. Uawongsuwan, A. Kataoka, T. Negoro, H. Hamada. The determination of interfacial shear strength in short fiber reinforced poly ethylene terephthalate by Kelly-Tyson theory. *OJCM* **2017**;07. 04:218–26. DOI:10.4236/ojcm.2017.74015.
- [171] J. L. Thomason. The Influence of fibre length and concentration on the properties of glass fibre-reinforced polypropylene: 7. Interface strength and fibre strain in injection moulded long fibre PP at high fibre content. *Compos. Part A Appl. Sci. Manuf.* **2007**;38. 1:210–6. DOI:10.1016/j.compositesa.2006.01.007.
- [172] J. L. Thomason, M. A. Vlug, G. Schipper, H. Krikor. Influence of fibre length and concentration on the properties of glass fibre-reinforced polypropylene: Part 3. Strength and strain at failure. *Compos. Part A Appl. Sci. Manuf.* **1996**;27. 11:1075–84. DOI:10.1016/1359-835X(96)00066-8.

- 
- [173] Z. Yu, J. Brisson, A. Ait-Kadi. Prediction of mechanical properties of short kevlar fiber-nylon-6,6 composites. *Polym. Compos.* **1994**;15. 1:64–73. DOI:10.1002/pc.750150110.
- [174] T. Lacroix, B. Tilmans, R. Keunings, M. Desaegeer, I. Verpoest. Modelling of critical fibre length and interfacial debonding in the fragmentation testing of polymer composites. *Compos. Sci. Technol.* **1992**;43. 4:379–87. DOI:10.1016/0266-3538(92)90061-7.
- [175] S. F. Zhandarov, E. V. Pisanova. Two interfacial shear strength calculations based on the single fiber composite test. *Mech. Compos. Mater.* **1996**;31. 4:325–36. DOI:10.1007/BF00632619.
- [176] P. A. Templeton. Strength predictions of injection molding compounds. *J. Reinf. Plast. Comp.* **1990**;9. 3:210–25. DOI:10.1177/073168449000900301.
- [177] H. Fukuda, T.-W. Chou. A probabilistic theory of the strength of short-fibre composites with variable fibre length and orientation. *J. Mater. Sci.* **1982**;17. 4:1003–11. DOI:10.1007/BF00543519.
- [178] J. C. Halpin, J. L. Kardos. Strength of discontinuous reinforced composites: I. Fiber reinforced composites. *Polym. Eng. Sci.* **1978**;18. 6:496–504. DOI:10.1002/pen.760180612.
- [179] Granta Design Limited. CES EduPack. Cambridge; **2019**; Available from: <https://www.ansys.com/products/materials/granta-edupack/>.
- [180] 3B Fibreglass. Technical data sheet chopped strands DS5163-13P; **2020**.
- [181] 3B Fibreglass. Technical data sheet direct roving 111AX11; **2020**.
- [182] R. von Turkovich, L. Erwin. Fiber fracture in reinforced thermoplastic processing. *Polym. Eng. Sci.* **1983**;23. 13:743–9. DOI:10.1002/pen.760231309.
- [183] R. K. Mittal, V. B. Gupta, P. K. Sharma. Theoretical and experimental study of fibre attrition during extrusion of glass-fibre-reinforced polypropylene. *Compos. Sci. Technol.* **1988**;31. 4:295–313. DOI:10.1016/0266-3538(88)90035-8.
- [184] T. Sasayama, M. Inagaki, N. Sato. Direct simulation of glass fiber breakage in simple shear flow considering fiber-fiber interaction. *Compos. Part A Appl. Sci. Manuf.* **2019**;124. 9:1–10. DOI:10.1016/j.compositesa.2019.105514.
- [185] V. B. Gupta, R. K. Mittal, P. K. Sharma, G. Mennig, J. Wolters. Some studies on glass fiber-reinforced polypropylene.: Part I: Reduction in fi-

- ber length during processing. *Polym. Compos.* **1989**;10. 1:8–15. DOI:10.1002/pc.750100103.
- [186] O. Forgacs, S. Mason. Particle motions in sheared suspensions: IX. Spin and deformation of threadlike particles. *J. Colloid Sci.* **1959**;14. 5:457–72. DOI:10.1016/0095-8522(59)90012-1.
- [187] C. Servais, J.-A. E. Månson, S. Toll. Fiber–fiber interaction in concentrated suspensions: Disperse fibers. *J. Rheo.* **1999**;43. 4:991–1004. DOI:10.1122/1.551014.
- [188] P. Ren, G. Dai. Fiber dispersion and breakage in deep screw channel during processing of long fiber-reinforced polypropylene. *Fibers Polym.* **2014**;15. 7:1507–16. DOI:10.1007/s12221-014-1507-y.
- [189] R. Meyer, K. E. Almin, B. Steenberg. Length reduction of fibres subject to breakage. *Br. J. Appl. Phys.* **1966**;17. 3:409–16. DOI:10.1088/0508-3443/17/3/314.
- [190] K. Shon, D. Liu, J. L. White. Experimental studies and modeling of development of dispersion and fiber damage in continuous compounding. *IPP* **2005**;20. 3:322–31. DOI:10.3139/217.1894.
- [191] B. Franzén, C. Klason, T. Kubát, T. Kitano. Fibre degradation during processing of short fibre reinforced thermoplastics. *Compos.* **1989**;20. 1:65–76. DOI:10.1016/0010-4361(89)90684-8.
- [192] R. Singh, F. Chen, F. R. Jones. Injection molding of glass fiber reinforced phenolic composites. 2: Study of the injection molding process. *Polym. Compos.* **1998**;19. 1:37–47. DOI:10.1002/pc.10073.
- [193] U. N. Gandhi, S. Goris, T. A. Osswald, Y.-Y. Song. Discontinuous fiber-reinforced composites: Fundamentals and Applications. Munich, Cincinnati: Hanser; **2020**.
- [194] T. Deringer, T. Kleffel, D. Drummer. Integrative manufacturing of thermoset injection molding components with continuous fiber-reinforcement. *Int. J. Plast. Technol.* **2019**. 1:169–87. DOI:10.3139/O999.03022019.
- [195] D. Niedziela, J. Tröltzsch, A. Latz, L. Kroll. On the numerical simulation of injection molding processes with integrated textile fiber reinforcements. *J. Thermoplast. Compos. Mater.* **2013**;26. 1:74–90. DOI:10.1177/0892705711419695.
- [196] T. Müller, D. Drummer. In-mould impregnation: An energy efficient process for lightweight construction. *Kunststoffe Int.* **2012**;102. 6:50–3.
- [197] R. Christie, A. Abel. Phthalocyanine pigments: General principles. *Phys. Sci. Rev.* **2021**;6. 11:671–7. DOI:10.1515/psr-2020-0194.

- 
- [198] DIN EN ISO. 11357-5 Differential scanning calorimetry (DSC): Determination of characteristic reaction-curve temperatures and times, enthalpy of reaction and degree of conversion; **2013**.
- [199] A. Šahinović, B. Mušič. Improvement of the mechanical properties of thermosetting-binding-system-based composites by means of kneading procedure modification and composite formulation. *Processes* **2020**;8. 5:1–13. DOI:10.3390/pr8050625.
- [200] J. C. Russ, F. B. Neal. The Image Processing Handbook. 7th ed. Boca Raton: CRC Press; **2018**.
- [201] R. M. Haralick, K. Shanmugam, I. Dinstein. Textural features for image classification. *IEEE Trans. Syst., Man, Cybern.* **1973**;3. 6:610–21. DOI:10.1109/TSMC.1973.4309314.
- [202] M. O'Byrne, B. Ghosh, V. Pakrashi, F. Schoefs. Texture analysis based detection and classification of surface features on ageing infrastructure elements. In: C. Caprani, A. O'Connor. *Proceedings of Bridge and Concrete Research in Ireland Conference*; **2012**, p. 223–228.
- [203] R. W. Connors, M. M. Trivedi, C. A. Harlow. Segmentation of a high-resolution urban scene using texture operators. *Comput. Gr. Image Process.* **1984**;25. 3:273–310. DOI:10.1016/0734-189X(84)90197-X.
- [204] N. C. da Silva, L. de Moura França, J. M. Amigo, M. Bautista, M. F. Pimentel. Evaluation and assessment of homogeneity in images. Part 2: Homogeneity assessment on single channel non-binary images. Blending end-point detection as example. *Chemom. Intell. Lab. Syst.* **2018**;180. 9:15–25.
- [205] L. de Moura França, J. M. Amigo, C. Cairós, M. Bautista, M. F. Pimentel. Evaluation and assessment of homogeneity in images. Part 1: Unique homogeneity percentage for binary images. *Chemom. Intell. Lab. Syst.* **2017**;171. 12:26–39. DOI:10.1016/j.chemolab.2017.10.002.
- [206] M. Ávila, D. Caballero, T. Antequera, M. L. Durán, A. Caro, T. Pérez-Palacios. Applying 3D texture algorithms on MRI to evaluate quality traits of loin. *J. Food Eng.* **2018**;222. 7:258–66. DOI:10.1016/j.jfoodeng.2017.11.028.
- [207] MathWorks. Derive statistics from GLCM and plot correlation. [August 09, 2022]; Available from: <https://de.mathworks.com/help/images/derive-statistics-from-g lcm-and-plot-correlation.html>.
- [208] L. Tesar, A. Shimizu, D. Smutek, H. Kobatake, S. Nawano. Medical image analysis of 3D CT images based on extension of Haralick texture

- features. *Comput. Med. Imaging Graph.* **2008**;32. 6:513–20. DOI:10.1016/j.compmedimag.2008.05.005.
- [209] L. Tesar, D. Smutek, A. Shimizu, H. Kobatake. 3D extension of Haralick texture features for medical image analysis. In: R. Sablatnig, O. Scherzer. *Proceedings of the Fourth IASTED International Conference on Signal Processing, Pattern Recognition, and Applications*. Anaheim: Acta Press; **2007**, p. 1–6.
- [210] A. Graumann, C. Dietz. ImageJ implementation of Haralick texture features. University of Konstanz; **2021**; Available from: <https://github.com/imagej/imagej-ops/tree/master/src/main/java/net/imagej/ops/features/haralick>.
- [211] R. W. Conners, C. A. Harlow. A theoretical comparison of texture algorithms. *IEEE Trans. Pattern Anal. Machine Intell.* **1980**;2. 3:204–22. DOI:10.1109/tpami.1980.4767008.
- [212] S. Tröster. Materialentwicklung und -charakterisierung für thermoplastische Faserverbundwerkstoffe im Direktverfahren. Original language: German. Translated title: Material development and characterization for thermoplastic fiber-reinforced composites in a direct processing method. Dissertation. Stuttgart: Stuttgart University; **2003**.
- [213] N. Weigel. Influence of fiber length and content on the quasi-static mechanical properties of long glass fiber reinforced phenolic resins. Bachelor Thesis. Karlsruhe: Karlsruhe Institute of Technology (KIT); **2021**.
- [214] T. König. Conveying and kneading elements, geometry of co-rotating extruders: Including clearance strategies. In: K. Kohlgrüber. *Co-Rotating Twin-Screw Extruders: Fundamentals*. Munich: Hanser; **2020**, p. 101–118.
- [215] H. Bremer. Compounding and characterization of glass fiber reinforced phenolic molding compounds. Master Thesis. Karlsruhe: Karlsruhe Institute of Technology (KIT); **2020**.
- [216] A. Dreiblatt, E. L. Canedo. Distribution of specific energy in twin-screw corotating extruders using one-dimensional process simulation. In: Society of Plastics Engineers. *ANTEC 2012*. Orlando; **2012**, p. 993–998.
- [217] C. Abeykoon, A. L. Kelly, E. C. Brown, J. Vera-Sorroche, P. D. Coates, E. Harkin-Jones et al. Investigation of the process energy demand in polymer extrusion: A brief review and an experimental study. *Applied Energy* **2014**;136. 24:726–37. DOI:10.1016/j.apenergy.2014.09.024.



- 
- [218] F. Inceoglu, J. Ville, N. Ghamri, J. L. Pradel, A. Durin, R. Valette et al. Correlation between processing conditions and fiber breakage during compounding of glass fiber-reinforced polyamide. *Polym. Compos.* **2011**;32. 11:1842–50. DOI:10.1002/pc.21217.
- [219] Brabender Technologie GmbH & Co. KG. Twin screw feeder DDSR20. [August 09, 2022]; Available from: <https://www.brabender-technologie.com/en/products/doppelschneckenextruder-ddsr20-56/>.
- [220] KraussMaffei Extrusion GmbH. UltraFeed side feeder vacuum degassing. [August 09, 2022]; Available from: <https://www.kraussmaffei.com/en/our-products/ultrafeed-side-feeder-vacuum-degassing>.
- [221] Van der Mast - Fiber Chopping Machines. Fiber chopper - chopcot® T5. [August 09, 2022]; Available from: <https://www.chopcot.com/fiber-chopping-machines/fiber-chopper-chopcot-T5.html>.
- [222] Universität Paderborn. PSI: Paderborner Spritzgießsimulation. Translated title: PSI - Paderborn injection molding simulation; **2021**; Available from: <https://ktp.uni-paderborn.de/en/foerderverein/software/psi>.
- [223] P. H. Squires. Screw extrusion-flow patterns and recent theoretical developments. *Polym. Eng. Sci.* **1964**;4. 1:7–16. DOI:10.1002/pen.760040104.
- [224] DIN EN ISO. 178 Plastics – Determination of flexural properties; **2013**.
- [225] R. Nock, F. Nielsen. Statistical region merging. *IEEE Trans. Pattern Anal. Machine Intell.* **2004**;26. 11:1452–8. DOI:10.1109/TPAMI.2004.110.
- [226] J. Schindelin, I. Arganda-Carreras, E. Frise, V. Kaynig, M. Longair, T. Pietzsch et al. Fiji: an open-source platform for biological-image analysis. *Nat. Methods* **2012**;9. 7:676–82. DOI:10.1038/nmeth.2019.
- [227] M. Nägele. Influence of fiber length and content on the dynamic mechanical properties of long glass fiber reinforced phenolic resins. Bachelor Thesis. Karlsruhe: Karlsruhe Institute of Technology (KIT); **2022**.
- [228] A. Hees. Characterisation of fibre length and mechanical properties of injection moulded fibre reinforced thermoset composites. Bachelor Thesis. Karlsruhe: Karlsruhe Institute of Technology (KIT); **2019**.
- [229] D. Methe, M. Gehde. Analysis of the flow-curing behavior of chemically foamable phenolic molding compounds in the extrusion process. *J. Plast. Tech.* **2020**. 5:227–54. DOI:10.3139/O999.04052020.

- [230] R. Rudolf. General overview of the compounding process: Tasks, selected applications, and process zones. In: K. Kohlgrüber. *Co-Rotating Twin-Screw Extruders: Fundamentals*. Munich: Hanser; **2020**.
- [231] M. Arroyo, F. Avalos. Polypropylene/low density polyethylene blend matrices and short glass fibers based composites. I. Mechanical degradation of fibers as a function of processing method. *Polym. Compos.* **1989**;10. 2:117–21. DOI:10.1002/pc.750100209.
- [232] M. Priebe, R. Schledjewski. Processing and properties of glass/polypropylene in long fibre compounding extrusion. *Plast. Rubber Compos.* **2011**;40. 6-7:374–9. DOI:10.1179/1743289810Y.0000000035.
- [233] J. L. Thomason, M. A. Vluc. Influence of fibre length and concentration on the properties of glass fibre-reinforced polypropylene: 1. Tensile and flexural modulus. *Compos. Part A Appl. Sci. Manuf.* **1996**;27. 6:477–84. DOI:10.1016/1359-835X(95)00065-A.
- [234] S. S. Teller, J. S. Bergstrom. Tensile specimen preparation method impacting failure behavior. In: Society of Plastics Engineers. *ANTEC 2021*. Online; **2021**, p. 280–285.
- [235] F. T. Wallenberger. Commercial and experimental glass fibers. In: F. T. Wallenberger, P. A. Bingham. *Fiberglass and glass technology: Energy-friendly compositions and applications*. New York, NY: Springer; **2010**, p. 3–90.
- [236] J. Shapiro, A. L. Halmos, J. Pearson. Melting in single screw extruders. *Polymer* **1976**;17. 10:905–18. DOI:10.1016/0032-3861(76)90258-5.
- [237] P. Elsner, P. Eyerer, T. Hirth. Verarbeitung (Urformen) von Kunststoffen zu Bauteilen. Translated title: Processing (primary shaping) of plastics into components. In: P. Elsner, P. Eyerer, T. Hirth. *Kunststoffe: Eigenschaften und Anwendungen*, 8th ed. Berlin, Heidelberg: Springer; **2012**, p. 65–104.
- [238] G. Schneider. Static mixing technology for extrusion and injection molding; **2012**.
- [239] Promix solutions. Static mixers solutions for injection molding; **2012**.
- [240] R. J. Farris. Prediction of the viscosity of multimodal suspensions from unimodal viscosity data. *Transactions of the Society of Rheology* **1968**;12. 2:281–301. DOI:10.1122/1.549109.
- [241] C. Chang, R. L. Powell. Effect of particle size distributions on the rheology of concentrated bimodal suspensions. *J. Rheo.* **1994**;38. 1:85–98. DOI:10.1122/1.550497.

- 
- [242] V. Fidleris, R. L. Whitmore. The physical interaction of spherical particles in suspensions. *Rheol. Acta* **1961**;1. 4-6:573–80. DOI:10.1007/BF01989126.
- [243] E. Moritzer, F. Bürenhaus. Influence of processing parameters on fiber length degradation during injection molding. In: Society of Plastics Engineers. *ANTEC 2021*. Online; **2021**, p. 219–223.
- [244] E. Lafranche, P. Krawczak, J.-P. Ciolczyk, J. Maugey. Injection moulding of long glass fiber reinforced polyamide 66: Processing conditions/microstructure/flexural properties relationship. *Adv. Polym. Tech.* **2005**;24. 2:114–31. DOI:10.1002/adv.20035.
- [245] E. Lafranche, P. Krawczak, J. P. Ciolczyk, J. Maugey. Injection moulding of long glass fibre reinforced polyamide 6-6: Guidelines to improve flexural properties. *Express Polym. Lett.* **2007**;1. 7:456–66. DOI:10.3144/expresspolymlett.2007.64.
- [246] T. Loken, T. A. Osswald, P. Gramann, S. Ziaee. The effects of injection molding process parameters on final fiber length of a short-fiber composite. In: Society of Plastics Engineers. *ANTEC 2007*. Cincinnati; **2007**, p. 1149–1161.
- [247] F. Willems, C. Bonten. Influence of processing on the fiber length degradation in fiber reinforced plastic parts. In: C. Holzer, M. Payer. *Proceedings of the Regional Conference Graz 2015: Polymer Processing Society PPS*. AIP Publishing; **2016**. DOI:10.1063/1.4965454.
- [248] S. J. DeTeresa. On the elastic buckling of rod-shaped particles in sheared suspensions. *J. Colloid Interface Sci.* **1993**;159. 2:400–4. DOI:10.1006/jcis.1993.1339.
- [249] L. M. Vas, S. Kling, T. Czigány, G. Czél. New method for determining the bending modulus of solid and hollow fibers from deflection tests. *Text. Res. J.* **2017**;87. 5:542–51. DOI:10.1177/0040517516632476.
- [250] H. D. Keyser, M. D. Muynck. Maertens, R. Composition of Porophen® long fiber granulate. Personal Communication; **2019**.